Universitat de Girona
Escola Politècnica Superior
Dept. d'Enginyeria Mecànica i de la Construcció Industrial

Simulation of interlaminar and intralaminar damage in polymer-based composites under low-velocity impact loading

Report for the FI grant of the Generalitat de Catalunya
supported by European Social funds.

Written by:

Emilio Vicente González Juan

2010

Advisors

Dr. Pedro P. Camanho
Universidade do Porto, Portugal

Dr. Pere Maimí Vert
Universitat de Girona, Spain

Contents

List de Figures **xi**

List de Tables **xiv**

1 Analytical description of the impact event **1**

1.1 Introduction 1

1.2 Impact behavior 2

1.3 Local deflection 5

1.3.1 Hertz contact law adapted for laminated composite plates . . 8

1.3.2 Unloading and reloading contact process 11

1.3.3 Elastic-plastic contact models 12

1.3.4 Linearized contact laws 14

1.4 Analytical impact models 14

1.4.1 Complete analytical models 16

1.4.2 Infinite plate impact models 21

1.4.3 Half-space impact models 27

1.4.4 Quasi-static impact models 28

1.5 Approaches for impact behavior description 30

1.5.1 Christoforou and Yigit characterization diagram 30

1.5.2 Olsson mass criterion 34

1.6 Impact damage and analytical thresholds 37

1.6.1 Matrix cracking 37

1.6.2 Delamination 42

1.6.3 Permanent indentation 48

1.6.4 Fiber failure 49

1.6.5 Perforation 49

2 Test configurations **53**

2.1 Introduction 53

2.2 Impact tests 54

2.2.1 Benchmark: ASTM drop-weight impact test 55

2.2.2 Selected studies: fixed and variable parameters 59

2.3 Compression after impact tests (CAI) 70

2.3.1 Benchmark: ASTM compression after impact test 70

2.3.2 Resources used and specimen instrumentation 72

3 Experimental results **75**

3.1 Introduction 75

3.2 Effect of ply thickness (clustering) 76

3.2.1 Impact tests 76

3.2.2 NDI: C-scan after impact 83

3.2.3 Dent-depth measurements 88

3.2.4 CAI tests 89

3.3 Effect of ply mismatch angle at interfaces 93

3.3.1 Impact tests 93

3.3.2 NDI: C-scan after impact 100

3.3.3 Dent-depth measurements 101

3.3.4 CAI tests 101

3.4 Effect of the laminate thickness 105

3.4.1 Impact tests 105

3.4.2 NDI: C-scan after impact 115

3.4.3 Dent-depth measurements 118

3.4.4 CAI tests 119

3.5 Summary of conclusions 121

4 Interlaminar damage model **129**

4.1 Introduction 129

4.2 Damage model formulation 133

4.2.1 Norm of the relative displacement vector 135

4.2.2 Surface of damage activation and law for damage evolution . . 136
4.2.3 Criterion for damage propagation 137
4.2.4 Criterion for damage onset 139
4.3 Formulation adaptations 140
4.3.1 Relation between relative displacements and strains 140
4.3.2 Penalty stiffness 141
4.3.3 Redefined onset and propagation damage criteria 142
4.4 Model implementation 145
4.4.1 Strategy of implementation 145
4.4.2 Input variables to define the model 146
4.4.3 Algorithm 147
4.5 Sizes of cohesive elements 151
4.5.1 Maximum thickness of volumetric cohesive elements 151
4.5.2 In-plane dimensions of the cohesive elements 153
4.6 Simulations 154
4.6.1 Considerations for quasi-static explicit simulations 155
4.6.2 MMB and ENF fracture toughness tests 156
4.6.3 TCT tests 162
4.7 Conclusions 167

A Governing equations of the plate 169
A.1 Ingredients for the development of the equations 170
A.1.1 Strain-displacement relations 171
A.1.2 Lamina constitutive equation 172
A.1.3 Laminate resultants 175
A.1.4 Frameworks to develop the governing equations 177
A.2 Plate theories and governing equations 182
A.2.1 Classical laminated plate theory 182
A.2.2 First-order shear plate theory 190

Bibliography 197

List of Figures

1.1 Impact responses (after Olsson [9]): (a) dominated by dilatational waves, (b) dominated by flexural and shear waves, and (c) quasi-static response. 3
1.2 Extreme plate responses under impact loading, (a) pure local deflection and (b) pure global deflection. 6
1.3 Coordinate systems. 9
1.4 Detail of the contact law phases. 14
1.5 Boundary conditions of simply supported plate. 16
1.6 Lumped-mass models for infinite plate behavior. 24
1.7 Spring-mass model for half-space impact behavior. 27
1.8 (a) Complete and (b) simplified spring-mass model for quasi-static impact behavior (Olsson [9]). 29
1.9 Impact characterization diagram (after Christoforou and Yigit [6, 7, 13, 14]): dimensionless maximum force $\bar{F}_{max}$ versus relative mobility ζ_w. 33
1.10 Type of matrix cracks in a [0/90/0] laminated composite plate (after Richardson and Wisheart [1]): (a) longitudinal view and (b) transverse view. 38
1.11 Projected damage patterns (after Abrate [5]): (a) pine tree and (b) reversed pine tree. 38
1.12 Example of peanut shaped delaminations. 44
1.13 Maximum delamination size as a function of the impact force for plates with different thickness (after Christoforou [6]). 45
1.14 Representative impact force versus time history (after ASTM D7136 / D7136M [45]). 45

2.1 (a) Impact support fixture; (b) detail of the support area and clamping points of the specimen. 56
2.2 Detail of the clamping system: (a) without specimen and (b) with specimen. 60
2.3 Analytical threshold load trend in function of h_p, for laminates L02, L03 and L04. The damage threshold F_{mc}^{ten} for laminates with thin plies is computed from the stresses of laminate type L03. 63
2.4 Analytical threshold trends for all laminates. 69
2.5 Buckling modes of delaminated plates in compression (Davies and Olsson [8]). 70
2.6 (a) CAI support fixture and (b) the corresponding constraints. 71
2.7 CAI test fixture: (a) base support, (b) top support adapted for the crosshead test machine, and (c) whole fixture. 73
2.8 Instrumentation of CAI tests (SGx: strain gage; LVDTx: displacement transducer). 73

3.1 Impact force histories of laminate L02 with (a) $E_i = 38.6$J and $M_i = 5$kg, and (b) $E_i = 19.3$J and $M_i = 5$kg. 76
3.2 Impact force histories of laminate L02 with (a) $E_i = 38.6$J and $M_i = 5$kg, and (b) $E_i = 19.3$J and $M_i = 5$kg. 77
3.3 Impact force histories of laminate L02 for each impact energy (blue: 38.6J; black: 28.6J; red: 19.3J). 77
3.4 Impact force histories of laminate L03 for each impact energy (blue: 38.6J; black: 28.6J; red: 19.3J). 78
3.5 Impact force histories of laminate L04 for each impact energy (blue: 38.6J; black: 28.6J; red: 19.3J). 78
3.6 Experimental and analytical impact force histories of laminate L02 for 38.6J and 19.3J impact energies. 79
3.7 Impact force histories for 38.6J of laminates L02 (blue), L03 (black), and L04 (red). 80
3.8 Impact force histories for 28.6J of laminates L02 (blue), L03 (black), and L04 (red). 80
3.9 Impact force histories for 19.3J of laminates L02 (blue), L03 (black), and L04 (red). 81

3.10 Experimental points (in gray) and analytical predictions (in black) of the impact force as a function of the ply thickness for the creation of the first significant damage. 82
3.11 Impactor (a) displacements and (b) velocities of all the laminates for 28.6J energy. 83
3.12 Evolution of the (a) absorbed energy and (b) impact force versus impactor displacement of each laminate for 38.6J. 84
3.13 Evolution of the (a) absorbed energy and (b) impact force versus impactor displacement of each laminate for 28.6J. 84
3.14 Evolution of the (a) absorbed energy and (b) impact force versus impactor displacement of each laminate for 19.3J. 85
3.15 Sample of C-scan inspections of laminates L02, L03 and L04. 86
3.16 Projected delamination areas in function of the impact energy. 88
3.17 Dent-depth inspections of laminates L02, L03 and L04. 90
3.18 Displacement transducer lectures of the specimens impacted with 29.6J: (a) L02, (b) L03, and (c) L04. 92
3.19 Strain gage lectures of the specimens impacted with 29.6J: (a) L02, (b) L03, and (c) L04. 93
3.20 DIC lectures of the specimen L04-S04 impacted at 29.6J: (a) horizontal displacement field, (b) vertical displacement field, and (c) out-of-plane displacement field (positive values indicate displacements in the out-of-plane direction). 94
3.21 Impact force histories of laminate L06 for each impact energy (blue: 38.6J; black: 28.6J; red: 19.3J). 95
3.22 Experimental and analytical impact force histories of laminate L06 for 38.6J and 19.3J impact energies. 95
3.23 Impact force histories for 38.6J of laminates L02 (blue) and L06 (black). 96
3.24 Impact force histories for 28.6J of laminates L02 (blue) and L06 (black). 96
3.25 Impact force histories for 19.3J of laminates L02 (blue) and L06 (black). 97
3.26 Experimental and analytical trends of the impact force as a function of the ply thickness for the creation of the first significant damage. . . 98
3.27 Impactor (a) displacements and (b) velocities of laminates L02 and L06 for 28.6J energy. 98

3.28 Evolution of the (a) absorbed energy and (b) impact force versus impactor displacement of laminates L02 and L06 for 38.6J. 99

3.29 Evolution of the (a) absorbed energy and (b) impact force versus impactor displacement of laminates L02 and L06 for 28.6J. 99

3.30 Evolution of the (a) absorbed energy and (b) impact force versus impactor displacement of laminates L02 and L06 for 19.3J. 100

3.31 Sample of C-scan inspections of laminates L02 and L06. 101

3.32 Dent-depth inspections of laminates L02 and L06. 102

3.33 Displacement transducer lectures of the specimens impacted with 29.6J: (a) L02 and (b) L06. 104

3.34 Strain gage lectures of the specimens impacted with 29.6J: (a) L02 and (b) L06. 104

3.35 Impact force histories of laminate L01 for each impact configuration (blue: $E_i = 38.6$J, $M_i = 5$kg; black: $E_i = 19.3$J, $M_i = 5$kg; red: $E_i = 19.3$J, $M_i = 6$kg; green: $E_i = 12.0$J, $M_i = 2$kg). 106

3.36 Impact force histories of laminate L05 for each impact configuration (blue: $E_i = 38.6$J, $M_i = 5$kg; black: $E_i = 57.8$J, $M_i = 6$kg; red: 57.9J, $M_i = 15$kg). 106

3.37 (a) Impact force histories of laminate L01 for 19.3J (black: $M_i = 5$kg; red: $M_i = 6$kg), and (b) impact force histories of laminate L05 for 58J (black: $M_i = 6$kg; red: $M_i = 15$kg). 107

3.38 Experimental and analytical impact force histories of laminate L01 for a constant impact energy 19.3J: $M_i = 5$kg (black), and $M_i = 6$kg (red). Two different contact laws are used: (a) bi-lineal elastic-plastic contact law [31], and (b) the Hertz contact law. 109

3.39 Experimental and analytical impact force histories of laminate L05 for a constant impact energy 57.8J: $M_i = 6$kg (black), and $M_i = 15$kg (red). Two different contact laws are used: (a) bi-lineal elastic-plastic contact law [31], and (b) the Hertz contact law. 109

3.40 (a) Impact force histories of laminates L01 (black) and L02 (blue) for 19.3J; (b) impact force histories of laminates L01 (black), L02 (blue) and L05 (red), for 38.6J. 110

3.41 Experimental and analytical threshold loads as a function of the plate thickness. 111
3.42 Impactor (a) displacement and (b) velocity of laminate L01 for 19.3J (black: $M_i = 5$kg; red: $M_i = 6$kg). 111
3.43 Impactor (a) displacement and (b) velocity of laminate L05 for 58J (black: $M_i = 6$kg; red: $M_i = 15$kg). 112
3.44 Evolution of the (a) absorbed energy and (b) impact force versus impactor displacement of laminate L01 for 19.3J (black: $M_i = 5$kg; red: $M_i = 6$kg). 112
3.45 Evolution of the (a) absorbed energy and (b) impact force versus impactor displacement of laminate L05 for 58J (black: $M_i = 6$kg; red: $M_i = 15$kg). 113
3.46 Impactor (a) displacement and (b) velocity of laminates L01 and L02 for 19.3J. 114
3.47 Impactor (a) displacement and (b) velocity of laminates L01, L02 and L05 for 38.6J. 114
3.48 Evolution of the (a) absorbed energy and (b) impact force versus impactor displacement of laminates L01 and L02 for 19.3J. 115
3.49 Evolution of the (a) absorbed energy and (b) impact force versus impactor displacement of laminates L01, L02 and L05 for 38.6J. . . . 115
3.50 Sample of C-scan inspections of laminate L01 with equal impact energies, but different impactor masses. 116
3.51 Sample of C-scan inspections of laminate L05 with equal impact energies, but different impactor masses. 116
3.52 Sample of C-scan inspections of laminates L01 and L02 for 19.3J. . . 117
3.53 Sample of C-scan inspections of laminates L02 and L05 for 38.6J. . . 117
3.54 C-scan inspection of specimen L01-S06 ($E_i = 12.0$J, $M_i = 2.0$kg). . . 118
3.55 Dent-depth inspections of laminate L01 with equal impact energies, but different impactor masses. 118
3.56 Dent-depth inspections of laminate L05 with equal impact energies, but different impactor masses. 119
3.57 Dent-depth inspections of laminates L01 and L02 for 19.3J. 119
3.58 Dent-depth inspections of laminates L02 and L05 for 38.6J. 119

3.59 (a) Displacement transducer and (b) strain gage lectures of laminate L05. . . . 121
3.60 (a) Displacement transducer and (b) strain gage lectures of laminates L01 and L02 for 19.3J. . . . 122
3.61 (a) Displacement transducer and (b) strain gage lectures of laminates L02 and L05 for 38.6J. . . . 123

4.1 Bilinear constitutive law. . . . 133
4.2 Propagation modes. . . . 134
4.3 Parameters of the bilinear constitutive equation. . . . 137
4.4 Constitutive charts defined by: (a) stresses and relative displacements, or by (b) stresses and strains. . . . 141
4.5 Transformations from strains to relative displacements for each propagation mode. . . . 145
4.6 Evolution of the maximum element thickness in function of the mixed-mode ratio. . . . 152
4.7 Constitutive equation charts defined by (a) relative displacements and (b) strains in function of the element thickness. . . . 153
4.8 Sketches of the (a) MMB test and (b) ENF test configurations. . . . 157
4.9 Experimental and numerical force-displacement relation of the MMB test $B = 0.0$ (pure mode I). . . . 159
4.10 Experimental and numerical force-displacement relation of the MMB test $B = 0.2$. . . . 160
4.11 Experimental and numerical force-displacement relation of the MMB test $B = 0.5$. . . . 160
4.12 Experimental and numerical force-displacement relation of the MMB test $B = 0.8$. . . . 161
4.13 Experimental and numerical force-displacement relation of the ENF test (pure mode II). . . . 161
4.14 : TCT specimen. . . . 163
4.15 Detail of the location of the cohesive elements. . . . 165
4.16 Numerical load-displacement relations for the TCT specimens. . . . 167

A.1 Laminated composite plate and coordinate systems. . . . 170

A.2 Transverse isotropic lamina. 174
A.3 Lamina coordinate systems. 175
A.4 Force and moment resultants on a lamina (or laminate). 176
A.5 Lamina location in a laminate. 177
A.6 Behavior of transverse section in classical plate theory. 183
A.7 Stress resultants on an arbitrary edge of a laminate. 187
A.8 Behavior of transverse section in first-order shear plate theory. 191

List of Tables

1.1 Energy release rates for unequal size delaminations [74], where $S_0 = n^3/\left(m^3 + (n-m)^3\right) - 1$, $S_1 = n^2 - S_0 - 1$, and m is the delamination number (numbering starts with the deepest back face delamination). . 48

2.1 ASTM D7136 / D7136M specifications for the specimen. 58
2.2 ASTM D7136 / D7136M specifications for the impactor. 58
2.3 Damage thresholds for AS4/8552 carbon-epoxy composite material. . 59
2.4 Impact configurations for laminates: L02, L03 and L04. 61
2.5 Damage thresholds for laminates: L02, L03 and L04. 62
2.6 Damage thresholds for laminate L06. 65
2.7 Impact configurations for laminate type L01. 66
2.8 Impact configurations for laminate type L05. 66
2.9 Maximum elastic impact force predictions for laminate type L01. . . . 67
2.10 Maximum elastic impact force predictions for laminate type L05. . . . 67
2.11 Damage thresholds for laminates: L01 and L05. 68
2.12 Selected laminates. 69

3.1 Experimental threshold loads F_d and peak loads F_{max}. 81
3.2 Absorbed energies of all laminates for each impact energy. 85
3.3 Projected delamination areas given by C-scan inspections. 88
3.4 Failure compressive loads F_{fc} of laminates L02, L03 and L04. 91
3.5 Maximum lectures of the displacement transducers of laminates L02, L03 and L04. 91
3.6 Experimental threshold loads F_d and peak loads F_{max} of laminates L02 and L06. 97
3.7 Absorbed energies of laminates L02 and L06 for each impact energy. . 100

3.8 Failure compressive loads F_{fc} of laminates L02 and L06. 102
3.9 Residual compressive strengths σ_{fc} of laminates L02 and L06. 103
3.10 Maximum lectures of the displacement transducers of laminates L02 and L06. 103
3.11 Experimental threshold loads F_d and peak loads F_{max} for laminate L01. 105
3.12 Experimental threshold loads F_d and peak loads F_{max} for laminate L05. 107
3.13 Residual compressive strengths σ_{fc} of laminates L01, L02 and L06. . . 120
3.14 Summary of analytical and experimental thresholds. 127

4.1 AS4/PEEK properties. 158
4.2 Interface properties. 158
4.3 Fracture toughnesses of the interface for different mixed-mode ratios [134, 135]. 158
4.4 Analytical equations of MMB test with $B = 0.0$, and ENF test ($B = 1.0$). 162
4.5 T300/914C properties. 165
4.6 Interface properties. 166
4.7 Experimental and numerical results. 166

A.1 Stress notations. 170
A.2 Strain notations. The engineering and contracted notation shear strains are twice the tensorial shear strain. 171

Chapter 1

Analytical description of the impact event

1.1 Introduction

The prediction of damage in laminated composite structures induced by the impact of an external object is a complex task. Damage results from the interaction between different failure mechanisms (matrix cracking, fiber-matrix interface debonding, delamination, and fiber breakage), and it depends on the governing parameters of the impact event. These parameters include the physical parameters and properties of the projectile, the structural configuration, and the environmental conditions.

Experimental evidence shows that impact damage is directly related to the nature of the impact behavior which, in turn, is controlled by the governing parameters. Therefore, it is useful to know the effects of each governing parameter on the impact behavior, and thus to have a qualitative understanding of the possible damage mechanisms that can occur. For example, under constant energy impact conditions, a quasi-static type of impact behavior will result mostly in delamination damage whereas a wave-controlled type of impact behavior will result mostly in permanent indentation and fiber breakage at the impact site [6]. There are approaches in the literature, based on analytical models, which predict the type of the impact response for a determined configuration, such as impact on flat and rectangular laminated composite plates [3, 7]. The initial knowledge of the impact behavior not only helps in assessing the possible type of damage induced, but it is also useful for the devel-

opment of efficient numerical models, for planning test programs, and for selecting a proper simplified analytical model to describe the impact event.

The analytical models are a suitable and powerful tool to obtain fast predictive results for a given impact configuration. Generally, these analytical models are limited to simple geometries of the structure and rely on stepwise solution of nonlinear differential equations or integral equations which describe the transitory response of the system until damage onset, i.e. in the elastic regime. The results given by these analytical models are suitable to compare different impact cases with different values of the governing parameters.

The framework and the ingredients used for the impact dynamics description on rectangular, flat, and monolithic laminated composite plates are presented in this chapter. Therefore, a literature survey of the analytical impact models available is presented. On the other hand, an overview of the main approaches used to identify quickly the nature of the impact behavior is done. Finally, a review of the analytical damage thresholds available in the literature, as well as the development of new proposals for some damage mechanisms are presented.

The issues analyzed in this chapter and in the related Appendix A are used to define a suitable set of low-velocity impact tests in order to capture different damage phenomena which can occur. The details of this task are described in Chapter 2.

1.2 Impact behavior

Experimental evidence shows that the nature of the impact behavior and the resulting damage are related. Since the impact behavior is defined by the governing parameters of the impact event, the damage created also depends on these parameters. For impacts on rectangular, flat, and monolithic laminated composite plates, the governing parameters are typically grouped in three sets: plate parameters (thickness, in-plane size, lamina type, elastic and fracture properties, density, stacking sequence, and boundary conditions), impactor parameters (shape, size, elastic properties, mass, velocity, and incidence angle), and the environmental conditions.

The impact behavior can be predicted easily in the elastic regime by means of approaches based on analytical models of the impact event. Thus, the information

obtained can be used to know the possible related damage which can occur. Damage starts when a suitable parameter of the elastic response, typically the impact force, is greater than the corresponding damage threshold (see Section 1.6).

Before to describe the models for the prediction of the impact response, it is useful to review the different types of impact responses for plates (impact behaviors), as the response type is crucial to have a qualitative insight of the resulting possible damage, and for the selection of a simplified model for impact description. Detailed descriptions of the impact behaviors are given by Olsson [3, 8–12], by Christoforou and Yigit [6, 7, 13, 14], by Abrate [5, 15], and by Lin and Fatt [16].

According to Olsson [9], an impact event initiates stress waves propagating from the impact point, where the influence of the waves gradually fade away due to material damping and wave scattering. For impact times t_i close to the time required for the waves to propagate through-the-thickness direction, the response is dominated by three-dimensional wave propagation (see Figure 1.1.a). For longer impact times, flexural and shear waves govern the response (see Figure 1.1.b). For times much longer than the time needed by these waves to reach the plate boundaries, the lowest vibration mode of the impactor-plate system predominates (see Figure 1.1.c). Eventually, the deformation mode approaches a purely static deformation.

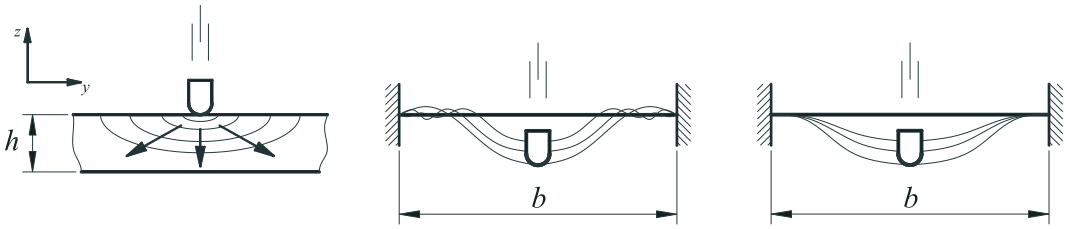

$t_i \leq \dfrac{h}{c_z}$ (a) $\qquad \dfrac{h}{c_z} < t_i \leq \dfrac{b}{2c_y}$ (b) $\qquad t_i > \dfrac{b}{2c_y}$ (c)

Figure 1.1: Impact responses (after Olsson [9]): (a) dominated by dilatational waves, (b) dominated by flexural and shear waves, and (c) quasi-static response.

The variables shown in Figure 1.1 are: h, the structure's thickness; b, the smallest in-plane size of the structure; and c_z and c_y, respectively the speed of sound in the z through-the-thickness direction and in the y in-plane direction.

The response dominated by through-the-thickness waves is typically associated with ballistic impact, which in most cases, causes localized and easily detectable damage. Related with the impacts that can have an aircraft, the response in Figure 1.1.b is typical for impacts by hail and runway debris, whereas the response in Figure 1.1.c is typical for dropping of heavy tools. The in-plane plate size and the boundary conditions affect the response shown in Figure 1.1.c, but not the responses shown in Figures 1.1.a and 1.1.b, because in these cases, the impact event is over before the stress waves have reached the edges of the structure. The load and the deflection are out of phase during a small mass impact while they are more or less in phase during a large mass impact. Furthermore, due to the more localized deflection, small mass impactors cause higher impact loads and earlier damage initiation than large mass impactors with the same kinetic energy.

Summarizing, the impact behaviors can be classified into three extreme categories that are referenced in the literature as: (a) *three-dimensional wave-controlled*, *through-the-thickness wave-controlled* or *ballistic impact*; (b) *global behavior with no size effects*, *flexural and shear wave-controlled*, or *impact on an infinite plate*; (c) *fully-global* or *quasi-static impact behavior*. If the global response of the plate can be neglected (extreme case of (b)), this impact behavior is typically called *half-space* impact.

The present thesis is focused on the response types shown in Figures 1.1.b and 1.1.c. *Barely Visible Impact Damage* (BVID) is associated with these responses, especially in the latter response type where delamination is the main damage mechanism. Delaminations are a major threat because they significantly reduce the compressive strength of the impacted structure.

Impacts are often categorized in the literature as *low-* or *high-velocity*, but there is not a clear transition between categories and authors disagree on its definition [1]. Some authors refer, improperly, to the response type under small mass of the impactor as high-velocity impact and under large mass impact as low-velocity impact. Olsson [3], and Christoforou and Yigit [7] demonstrate that the response type under elastic conditions depends on the impactor mass, the mass of the surface of the plate affected by the impact and the structural stiffness. Increasing the velocity, the impact force increases and induces a large damage extension or even a change in the main damage mechanism type, but the velocity does not affect the impact behavior.

The classification by means of the velocity may be motivated from a practical point of view for damage creation, since large mass impactors usually cause damage at a lower velocity than small mass impactors with the same kinetic energy. When an impact is categorized as low-velocity impact, the material properties are assumed to be rate independent [17].

A physically based criterion to distinguish low- or high-velocity impact categories was suggested in Davies and Godwin [18], which defined high-velocity impact as cases where the ratio of the impactor velocity V_0 versus the speed of sound in the plate thickness direction c_z, exceeds the through-the-thickness compressive failure strain ϵ_c. That is:

$$\epsilon_c = \frac{V_0}{c_z} \tag{1.1}$$

The assumed failure mode implies a response governed by through-the-thickness waves (i.e. ballistic impact). For typical composite materials, the corresponding impactor velocity ranges from 10 to 20m/s [19]. However, the large strains associated with contact stresses are highly localized and the resulting failure may often not affect the general response of the plate. Thus, response governed by flexural and shear waves has been experimentally demonstrated in carbon/epoxy laminates at velocities of 45m/s. Thus, the use of velocity for classifying impact events is highly debatable [3].

Finally it should be noted that the term *hyper-velocity* has come to be applied to satellites and spacecraft which may be struck by micro-meteorites where the impact duration is measured in nanoseconds, and both the meteorite and impacted structure will vaporize [8].

1.3 Local deflection

Impact on monolithic plates involves local and global deflection. Therefore, impact damage may be caused due to local contact stresses and/or stresses resulting from the structural response. Figure 1.2 shows two extreme responses of a plate under impact loading. Only local deflection is shown in Figure 1.2.a, which can result from small-mass and high-velocity impact on thick laminate plates. However, only global

deflection is shown in Figure 1.2.b, which can occur from large-mass and low-velocity impact on thin laminate plates.

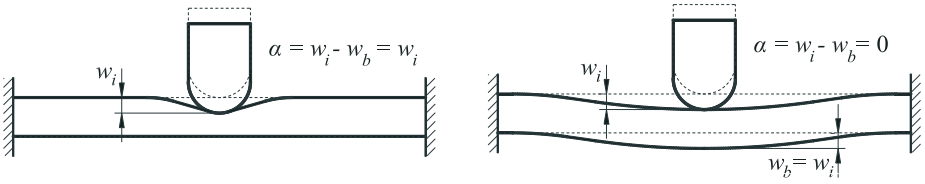

(a) (b)

Figure 1.2: Extreme plate responses under impact loading, (a) pure local deflection and (b) pure global deflection.

The local deflection typically is described by means of a proper contact law, which relates the concentrated contact load F_c and the indentation α as:

$$F_c = k_\alpha \alpha^q \tag{1.2}$$

where k_α is the contact stiffness, q is a power parameter, and α is the indentation defined as the difference between the displacement of the impactor w_i and the displacement of the back face w_b [5], or mid-plane w_o [9], of the plate at the impact point. That is:

$$\alpha = w_i - w_o \tag{1.3}$$

As it will be shown in next sections, the contact law is a required ingredient for the development of analytical models of the impact event. Alternative models, such as spring-dashpot and the momentum balance methods, use the coefficient of restitution to characterize the local energy loss due to impact [14]. The contact law can be obtained experimentally or by analytical methods, and depends on the material properties of the bodies, the stacking sequence, and the size and shape of the impactor.

For composite materials it is accepted that local deflection can be modeled using a statically determined contact law for moderate strain rates [20, 21], as happens in low-velocity impact events. The static contact load between two linear elastic bodies is described by the *Hertz contact law*, which is based on the following assumptions:

infinite plate thickness (i.e. impact on a half-space plate), the bodies in contact are isotropic, frictionless contact between the impactor and the plate, and negligible curvature of the plate surface during contact (i.e. the wrapping effect is neglected). The Hertz contact law has been applied in a wide range of cases even when if all assumptions are not satisfied (e.g. indentation on laminated composite plates), because usually it fits quite well the experimental data obtained from indentation tests.

In the literature there are advanced developments for the contact description which take into account the anisotropy of laminated composite materials. These models are not often simple as the Hertz contact law, because the resulting laws require the numerical solution of differential or integral equations. Some examples for transversely isotropic materials are the work presented by Dahan and Zarka [22], and Turner [23]. For orthotropic materials, the work of Wu and Yen [24], Chao and Tu [25], and Swanson [26] should be mentioned.

A comprehensive justification of the Hertz contact law agreement for local deflection modeling of laminated composite plates in contact with a hemispherical indentor, and a collection of some developments available in the literature to get over some of the Hertz assumptions are given by Abrate [5], and Davies and Olsson [8]. In [8], the descriptions are given in function of the static indentation tests which can be performed:

- **Measuring differences between front and back face deflections on plates with an unsupported back face.** This test is suitable for local deflection analysis in flexible plates. Under low contact loads, the load-indentation behavior is in agreement with the Hertz contact law [27, 28]. Under high contact loads, the plate may result in a large flexural curvature, which increases the contact area (i.e. the wrapping effect). Also, matrix cracking and delamination reduces the flexural stiffness which contributes to a large flexural curvature. Due to this increase of the contact area, the pressure distribution changes from a bell-shaped (Hertzian-type distribution) to a saddle-shaped. As a result of this redistribution, the indentation decreases as the force keeps increasing [5]. However, this effect has a small influence on the response, which is then dominated by global plate deflections.

- **Placing the plate on a flat rigid support.** This test is suitable for the local deflection analysis in rigid plates. Under low contact loads, the load-indentation behavior is in agreement with the Hertz contact law. However, under moderate loads the behavior results in a softening response caused by the fiber damage and plasticity of the matrix. There are some simple models which take into account this effect and they yield more realistic results, such as the work of Cairns [29], Christoforou [30], and Yigit and Christoforou [31]. On the other hand, if the thickness of the plate is small enough there is a stiffening effect on the load-indentation behavior which depends on the ratio between the indentation depth and plate thickness [32]. This effect is included in the contact models of Suemasu et al. [33] and Chen et al. [34].

1.3.1 Hertz contact law adapted for laminated composite plates

Considering Equation (1.2) and the case of a hemispherical impactor indenting a plate (see Figure 1.3), the Hertz contact law is defined by equaling the power q to $3/2$, and the contact stiffness k_α to k_H which is given by:

$$k_H = \frac{4}{3} Q_\alpha \sqrt{R} \tag{1.4}$$

where:

$$Q_\alpha = \left(\frac{1}{Q_{zi}} + \frac{1}{Q_{zp}} \right)^{-1} \tag{1.5}$$

The parameters Q_{zi} and Q_{zp} are the effective contact modulus along the loading axis z of the impactor and the plate, respectively. R is the impactor tip radius.

The normal contact pressure $p(r)$ of the Hertz theory varies within the contact radius R_c as:

$$p(r) = p_0 \sqrt{1 - \frac{r_c^2}{R_c^2}}, \quad 0 \leq r_c \leq R_c \tag{1.6}$$

$$R_c = \frac{3}{4} \frac{F_c R}{Q_\alpha} = \sqrt{R\alpha} \tag{1.7}$$

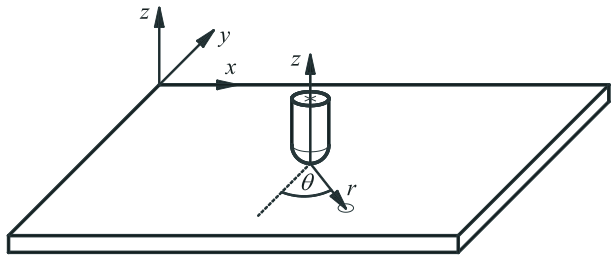

Cartesian coordinates: (x, y, z)
Cylindrical coordinates: (r, θ, z)

Figure 1.3: Coordinate systems.

where r_c is the radial position of an arbitrary point in the contact zone, and p_0 is the maximum pressure located at $r_c = 0$ given by:

$$p_0 = \frac{3F_c}{2\pi R_c^2} \tag{1.8}$$

For isotropic materials (e.g. a steel impactor), the effective contact modulus is defined by:

$$Q_z = \frac{E}{(1-\nu^2)} \tag{1.9}$$

where E and ν are the Young modulus and the Poisson ratio, respectively. For the case where the indentor is much stiffer than the plate, Equation (1.5) simplifies to $Q_\alpha \approx Q_{zp}$.

The extension of Equation (1.9) for materials with transverse isotropy (along the loading axis z) is [9]:

$$Q_{zp} = \frac{E_z}{(1-\nu_{rz}\nu_{zr})} \tag{1.10}$$

where ν_{rz} and ν_{zr} are the through-the-thickness Poisson ratios. In most laminate plates $\nu_{rz}\nu_{zr} \approx 0$, and Equation (1.10) can be simplified to $Q_{zp} = E_z$ [27, 32]. The through-the-thickness Young modulus of the laminate E_z is common to set equal to the transversal Young modulus of a single ply (i.e. $E_z = E_{22}$).

It is important to remark that Equation (1.10) is an approximation of the effective modulus of transversally isotropic plates which underestimates the contact modulus of typical composite plates by 10-20% [10, 26].

More advanced expressions of Q_{zp} for transversally isotropic materials are available in the literature: Turner [23, 26, 35], or that of Greszczuk [10, 36].

The expression of Q_{zp} proposed by Turner [23] is given as:

$$Q_{zp} = \frac{2}{\beta_1 \beta_3} \tag{1.11}$$

where:

$$\begin{gathered} \beta_1 = \left(\frac{\dfrac{E_r}{E_z} - \nu_{rz}^2}{1 - \nu_r^2} \right)^{1/2}, \quad \beta_2 = \frac{1 + \left(\dfrac{E_r}{2G_{rz}} - 1 \right) - \nu_{rz}\left(1 + \nu_r\right)}{1 - \nu_r^2} \\ \beta_3 = \left(\frac{\beta_1 + \beta_2}{2} \right)^{1/2} \left(\frac{1 - \nu_r}{G_r} \right) \end{gathered} \tag{1.12}$$

The expression developed by Greszczuk [36] is given as:

$$Q_{zp} = \frac{2\sqrt{\dfrac{G_{rz}}{C_{rr}}}\left(C_{rr}C_{zz} - C_{rz}^2\right)}{\sqrt{\left(\sqrt{C_{rr}C_{zz}} + G_{zr}\right)^2 - \left(C_{rz} + G_{zr}\right)^2}} \tag{1.13}$$

where:

$$\begin{aligned} C_{rr} &= \frac{E_r\left(1 - \nu_{rz}\nu_{zr}\right)\Omega}{\left(1 + \nu_r\right)}, \quad & C_{rz} &= E_r \nu_{zr} \Omega \\ C_{zz} &= E_z\left(1 - \nu_r\right)\Omega, & \Omega &= \frac{1}{\left(1 - \nu_r - 2\nu_{rz}\nu_{zr}\right)} \end{aligned} \tag{1.14}$$

In an orthotropic plate, the effective contact modulus Q_{zp} defined by Equation (1.10) becomes directionally dependent. Then, the shape of the indentation, which is circular in transverse isotropic plates along z axis, becomes elliptical in orthotropic plates. The effective contact modulus can be estimated by integrating $E_r\left(\theta\right)$ over 2π and taking the average [9]. However, since in most laminated plates $\nu_{rz}\nu_{zr} \approx 0$, the solution again simplifies to $Q_{zp} = E_z$.

1.3.2 Unloading and reloading contact process

Typically, in an impact event the contact force increases to a maximum value and then decreases back to zero. During the unloading phase, Yang and Sun [27] found that the Hertzian contact law was not adequate. The unloading phase is significantly different from the loading phase due to permanent indentation. In order to account this effect, Crook [37] proposed the following equation:

$$F_c = F_m \left(\frac{\alpha - \alpha_0}{\alpha_m - \alpha_0} \right)^{5/2} \tag{1.15}$$

where F_m is the contact force at the start of the unloading, α_m is the indentation corresponding to F_m (i.e. maximum indentation) and α_0 is the permanent indentation. Equation (1.15) can be rewritten as:

$$F_c = s \left(\alpha - \alpha_0 \right)^{5/2} \tag{1.16}$$

where:

$$s = \frac{F_m}{\left(\alpha_m - \alpha_0 \right)^{5/2}} \tag{1.17}$$

is called unloading rigidity. Equaling the Hertz contact law for loading with Equation (1.15), the permanent indentation α_0 and the critical indentation α_{cr} as from of it permanent indentation starts, are given as:

$$\alpha_0 = \begin{cases} \alpha_m \left(1 - \left(\dfrac{\alpha_{cr}}{\alpha_m} \right)^{2/5} \right) & \text{if} \quad \alpha_m > \alpha_{cr} \\ 0 & \text{if} \quad \alpha_m \leq \alpha_{cr} \end{cases} \tag{1.18}$$

$$\alpha_{cr} = \frac{k_H}{s} \tag{1.19}$$

The procedure in order to define α_{cr} starts by the selection of a proper value of α_0 by means of the unloading contact law (Equation (1.15)), so that the areas under the analytical unloading curves are equal to that calculated from the corresponding experimental curves. If these values of α_0 are substituted into Equation (1.17), a range of values of s is obtained. Using the average of s values, the value of α_{cr} is finally obtained.

If a subsequent reloading phase is done, the contact law is also distinct from the unloading curve but always returns to the point where unloading began [27]. The reloading curve is modeled by:

$$F_c = F_m \left(\frac{\alpha - \alpha_0}{\alpha_m - \alpha_0} \right)^{3/2} \tag{1.20}$$

In this case, there is no need to perform reloading experiments to find the parameters of the contact law.

1.3.3 Elastic-plastic contact models

Permanent deformations can be introduced in composite materials when the indentation exceeds a critical value because the material behavior is mainly governed by the properties of the matrix where a plastic behavior is expected. Under this circumstance, the Hertz contact law overestimates the maximum contact force and elastic-plastic contact laws can yield more realistic results. In these models, the critical indentation is taken into account during the loading process, unlike the previous approach where the critical indentation is accounted for using the unloading phase.

Elastic-plastic models assume that initially the material behaves elastically until a critical indentation is reached (see Figure 1.4). At this point, the contact area is divided into a plastic zone and an elastic zone as the loading increases and a new contact law is obtained [5]. Some elastic-plastic contact models are described below.

The elastic-plastic model developed by Christoforou [30] describes the contact loading and unloading between a rigid sphere and a thin laminated composite plate supported on a rigid substrate. Thus, the model is focused only on local deflections since the global response becomes negligible. The material is assumed to be transversely isotropic and follows an elastic-perfectly plastic behavior of the through-the-thickness normal stress-strain law. As yielding stress, a maximum shear failure criterion governed only by the fiber shear strength S_u is considered, although it is approached to the shear strength of the laminate S^L [7]. The development of Cairns [29] results in the same contact law for loading by assuming that the contact radius and the indentation are much smaller than the impactor radius.

Therefore, for the loading case, the contact law is defined by:

$$F_c = \begin{cases} \dfrac{\pi R E_z}{(1-\nu_{rz}\nu_{zr})\,h}\alpha^2 & \text{if} \quad 0 \le \alpha \le \alpha_{cr} \\ 2\pi R S_u\,(2\alpha - \alpha_{cr}) & \text{if} \quad \alpha_{cr} < \alpha \le \alpha_m \end{cases} \tag{1.21}$$

and for the elastic unloading phase, the contact law is:

$$F_c = \frac{\pi R E_z}{(1-\nu_{rz}\nu_{zr})\,h}\left(\alpha^2 - \alpha_0^2\right) \tag{1.22}$$

where h is the specimen thickness. The critical indentation α_{cr} and the permanent indentation α_0 are given by:

$$\alpha_{cr} = \frac{2S_u h\,(1-\nu_{rz}\nu_{zr})}{E_z} \tag{1.23}$$

$$\alpha_0 = \alpha_m - \alpha_{cr} \tag{1.24}$$

Another contact law is proposed by Yigit and Christoforou [31]. It is obtained by combining the classical Hertz contact theory and the elastic-plastic indentation theory given in Johnson [20]. In this case, the contact law for loading is given by:

$$F_c = \begin{cases} k_H \alpha^{3/2} & \text{if} \quad 0 \le \alpha \le \alpha_{cr} \\ k_H \alpha_{cr}^{3/2} + k_y\,(\alpha - \alpha_{cr}) & \text{if} \quad \alpha_{cr} < \alpha \le \alpha_m \end{cases} \tag{1.25}$$

and for the elastic unloading phase, the contact law is:

$$F_c = k_H\left(\alpha^{3/2} - \alpha_m^{3/2} + \alpha_{cr}^{3/2}\right) + k_y\,(\alpha_m - \alpha_{cr}) \tag{1.26}$$

where k_y is the linear stiffness of the elastic-plastic loading phase which is equal to the slope of the elastic indentation curve at $\alpha = \alpha_{cr}$:

$$k_y = \frac{3}{2}k_H\sqrt{\alpha_{cr}} \tag{1.27}$$

The critical indentation α_{cr} can be obtained from the contact stress distribution using a maximum shear failure criterion [20]. Knowing that Y^C is the compressive strength of the laminate, α_{cr} is approached to [13]:

$$\alpha_{cr} = \frac{0.68\left(Y^C\right)^2\pi^2 R}{Q_\alpha^2} \tag{1.28}$$

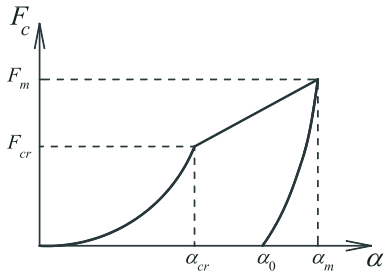

Figure 1.4: Detail of the contact law phases.

1.3.4 Linearized contact laws

In the analytical models of the impact event (see Section 1.4), the local deflections are simply described using a proper contact law. When the contact law is replaced in the governing equations of the plate and of the impactor, an exact solution of these equations generally are not available and a numerical solution is required. However, in some cases a closed-form solution can be obtained if the contact law is linearized (e.g. Christoforou and Swanson [38]; Olsson [21]). The resulting closed-form equations are more useful to gain a better understanding of the effects of the governing parameters on the behavior of the impact event.

Yigit and Christoforou [39] proposed a linearization of the elastic-plastic contact law of Christoforou [30]. Also, the loading contact law presented in [31] is linearized by Christoforou and Yigit [14], and used in [7, 13, 40]. In addition, Choi and Lim [41] developed a linearization of the Hertz contact law which allows to model low-velocity impact problems in a general-purpose finite element method software.

1.4 Analytical impact models

The analytical impact models are a powerful tool to get fast predictive results for a given impact configuration. These models are usually developed to predict the response of the system until damage onset, which is sufficient to compare different impact cases with different values of the governing parameters.

These models describe the motion of the impactor, the motion of the structure (e.g. laminated composite plates) and the local deflections in the area surrounding the impact point. To consider these local deflections, a contact law is commonly used.

Closed-form solutions can be obtained for some cases. Usually, these solutions are developed by means of *Duhamel integral* (i.e. *convolution integral*), *Laplace* and *Fourier transforms*. If a closed-form solution is not possible, then a numerical method is required, such as *Newmark step-by-step time integration method*.

It is essential to identify the effects of the large number of governing parameters on the impact behavior. In order to make the analysis more manageable, a dimensionless framework for the formulation of analytical models is recommended [42]. The goal is to reduce the number of governing parameters into a set of suitable governing dimensionless parameters that provide more insight into the impact problem, minimize the amount of computations required, and produce the output in particularly instructive forms [31]. The definition of these dimensionless parameters are usually given by means of *Buckingham Pi Theorem* [43], such as in Yigit and Christoforou [13].

The analytical models are often classified in function of how the plate is modeled [5, 15]. Davies and Olsson [8] classify the models in two main groups: *multi-degree-of-freedom models* and *one-* or *two-degree-of-freedom models*. The first group yields the typically so-called *complete analytical models*, and are based on numerical mode summation which rarely allows explicit expressions for the assessment of the influence of the different parameters. The second group includes *energy-balance models* and *spring-mass models*. These usually allow closed-form solutions which explicitly show the influence of the governing parameters, but have limited flexibility in handling complex geometries and different impact behaviors.

For the impact cases discussed in the present thesis, the inertia of the impactor is usually treated by considering its rigid motion described by Newton law. The inertia of the plate is more complicated, because during impact space deflections and transverse rotations are experimented. Typically, the weight force of the impactor is neglected, because it may be expected that the gravitational force is small relative to the contact force during the impact. On the other hand, the static properties of a material for low-velocity impacts are used without discussion of possible strain-rate effects [44].

1.4.1 Complete analytical models

The governing equations of a laminated composite plate (resulting from a selected plate theory) added with the governing equation of the impactor, a suitable contact law, and a proper approximation of the unknown variables yield to called *complete analytical models* of the impact event [7, 15]. The complete models fully describe the dynamic behavior of the plate and often are taken as a reference to validate analytical simplified models (e.g. Yigit and Christoforou [7]). The complete analytical models are valid in cases where dilatational waves are not important. In addition, from the complete models, it is possible to deduce simplified models which predicts the response for extreme behaviors (infinite plate and quasi-static impact behaviors).

The boundary conditions considered for the drop-weight test referenced in ASTM D7136 / D7136M [45] are approached to simply supported boundary conditions [46]. Under this consideration, the displacement solutions are assumed by means of *Navier method* which gives, for some laminate configurations, the exact solution of the governing equations for both plate theories presented in Appendix A: *classical laminated plate theory* and *first-order shear deformation plate theory*. In practice, exact solutions for the dynamic response of plates generally are not available due to the boundary conditions or the laminate configuration. In these cases, classical variational methods are used, such as *Raleigh-Ritz* method [44, 47].

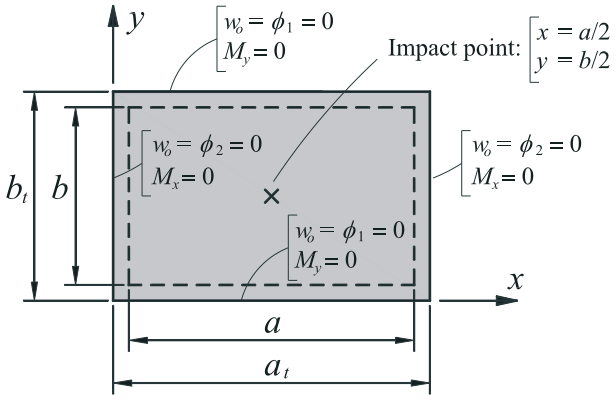

Figure 1.5: Boundary conditions of simply supported plate.

The boundary conditions for simply supported and first-order shear deformation plate theory can be expressed as (see Figure 1.5):

$$\begin{aligned} &w_o(x,0,t)=0, \quad w_o(x,b,t)=0, \quad w_o(0,y,t)=0, \quad w_o(a,y,t)=0 \\ &\phi_1(x,0,t)=0, \quad \phi_1(x,b,t)=0, \quad \phi_2(0,y,t)=0, \quad \phi_2(a,y,t)=0 \\ &M_y(x,0,t)=0, \quad M_y(x,b,t)=0, \quad M_x(0,y,t)=0, \quad M_x(a,y,t)=0 \end{aligned} \tag{1.29}$$

where t is the time, w_o is the mid-plane displacement in the normal direction z, ϕ_1 and ϕ_2 are respectively the rotations of a transverse normal about the y and x axis, and M_y and M_x are respectively the bending moments respect x and y axis (see Appendix A). In addition, a_t and b_t are the in-plane dimensions of the plate, and a and b are the effective in-plane dimensions of the plate.

The governing equations are solved by expansion of unknown displacements and rotations in Fourier series (i.e. mode summation) which satisfies the corresponding boundary conditions of the plate. For the plate theory considered, they are:

$$w_o(x,y,t)=\sum_{m=1}^{\infty}\sum_{n=1}^{\infty} W_{mn}(t)\sin\frac{m\pi x}{a}\sin\frac{n\pi y}{b} \tag{1.30}$$

$$\phi_1(x,y,t)=\sum_{m=1}^{\infty}\sum_{n=1}^{\infty} X_{mn}(t)\cos\frac{m\pi x}{a}\sin\frac{n\pi y}{b} \tag{1.31}$$

$$\phi_2(x,y,t)=\sum_{m=1}^{\infty}\sum_{n=1}^{\infty} Y_{mn}(t)\sin\frac{m\pi x}{a}\cos\frac{n\pi y}{b} \tag{1.32}$$

where $W_{mn}(t)$, $X_{mn}(t)$ and $Y_{mn}(t)$ are the coefficients to be determined such that corresponding governing equations are satisfied everywhere in the domain of the plate.

All laminates considered in the thesis are symmetrical and balanced. Therefore, the following simplifications for the governing equations may be used:

1. Symmetric plates: the bending-extensional coupling stiffness matrix $[B]$ is equal to zero. This simplification allows to decouple the equation which gives the flexural displacement w_o of the other two equations for displacements u_o and v_o for classical laminated plate theory. And for first-order shear deformation plate theory, the rotation equations are decoupled of the in-plane displacements.

2. Symmetric and balanced plates: the components A_{16} and A_{26} of the extensional stiffness matrix $[A]$ are qual to zero.

3. All lamina of the laminate is manufactured with the same material and the center of masses is located in the laminate centerline: the inertia term $I_2 = \int_{-h/2}^{h/2} z\rho\, dz$ is equal to zero.

4. All lamina is modeled as a transverse isotropic material: if first-order shear deformation plate theory is considered, the transverse shear stiffness component A_{45} is equal to zero .

In addition, geometric nonlinear effects are not considered in the development of the governing equations. These geometric nonlinearities are typically called membrane effects which are significant when the deflection of the plate reaches the order of the plate thickness. On the other hand, the nonlinear terms $\mathcal{N}$ considered in the development of the governing equations are omitted (see Appendix A).

Classical laminated plate theory

The resulting simplified governing equation obtained from the classical laminated plate theory is:

$$\begin{aligned}
&\frac{\partial^2}{\partial x^2}\left[D_{11}\left(-\frac{\partial^2 w_o}{\partial x^2}\right)+D_{12}\left(-\frac{\partial^2 w_o}{\partial y^2}\right)+D_{16}\left(-2\frac{\partial^2 w_o}{\partial x\partial y}\right)\right]\\
&+2\frac{\partial^2}{\partial x\partial y}\left[D_{16}\left(-\frac{\partial^2 w_o}{\partial x^2}\right)+D_{26}\left(-\frac{\partial^2 w_o}{\partial y^2}\right)+D_{66}\left(-2\frac{\partial^2 w_o}{\partial x\partial y}\right)\right]\\
&+\frac{\partial^2}{\partial y^2}\left[D_{12}\left(-\frac{\partial^2 w_o}{\partial x^2}\right)+D_{22}\left(-\frac{\partial^2 w_o}{\partial y^2}\right)+D_{26}\left(-2\frac{\partial^2 w_o}{\partial x\partial y}\right)\right]\\
&+q = I_1\frac{\partial^2 w_o}{\partial t^2}
\end{aligned} \tag{1.33}$$

On the other hand, the load $q(x, y, t)$ is set as a concentrated impact force located at $x = a/2$ and $y = b/2$, and it is defined as [5]:

$$q(x, y, t) = F_c(t)\delta(x - \frac{a}{2})\delta(y - \frac{b}{2}) \tag{1.34}$$

where $F_c(t)$ is the contact force described by a desired contact law (see Section 1.3). The function $\delta(\cdot)$ is the *Dirac delta function*, which has the following property:

$$\int_{-\infty}^{\infty} \mu(\xi)\delta(\xi - \xi_0)\, d\xi = \mu(\xi_0) \tag{1.35}$$

Replacing the Navier solution (Equation (1.30)) and their respective space derivatives into Equation (1.33), multiplying all equation terms by $\sin\left(\frac{m\pi x}{a}\right)\sin\left(\frac{n\pi y}{b}\right)$ and finally integrating the $x-y$ space, the governing equation at impact point (i.e. at $x = a/2$ and $y = b/2$) takes the form:

$$\ddot{W}_{mn} + \omega_{mn}^2 W_{mn} = \frac{4}{ab\chi} F_c(t) \sin\frac{m\pi}{2} \sin\frac{n\pi}{2} \tag{1.36}$$

If m and n vary respectively from 1 to p and 1 to q, the motion of the plate is then described by $N = p \cdot q$ equations. Note that due to the impact location, only odd numbered terms m and n are contributing to the solution. For the other plate material points, the right hand side of Equation (1.36) is equal to zero. The term χ is defined by Equation (1.37) and ω_{mn}^2 is the natural frequency defined by Equation (1.38).

$$\chi = I_1 + I_3 \left[\left(\frac{m\pi}{a}\right)^2 + \left(\frac{n\pi}{b}\right)^2 \right] \tag{1.37}$$

$$\begin{aligned} \omega_{mn}^2 = \frac{1}{\chi} \Bigg[& D_{11} \left(\frac{m\pi}{a}\right)^4 + 2\left(D_{12} + 2D_{66}\right) \left(\frac{m\pi}{a}\right)^2 \left(\frac{n\pi}{b}\right)^2 \\ & -4D_{16} \left(\frac{m\pi}{a}\right)^3 \left(\frac{n\pi}{b}\right) - 4D_{26} \left(\frac{m\pi}{a}\right) \left(\frac{n\pi}{b}\right)^3 + D_{22} \left(\frac{n\pi}{b}\right)^4 \Bigg] \end{aligned} \tag{1.38}$$

The governing equation of the impactor is easily found by applying *D'Alembert Principle* [48]. By neglecting the gravitational force of the impactor, the resulting equation is:

$$F_c(t) + M_i \ddot{w}_i = 0 \tag{1.39}$$

If a closed-form solution is not possible, the dynamic response of the plate and the impactor can be obtained by time integration of set $N+1$ second order ordinary differential equations with appropriate initial conditions (see Equation (1.40)) by

using a numerical solution procedure such as *Newmark step-by-step time integration method*.

$$W_{mn}(0) = 0, \quad \dot{W}_{mn}(0) = 0, \quad w_i = 0, \quad \dot{w}_i = V_0 \tag{1.40}$$

V_0 is the initial impact velocity of the impactor.

First-order shear deformation plate theory case

For the first-order shear deformation plate theory, the resulting simplified governing equations to predict the unknown variables w_o, ϕ_1 and ϕ_2 are:

$$A_{55}\left(\frac{\partial^2 w_o}{\partial x^2} + \frac{\partial \phi_1}{\partial x}\right) + A_{44}\left(\frac{\partial^2 w_o}{\partial y^2} + \frac{\partial \phi_2}{\partial y}\right) + q = I_1 \frac{\partial^2 w_o}{\partial t^2} \tag{1.41}$$

$$\begin{aligned} &\frac{\partial}{\partial x}\left[D_{11}\frac{\partial \phi_1}{\partial x} + D_{12}\left(\frac{\partial \phi_2}{\partial y}\right) + D_{16}\left(\frac{\partial \phi_1}{\partial y} + \frac{\partial \phi_2}{\partial x}\right)\right] \\ &+\frac{\partial}{\partial y}\left[D_{16}\frac{\partial \phi_1}{\partial x} + D_{26}\frac{\partial \phi_2}{\partial y} + D_{66}\left(\frac{\partial \phi_1}{\partial y} + \frac{\partial \phi_2}{\partial x}\right)\right] \\ &-A_{55}\left(\frac{\partial w_o}{\partial x} + \phi_1\right) = I_3 \frac{\partial^2 \phi_1}{\partial t^2} \end{aligned} \tag{1.42}$$

$$\begin{aligned} &\frac{\partial}{\partial x}\left[D_{16}\frac{\partial \phi_1}{\partial x} + D_{26}\left(\frac{\partial \phi_2}{\partial y}\right) + D_{66}\left(\frac{\partial \phi_1}{\partial y} + \frac{\partial \phi_2}{\partial x}\right)\right] \\ &+\frac{\partial}{\partial y}\left[D_{12}\frac{\partial \phi_1}{\partial x} + D_{22}\frac{\partial \phi_2}{\partial y} + D_{26}\left(\frac{\partial \phi_1}{\partial y} + \frac{\partial \phi_2}{\partial x}\right)\right] \\ &-A_{44}\left(\frac{\partial w_o}{\partial y} + \phi_2\right) = I_3 \frac{\partial^2 \phi_2}{\partial t^2} \end{aligned} \tag{1.43}$$

Following the same procedure as in classical laminated plate theory, the resulting system of equations which describe the dynamic response of the plate is:

$$\begin{bmatrix} s_{11} & s_{12} & s_{13} \\ s_{12} & s_{22} & s_{23} \\ s_{13} & s_{23} & s_{33} \end{bmatrix} \begin{Bmatrix} W_{mn} \\ X_{mn} \\ Y_{mn} \end{Bmatrix} + \begin{bmatrix} I_1 & 0 & 0 \\ 0 & I_3 & 0 \\ 0 & 0 & I_3 \end{bmatrix} \begin{Bmatrix} \ddot{W}_{mn} \\ \ddot{X}_{mn} \\ \ddot{Y}_{mn} \end{Bmatrix} = \begin{Bmatrix} q_{mn} \\ 0 \\ 0 \end{Bmatrix} \tag{1.44}$$

Defining $\alpha_m = \frac{m\pi}{a}$ and $\beta_n = \frac{n\pi}{b}$, the terms s_{ij} and q_{mn} are obtained by:

$$
\begin{aligned}
s_{11} &= \beta_n^2 A_{44} + \alpha_m^2 A_{55}, \quad s_{12} = \alpha_m A_{55}, \quad s_{13} = \beta_n A_{44} \\
s_{22} &= \alpha_m^2 D_{11} + \beta_n^2 D_{66} + A_{55} - \left(\frac{1}{2ab}\right) D_{16} \\
s_{23} &= \alpha_m \beta_n \left(D_{12} + D_{66}\right) - \left(\frac{m}{4na^2}\right) D_{16} - \left(\frac{n}{4mb^2}\right) D_{26} \\
s_{33} &= \beta_n^2 D_{22} + \alpha_m^2 D_{66} + A_{44} - \left(\frac{1}{2ab}\right) D_{26}
\end{aligned}
\tag{1.45}
$$

$$
q_{mn} = \frac{4F_c(t)}{ab} \sin(\alpha_m \frac{a}{2}) \sin(\beta_n \frac{b}{2}) \tag{1.46}
$$

For each (m, n) combination, a system of three equations with three unknowns is solved for the coefficients $W_{mn}(t)$, $X_{mn}(t)$ and $Y_{mn}(t)$. The motion for the impactor is again governed by Equation (1.39). The initial conditions are defined by:

$$
\begin{aligned}
&W_{mn}(0) = 0, \quad \dot{W}_{mn}(0) = 0, \quad w_i = 0, \qquad \dot{w}_i = V_0 \\
&X_{mn}(0) = 0, \quad \dot{X}_{mn}(0) = 0, \quad Y_{mn}(0) = 0, \quad \dot{Y}_{mn}(0) = 0
\end{aligned}
\tag{1.47}
$$

where V_0 is the initial impact velocity of the impactor.

1.4.2 Infinite plate impact models

The response of a plate under impact is governed by flexural and shear waves when the major wave emanating from the impact point has not time to reach the boundaries of the plate (see Figure 1.1.b). This situation is similar to an impact on an infinite plate. Therefore, the in-plane plate size and the boundary conditions do not affect the response. In the literature this behavior is referenced by the descriptors: global behavior with no size effects, flexural and shear wave-controlled, or impact on an infinite plate.

There are some analytical models in the literature for the description of this response type. Olsson [21] developed a model for orthotropic plates without shear deformation and assuming a Hertzian contact law. Closed-form solutions for this problem with a linearized contact law are proposed in Yigit and Christoforou [13]. A solution for Hertzian contact law on quasi-isotropic plates with transverse shear deformation is given in Mittal [49]. An extension of the model to both linear and

Hertzian contact law on orthotropic plates was presented in Olsson [50]. A closed-form prediction of the peak load for small mass impact based on three asymptotic cases with purely deformation by indentation, bending or shear, is developed in Olsson [12].

The model described here was proposed by Olsson [3, 21], which in turn was based on the work of Zener [51]. This model is referenced in many publications and used in the development of approaches for predicting the response type for a determined impact configuration [3, 7, 12–15] (see Section 1.5). The solution was proposed for the description of the impact until the waves are reflected back from the boundaries in orthotropic plates impacted by an impactor with a hemispherical tip.

In orthotropic plates, waves propagate at different speeds in different directions and the flexural wavefront will have an almost elliptical shape centered at the impact point. The analysis assumes that the area affected by the major wave emanating form the impact point can be approximated by a rectangular simply supported plate with side lengths a and b. Thus, the development of the model can be performed by using the framework explained for the complete analytical models (see Section 1.4.1) assuming classical laminated plate theory for orthotropic plates, and equal contact law for loading and unloading process. Therefore, no account was made for transverse shear deformation waves. In applications, shear deformations are usually of minor importance for monolithic laminates, while the influence on sandwich panels may be substantial [3].

The governing equation for transverse displacement description in a simply supported orthotropic plate assuming classical laminated plate theory, neglecting the I_3 term (see Appendix A) and impacted in $x = a/2$ and $y = b/2$ (see Figure 1.5) is:

$$\ddot{W}_{mn} + \omega_{mn}^2 W_{mn} = \frac{4}{abI_1} F_c(t) \tag{1.48}$$

where the natural frequencies ω_{mn} are described by:

$$\omega_{mn}^2 = \frac{1}{I_1}\left[D_{11}\left(\frac{m\pi}{a}\right)^4 + 2\left(D_{12} + 2D_{66}\right)\left(\frac{m\pi}{a}\right)^2\left(\frac{n\pi}{b}\right)^2 + D_{22}\left(\frac{n\pi}{b}\right)^4\right] \tag{1.49}$$

The solution of the differential Equation (1.48) can be found by means of the Duhamel integral:

$$W_{mn} = \frac{4}{abI_1\omega_{mn}} \int_0^t F_c(\tau) \sin\left[\omega_{mn}(t-\tau)\right]\, d\tau \tag{1.50}$$

By inserting Equation (1.50) into Equation (1.30), the transverse displacement of the plate at the impact point, $x = a/2$ and $y = b/2$, is :

$$w_o(a/2, b/2, t) = \frac{4}{abI_1} \int_0^t F_c(\tau) \sum_{n=1}^{\infty} \sum_{m=1}^{\infty} \frac{1}{\omega_{mn}} \sin\left[\omega_{mn}(t-\tau)\right]\, d\tau \tag{1.51}$$

The double sum in Equation (1.51) can be approximated by a continuous integration over m and n. Since only odd values of m and n are used in the summations, only half of the continuous integrals should be retained:

$$w_o(a/2, b/2, t) = \frac{1}{abI_1} \int_0^t F_c(\tau) \int_0^{\infty} \int_0^{\infty} \frac{1}{\omega_{mn}} \sin\left[\omega_{mn}(t-\tau)\right]\, dm\, dn\, d\tau \tag{1.52}$$

The fact that the waves are closed ellipses implies $m \equiv n$, which allows to consider the ratio a/b equal to the ratio of wavelengths λ_x/λ_y. The wavelengths are the inverses of the wave numbers $k_i = \omega_{mn}/c_{bend,i}$ $(i = x, y)$, where $c_{bend,i}$ are the flexural wave velocities. Knowing $c_{bend,x} = \sqrt{\omega_{mn}}(D_{11}/I_1)^{1/4}$ and $c_{bend,y} = \sqrt{\omega_{mn}}(D_{22}/I_1)^{1/4}$, the following relation is obtained:

$$\frac{a}{b} = \frac{c_{bend,x}}{c_{bend,y}} = \left(\frac{D_{11}}{D_{22}}\right)^{1/4} \tag{1.53}$$

Then, the natural frequencies can be expressed as:

$$\omega_{mn} = \frac{2\pi^2 mn}{ab}\sqrt{\frac{D^*}{I_1}} \tag{1.54}$$

where D^* is called *effective plate stiffness* [21] and is defined by fairly complicated expressions involving elliptic functions. A sufficient approximation is [3, 12]:

$$D^* \approx \sqrt{\left(\frac{A+1}{2}\right) D_{11}D_{22}}, \quad \text{where} \quad A = \frac{D_{12} + 2D_{66}}{\sqrt{D_{11}D_{22}}} \tag{1.55}$$

Therefore, the plate displacement can be rewritten by:

$$w_o(a/2, b/2, t) = \frac{1}{8\sqrt{I_1 D^*}} \int_0^t F_c(\tau)\, d\tau \tag{1.56}$$

On the other hand, the governing equation of the impactor is described by Equation (1.39). After integrating twice, the displacement of the impactor can be expressed by:

$$w_i(t) = V_0 t - \frac{1}{M_i} \int_0^t \int_0^\tau F_c(\tau')\, d\tau'\, d\tau \tag{1.57}$$

The indentation of the plate was defined by Equation (1.3). Differentiating twice with respect the time and using Equations (1.56) and (1.57), and the contact law defined by Equation (1.2), the indentation is found to be governed by the nonlinear differential equation:

$$\ddot{\alpha} + \frac{1}{8\sqrt{I_1 D^*}} q k_\alpha \alpha^{q-1} \dot{\alpha} + \frac{k_\alpha}{M_i} \alpha^q = 0 \tag{1.58}$$

If a linear contact law is used, $q = 1$, Equation 1.58 yields to the well-known differential equation of a damped harmonic oscillator which has closed-form solutions. In Yigit and Christoforou [13] these closed-form solutions are developed. On the other hand, the model defined by the governing Equation (1.58) can be represented by a simplified lumped-mass model shown in Figure 1.6.a [3], which is equivalent to the single degree of freedom model shown in Figure 1.6.b.

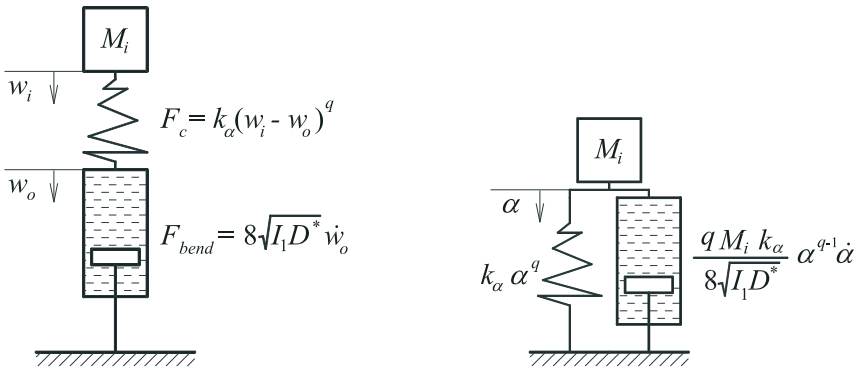

(a) (b)

Figure 1.6: Lumped-mass models for infinite plate behavior.

The governing Equation (1.58) can be expressed in a dimensionless form, which is more effective in order to analyze the effects of the governing parameters on the impact behavior. That is because the governing parameters are set on key dimensionless parameters, yielding to less characterization parameters of the impact response. This framework can be developed by defining all the basic magnitudes of the problem (i.e. mass $[M]$, length $[L]$, and time $[T]$) by means of selected parameters of the impact problem [13, 43]. The chosen definitions are [51]: mass $[M] = M_i$, length $[L] = V_0[T]$, and time $[T]$ is extracted from the contact stiffness k_α which depends on the selected contact law. Therefore $[T] = \left(k_\alpha^{-1}[M][L]^{(1-q)}\right)^{1/2} = \left(k_\alpha^{-1} M_i V_0^{(1-q)}\right)^{1/(1+q)}$.

The explained definitions are equivalent to define the variable $[L]$ equal to α_{max} [7, 13, 40]. The α_{max} corresponds to the maximum indentation of the plate (i.e. when the global response of the plate is neglected, which is called *half-space* impact). The expression of α_{max} is simply found by equalling all impact energy with the indentation energy. Consequently, the impact force is normalized with respect to the maximum impact force for a half-space behavior. Therefore, the equation of α_{max} for a general contact law yields to:

$$\alpha_{max} = \left(\frac{1+q}{2}\frac{M_i V_0^2}{k_\alpha}\right)^{1/(1+q)} \tag{1.59}$$

The resulting dimensionless differential equation is:

$$\ddot{\bar{\alpha}} + \zeta q \bar{\alpha}^{q-1}\dot{\bar{\alpha}} + \bar{\alpha}^q = 0 \tag{1.60}$$

where the over bar indicates dimensionless parameters and the initial conditions are $\bar{\alpha}(0) = 0$ and $\dot{\bar{\alpha}}(0) = 1$. All parameters that describe the impact behavior are now lumped in a single dimensionless parameter ζ. This parameter is defined by:

$$\zeta = \frac{1}{8\sqrt{I_1 D^*}}\left(k_\alpha M_i^q V_0^{q-1}\right)^{1/(1+q)} \tag{1.61}$$

In the bibliography, the ζ parameter is called *relative plate mobility* [3], *inelastic parameter* [5, 15], or *loss factor* [7]. The highest contact force is obtained for $\zeta = 0$, in which case the plate is very rigid and the problem is reduced to that of an impact

on a half-space impact behavior where the impactor will rebound with the initial velocity V_0 [9]. As the impact parameter ζ increases, the contact force history becomes asymmetrical and the contact duration increases because the flexural deformation of the target becomes more significant (i.e. the behavior approaches to a quasi-static response type). Under high values of ζ the model is not appropriate since the model is affected by the boundary conditions and the global deformation of the structure.

In Olsson [3] the parameter ζ is defined by introducing the concept of *mobility*, C, which is defined as velocity per unit force applied to a component. The mobility of the plate, C_p, is given by:

$$C_p = \frac{\dot{w}_o}{F_{bend}} = \frac{1}{8\sqrt{I_1 D^*}} \tag{1.62}$$

The impactor mobility, C_i, may be defined from peak (initial) velocity, V_0, per peak load, F_{max} for a complete immovable plate (i.e. $C_p = 0$ and the indentation is maximum α_{max}):

$$C_i = \frac{V_0}{F_{max}} = \frac{V_0}{k_\alpha \alpha_{max}^q} = \left(k_\alpha^{-1} V_0^{1-q} \left(\frac{1+q}{2} M_i \right)^{-q} \right)^{1/(1+q)} \tag{1.63}$$

By means of the mobility definitions, the ζ parameter can be redefined by the following expression:

$$\zeta = \left(\frac{2}{1+q} \right)^{q/(1+q)} \frac{C_p}{C_i} \tag{1.64}$$

The simplified model can be applied until the waves are reflected back from the boundaries. Equation (1.65) was proposed by Olsson [3], and it gives the position in polar coordinates r and θ for the leading edge of the n-th wave mode in an orthotropic plate. Therefore, the simplified model is not suitable if the value given by this equation is greater than the minimum distance from the impact point to the boundaries of the plate.

$$r_n(\theta) = \left(\frac{2 D_r(\theta) D^*}{I_1 \sqrt{D_{11} D_{22}}} \right)^{1/4} \sqrt{\pi n t} \tag{1.65}$$

where $D_r(\theta)$ is the radial plate bending stiffness in direction θ.

1.4.3 Half-space impact models

When the impactor mass is very small, and the target is fairly stiff, impact does not produce significant global structure response and can be approximated by impact on a half-space (i.e. the response is fully local). Then, this behavior can be approached by single mass-spring-damper model shown in Figure 1.7. The resulting governing equation is:

$$M_i \ddot{w}_i + F_c = 0 \tag{1.66}$$

where the contact law is defined by $F_c = k_\alpha \alpha^q = k_\alpha w_i^q$, and the initial conditions are $w_i(0) = 0$ and $\dot{w}_i(0) = V_0$.

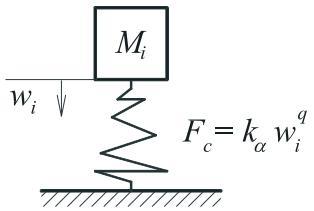

Figure 1.7: Spring-mass model for half-space impact behavior.

The dimensionless framework described in Yigit and Christoforou [31] defines the problem magnitudes as $[M] = M_i$, $[L] = \alpha_{cr}$, and $[T] = \left(k_\alpha^{-1} M_i \alpha_{cr}^{(1-q)}\right)^{1/2}$. The α_{cr} term is the yielding indentation for plastic indentation which is defined by Equation (1.28) (see Section 1.3.3). Using these definitions, the dimensionless form of the governing Equation (1.66) is:

$$\ddot{\bar{w}}_i + \bar{w}_i = 0 \tag{1.67}$$

On the other hand, the resulting normalized impact velocity β groups all the parameters for half-space behavior. Therefore, the β parameter fully characterizes the half-space behavior and is termed *characteristic impact parameter*. That is:

$$\beta = \frac{V_0}{\omega \alpha_{cr}} \tag{1.68}$$

where ω is the contact frequency given as:

$$\omega = [T]^{-1} = \left(k_{\alpha}^{-1} M_i \alpha_{cr}^{(1-q)}\right)^{-1/2} \tag{1.69}$$

However, by using the dimensionless framework explained in Section 1.4.2, i.e. mass $[M] = M_i$, length $[L] = \alpha_{max}$, and time $[T] = \left(k_{\alpha}^{-1} M_i \alpha_{max}^{(1-q)}\right)^{1/2}$, the β parameter remains constant. In particular, for linear contact law $q = 1$, β parameter is equal to 1, and for Hertzian contact law $q = 3/2$, β parameter is equal to $(5/4)^{-1/2}$. This result implies that the predicted normalized response given for this behavior is constant whatever the values of the governing parameters of this behavior. This interesting consideration is used in the impact characterization diagram of Chritoforou and Yigit [7, 13, 14] which is explained in Section 1.5.

On the other hand, the model defined for wave-controlled impact behavior can be used in order to describe the half-space behavior. As it has been noted, the half-space impact behavior will be obtained when the ζ parameter yields to zero.

1.4.4 Quasi-static impact models

For sufficiently large impact times, the response is more or less quasi-static, in the sense that load and deflection give the same relation as during a static loading. Based on extensive experimental and computational experience, researchers suggest that the response is almost quasi-static if the effective mass ratio μ is greater than a threshold value [52]. This effective mass ratio is given by:

$$\mu = \frac{M_i}{M_p^*} \tag{1.70}$$

where M_i is the impactor mass and M_p^* is the equivalent lumped mass of the structure which depends on the type of structure and support conditions. For rectangular and simply supported plates it is set equal to 1/4 of the total plate mass M_p, as can be deduced from Equation (1.36).

The most complete simplified model for quasi-static behavior description is shown in Figure 1.8.a [53], where the terms k_s, k_b and k_m are the shearing, bending and membrane stiffness of the plate under static load. The expression of k_s, k_b and k_m are function of the boundary conditions, the shape and the laminate configuration of the structure. The stiffness values can be obtained experimentally, by using numerical methods, or analytically in cases with simple laminate configurations [8]. A

list of stiffness expressions for transverse isotropic plates is done in Sierakowski et al. [54].

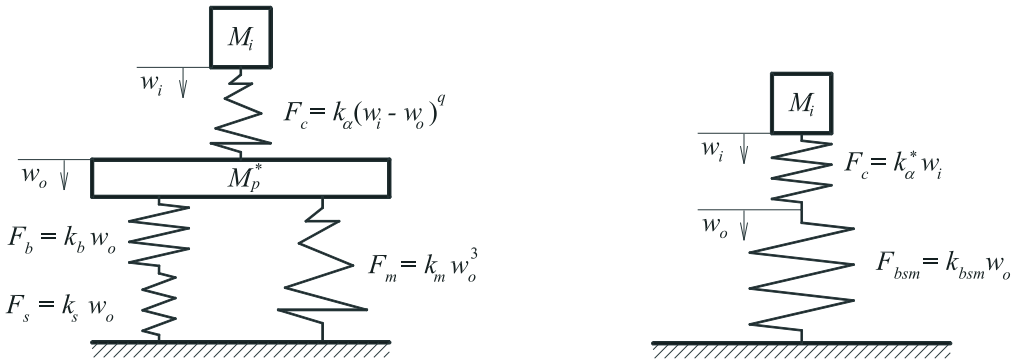

(a) (b)

Figure 1.8: (a) Complete and (b) simplified spring-mass model for quasi-static impact behavior (Olsson [9]).

The governing equations for each mass by neglecting the gravitational forces are (Figure 1.8.a):

$$M_i \ddot{w}_i + k_\alpha (w_i - w_o)^q = 0 \tag{1.71}$$

$$M_p^* \ddot{w}_o + k_s w_o + k_b w_o + k_m w_o^3 - k_\alpha (w_i - w_o)^q = 0 \tag{1.72}$$

where the initial conditions are $w_i = w_o = 0$, $\dot{w}_o = 0$ and $\dot{w}_i = V_0$. In Olsson [11] this model is used in conjunction with a delamination force threshold and a critical energy for delamination growth in order to predict the impact damage initiation and growth during quasi-static response caused by large mass impactors.

The equivalent plate mass M_p^* is negligible when the impactor mass is larger than twice the total plate mass. By neglecting the plate mass and linearizing the stiffness k_m and k_α (i.e. linear stiffness k_m^* and k_α^*), the model yields to the model shown in Figure 1.8.b [3]. In this case, all stiffness can be lumped to a single stiffness k_Σ which is defined by:

$$k_\Sigma = \frac{k_\alpha^* k_{bsm}}{k_\alpha^* + k_{bsm}}, \quad \text{where} \quad k_{bsm} = \left(\frac{1}{k_b} + \frac{1}{k_s} \right)^{-1} + k_m^* \tag{1.73}$$

The governing equation for this case is:

$$M_i \ddot{w}_i + k_\Sigma w_i = 0 \tag{1.74}$$

where the initial conditions are $w_i = 0$ and $\dot{w}_i = V_0$. More simplified versions are proposed in the literature, such as models with neglected membrane effects and/or shear effects [7]. Equation (1.74) can be written in a dimensionless form by using the magnitude definitions shown in Section 1.4.2 specified for a linear contact law (i.e. $q = 1$). That is:

$$\ddot{\bar{w}}_i + \left(\frac{k_{bsm}}{k_{bsm} + k_\alpha^*} \right) \bar{w}_i = 0 \tag{1.75}$$

1.5 Approaches for impact behavior description

There are approaches in the literature which predict the impact behavior type of rectangular, flat, and monolithic laminated composite plates. These approaches are based on simplified analytical models of extreme impact behaviors and develop key characterization parameters which inform of the behavior type. As it has been noted in Section 1.2, the behaviors considered are those that yield to Barely Visible Impact Damage (BVID) if the resulting peak load reaches a designed damage threshold. Ballistic impact behavior is beyond the scope of the present thesis.

The approaches detailed in this section are the characterization diagram proposed by Christoforou and Yigit [7, 13, 14], and the mass criterion proposed by Olsson [3]. It should be noted that not all impact cases are adequately characterized by the approaches explained at following. This is due to the fact that these approaches are based on simplified models based on certain hypothesis that may not be true for certain impact configurations.

1.5.1 Christoforou and Yigit characterization diagram

The characterization impact diagram proposed by Christoforou and Yigit [6, 7, 13, 14] predicts the behavior type, as well as the maximum elastic impact force for a wide range of impact cases. The prediction of the maximum impact force is useful

since it can be compared with a damage threshold for damage onset (see Section 1.6).

The construction of the diagram is based on simplified analytical models of the infinite plate and quasi-static impact behaviors, and uses the dimensionless framework described in Section 1.4.2 (i.e. the normalization with respect to the maximum indentation α_{max}). On the other hand, a linearized contact law of the elastic-plastic contact model proposed in Yigit and Christoforou [31] is used, that results in closed-form solutions for the impact models.

Infinite plate behavior

The closed-form solutions, Equation (1.76), are the expressions of the normalized impact force as a function of the relative mobility parameter ζ with $q = 1$ (see Equations (1.60) and (1.61)). It should be noted that ζ parameter is changed to $\zeta = 2\zeta_w$ which simplifies the resulting equations:

$$\bar{F}_w(\bar{t}) = \bar{\alpha}(\bar{t}) = \begin{cases} \dfrac{\exp^{-\zeta_w \bar{t}}}{\sqrt{1-\zeta_w^2}} \sin\left(\sqrt{1-\zeta_w^2}\bar{t}\right) & \text{if } \zeta_w < 1 \\ \bar{t}\exp^{-\bar{t}} & \text{if } \zeta_w = 1 \\ \dfrac{1}{2\sqrt{\zeta_w^2-1}}\left(\exp^{\left(-\zeta_w+\sqrt{\zeta_w^2-1}\right)\bar{t}} - \exp^{\left(-\zeta_w-\sqrt{\zeta_w^2-1}\right)\bar{t}}\right) & \text{if } \zeta_w > 1 \end{cases} \tag{1.76}$$

The dimensionless time at which the maximum impact force occurs can be found by setting the derivatives with respect to time equal to zero, in Equation (1.76), yielding:

$$\bar{t}_w = \begin{cases} \arccos\left(\dfrac{\zeta_w}{\sqrt{1-\zeta_w^2}}\right) & \text{if } \zeta_w < 1 \\ 1 & \text{if } \zeta_w = 1 \\ \dfrac{1}{2\sqrt{\zeta_w^2-1}} \ln\left(\dfrac{\zeta_w+\sqrt{\zeta_w^2-1}}{\zeta_w-\sqrt{\zeta_w^2-1}}\right) & \text{if } \zeta_w > 1 \end{cases} \tag{1.77}$$

Then, the maximum normalized impact force can be calculated by replacing Equation (1.77) into Equation (1.76) as:

$$\bar{F}_{w,max}(\bar{t}_w) = \bar{\alpha}(\bar{t}_w) \tag{1.78}$$

From Equation (1.78), it is concluded that the infinite plate behavior is function of only the parameter ζ_w, because $\bar{t}_w$ only depends on it.

Half-space behavior

As noted in Section 1.4.3, the half-space behavior can be described by the spring-mass model shown in Figure 1.7. Due to the dimensionless framework used, the dependence on the characterizing half-space parameter β is avoided and the normalized impact force can be obtained by normalizing Equation (1.66):

$$\bar{F}_{hs}(\bar{t}) = \bar{\alpha}(\bar{t}) = \bar{w}_i(\bar{t}) = \sin \bar{t} \tag{1.79}$$

Thus, if an impact response is locally dominated, the maximum normalized impact occurs at time $\bar{t}_{hs} = \pi/2$ and this force will be close to the unity $\bar{F}_{hs,max} = 1$. This development also can be deduced by means of the governing Equation (1.60) of the wave-controlled impact model and letting the ζ_w parameter equal to zero.

Quasi-static behavior

The quasi-static behavior is described by the model shown in Figure 1.8.b. Equaling the linear contact stiffness k_α^* to k_y (Equation (1.27)), and defining $\lambda = k_{bsm}/k_y$ (i.e. *relative stiffness*), the solution of the dimensionless governing Equation (1.75) (see Section 1.4.4) is:

$$\bar{w}_i(\bar{t}) = \sqrt{\frac{1+\lambda}{\lambda}} \sin\left(\sqrt{\frac{\lambda}{1+\lambda}}\bar{t}\right) \tag{1.80}$$

and the normalized impact force for quasi-static behavior is:

$$\bar{F}_q(\bar{t}) = \sqrt{\frac{\lambda}{1+\lambda}} \sin\left(\sqrt{\frac{\lambda}{1+\lambda}}\bar{t}\right) \tag{1.81}$$

From Equation (1.81), the maximum normalized impact force occurs at time:

$$\bar{t}_q = \frac{\pi}{2}\sqrt{\frac{1+\lambda}{\lambda}} \tag{1.82}$$

and is defined as:

$$\bar{F}_{q,max} = \sqrt{\frac{\lambda}{1+\lambda}} \tag{1.83}$$

As Equation (1.83) shows, the maximum normalized impact force for quasi-static behavior only depends on λ parameter.

Impact characterization diagram

Using the analytical solutions of the extreme cases explained above, a characterization diagram can be constructed as shown in Figure 1.9. This diagram represents the variation of the maximum normalized impact force $\bar{F}_{max}$ as a function of the relative mobility parameter ζ_w. For the construction of the diagram, the curve representing infinite plate behavior is obtained from Equation (1.78), and the horizontal lines with different values of relative stiffness λ are obtained by using Equation (1.83).

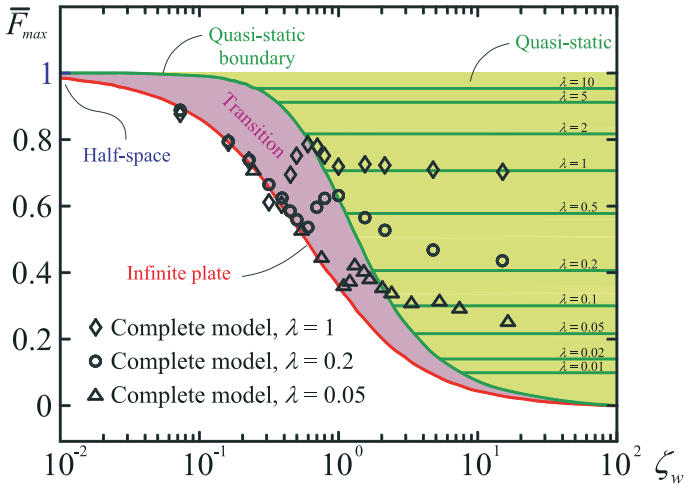

Figure 1.9: Impact characterization diagram (after Christoforou and Yigit [6, 7, 13, 14]): dimensionless maximum force $\bar{F}_{max}$ versus relative mobility ζ_w.

Four different regions can be identified in the diagram. Impact configurations which define points in the right part of the diagram behave as quasi-static. For points which fall close to the dashed curve behave as infinite plate. Between the quasi-static and the infinite plate behaviors there is a transition zone where the resulting response is a combination of both behaviors. The curve which represents the boundary of the quasi-static response is obtained by $\bar{F}_b = \sqrt{\frac{0.68}{0.68+\zeta_w^2}}$, as suggested in [13, 52]. Finally, the points that fall close to the maximum dimensionless force

$\bar{F} = 1$ results in the half-space behavior, and can be obtained by setting in the simplified models (infinite plate and quasi-static): $\zeta_w = 0$ or $\lambda \to \infty$.

In order to demonstrate the validity of the characterization diagram several impact situations covering all behavior type regions are simulated. The simulations are carried out by numerical integration of the complete analytical model which considers classical laminated plate theory and simply supported boundary conditions (see Section 1.4.1). As can be seen, the simulations follow reasonably well the trends of the characterization diagram. In the transition zone, a complete analytical model is required in order to better describe the response.

Summarizing, the prediction of the behavior type as well as the maximum impact force for a given impact case can be done by calculating only two key parameters: λ (i.e. key parameter of quasi-static impact behavior) and ζ_w (i.e. key parameter of wave-controlled impact behavior). However, the contribution of structural dynamics should be included and it can be represented by the relative impactor mass μ given by Equation (1.70). When different impact situations (respect to their boundary conditions, materials, size, etc.) with similar key parameters are compared, the resulting dynamics, behavior type and normalized response are similar [40].

1.5.2 Olsson mass criterion

Olsson [3] developed a criterion for the prediction of the elastic impact behavior of orthotropic plates. The model is based on the models for infinite plate and quasi-static extreme behaviors described in Sections 1.4.2 and 1.4.4, respectively. This criterion demonstrates that the response type under elastic conditions (i.e. prior to damage onset) depends basically on the impactor/plate mass ratio. In order to develop the criterion, the dimensionless framework presented in Section 1.4.2 was also used.

Small-mass impactor

For small-mass impactor, it is demonstrated that the impact time t_i has the following approximate lower bound [3]:

$$t_i \geq \frac{1}{4}\frac{M_i}{\sqrt{I_1 D^*}} \tag{1.84}$$

The mass of the plate area affected by the first wave, $M_{p,wave}$, is approached by:

$$M_{p,wave} = \pi I_1 r_1(0^o) r_1(90^o) = \pi^2 t_i \sqrt{2 I_1 D^*} \tag{1.85}$$

where $r_1(0^o)$ and $r_1(90^o)$ are respectively the distances at 0^o and 90^o directions from the impact point site to the leading edge of the first wave mode. They are calculated by means of Equation (1.65).

On the other hand, the largest plate mass which can remain unaffected by the boundaries, $M_{p,max}$, is found by considering the plate area affected when the first wave mode reaches a boundary. Therefore, it can be defined as:

$$M_{p,max} = \pi I_1 \min \left\{ \left(\frac{D_{22}}{D_{11}} \right)^{1/4} r_{x,min}^2, \left(\frac{D_{11}}{D_{22}} \right)^{1/4} r_{y,min}^2 \right\} \tag{1.86}$$

where $r_{x,min}$ and $r_{y,min}$ are the distances from the impact to the closest boundary in the $x-$ (i.e. 0^o direction) and $y-$direction (i.e. 90^o direction). Therefore, an impact located at middle of the panel implies $r_{x,min} = a/2$ and $r_{y,min} = b/2$.

By replacing Equation (1.84) into Equation (1.85) and making the ratios respect the impactor mass, M_i, the condition for small-mass impact (i.e. infinite plate impact) is approached by:

$$\frac{M_i}{M_{p,max}} \leq \frac{M_i}{M_{p,wave}} \leq \frac{2\sqrt{2}}{\pi^2} \tag{1.87}$$

For rectangular plates with leading edges a and b (see Figure 1.5), the term I_1 is equal to $\frac{M_p}{ab}$. Therefore, the condition for small-mass impact can be expressed as:

$$\frac{M_i}{M_p} \leq \frac{1}{\sqrt{2}\pi} \min \left\{ \frac{a}{b} \left(\frac{D_{22}}{D_{11}} \right)^{1/4}, \frac{b}{a} \left(\frac{D_{11}}{D_{22}} \right)^{1/4} \right\} \tag{1.88}$$

Large-mass impactor

For large-mass impactor, the model considered is shown in Figure 1.8.b which neglects the lumped plate mass M_p^* and considers linear conditions. For this case, the natural frequency is:

$$\omega_i = \sqrt{\frac{k_\Sigma}{M_i}} \tag{1.89}$$

If the lumped plate mass is not neglected, the natural frequency of the plate is approached by:

$$\omega_p = \sqrt{\frac{k_{bsm}}{M_p^*}} \tag{1.90}$$

By means of Equation (1.89) the impact time is obtained:

$$t_i = \pi\sqrt{\frac{M_i}{k_\Sigma}} \tag{1.91}$$

On the other hand, using Equation (1.90) the first vibration mode of the plate results in:

$$t_{p,1} = \pi\sqrt{\frac{M_p^*}{k_{bsm}}} \tag{1.92}$$

Quasi-static response occurs for impact times much longer than the fundamental vibration period of the plate, which is described by:

$$t_i/t_{p,1} >> 1 \tag{1.93}$$

Replacing Equations (1.91) and (1.92) in Equation (1.93), and considering $M_p^* = (1/4)M_p$, the criterion for quasi-static behavior yields to $\frac{M_i}{M_p} >> \frac{1}{4}$. A sufficient condition is:

$$\frac{M_i}{M_p} \geq 2 \tag{1.94}$$

Intermediate-mass impactor

Finally, a complex response occurs for intermediate-mass impactors, which can be modeled by including the equivalent plate mass M_p^* as shown in Figure 1.8.a. Therefore, the condition for intermediate mass behavior for rectangular plates is:

$$\frac{1}{\sqrt{2}\pi}\min\left\{\frac{a}{b}\left(\frac{D_{22}}{D_{11}}\right)^{1/4}, \frac{b}{a}\left(\frac{D_{11}}{D_{22}}\right)^{1/4}\right\} < \frac{M_i}{M_p} < 2 \tag{1.95}$$

1.6 Impact damage and analytical thresholds

The phenomenon of impact damage in laminated composite structures is very complex and difficult to model analytically due to the large variety of damage modes (matrix cracking, fiber-matrix interface debonding, delamination and fiber breakage) and to their complex interaction process. The identification of the initiation and propagation of the damage modes is quite relevant because it will yield information regarding the residual strength of the structure.

Similarly to the impact response, depending on the impact governing parameters, the resulting damage can be local, global or both [6, 8]. Local impact damage consists mainly of visible permanent indentation on the contact zone involving fiber and matrix damage modes, whereas global impact damage consists mainly of invisible extensive delaminations. The extreme local damage is the complete penetration of the plate. Associated with these types of damages, there are complicated patterns of matrix cracks and fiber fractures.

To bridge the analytical prediction of the impact behavior and the onset of damage, the impact force is typically used and compared with a damage threshold allowable. Damage occurs if the predicted elastic impact force is greater than a well-suited threshold for the corresponding dynamic response type [5, 6, 12, 55, 56]. Therefore, the impact force is a key parameter in determining the criticality of an impact, i.e. the risk for initiating damage.

1.6.1 Matrix cracking

The impact damage process starts with localized matrix cracks and fiber-matrix interfacial debondings which normally are not detectable neither by the impactor load cells used during impact tests nor using the typical *Non-Destructive Inspection methods* (NDI), e.g. ultrasonic techniques. It has been shown by Sjöblom et al. [57] that the presence of matrix cracks does not dramatically affect the overall laminate stiffness during an impact event. However, matrix crack tips act as initiation points for delaminations at interfaces between plies with different fiber orientations. These delaminations change the local and/or global stiffness of the structure [17].

Two types of matrix cracks can be observed: vertical and oblique cracks (Figure 1.10). Vertical cracks are introduced by the flexural deformation of the plate due to

tensile stresses and consequently they are located at the bottom plies. Therefore, vertical cracks are typical in impact events that behave as quasi-static. Oblique cracks are formed by the high transverse shear stresses resulting from the contact load and the flexural deformation of the plate. These cracks are typically located at top and middle plies.

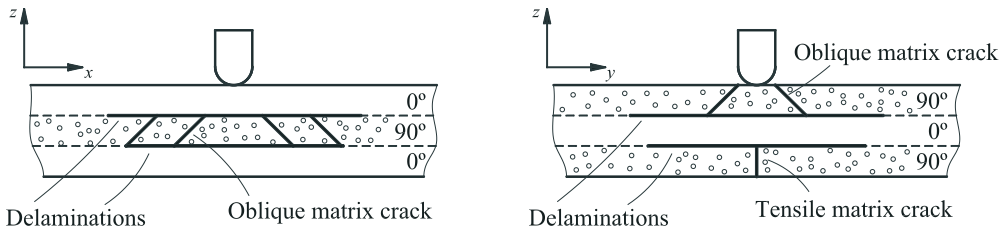

(a) (b)

Figure 1.10: Type of matrix cracks in a [0/90/0] laminated composite plate (after Richardson and Wisheart [1]): (a) longitudinal view and (b) transverse view.

Typically, in thick laminates matrix cracking starts on the impacted face of the specimen as a result of the high and localized contact stresses. Damage propagates downward by a succession of intra-ply cracks and interface delaminations, resulting in a pine tree pattern (Figure 1.11.a). For thin laminates, bending stresses on the back of the laminate introduce tensile matrix cracks, and damage progresses from the non-impacted face up toward the impactor yielding a reverse pine tree appearance (Figure 1.11.b).

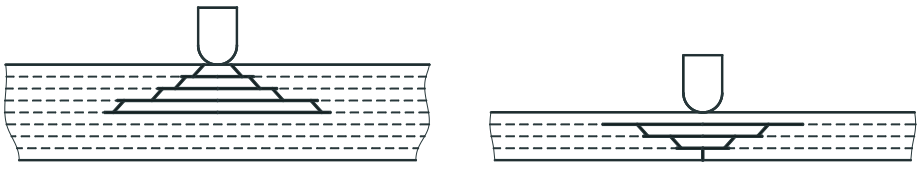

(a) (b)

Figure 1.11: Projected damage patterns (after Abrate [5]): (a) pine tree and (b) reversed pine tree.

Threshold load for vertical matrix crack

A new damage threshold for the prediction of matrix cracking at the first outer ply located at the back face of a rectangular laminated composite plate due to bending is proposed herein.

The maximum values of the in-plane tensile stresses due to the flexural deformation created by a uniformly distributed static load of radius R, $q_0 = F_{mc}^{ten}/(\pi R^2)$, centered at $(x, y, z) = (a/2, b/2, -h/2)$ in a simply supported, rectangular and orthotropic plate (see Figure 1.5), can be approached by [47]:

$$(\sigma_x)_{max} = \frac{8b^2}{\pi^5 R^2 h^2} f_x\left(s, C_{ij}, D_{ij}/h^3\right) F_{mc}^{ten} \tag{1.96}$$

$$(\sigma_y)_{max} = \frac{8b^2}{\pi^5 R^2 h^2} f_y\left(s, C_{ij}, D_{ij}/h^3\right) F_{mc}^{ten} \tag{1.97}$$

where R is the impactor tip radius and h is the plate thickness. These maximum in-plane tensile stresses are located at $(x, y, z) = (a/2, b/2, h/2)$, i.e. at the impact point and at the opposite point at the back face of the plate, and are obtained by means of the classical laminated plate theory, using the Navier solution for simply supported plates, and neglecting membrane strains and local deflections. The terms $f_x\left(s, C_{ij}, D_{ij}/h^3\right)$ and $f_y\left(s, C_{ij}, D_{ij}/h^3\right)$ are defined respectively as:

$$f_x\left(s, C_{ij}, D_{ij}/h^3\right) = h^3 \sum_{m=1}^{\infty}\sum_{n=1}^{\infty} \frac{\xi}{\vartheta}\left(s^2 m^2 C_{11} + n^2 C_{12}\right) \tag{1.98}$$

$$f_y\left(s, C_{ij}, D_{ij}/h^3\right) = h^3 \sum_{m=1}^{\infty}\sum_{n=1}^{\infty} \frac{\xi}{\vartheta}\left(s^2 m^2 C_{12} + n^2 C_{22}\right) \tag{1.99}$$

where $s = b/a$, $\xi = \frac{1}{mn}\sin\left(\frac{m\pi R}{a}\right)\sin\left(\frac{n\pi R}{b}\right)$, $\vartheta = D_{11}m^4 s^4 + 2(D_{12} + 2D_{66})m^2 n^2 s^2 + D_{22}n^4$, and C_{ij} and D_{ij} are respectively the constitutive and bending stiffness components of the laminated composite plate calculated by means of the homogenized engineering constants [58]. Equations (1.98) and (1.99) are valid only for odd values of m and n. By adding enough terms, the solution of Equations (1.96) and (1.97) can converge, whereas convergence is not possible for a point load case [47].

The maximum stresses given by Equations (1.96) and (1.97) must be transformed to the stress components on the back outer ply of the laminate (i.e. $(\sigma_1, \sigma_2, \sigma_6)_p$).

This is done by calculating the strain components of the plate; afterwards, the strain components are rotated to the local coordinates of the ply (axis 1 is aligned with the fibers, and axis 2 corresponds to the transverse direction to the fibers); finally, by means of the constitutive matrix of the ply, the corresponding stresses are obtained. All these operations are collected in the following equation:

$$\begin{Bmatrix} \sigma_1 \\ \sigma_2 \\ \sigma_6 \end{Bmatrix}_p = [C]_p [T]_\gamma [S] \begin{Bmatrix} (\sigma_x)_{max} \\ (\sigma_y)_{max} \\ 0 \end{Bmatrix} \tag{1.100}$$

where $[C]_p$ is the constitutive matrix of the back outer ply in the ply coordinate system, $[T]_\gamma$ is the rotation matrix of the engineering strains from the plate coordinate system to the ply coordinate system (see Appendix A), and $[S]$ is the compliance matrix of the plate in the plate coordinate system (i.e. $[S] = [C]^{-1}$). Developing Equation (1.100), the resulting ply stresses are:

$$\begin{aligned} (\sigma_1)_p = \quad & \left((C_{11})_p c^2 + (C_{12})_p s^2\right) \left(S_{11} (\sigma_x)_{max} + S_{12} (\sigma_y)_{max}\right) \\ & + \left((C_{11})_p s^2 + (C_{12})_p c^2\right) \left(S_{12} (\sigma_x)_{max} + S_{22} (\sigma_y)_{max}\right) \end{aligned} \tag{1.101}$$

$$\begin{aligned} (\sigma_2)_p = \quad & \left((C_{12})_p c^2 + (C_{22})_p s^2\right) \left(S_{11} (\sigma_x)_{max} + S_{12} (\sigma_y)_{max}\right) \\ & + \left((C_{12})_p s^2 + (C_{22})_p c^2\right) \left(S_{12} (\sigma_x)_{max} + S_{22} (\sigma_y)_{max}\right) \end{aligned} \tag{1.102}$$

$$(\sigma_6)_p = 2cs (C_{66})_p \left[(S_{12} - S_{11}) (\sigma_x)_{max} + (S_{22} - S_{12}) (\sigma_y)_{max}\right] \tag{1.103}$$

where $c = \cos(\theta)$, $s = \sin(\theta)$, and θ is the fiber orientation of the ply respect to the plate coordinate system.

In addition, the in-situ transverse tensile strength Y_{is}^T and the in-situ in-plane shear strength S_{is}^L for an outer ply, which is considered thin enough in comparison with the whole laminate thickness, can be calculated as [59, 60] (see Chapter **??**):

$$\text{Thin outer ply} \begin{cases} Y_{is}^T = 1.12^2 \sqrt{\dfrac{E_{22}}{1 - \nu_{12}\nu_{21}} \dfrac{\mathcal{G}_{Ic}}{\pi h_p}} \\ S_{is}^L = 2\sqrt{\dfrac{G_{12}\mathcal{G}_{IIc}}{\pi h_p}} \end{cases} \tag{1.104}$$

where E_{11}, E_{22}, G_{12} and ν_{21} are the elastic properties of the ply, h_p is the ply thickness, and $\mathcal{G}_{Ic}$ and $\mathcal{G}_{IIc}$ are respectively the fracture toughness in mode I and mode II. Equation (1.104) is obtained by applying Linear Elastic Fracture Mechanics (LEFM) for longitudinal crack growth and assuming a uniform stress state. On the other hand, the tensile strength and the in-plane shear strength for thick plies are approached to the values measured from tests on unidirectional laminates, $Y_{is}^T = Y^T$ and $S_{is}^L = S^L$.

Under the presence of both in-plane shear and transverse tension, the critical energy release rate $\mathcal{G}_c$ depends on the combined effect of all microscopic energy absorbing mechanisms such as the creation of new fracture surface. The LaRC failure criterion [59, 60, 62–64] is used to predict matrix cracking under multi-axial loading:

$$(1-g)\frac{(\sigma_2)_p}{Y_{is}^T} + g\left(\frac{(\sigma_2)_p}{Y_{is}^T}\right)^2 + \left(\frac{(\sigma_6)_p}{S_{is}^L}\right)^2 \leq 1 \tag{1.105}$$

where $g = \mathcal{G}_{Ic}/\mathcal{G}_{IIc}$.

Replacing the transverse and shear stresses ($(\sigma_2)_p$ and $(\sigma_6)_p$) in Equation (1.105), and the corresponding strengths for thin and thick outer plies, the threshold load for tensile matrix cracking F_{mc}^{ten} can be calculated by simply taking the maximum value of the two extreme cases, thin and thick: $F_{mc}^{ten} = \max\left\{(F_{mc}^{ten})_{thin}, (F_{mc}^{ten})_{thick}\right\}$.

Threshold load for oblique matrix crack

The stress state at the impact point $(x, y, z) = (a/2, b/2, -h/2)$ is 3-D due to the flexural deformation and the contact load. The in-plane compressive and shear stresses due to the flexural deformation can be approached in the same way as it is indicated in the previous section for determining a threshold load for vertical matrix crack on the back outer ply of the laminate. Solutions for the stresses due to concentrated loads in anisotropic plates are scarce and closed-form solutions are limited to transversely isotropic plates loaded along their axis of symmetry, and assuming a Hertzian pressure distribution as well as that the plate is semi-infinite, i.e. half-space [22, 65]. To approximate in a simplified form the stress state at the impact point, the superposition of the flexural stresses and the contact stresses of a half-space plate can be applied as it was shown by Olsson [66].

On the other hand, the maximum through-the-thickness shear stresses due to the flexural deformation created by a transverse static point load F_{mc}^{sh} located at the center of a simply supported, rectangular and orthotropic plate (see Figure 1.5), can be computed using the 3-D stress equilibrium equations [47]. These maximum stresses are located at the edges and middle plane of the plate (i.e. $(\sigma_r)_{max}$: $(x, y, z) = (0, b/2, 0)$, and $(\sigma_q)_{max}$: $(x, y, z) = (a/2, 0, 0)$).

For determining the threshold load for matrix cracking at the impact point or at the edges of plate, a 3-D failure criterion is required. The appearance of matrix cracks located at these points is not as critical as the matrix cracks located at other points since the former do not act as crack tips for large delaminations. Therefore, these matrix cracks do not imply a significant reduction of the residual strength of the structure, and for this reason a threshold load for these matrix cracks is not developed here.

Olsson et al. [10] proposed a simple threshold load for matrix cracking due to the through-the-thickness shear stress created by a static concentrated contact load. The threshold load is calculated by considering the Hertz distribution of the contact pressure, and the corresponding maximum value of the shear stress in the through-the-thickness direction and inside the contact radius. In the same way of the simplified shear stress field indicated by Davies et al. [55], the distribution of the through-the-thickness shear stress is assumed parabolical with the maximum located in the middle plane. The threshold load is defined as:

$$F_{mc}^{sh} = \frac{8\sqrt{3}}{9} \left(\pi S^L h\right)^{3/2} \sqrt{\frac{R}{Q_\alpha}} \tag{1.106}$$

where h is the plate thickness, R is the impactor tip radius, and Q_α is the effective contact modulus (see Equation (1.5)).

1.6.2 Delamination

Delaminations are induced by interlaminar shear stresses which are promoted by matrix cracks, by stiffness mismatch between the adjacent plies, by the thickness of the ply (ply clustering), and by the laminate deflection. Increasing any of these factors will result in an increased mismatch in the bending deformations of adjacent ply groups with different orientations, yielding to large delaminations.

The study of the stiffness mismatch yields important information regarding the location, orientation, and size of delaminations. Liu [67] proposed the following dimensionless mismatch parameter M_L for two-layer plates based on the difference of their bending stiffness respect the global coordinate system of the plate:

$$M_L = \frac{D_{ij}\left(\theta_b\right) - D_{ij}\left(\theta_t\right)}{D_{ij}\left(0^{\mathrm{o}}{}_b\right) - D_{ij}\left(90^{\mathrm{o}}{}_t\right)} \tag{1.107}$$

where D_{ij} are the components of the bending stiffness matrix. Each ply is considered separately, so $D_{ij}\left(\theta_b\right)$ is the stiffness of the bottom layer acting alone, and the subscript t refers to the top layer. While a mismatch coefficient can be defined for each bending coefficient D_{ij}, usually only D_{11} is considered.

The mismatch parameter proposed in Equation (1.107) is inadequate for unidirectional plates since M_L is not equal to 0 despite the fact that these laminates do not have interfaces with mismatched adjacent fiber angles. Moreover, for plates with more than one interface with mismatched fiber orientations of the adjacent plies, this parameter is not applicable. To solve these limitations, Morita et al. [68] proposed a new parameter M_M which is calculated as:

$$M_M = \frac{1}{2\pi}\int_0^{2\pi} \frac{\left[\Delta Q_{11}(\theta) z_i\right]_{max}}{D_{11}(\theta)}\, d\theta \tag{1.108}$$

where $\Delta Q_{11}(\theta)$ is the difference of the in-plane stiffness between the adjacent plies in direction θ, z_i is the through-the-thickness distance from the neutral surface to the considered interface, and $D_{11}(\theta)$ is the bending stiffness of the entire laminate in the direction θ. The parameter M_M is a measure of the maximum bending stress discontinuity given as an integrated quantity with respect to θ. It is considered empirically that the larger the parameter M_M, the larger the impact damage area.

Delaminations only occur at interfaces between plies of different orientation. The shape of the delamination is generally that of an oblong peanut, where its major axis follows the orientation of the lower ply at the interface [5, 8]. These shapes are a result of the shear stress distribution around the surrounding area of the impactor, of the low interlaminar shear strength along or close to the direction of the fibers, and of the matrix cracks created by the flexural in-plane stresses [69]. Figure 1.12 shows a typical distribution of these delaminations.

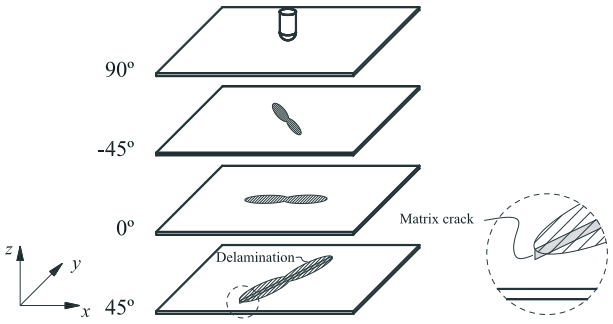

Figure 1.12: Example of peanut shaped delaminations.

There are two different phases during the impact driven delamination process (see Figure 1.13). Firstly, when the impact force reaches a threshold value F_d, there is unstable crack propagation leading to instantaneous large delaminated areas. This often causes the impact force to drop in the response, indicating sudden loss of stiffness [70]. The threshold load F_d does not physically represent the initiation of damage, as sub-critical matrix cracks and small delaminations may initiate at lower forces. Rather, it represents the initial value at which a change in the stiffness properties of the laminate can be detected [17, 45]. Normally, the threshold value is greater for thick laminates than for thin laminates, as shown in Figure 1.13. Secondly, after unstable crack growth, the size of the delaminations increase linearly with the force indicating stable delamination growths. Jackson and Poe [71] suggested the following semi-empirical formula which relates the maximum delamination size d_s and the impact force F:

$$d_s = \frac{1}{\pi S^L h} F \tag{1.109}$$

where S^L is the interlaminar shear strength and h is the plate thickness.

Figure 1.14 shows the typical profile of the impact force versus time history for a monolithic laminated composite plate, where the threshold load F_d and the peak force F_{max} are identified. Depending on the impact velocity, F_d can be equal to F_{max}. On the other hand, the identification of F_d is not always clear, due to the effects of the governing parameters (see Chapter 3), or due to the harmonic resonances of the impactor, of the load cell or of the plate during the impact event [45].

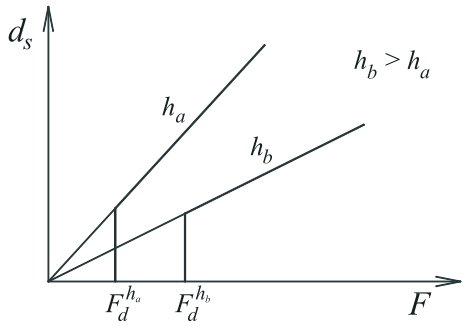

Figure 1.13: Maximum delamination size as a function of the impact force for plates with different thickness (after Christoforou [6]).

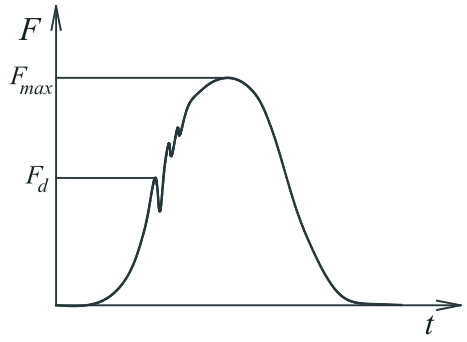

Figure 1.14: Representative impact force versus time history (after ASTM D7136 / D7136M [45]).

Threshold load for delamination

The criteria for matrix cracking given by Equations (1.105) and (1.106) can be used as delamination threshold loads assuming that the matrix crack tips act as initiation points for delaminations in impact events with quasi-static behavior.

A delamination growth criterion for static conditions was derived by Davies et al. [55, 72]. The model was based on Linear Elastic Fracture Mechanics (LEFM) and assumed that mode II fracture determines delamination growth in a simply supported circular plate. To simplify the development of the model, static loading conditions were considered, the laminate was treated as isotropic, only small deflections were considered (membrane effects are neglected), and the through-thickness distributed delaminations were collapsed into a single and perfectly circular mid-plane delamination. In detail, the relationship between the out-of-plane displacement w_o and an external point load F_{d1}^{stat} is given by the theory for thin plates as:

$$w_o = \frac{3r_p^2\left(1-\nu^2\right)}{4\pi E h^3}\left(F_{d1}^{stat}\right) \tag{1.110}$$

where E, ν, h, and r_p are respectively the elastic modulus, the Poisson ratio, the thickness, and the radius of the plate. Assuming that the system is linear allows to apply the principle of superposition for the development of the elastic energy of a plate with a circular mid-plane delamination of radius a_c:

$$\begin{aligned} U = &\frac{3r_p^2\left(1-\nu^2\right)}{8\pi E h^3}\left(F_{d1}^{stat}\right)^2 - \frac{3a_c^2\left(1-\nu^2\right)}{8\pi E h^3}\left(F_{d1}^{stat}\right)^2 \\ &+2\left(\frac{3a_c^2\left(1-\nu^2\right)}{8\pi E\left(\frac{h}{2}\right)^3}\left(\frac{F_{d1}^{stat}}{2}\right)^2\right) \end{aligned} \tag{1.111}$$

The first term of Equation (1.111) is the elastic energy of the plate without the delamination. The second term is the energy of a circular plate of radius a_c. The last term is related to the elastic energy of two circular plates of radius a_c and height $h/2$. Knowing that $-\frac{\partial U}{\partial a} = 2\pi a_c \mathcal{G}_{IIc}$, the threshold load for a mid-plane circular delamination is:

$$F_{d1}^{stat} = \frac{\pi}{3}\sqrt{\frac{8E\mathcal{G}_{IIc}}{1-\nu^2}}h^{3/2} \tag{1.112}$$

By letting $E/(1-\nu^2) = (12D)/h^3$, where D is the bending stiffness, Equation (1.112) can be rewritten as:

$$F_{d1}^{stat} = \pi\sqrt{\frac{32D\mathcal{G}_{IIc}}{3}} \tag{1.113}$$

Equations (1.112) and (1.113) show that delamination grows under a constant load independently of the delamination size. Therefore, an initial flaw is not required and thus the criterion can be used for the prediction of delamination onset. In addition, experimental data and finite element simulations indicate that the delamination threshold load is independent of the boundary conditions and of the in-plane size of the plate [10, 11, 17]. Although the delamination criterion was developed assuming static loading conditions, it may be used for impact responses with dynamic effects, such as in an infinite plate behavior [12]. Probably, this result is due to fact that F_{d1}^{stat} does not depend on the in-plane dimensions of the plate, in

contrast with the threshold F_{mc}^{ten} developed in previously. In Davies et al. [73], this criterion was used in conjunction with a quasi-static, energy-balanced model based on finite element solutions to predict the threshold impact energy for delamination onset.

A more rigorous solution for an arbitrary number of delaminations located at same intervals through-the-thickness of the plate was derived by Suemasu and Majima [74]. The threshold impact load is defined as:

$$F_{dn_d}^{stat} = \pi \sqrt{\frac{32 D \mathcal{G}_{IIc}}{n+1}} \tag{1.114}$$

where n is the number of same thickness plate regions separated by $n_d = n - 1$ same size delaminations. In the work developed by Olsson [11], Equation (1.114) is used for orthotropic plates by simply changing the isotropic plate stiffness D by the effective plate stiffness D^* for orthotropic plates (see Equation (1.55)).

The accumulation process of multiple delaminations was also described by Suemasu and Majima [74]. For equally sized multiple delaminations, the energy release rate is distributed nearly parabolic and symmetric about the middle surface, which corresponds to the location where the energy release rate reaches its maximum. For this case, the energy release rates are independent of the delamination size, and the more delaminations exist, the easier the delamination propagation is. Delaminations of unequal size, they tend to an equal size by the growth of the smaller delaminations regardless of their location through-the-thickness of the laminate. These conclusions were obtained from closed-form energy release rate expressions summarized in Table 1.1, and by verifications with finite element analysis.

Geometric nonlinear effects on the in-plane stresses becomes significant and must be considered when the deflection of the plate reaches the order of the plate thickness or that of the delaminated portions. A numerical Rayleigh-Ritz solution for large deflections was derived in a later paper of Suemasu and Majima [75]. Membrane effects increase the threshold load and cause an asymmetrical distribution of the energy release rate so that the delaminations near the back surface grow faster than those located elsewhere when the load is increased. Also, geometric non-linearity implies large impact energies for delaminations to propagate farther. Therefore, the result using the linear assumption that the more delaminations exist the easier is their propagation may not be true. Considering the finite bending strength and the

Delamination case	Energy release rates	
	mth delamination	$n-2$ delaminations (average)
One delamination larger than the others	$\bar{\mathcal{G}}_{II} = \dfrac{F^2}{32\pi^2 D} S_0$	$\tilde{\mathcal{G}}_{II} = \dfrac{F^2}{32\pi^2 D} \dfrac{S_1}{n-2}$
One delamination smaller than the others	$\bar{\mathcal{G}}_{II} = \dfrac{F^2}{32\pi^2 D} \dfrac{6n^2}{n+6}$	$\tilde{\mathcal{G}}_{II} = \dfrac{F^2}{32\pi^2 D} \dfrac{n^2+2n+3}{n+6}$

Table 1.1: Energy release rates for unequal size delaminations [74], where $S_0 = n^3/\left(m^3 + (n-m)^3\right) - 1$, $S_1 = n^2 - S_0 - 1$, and m is the delamination number (numbering starts with the deepest back face delamination).

critical perforation load, it can be said that a critical radius of the delaminations from which delamination propagation is difficult may exist. This critical radius is function of the interlaminar toughness and of an expected number of delaminations.

Olsson et al. [10] developed a fracture mechanics criterion for dynamic growth of an arbitrary number n_d of delaminations in a transverse isotropic plate. Again, the delaminations are located at the same intervals through-the-thickness of the laminate, small deflections are considered, and shear deformation is neglected. The theory is validated for a wide range of test cases by comparison with 3-D finite element simulations. The threshold impact load is:

$$F_{dn_d}^{dyn} = \frac{F_{dn_d}^{stat}}{\sqrt{1 - \dfrac{7\pi^2}{216}}} \approx 1.213 F_{dn_d}^{stat} \tag{1.115}$$

where $F_{dn_d}^{stat}$ is the quasi-static threshold delamination load given by Equation (1.114). The resulting delamination threshold load is about 21% higher than the corresponding quasi-static threshold load.

1.6.3 Permanent indentation

An impact on a laminated composite plate, usually results with a visible permanent indentation at the impact point as a result of the matrix plasticity, disorder of the broken fibers, and friction between these fibers and the matrix. Just after the

impact, the permanent indentation has its highest value and gradually its depth is reduced due to the material relaxation.

The prediction of the threshold load at which permanent indentation initiates can be approached by the following simple equation:

$$F_{ind} = k_y \alpha_{cr} \tag{1.116}$$

where k_y is a linearized stiffness of the elastic-plastic loading phase (Equation (1.27)), and α_{cr} is the critical indentation as from of it permanent indentation starts and is defined by Equation (1.28).

The corresponding threshold velocity for permanent indentation can be calculated by means of a simple energy balance of the simplified quasi-static model described in Section 1.4 and represented in Figure 1.8.b. Assuming that the impact energy is used for local and global deformation of the plate, the threshold velocity yields to:

$$V_{ind} = \frac{\alpha_{cr}}{M_i^{1/2}} \left[k_y + \frac{k_y^2}{k_{bsm}} \right]^{1/2} \tag{1.117}$$

where k_{bsm} is the plate global stiffness.

1.6.4 Fiber failure

Fiber failure generally occurs much later in the fracture process than matrix cracking and delamination, and it is considered as a precursor of plate perforation. Fiber failure occurs under the impactor due to locally compressive and shear stresses, and on the non-impacted face due to tensile bending stresses. More extensive fiber failure normally occurs in the central part of the delaminated region and appears to be fairly uniformly through-the-thickness of the laminate. Fiber failure in thin laminates generally affects more plies and is more extensive than in thick laminates, indicating the importance of membrane stresses in formation of fiber fracture [8].

1.6.5 Perforation

There are numerous modes of failure in which energy can be dissipated in impacts that result in complete penetration of the plates. Caprino and Lopresto [76] reported

that the perforation energy depends on the total fiber volume of the plate and on the impactor tip shape, whereas the architecture of the fibers, the stacking sequence of the laminate and the type of matrix have no effect. Research into perforation impact is mainly concentrated on the ballistic range, although perforation can also occur for other types of impact behavior (see Section 1.2).

Perforation occurs when the fibers reach their critical strain, enabling the impactor to completely penetrate the material. Under this assumption, a conservative estimate of the quasi-static threshold load for perforation F_{per}^{ten} can be obtained by simply replacing the in-plane longitudinal stress on the back outer ply (Equation (1.101)) in the following fiber tensile failure criterion [63]:

$$\frac{(\sigma_1)_p}{X^T} \leq 1 \tag{1.118}$$

where X^T is the fiber tensile strength. Therefore, the threshold load for perforation F_{per}^{ten} yields:

$$F_{per}^{ten} = \frac{\pi^5 R^2 h^2 X^T}{8 b^2 \mathcal{X}} \tag{1.119}$$

where $\mathcal{X}$ is defined as:

$$\begin{aligned} \mathcal{X} = \quad & \left[\left((C_{11})_p\, c^2 + (C_{12})_p\, s^2\right) S_{11} + \left((C_{11})_p\, s^2 + (C_{12})_p\, c^2\right) S_{12}\right] \\ & \times f_x\left(s, C_{ij}, D_{ij}/h^3\right) \\ & + \left[\left((C_{11})_p\, c^2 + (C_{12})_p\, s^2\right) S_{12} + \left((C_{11})_p\, s^2 + (C_{12})_p\, c^2\right) S_{22}\right] \\ & \times f_y\left(s, C_{ij}, D_{ij}/h^3\right) \end{aligned} \tag{1.120}$$

On the other hand, by considering the Hertz contact law and a uniform distribution of the through-the-thickness shear stress, a perforation threshold load due to laminate shear failure can be obtained [5, 77]. The resulting threshold load is:

$$F_{per}^{sh} = \sqrt{6}\left(\pi S^L h\right)^{3/2} \sqrt{\frac{R}{Q_\alpha}} \tag{1.121}$$

where S^L is the shear strength, h is the plate thickness, R is the impactor tip radius, and Q_α is the effective contact modulus (see Equation (1.5)). The corresponding

velocity at which perforation occurs can be formulated by means of a simple energy balance similar to that used in the determination of the threshold velocity for permanent indentation. Assuming that impact energy is used for the perforation and for the global deformation of the plate, the threshold velocity yields:

$$V_{per}^{sh} = M_i^{-1/2} \left[\frac{4(2\pi)^{5/2}}{5} k_H^{-3/2} R^{5/4} \left(hS^L\right)^{5/2} + 8\pi^3 k_H^{-1} k_{bsm}^{-1} R^{3/2} \left(hS^L\right)^3 \right]^{1/2} \quad (1.122)$$

where k_{bsm} is the plate stiffness. If the global deformation of the plate is neglected (i.e. half-space behavior), the second term of Equation (1.122) is removed.

In Wen [78, 79], velocity thresholds for impact perforation on rectangular, flat, and monolithic laminated composite plates struck by impactors with different tip shapes are proposed. The approach is based on the assumption that the deformation is localized and the mean pressure offered by the plate to resist the impactor can be decomposed into two parts. One part is a cohesive quasi-static resistive pressure due to the elastic-plastic deformation of the plate. The other is a dynamic resistive pressure arising from velocity effects. The corresponding threshold for hemispherical-ended impactor is:

$$V_{per}^{com} = \frac{3\pi R^2 h \sqrt{\rho_p \sigma_{yc}}}{32 M_i} \left[1 + \sqrt{1 + \frac{128 M_i}{9\pi \rho_p R^2 h}} \right] \quad (1.123)$$

where R is the impactor tip radius, M_i is the impactor mass, h is the plate thickness, ρ_p is the plate density, and σ_{yc} is the elastic limit of the plate in through-the-thickness compression which can be approached to the transverse compressive strength Y^C. It should be noted that Y^C is a strain rate dependent strength [80].

Chapter 2

Test configurations

2.1 Introduction

In the aeronautical industry, drop-weight impact tests are performed to assess the damage resistance of a structure. These tests create delaminations which are typically categorized as *Barely Visible Impact Damage* (BVID). Delaminations reduce significantly the compressive strength of the impacted structure. For this reason, *Compression After Impact tests* (CAI) are performed in order to assess the damage tolerance of the structure.

The sequential experimental tasks which are carried out in the present thesis in order to analyze laboratory coupons are: definition of the impact configurations (i.e. selection of the governing parameters), manufacturing of the specimens, non-destructive inspections for the detection of manufacturing flaws (e.g. ultrasonic techniques), drop-weight impact tests, non-destructive inspections to detect the BVID, and finally, compression after impact tests.

This chapter presents the definition of a set of low-velocity impact tests on laminated composite plates which allow the study of the effects of some governing parameters on the damage resistance. The goal is to obtain a range of different experimental results that will be used to assess whether the predictions given by the numerical simulations accurately account the complexity of the impact damage (see Chapter **??**). It should be noted that all studies are focused on the effects of the governing parameters on the impact damage rather than on the results of the compression after impact tests. Furthermore, the description of the compression

after impact test set-up is also explained in detail.

2.2 Impact tests

The procedure for the design of the experiments is of great importance since it must ensure that one given analysis is focused on the effects of only one governing parameter. Moreover, the procedure must provide a qualitative understanding whether damage will occur, as well as its type and extension.

The procedure used is mainly based on the impact characterization diagram proposed by Christoforou and Yigit [6, 7, 13, 14] (see Section 1.5). Given an impact configuration, the diagram predicts the behavior type and the maximum impact force by calculating only two key parameters, λ (i.e. relative stiffness) and ζ_w (i.e. relative mobility):

$$\lambda = \frac{k_{bsm}}{k_y} \tag{2.1}$$

$$\zeta_w = \frac{\sqrt{M_i k_y}}{16\sqrt{I_1 D^*}} \tag{2.2}$$

It should be noted that the key parameters are obtained by considering a linear contact law [7] (see Section 1.3.4), and a dimensionless framework based on the maximum indentation where the magnitudes are defined as: mass $[M] = M_i$, time $[T] = M_i^{1/2} k_y^{-1/2}$, and length $[L] = M_i^{1/2} k_y^{-1/2} V_0$ (see Section 1.4.2). In particular, the linear contact stiffness k_y is calculated by means of Equation (1.27) and the plate stiffness k_{bsm} can be approached experimentally, by using numerical methods, or analytically in cases with simple structure geometries. The expression used by Yigit and Christoforou [13] to predict the stiffness k_{bsm}, for a simply supported plate without considering shear and membrane effects, is:

$$k_{bsm} = k_b = \frac{D^*}{0.0116 b^2} \tag{2.3}$$

where b is the smallest width of the plate [11].

The prediction of the maximum elastic impact force is useful because it can be compared with a damage threshold load (see Section 1.6). Using the dimensionless framework, the maximum dimensional elastic force can be obtained as:

$$F_{max} = \bar{F}_{max} V_0 \sqrt{M_i k_y} = \bar{F}_{max} \sqrt{k_y} \sqrt{2E_i} \tag{2.4}$$

where $\bar{F}_{max}$ is the dimensionless maximum elastic force extracted from the impact characterization diagram by means of the key parameters λ and ζ_w. The variable E_i is the impact energy.

2.2.1 Benchmark: ASTM drop-weight impact test

The ASTM test method for measuring the damage resistance of a fiber-reinforced polymer matrix composite when subjected to a drop-weight impact event (i.e. ASTM D7136 / D7136M [45]) is taken as a reference in order to fix some of the governing parameters. Other guidelines for a drop-weight impact test provided by the aeronautical industry are available (e.g. Airbus AITM1-0010 [81]; Boeing 7260 [82]; NASA ST-1 [83]), however the set-ups are all essentially the same.

The standard is focused on rectangular, flat, and monolithic laminated composite plates with 150mm x 100mm in-plane dimensions. If the laminates are manufactured using unidirectional plies, a balanced and symmetric stacking sequence $[(45/0/-45/90)_n]_S$ is defined. The whole number n is selected in such a way that the cured plate thickness is close to 5mm. The plate stacking sequence is defined by taking the 0° fiber orientation aligned with the longer in-plane dimension of the plate.

The specimens are placed over a flat support fixture base with a 125mm x 75mm rectangular cut-out which allows the impactor to contact through the specimen without interferences (see Figure 2.1.a). Guiding pins are located such that the specimen can be centrally positioned over the cut-out. The support fixture base has four rubber-tipped clamps which restrain the specimen during impact and provide a minimum holding capacity of 1100N. These rubber-tipped points clamp the specimen at 12.5mm and 6mm from each edge of the open window of the fixture base (see Figure 2.1.b) [81]. The boundary conditions provided by the clamping system can be approached to simply supported [46].

The impact tests are carried out with an impact tester, which includes a guide mechanism, a rigid clamping system, a drop-weight instrumented impactor, a velocity sensor, and a rebound catcher. The impacts are performed by releasing the

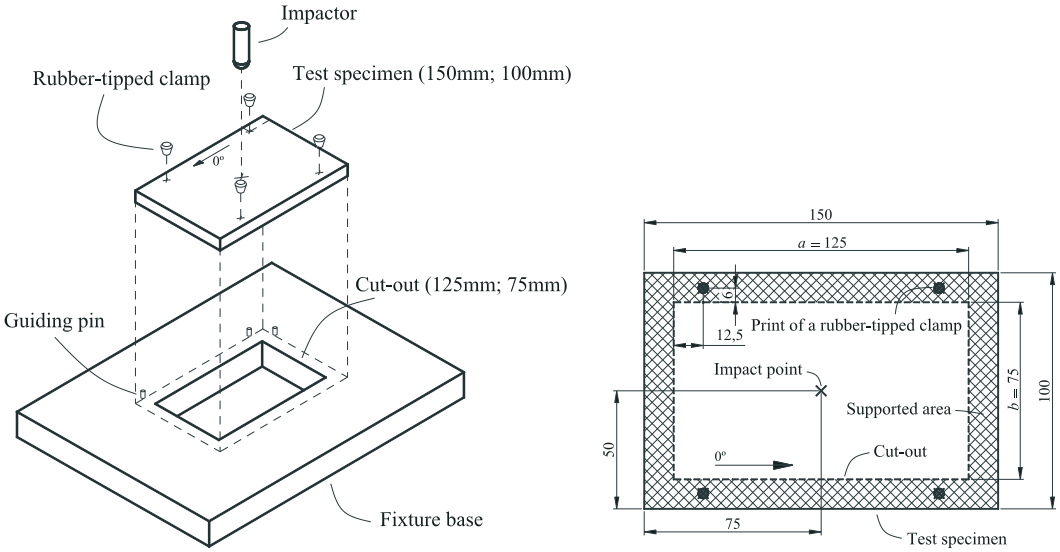

Figure 2.1: (a) Impact support fixture; (b) detail of the support area and clamping points of the specimen.

impactor with a selected mass from a desired preset height, and dropped freely according to the gravitational force and following a guide mechanism. A normal incidence angle impact occurs at the center of the plate caused by a 16mm diameter hemispherical-shaped impactor made of hardened steel. Just prior to impact on the specimen, a steel flag connected to the impactor is passed through an optical sensor which triggers the data acquisition system and calculates the initial impact velocity V_0. The velocity is calculated from the distance between two edges of the flag and the time interval to pass through the sensor. Once impact begins, the contact force is detected by the force transducer attached to the impactor. The force history is stored in a computer. Finally, if perforation does not occur, a rebound catcher is also triggered by the optical sensor so that a re-strike does not occur.

The velocity and displacement history of the impactor, $V(t)$ and $w_i(t)$ respectively, can be calculated by integrating once and twice the force history:

$$V(t) = V_0 + gt - \int_0^t \frac{F(t)}{M_i}\, dt \tag{2.5}$$

$$w_i(t) = w_0 + V_0 t + \frac{gt^2}{2} - \int_0^t \left(\int_0^t \frac{F(t)}{M_i}\, dt \right) dt \tag{2.6}$$

where V_0 is the initial impact velocity, g is the acceleration due to the gravity, t is the time, and w_0 is the impactor position from reference location at time $t = 0$. Additionally, the energy absorbed by the specimen, $E_a(t)$, can be calculated as:

$$E_a(t) = \frac{M_i \left(V_0^2 - V(t)^2\right)}{2} + M_i g w_i(t) \tag{2.7}$$

The standard suggests testing a sample of 5 specimens using a constant impactor mass of 5.5kg and a constant impact energy calculated in function of the specimen thickness:

$$E_i = C_E h \tag{2.8}$$

where h is the plate thickness and C_E is a ratio of the impact energy to the specimen thickness equal to 6.7J/mm. The reason for defining the impact energy by means of Equation (2.8) is related to the effects of the support conditions on the impact damage. When an impact is performed following the standard specifications, the specimen will develop damage sizes less than half of the unsupported specimen width (i.e. 38mm), thus avoiding significant interactions of the damage areas with the edge support conditions.

Tables 2.1 and 2.2 summarize the specifications of the standard regarding the specimen coupons and the impactor.

Following the specifications proposed by the standard and using the properties summarized in Table **??** for AS4/8552 carbon-epoxy composite material (see Chapter **??**), the resulting laminate is $[(45/0/-45/90)_3]_S$ with a total nominal thickness $h = 4.42$mm, which defines an impact energy of $E_i = 29.6$J (see Equation (2.8)) and an impact velocity of $V_0 = 3.28\text{ms}^{-1}$.

The terms required to find the key parameters of the impact characterization diagram can be respectively calculated as: k_{bsm} by Equation (2.3), k_y by Equation (1.27), I_1 by Equation (A.47), and D^* by Equation (1.55). Using these definitions and assuming that the effective in-plane dimensions of the plate are $a = 125$mm and $b = 75$mm (see Figure 2.1.b), yield to: $\lambda = 0.71$ and $\zeta_w = 8.11$. These parameters

Specimen coupons	
Shape	Flat and rectangular
Thickness	$h \approx 5$mm
In-plane size	$a_t = 150$mm x $b_t = 100$mm
Lamina type	Unidirectional or woven fabric
Stacking sequence	$[(45/0/-45/90)_n]_S$ (for unidirectional laminas)
Boundary conditions	Four rubber-tipped clamps

Table 2.1: ASTM D7136 / D7136M specifications for the specimen.

Impactor	
Shape	Hemispherical
Radius	$R = 8$mm
Material	Steel (60 to 62 HRC)
Mass	$M_i = 5.5$kg
Velocity	$V_0 = \sqrt{\frac{2\,(C_E h)}{M_i}}$
Incidence impact angle	Normal to the plate

Table 2.2: ASTM D7136 / D7136M specifications for the impactor.

predict a quasi-static behavior and a maximum dimensionless force of $\bar{F}_{max} = 0.65$. Finally, using Equation (2.4), the maximum impact force is $F_{max} = 14.28$kN.

The analytical damage thresholds can be calculated and compared with the maximum impact force in order to predict qualitatively the damage occurrence. As it is noted in the standard, matrix cracking and delamination damage are ensured if all the specifications of the standard are followed. This is demonstrated in Table 2.3, where the corresponding damage thresholds for matrix cracking and delamination are below the maximum predicted force.

Furthermore, the maximum load is close to the perforation threshold which indicates that perforation can occur. However, it is difficult to develop perforation because other damage mechanisms are generated previously so they absorb energy

and avoid the subsequent perforation process.

Damage mechanism	Equation	Value [kN]
Matrix cracking	(1.105)	$F_{mc}^{ten} = 5.92$
	(1.106)	$F_{mc}^{sh} = 1.82$
Delamination	(1.112), using D^*	$F_{d1}^{stat} = 5.66$
Permanent indentation	(1.116)	$F_{ind} = 0.33$
Perforation	(1.119)	$F_{per}^{ten} = 13.98$

Table 2.3: Damage thresholds for AS4/8552 carbon-epoxy composite material.

2.2.2 Selected studies: fixed and variable parameters

Taking as a reference the standard for drop-weight impact test [45], different experimental studies will be performed. All these studies will be focused mainly on the damage onset which produces a significant reduction on the structure stiffness and/or residual strength, i.e. F_d (see Figure 1.14).

The variables selected in order to study their effects are: the ply thickness h_p (ply clustering), the laminate thickness h, stacking sequence, the impactor mass M_i and the impact velocity V_0. The variation of these parameters yield to three main studies: effect of ply thickness (clustering), effect of the mismatch angles of the plies, and effect of the laminate thickness. As will be demonstrated in the following sections, all these studies are under quasi-static impact behavior. Therefore, the prediction of the maximum elastic impact force can also be obtained by means of Equation (1.83).

For all laminates, the composite material used is AS4/8552 carbon-epoxy unidirectional pre-preg. The properties of the material are summarized in Table **??** (see Chapter **??**). It should be noted that for the calculation of the ply thickness, the corresponding cured value of the laminate thickness will be used (known after specimen manufacturing).

All the impact tests described below are performed using a commercially available CEAST Fractovis Plus instrumented impact drop-weight tower. The impact tester disposes of a load cell of 22kN attached to the impactor, an automatic pneu-

matic rebound brake system, and a clamping system with a holding capacity of 3000N at each of the four clamping points (see Figure 2.2).

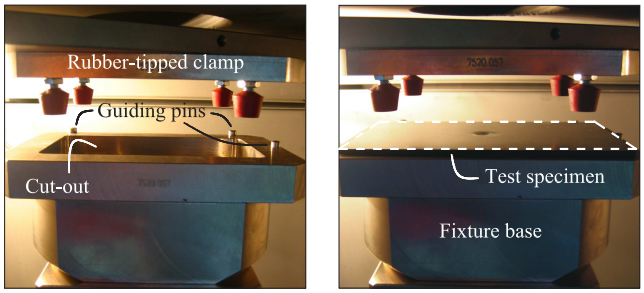

(a) (b)

Figure 2.2: Detail of the clamping system: (a) without specimen and (b) with specimen.

Finally, the non-destructive inspections before and after impact will be performed by the C-scan ultrasonic technique, which gives the projected damaged areas over the structure thickness. Additionally, the measurements of the dent-depth are performed by means of a Mitutoyo 3D coordinate measuring machine. It should be noted that not all the impacted specimens are selected for the dent-depth measurements.

Effect of ply thickness (clustering)

Ply clustering was found to reduce the damage resistance of a laminate [46, 68]. Stacking plies with the same fiber orientation increases the interlaminar shear stresses at the adjacent interfaces due to the increased difference in the bending stiffness of the ply groups. This increase in stress, in turn, leads to larger delaminations.

Ply clustering also reduces the number of interfaces available for delamination, because delamination typically occurs at interfaces with different fiber orientations. Reducing the number of locations available for delamination will increase the delamination size at the remaining interfaces [84, 85], since delamination acts as an energy dissipating mechanism during the impact event.

The transverse tensile and shear strengths of a ply are function of the ply thickness, of the ply position in the laminate, and of the fiber orientation of the adjacent plies. This is called the *in-situ effect* (see Chapter **??**). Since matrix cracks act as

initiation points for delaminations, the in-situ effect must be considered for a proper analysis of the ply clustering effect.

The effect of ply clustering on the damage tolerance, assessed by means of the residual compressive load, is not yet fully clear. In fact, the compressive strength decreases if the plate bending stiffness is reduced. In addition, the laminate bending stiffness decreases if the size of the delaminations created by impact are large (i.e. when clustering is increased) but also when the number of delamination planes is increased (i.e. when clustering is reduced). Therefore, giving these counteracting effects, it is difficult to assess whether ply clustering reduces the damage tolerance of a structure.

The stacking sequences proposed for this study are $[(45/0/-45/90)_4]_S$, $[(45_2/0_2/-45_2/90_2)_2]_S$, and $[45_4/0_4/-45_4/90_4]_S$ (in the following, these laminates are respectively identified as L02, L03, and L04). All laminates have the same plate thickness h because an equal number of plies is used (i.e. 32 plies; $h = 5.8$mm). However, the clusterings h_p are different (i.e. L02: $h_p = h_{pp}$, L03: $h_p = 2h_{pp}$, and L04: $h_p = 4h_{pp}$, where h_{pp} is the thickness of a single ply), yielding to different number of interfaces for delamination (i.e. L02: $n_d = 30$, L03: $n_d = 14$, and L04: $n_d = 6$).

Three different impact energies are considered: 38.6J, 28.6J and 19.3J. Given that the impactor mass is kept constant at 5kg, the different energies also enable the study of the effects of velocity. In detail, Table 2.4 shows the impact configurations for all the laminates. Since the repeatability of the impact test is quite good (see Chapter 3), a sample of less than three specimens is used for some cases.

Specimen name	Impact energy [J]	Impactor mass [kg]	Impact velocity [ms^{-1}]	Drop height [mm]
L0x-S01				
L0x-S02	38.6	5	3.93	787.5
L0x-S03				
L0x-S04	28.6	5	3.38	582.5
L0x-S05	19.3	5	2.78	394.0
L0x-S06				

Table 2.4: Impact configurations for laminates: L02, L03 and L04.

Using the material properties summarized in Table **??**, the resulting key pa-

rameters of the impact characterization diagram are: $\lambda = 1.62$ and $\zeta_w = 4.48$ for laminate L02, $\lambda = 1.60$ and $\zeta_w = 4.50$ for laminate L03, and $\lambda = 1.55$ and $\zeta_w = 4.58$ for laminate L04. Since the key parameters are independent of the impact velocity, the resulting values are constant for each laminate at any impact energy (see Equations (2.1) and (2.2)). Additionally, the key parameters are almost equal for all laminates due to the fact that the stiffness of the laminates is similar. Therefore, the dimensional elastic response of the laminates for each impact energy is also expected to be similar.

Introducing the key parameters in the impact characterization diagram, a quasi-static behavior and a maximum dimensionless force of $\bar{F}_{max} = 0.78$ are predicted for all the laminates. The dimensionless force yields to the following maximum elastic impact forces for each impact energy: $F_{max} = 19.8$kN for $E_i = 38.6$J, $F_{max} = 17.1$kN for $E_i = 28.6$J, and $F_{max} = 14.0$kN for $E_i = 19.3$J.

Finally, the damage thresholds explained in Section 1.6 are summarized in Table 2.5. Again, these thresholds are constant for each impact energy since no dependence with velocity is considered in the formulations. Comparing the threshold loads with the maximum elastic impact forces, the occurrence for damage can be analyzed easily.

Damage mechanism	Equation		Values [kN]		
			L02	L03	L04
Matrix cracking	(1.105)	F_{mc}^{ten}:	10.34 (thin)	7.20 (thin)	4.92 (thin)
	(1.106)	F_{mc}^{sh}:	2.74	2.74	2.74
Delamination	(1.112), using D^*	F_{d1}^{stat}:	8.53	8.49	8.34
	(1.114), using D^*	$F_{dn_d}^{stat}$:	2.61	3.68	5.11
	(1.115), using D^*	F_{d1}^{dyn}:	10.35	10.30	10.11
	(1.115), using D^*	$F_{dn_d}^{dyn}$:	3.17	4.46	6.19
Permanent indentation	(1.116)	F_{ind}:	0.33	0.33	0.33
Perforation	(1.119)	F_{per}^{ten}:	24.23	23.88	23.16

Table 2.5: Damage thresholds for laminates: L02, L03 and L04.

The most significant damage threshold loads are the ones which indicate important reductions on the plate stiffness and/or strength. Basically, these thresholds are given by Equations (1.105) and (1.112) (i.e. F_{mc}^{ten} and F_{d1}^{stat}, respectively). The

first gives a value for matrix cracking on the back outer ply which can create an elongated delamination at the first interface from the back face of the plate. The second gives a threshold for a circular mid-plane delamination.

As shown in Table 2.5, for laminate type L02 the first delamination appears in the mid-plane of the plate ($F_d = F_{d1}^{stat}$), and for laminate types L03 and L04 the delamination is located on the back-face ($F_d = F_{mc}^{ten}$). Figure 2.3 shows these threshold loads as a function of the ply thickness on a logarithmic scale. Only F_{mc}^{ten} for thin plies depends on the ply thickness (see Equation (1.104)). The solid gray line shows the trend of the analytical threshold load in function of the ply thickness for the laminates considered.

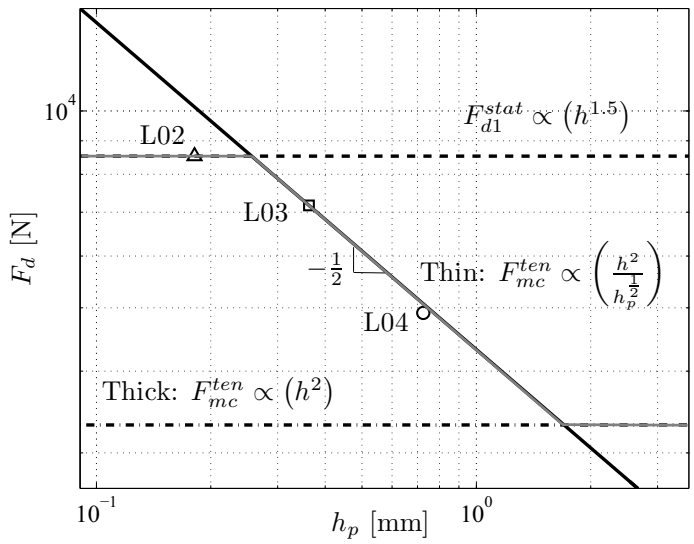

Figure 2.3: Analytical threshold load trend in function of h_p, for laminates L02, L03 and L04. The damage threshold F_{mc}^{ten} for laminates with thin plies is computed from the stresses of laminate type L03.

Furthermore, it is predicted that perforation will not occur for any impact energy because all the maximum elastic forces are below the perforation threshold.

Finally, the values of the mismatch parameter proposed by Morita et al. [68] (see Equation (1.108)) for each laminate are: $M_M = 0.270\text{mm}^{-2}$ for L02, $M_M = 0.235\text{mm}^{-2}$ for L03, and $M_M = 0.198\text{mm}^{-2}$ for L04. The mismatch parameter provides information about the effects of the mismatch interface angles of the plies on the resulting projected delamination area. It is considered that the larger the

parameter M_M is, the larger the projected delamination area is. The results obtained indicate that the laminate with thin plies will have larger projected delamination area than that of the laminate with thick plies. However, this deduction is not valid because it is expected that laminate L04 will have larger delaminations due to the reduced number of available interfaces for delamination. Therefore, the Morita parameter is not suitable to compare different stacking sequences to predict the largest resulting delamination area.

Effect of ply mismatch angle at interfaces

The mismatch angle of an interface is the difference in the fiber orientation of the adjacent plies. Increasing the mismatch angle increases the stress concentration at the interface due to an increased difference in the bending stiffness. Therefore, the damage resistance can be reduced if the mismatch angle is increased because larger delaminations are expected. For this reason, the damage tolerance is also expected to be reduced.

For this study, the laminate type L02 presented in previous study is compared with a new laminate $[(0/90)_9]_S$ (in the following, it is identified as L06). As it can be seen, laminate L06 has a stacking sequence with increased mismatch angles in comparison with laminate L02. Laminates L02 and L06 have practically equal cured ply thickness h_p, but different laminate thickness h since more plies are used for L06 (i.e. L02: $h = 5.8$mm and L06: $h = 6.8$mm).

The impact configurations considered are the same as the described ones for ply clustering study. Accordingly, three different impact energies are defined 38.6J, 28.6J and 19.3J, with a constant impactor mass of 5kg (see Table 2.4). Therefore, the predictions for laminate type L02 given in previous study can be reused herein.

Using the material properties summarized in Table **??**, the resulting key parameters of the impact characterization diagram for laminate type L06 are: $\lambda = 2.52$ and $\zeta_w = 3.31$. Introducing the key parameters in the impact characterization diagram, a quasi-static behavior and a maximum dimensionless force of $\bar{F}_{max} = 0.85$ are expected for all the impact energies. The dimensionless force yields to the following maximum elastic impact forces: $F_{max} = 21.4$kN for $E_i = 38.6$J, $F_{max} = 18.4$kN for $E_i = 28.6$J, and $F_{max} = 15.1$kN for $E_i = 19.3$J.

Table 2.6 summarizes the main damage threshold loads. The significant first

damage for laminate L06 is $F_d = F_{d1}^{stat}$ which predicts a circular mid-plane delamination. In addition, it should be noted that the threshold load F_{mc}^{ten} is close to F_{d1}^{stat}. Therefore, the first drop in the impact load history may be triggered by a combination of both delamination types.

Finally, it is predicted that perforation will not occur for any impact energy because all the maximum elastic forces are below the perforation threshold.

Damage mechanism	Equation	Values [kN]	
Matrix cracking	(1.105)	F_{mc}^{ten}:	11.26 (thin)
	(1.106)	F_{mc}^{sh}:	3.47
Delamination	(1.112), using D^*	F_{d1}^{stat}:	10.65
	(1.114), using D^*	$F_{dn_d}^{stat}$:	3.07
	(1.115), using D^*	F_{d1}^{dyn}:	12.92
	(1.115), using D^*	$F_{dn_d}^{dyn}$:	3.73
Permanent indentation	(1.116)	F_{ind}:	0.33
Perforation	(1.119)	F_{per}^{ten}:	37.16

Table 2.6: Damage thresholds for laminate L06.

Effect of the laminate thickness

Another proposed study is to analyze the effects of the laminate thickness on the damage resistance. Modifying the plate thickness and the impactor mass, the behavior of an impact can be local or global dominated. Because of that, the resulting damage mechanisms as well as their extensions can vary. For instance, in thick laminates, the delaminations initiate close to the loaded surface since contact stresses are high. However, in thin laminates, the delaminations initiate close to the mid-plane since contact stresses are negligible. In addition, thin laminates stand large global bending deflections which often generate, at a certain point, geometric nonlinear effects, i.e. membrane effects. These effects stiff the impact response of the structure because the stiffness evolves from bending to axial.

On the other hand, it is obvious that the damage tolerance is also improved if the laminate thickness is increased. However, the resulting structures are heavier

and more expensive.

For this study, the laminate type L02 presented in the previous studies is compared with two new laminates: $[(45/0/-45/90)_2]_S$ and $[(45/0/-45/90)_6]_S$ (in the following, they are identified as L01 and L05, respectively). As it can be verified, the stacking sequences are equal but the number of repeated ply groups are different, yielding to three different laminate thicknesses (i.e. L01: $h = 3.0$mm, L02: $h = 5.8$mm, and L05: $h = 8.8$mm).

The impact configurations considered for laminates L01 and L05 are respectively summarized in Tables 2.7 and 2.8 (see Table 2.4 for the configurations of the laminate type L02). The comparable cases of impact energy which allow to analyze the effects of laminate thickness are: 19.3J for laminates L01 and L02, and 38.6J for laminates L01, L02 and L05. For both cases of energy, the impactor mass is kept constant and equal to 5kg.

Specimen name	Impact energy [J]	Impactor mass [kg]	Impact velocity [ms^{-1}]	Drop height [mm]
L01-S01	38.6	5	3.93	787.5
L01-S02	19.3	5	2.78	394.0
L01-S03				
L01-S04	19.3	6	2.54	328.9
L01-S05				
L01-S06	12.0	2	3.46	610.4

Table 2.7: Impact configurations for laminate type L01.

Specimen name	Impact energy [J]	Impactor mass [kg]	Impact velocity [ms^{-1}]	Drop height [mm]
L05-S01	38.6	5	3.93	787.5
L05-S02				
L05-S03	57.8	6	4.39	982.6
L05-S04				
L05-S05	57.9	15	2.78	394.0
L05-S06				

Table 2.8: Impact configurations for laminate type L05.

Besides the configurations considered for the study of the laminate thickness, Tables 2.7 and 2.8 describe other impact configurations for laminates L01 and L05,

respectively. These configurations allow to analyze the effects of changing the impactor mass and the impact velocity but keeping constant the impact energy. In detail, this study is performed by means of: specimens S02 and S03 (M_i = 5kg) compared with S04 and S05 (M_i = 6kg) for laminate L01, and specimens S03 and S04 (M_i = 6 kg) compared with S05 and S06 (M_i = 15kg) for laminate L05. In addition, the impact configuration of specimen L01-S06 is used in order to analyze if the resulting damage behavior is more localized than other configurations with larger impactor mass.

Using the material properties summarized in Table **??**, the resulting key parameters of the impact characterization diagram and the resulting maximum elastic impact forces are summarized in Table 2.9 for laminate L01, and in Table 2.10 for laminate L05.

Specimen	M_i [kg]	λ	ζ_w	$\bar{F}_{max}$	V_i [ms^{-1}]	F_{max} [kN]
L01-S01	5	0.22	16.82	0.43	3.93	10.8
L01-S02 L01-S03	5	0.22	16.82	0.43	2.78	7.6
L01-S04 L01-S05	6	0.22	18.42	0.43	2.54	7.6
L01-S06	2	0.22	10.64	0.43	3.46	6.0

Table 2.9: Maximum elastic impact force predictions for laminate type L01.

Specimen	M_i [kg]	λ	ζ_w	$\bar{F}_{max}$	V_i [ms^{-1}]	F_{max} [kN]
L05-S01 L05-S02	5	5.67	1.94	0.92	3.93	23.32
L05-S03 L05-S04	6	5.67	2.13	0.92	4.39	28.5
L05-S05 L05-S06	15	5.67	3.36	0.92	2.78	28.5

Table 2.10: Maximum elastic impact force predictions for laminate type L05.

Table 2.11 summarizes the main damage threshold loads for laminates L01 and L05. Perforation damage clearly will occur for specimen L01-S01 because the maximum elastic impact force is higher than the perforation threshold load. Additionally, specimens from L01-S02 to L01-S05 (i.e. with an impact energy of 19.3J), the maximum load is close to the perforation threshold which indicates that perforation can also occur. In reality, it is difficult to develop perforation in these specimens because other damage mechanisms are generated previously so they absorb energy and avoid the subsequent perforation process. Therefore, except for specimen L01-S01, it is expected that all impact configurations of laminate L01 will develop a first drop in the impact load history produced by a narrow and elongated delamination at the first interface from the back face of the plate ($F_d = F_{mc}^{ten}$). On the other hand, perforation will not occur for any impact configuration of laminate type L05. Moreover, the significant first damage for laminate L05 is $F_d = F_{d1}^{stat}$. Thus, it is expected that the first drop in the impact load histories is produced by a circular mid-plane delamination as it was also predicted for laminate type L02.

Damage mechanism	Equation		Values [kN]	
			L01	L05
Matrix cracking	(1.105)	F_{mc}^{ten}:	2.68 (thin)	23.80 (thin)
	(1.106)	F_{mc}^{sh}:	1.02	5.11
Delamination	(1.112), using D^*	F_{d1}^{stat}:	3.16	15.97
	(1.114), using D^*	$F_{dn_d}^{stat}$:	1.37	3.99
	(1.115), using D^*	F_{d1}^{dyn}:	3.83	19.37
	(1.115), using D^*	$F_{dn_d}^{dyn}$:	1.66	4.84
Permanent indentation	(1.116)	F_{ind}:	0.33	0.33
Perforation	(1.119)	F_{per}^{ten}:	6.39	56.04

Table 2.11: Damage thresholds for laminates: L01 and L05.

As a summary of the analytical threshold loads for all the laminates described in the previously proposed studies, Figure 2.4 shows the trends of these loads in function of the ply thickness on a logarithmic scale. The predicted critical values have been divided by h^2 in order to keep constant the profiles for matrix cracking on the back outer ply for each stacking sequence type (i.e. type TI: $[(45_x/0_x/-45_x/90_x)_n]_S$;

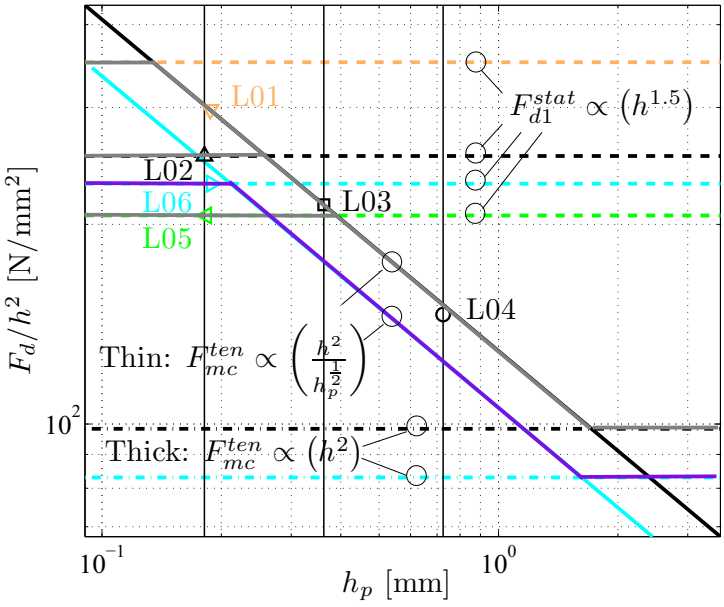

Figure 2.4: Analytical threshold trends for all laminates.

type CP: $[(0_x/90_x)_n]_S$). The ticked gray lines indicate the threshold trend for the stacking sequence type TI, and the blue lines indicate the expected trend for the stacking sequence type CP.

Summary of selected laminates

As a summary, the laminate types selected for the impact and compression impact tests are collected in Table 2.12. As was noted previously, the sample for each laminate are 6 specimens, most of them with different impact configurations.

Name	Stacking sequence	Number of plies	Number of interfaces for delamination (n_d)	Cured ply thickness [mm]	Cured plate thickness [mm]
L01	$[(45/0/-45/90)_2]_S$	16	14	0.1875	3.0
L02	$[(45/0/-45/90)_4]_S$	32	30	0.18125	5.8
L03	$[(45_2/0_2/-45_2/90_2)_2]_S$	32	14	0.18125	5.8
L04	$[45_4/0_4/-45_4/90_4]_S$	32	6	0.18125	5.8
L05	$[(45/0/-45/90)_6]_S$	48	46	0.1833	8.8
L06	$[(0/90)_9]_S$	36	34	0.1889	6.8

Table 2.12: Selected laminates.

The laminated composite plates proposed were manufactured using Hexply AS4-8552 carbon-epoxy unidirectional pre-preg. The pre-preg was cut automatically and the lamination was done manually. The laminated plates were cured in an autoclave following the curing cycle specified by the supplier. The cured ply thickness varies in function of the plate thickness.

2.3 Compression after impact tests (CAI)

The *Compression After Impact test* (CAI) is performed to obtain the compressive residual strength of drop-weight impacted laminates. This is often called the study of damage tolerance since it refers to the experimental determination or the numerical prediction of the residual mechanical properties of the damaged structure [5].

Compressive loading causes buckling of sub-laminates in the *Barely Visible Impact Damage* (BVID) region which forces opening delaminations and then allowing the damage to propagate from the initial state until the subsequent failure of the structure. Figure 2.5 shows different buckling modes which can be done during the CAI test.

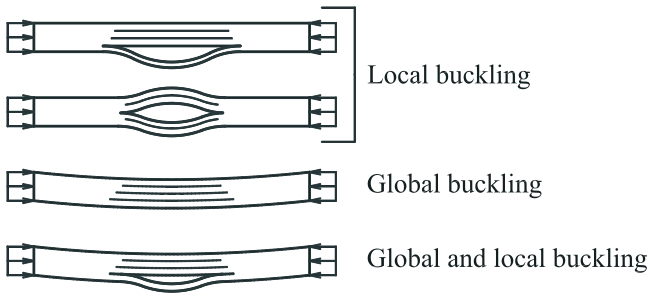

Figure 2.5: Buckling modes of delaminated plates in compression (Davies and Olsson [8]).

2.3.1 Benchmark: ASTM compression after impact test

The ASTM test method for measuring the compressive residual strength of a damaged fiber-reinforced polymer matrix composite plate (i.e. ASTM D7137 / D7137M [4]) is taken as a reference in order to perform the CAI tests. This guideline is

linked to the standard ASTM D7136 / D7136M [45] for drop-weight impact test (see Section 2.2.1).

The CAI test consists on install the damaged laminate in a multi-piece support fixture (see Figure 2.6.a), that has been aligned to minimize loading eccentricities and induced specimen bending. The specimen fixture assembly is placed between flat plates and end-loaded under compressive force until specimen failure.

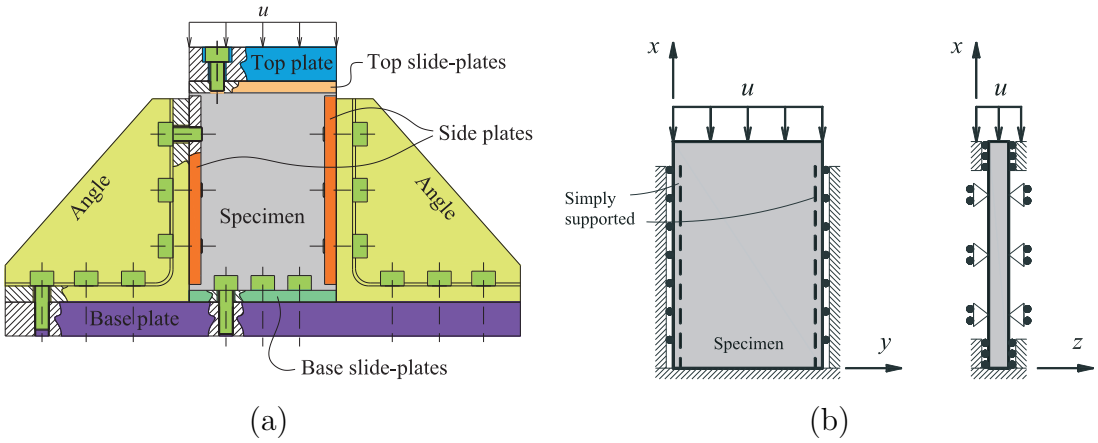

Figure 2.6: (a) CAI support fixture and (b) the corresponding constraints.

The standard compressive test fixture uses adjustable retention plates to support the specimen edges. In detail, the top and bottom supports extend the compressive displacement to the specimen. These supports are ground flat and parallel, and provide no clamp-up but some restraint to out-of-plane rotation due to the fixture geometry. The unloaded edges of the specimen are constrained by side supports which are knife-edge type supports and provide no rotational restraint. All these constraints are represented in Figure 2.6.b.

The configuration of the support fixture system can have a significant effect on the test results [4]. Results are affected by the geometry of the various slide plates. Results are also affected by the presence of gaps between the slide plates and the specimen, which can reduce the effective edge support and can result in concentrated load introduction conditions at the top and bottom specimen surfaces. Additionally, results may be affected by variations in torque applied to the slide plate fasteners; loose fasteners may also reduce the effective edge support.

Errors can result if the test fixture is not centered with respect to the loading

axis of the test machine. For this reason, the standard proposes to glue four strain gages at selected locations (see Figure 2.8) in order to detect evidence of specimen bending before and during the test.

The test procedure starts with a compressive displacement which pre-loads the specimen fixture assembly with 450N. This pre-load is applied in order to ensure that all loading surfaces are in contact and to align the plates if necessary. After, the load is reduced to 150N and the test machine is reset to zero. Next, a compressive displacement is applied at the specified rate (i.e. maximum rate: $u = 1.25$mm/min) while recording data, until approximately 10% of the anticipated ultimate force (normally, the ultimate force is unknown). Subsequently, the compressive force is again reduced to 150N with an equivalent unloading rate. Finally, the recorded strain gage data is reviewed to evidence any specimen bending. A difference in the stress-strain or force-strain slope from opposite faces of the specimen indicates bending in the specimen. Equation (2.9) determines a percent of bending P_B at the maximum applied force for each of the back-to-back gage locations:

$$P_B = \frac{\epsilon_{SG1} - \epsilon_{SG3}}{\epsilon_{SG1} + \epsilon_{SG3}} \text{x} 100 \tag{2.9}$$

where ϵ_{SG1} and ϵ_{SG3} are the strains from the gages on one face and on the opposite face, respectively (see Figure 2.8). The sign of the calculated percent of bending indicates the direction in which the bending is occurring. It should be noted that bending is often introduced by the own asymmetry of the specimen created by the impact damage.

After verifications of the strain gage lectures and re-alignments of the specimen fixture assembly, the CAI test is performed by loading the specimen at the specified rate while recording data. The specimen is loaded until the maximum force is reached and the force has dropped off about 30% from the maximum.

2.3.2 Resources used and specimen instrumentation

In the present thesis, all CAI tests are performed using an Instron-4208 electro-mechanic universal testing machine with a load cell of 300kN. The fixture support used follows the ASTM specifications (see Figure 2.7).

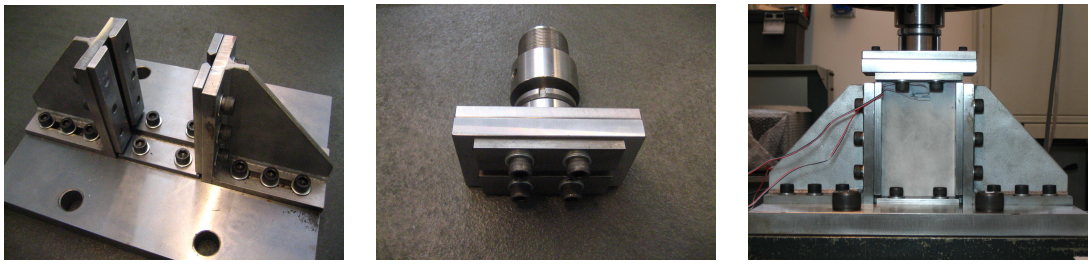

(a) (b) (c)

Figure 2.7: CAI test fixture: (a) base support, (b) top support adapted for the crosshead test machine, and (c) whole fixture.

It should be noted that not all the specimens described in the impact studies were tested for CAI. A suitable sample of the impacted specimens was selected.

The instrumentation of the specimens is composed by: two displacement transducers (LVDT) which are used to measure the out-of-plane displacement on two points of the non-impacted face of the specimen, and four back-to-back strain gages (SG). The LVDT's allow to evidence the buckling mode at one face and are located at the specimen points indicated in Figure 2.8. The strain gages are used to detect evidence of specimen bending during the test and are located at 25mm from each specimen edge (see Figure 2.8). Therefore, the results obtained are the applied force, the crosshead displacement, the strain data from the gages and the out-of-plane displacement given by the LVDT's.

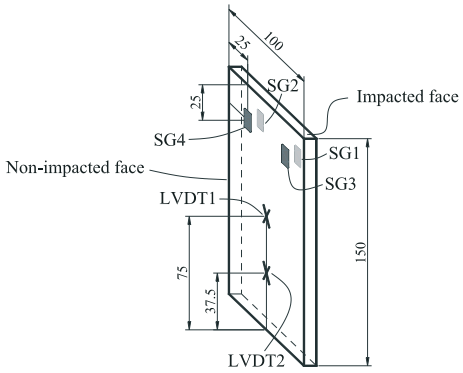

Figure 2.8: Instrumentation of CAI tests (SGx: strain gage; LVDTx: displacement transducer).

In addition, for some CAI tests the *Digital Image Correlation* (DIC) method is used to analyze the impacted face of the specimen (Aramis software [86]). This method provides the measurement of the 3D displacement field of the surface of interest of an object, generated when this is submitted to an external loading. The surface to be analyzed must have a textured pattern in which the light intensity, reflected on the surface, will vary continuously with a suitable contrast. Therefore, a speckle pattern is created by applying a thin coating of white spray paint followed by a spread distribution of spots of black spray paint. The optical systems uses two cameras and a computer to record the deformation pattern of the panel surface at regular intervals. The computer calculates the motion of each location based on the two photographs from different angles to the surface of the specimen. In-plane displacements and strains, and out-of-plane displacements can accurately be determined based on these figures.

Chapter 3

Experimental results

3.1 Introduction

In this chapter, the experimental results of the configurations explained in Chapter 2 are shown and discussed in detail. Moreover, comparisons between the experimental results and the analytical predictions are also analyzed.

The experimental results comprise the data from the impact tests, non-destructive inspections (NDI) and compression after impact (CAI) tests. It should be noted that for test configurations with a sample greater than one specimen, the mean values are used. The C-scan inspections performed before impact are not shown here because all specimens were not shown manufacturing flaws. Finally, not all the specimens described in the impact studies were tested for CAI, a sample of the impacted specimens was selected.

The content of this chapter is structured according to the three main proposed studies, which are: effect of the ply thickness (clustering), effect of the mismatch angles of the plies, and effect of the laminate thickness.

3.2 Effect of ply thickness (clustering)

3.2.1 Impact tests

Impact force versus time

In order to illustrate the excellent repeatability of the impact tests, Figures 3.1 and 3.2 show the evolutions of the impactor reaction force for repeated impact configurations of laminates L02 and L04, respectively. Therefore, for configurations with more than one specimen, the mean value is used.

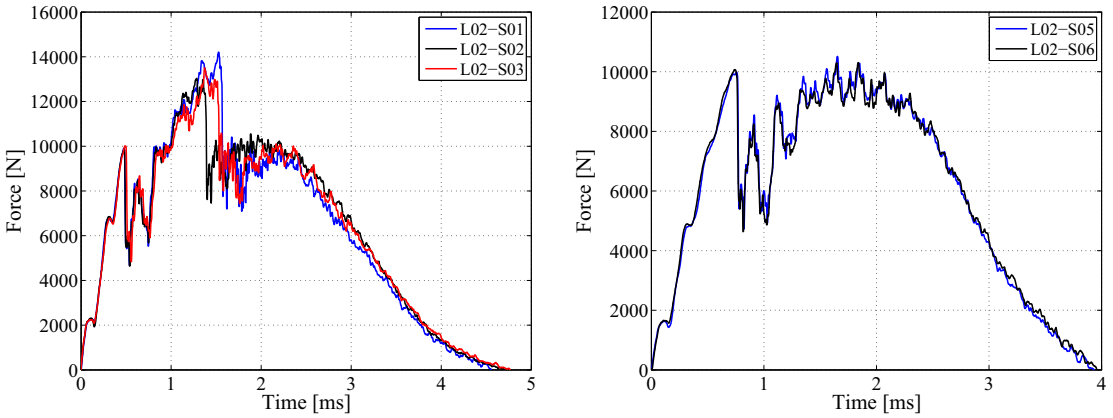

(a) (b)

Figure 3.1: Impact force histories of laminate L02 with (a) $E_i = 38.6$J and $M_i = 5$kg, and (b) $E_i = 19.3$J and $M_i = 5$kg.

Figures 3.3, 3.4 and 3.5 show the histories of the impactor reaction force for each impact energy of laminates L02, L03 and L04, respectively. An interesting piece of evidence on these Figures is that the threshold load, F_d, at which significant loss of stiffness occurs, remains constant for each laminate independently of the impact energy. Therefore, F_d is independent of the impact velocity since the impactor mass is the same for all the energies defined. Moreover, as expected, the peak loads F_{max} and the slopes of the elastic regime increase by increasing the velocity, for all laminate types.

It is also observed that, increasing the velocity, the response is extended in time because the plate develops more damage. In other words, the behavior is more quasi-static since the bending stiffness of the structure is reduced. This argument

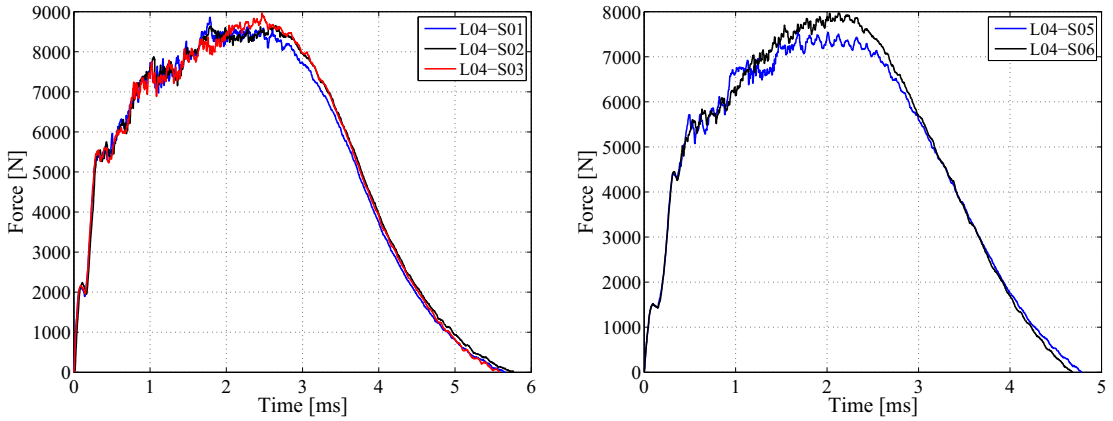

(a) (b)

Figure 3.2: Impact force histories of laminate L02 with (a) $E_i = 38.6$J and $M_i = 5$kg, and (b) $E_i = 19.3$J and $M_i = 5$kg.

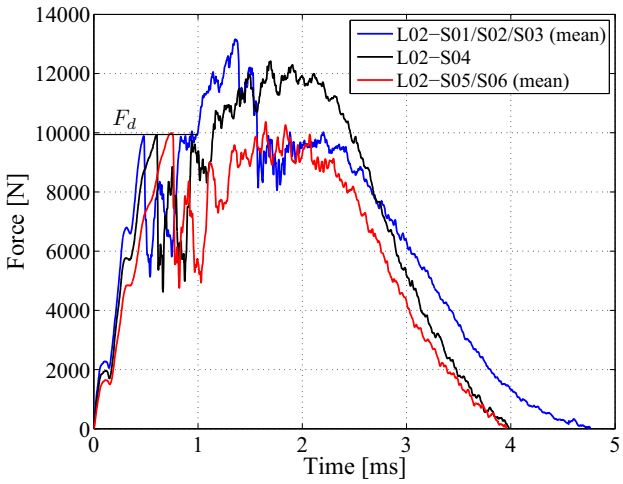

Figure 3.3: Impact force histories of laminate L02 for each impact energy (blue: 38.6J; black: 28.6J; red: 19.3J).

can be explained using the complete analytical models for the elastic prediction of the impact response. For instance, Figure 3.6 shows the analytical predictions of laminate type L02 for the impact configurations with 38.6J and 19.3J energies. These predictions are obtained by using the complete analytical impact model fed with the classical laminated plate theory and the bi-lineal elastic-plastic contact law proposed by Yigit and Christoforou [31]. The number of modes considered for

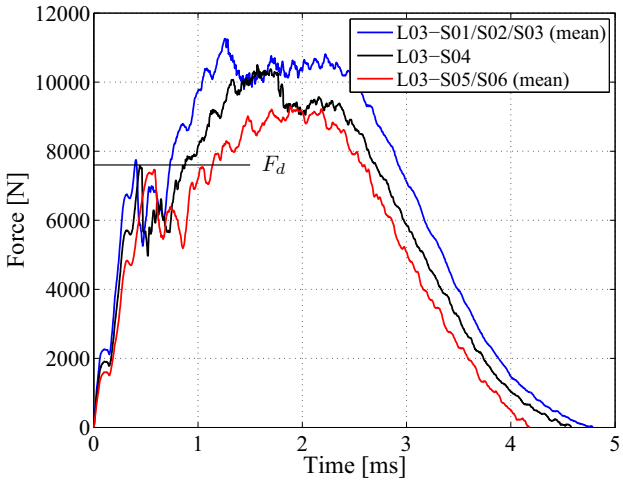

Figure 3.4: Impact force histories of laminate L03 for each impact energy (blue: 38.6J; black: 28.6J; red: 19.3J).

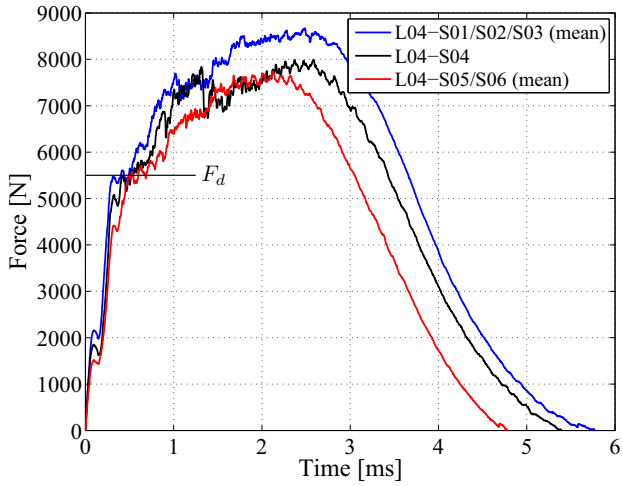

Figure 3.5: Impact force histories of laminate L04 for each impact energy (blue: 38.6J; black: 28.6J; red: 19.3J).

the Navier solution is 5 for each in-plane x and y directions, although the first mode alone is enough since the behaviors are quasi-static. As can be observed, the resulting elastic responses yield different slopes and peak loads, but the contact times are the same. Therefore, the experimental force histories show that when the velocity increases, larger damaged areas develop and so the impact contact duration

increases.

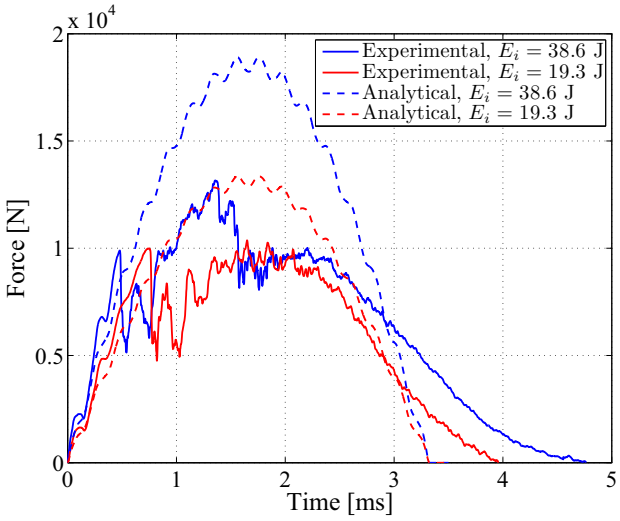

Figure 3.6: Experimental and analytical impact force histories of laminate L02 for 38.6J and 19.3J impact energies.

Focusing again on Figures 3.3, 3.4 and 3.5, the determination of the threshold loads for laminates L02 and L03 can be easily identified whereas for the laminate with the thickest plies, L04, this identification is more difficult. Moreover, the whole profile of the force history of laminate L04 does not have the large oscillations which occur for laminates L02 and L03. This fact indicates that changes in the stiffness during the impact are expected to be more progressive and smooth for laminates with thick plies than for laminates with thin plies. This behavior can be caused by the large matrix cracks which can occur when the plies are thick.

Despite the fact that all the laminate types considered have practically the same stiffness, the resulting impact force histories are clearly different from the point where significant damage starts. This is due to the differences in the ply thicknesses of the laminates, and further highlighted in Figures 3.7, 3.8 and 3.9, which compare the results for the different laminates for each impact energy 38.6J, 28.6J and 19.3J. The first part of the results is the elastic regime of the impact process which is common for all laminates at each impact energy. However, the points where significant damage starts are clearly different, and from these points, the force histories separate and follow different paths. Table 3.1 shows the differences in the threshold

loads as well as in the peak loads for each impact energy.

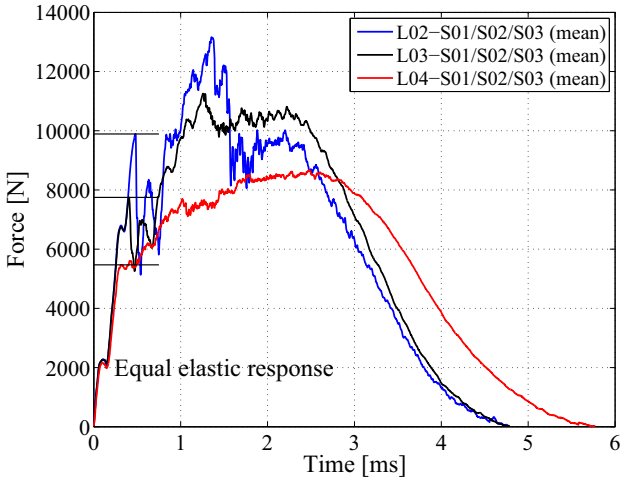

Figure 3.7: Impact force histories for 38.6J of laminates L02 (blue), L03 (black), and L04 (red).

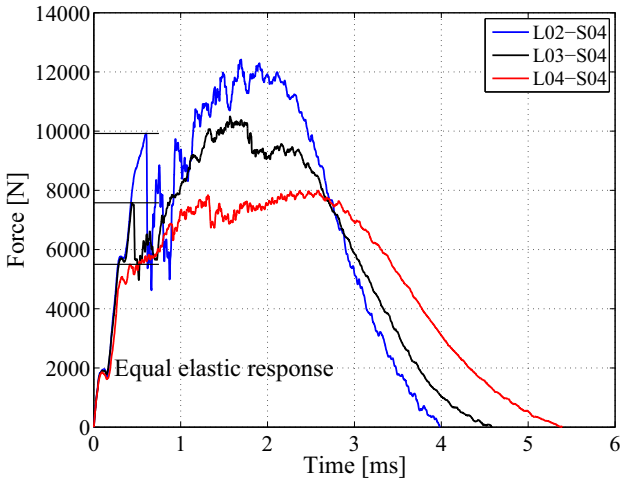

Figure 3.8: Impact force histories for 28.6J of laminates L02 (blue), L03 (black), and L04 (red).

Furthermore, Figures 3.7, 3.8 and 3.9 show that the impact response is elongated by increasing the ply clustering of the laminate. Since delaminations cause a reduction of the stiffness, it is clear that larger delaminations should develop for laminate

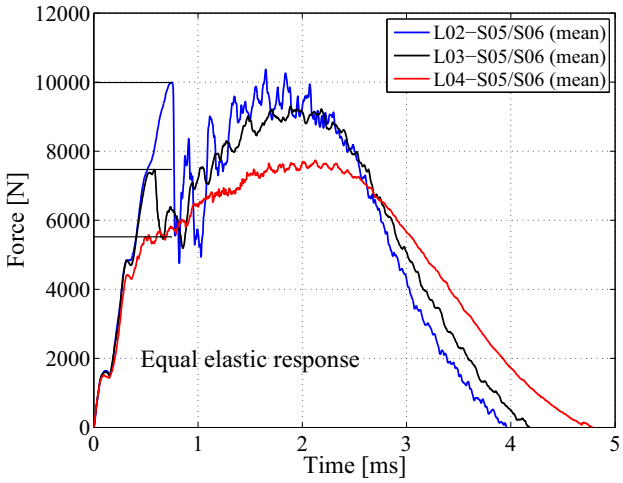

Figure 3.9: Impact force histories for 19.3J of laminates L02 (blue), L03 (black), and L04 (red).

Laminate	Threshold loads F_d [kN]				Peak loads F_{max} [kN]			
	Energy [J]:	38.6 (mean)	28.6	19.3 (mean)	Mean	Energy [J]:	38.6 (mean)	28.6	19.3 (mean)
L02		9.89	9.92	9.99	9.94		13.57	12.42	10.41
L03		7.75	7.58	7.47	7.60		11.37	10.50	9.34
L04		5.47	5.50	5.52	5.50		8.83	8.00	7.78

Table 3.1: Experimental threshold loads F_d and peak loads F_{max}.

L04 because less interfaces are available for delamination in comparison with the other laminates.

Focusing on the values of the experimental damage thresholds F_d (see Table 3.1), these can be represented as a function of the ply thickness on a natural logarithmic scale, as shown in Figure 3.10. The black points and lines describe the analytical predictions, whereas the points colored in gray correspond to the experimental values for each laminate type. As can be observed, the analytical threshold load for matrix cracking in thin outer plies located on the back face of the laminate is in agreement with all the experimental points. Additionally, if the line which fits the experimental results is calculated, the corresponding slope is equal to -0.427. This value is close to the slope of the analytical threshold F_{mc}^{ten} (i.e. slope: -0.5, since $F_{mc}^{ten} \propto h^2 h_p^{-0.5}$). The small difference in the slopes can be due to scattering of the material properties or to the assumptions considered in the formulation of the damage threshold functions,

such as strain rate effects.

Therefore, according to the analytical predictions, the first significant damage for all laminate types can be an elongated delamination at the first interface from the back face of the plate. This result disagrees with the initial prediction for laminate L02, where the first damage was linked to a mid-plane delamination $F_d = F_{d1}^{stat}$. However, it can be considered that this delamination may occur subsequently because the predicted load is slightly smaller than the experimental value.

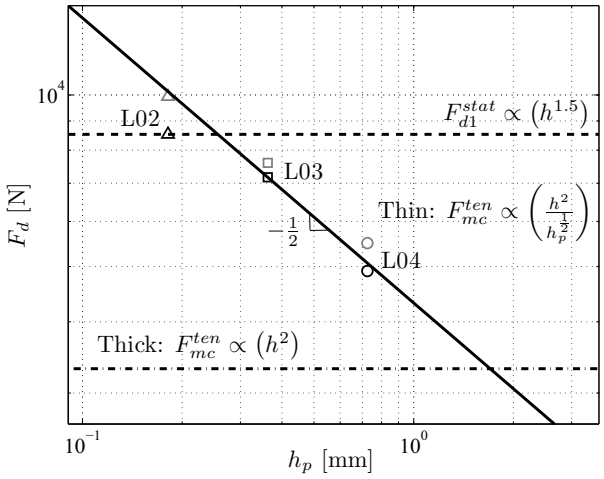

Figure 3.10: Experimental points (in gray) and analytical predictions (in black) of the impact force as a function of the ply thickness for the creation of the first significant damage.

Impactor displacement, impactor velocity, and absorbed energy

Using Equations (2.6) and (2.5), the displacement and velocity histories of the impactor can be calculated, respectively. As an example, Figure 3.11 shows the displacement and the velocity histories of all the laminates for an impact energy of 28.6J. As detected in the impact force histories, the displacement of L04 is the largest because a higher bending occurs. Accordingly, the velocity history of L04 is the slowest since its response is the most quasi-static.

Using Equation (2.7), the histories of the absorbed energy by the specimens $E_a(t)$ can be obtained. Figures 3.12.a, 3.13.a and 3.14.a show these histories of each

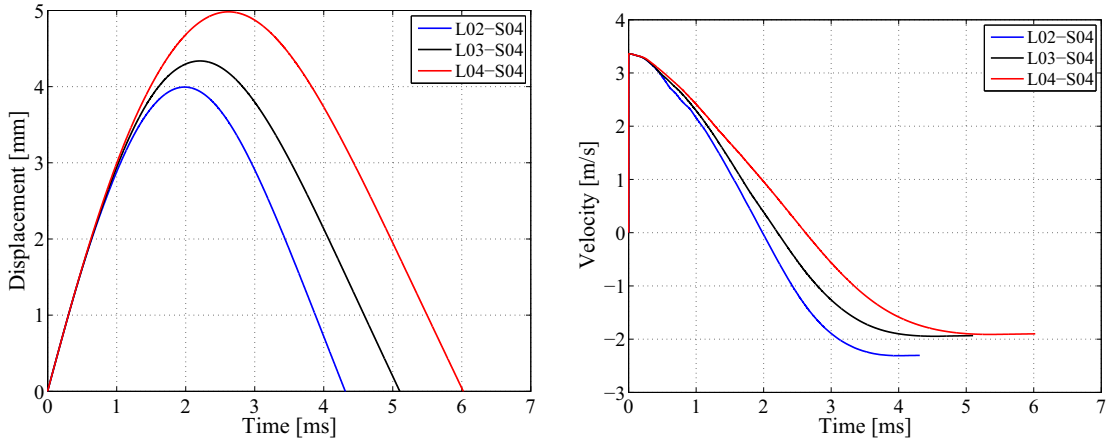

(a) (b)

Figure 3.11: Impactor (a) displacements and (b) velocities of all the laminates for 28.6J energy.

laminate type for each impact energy 38.6J, 28.6J and 19.3J, respectively. From these evolutions, it is possible to know the dissipated energy by the specimen as it is indicated for laminate type L04 in Figure 3.12.a. In addition, the impact force can be plotted in function of the impactor displacement. These plots are shown in Figures 3.12.b, 3.13.b and 3.14.b. It results that the area enclosed in these charts corresponds to the dissipated energy identified in the evolutions of the absorbed energy. For instance, Figure 3.12.b indicates, in gray color, the corresponding energy dissipated by the laminate L04.

As can be observed in Table 3.2, the dissipated energies for laminate L04 are slightly greater than the values of the other laminate types. However, it is reasonable to conclude that the energy dissipated is fairly independent of the laminate type. Moreover, as expected, the dissipated energies increase by increasing the velocity, for all laminate types.

3.2.2 NDI: C-scan after impact

The ultrasonic C-scan inspections of the impacted laminates identify the projection of the delamination areas over the structure thickness. Therefore, the delaminations which are close to the impact face hide the existence of deeper delaminations. How-

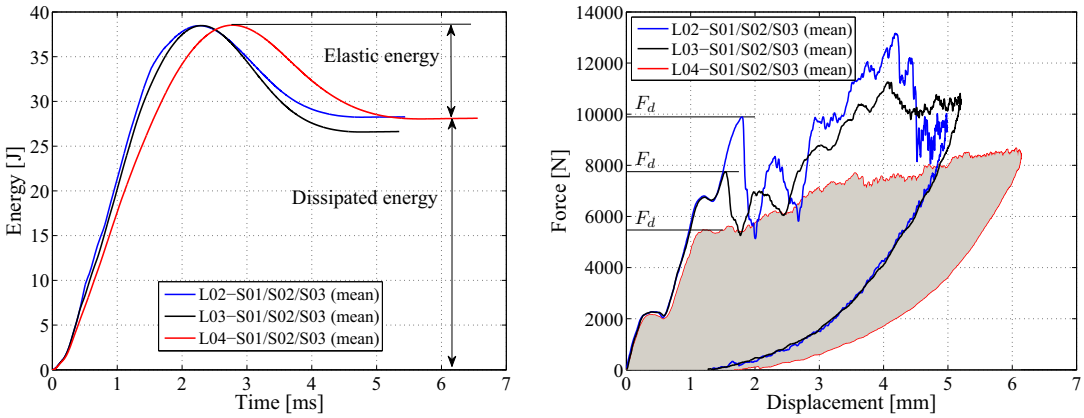

(a) (b)

Figure 3.12: Evolution of the (a) absorbed energy and (b) impact force versus impactor displacement of each laminate for 38.6J.

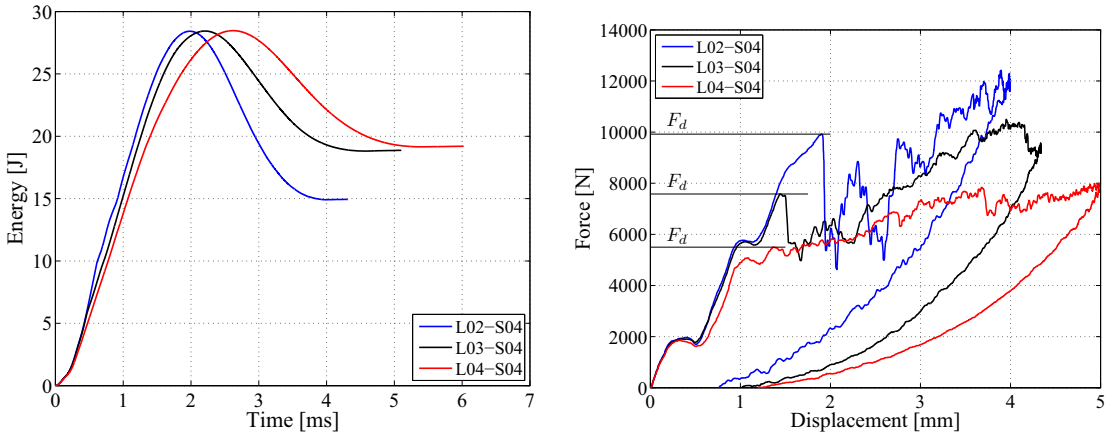

(a) (b)

Figure 3.13: Evolution of the (a) absorbed energy and (b) impact force versus impactor displacement of each laminate for 28.6J.

ever, the delaminations are often larger as the interface is deeper in the laminate, and they can usually be seen.

Normally, each delamination has the so-called peanut shape and the superposition of all these delaminations yields to a circular projected area. The proper interpretation of the through-the-thickness location of the delamination depends on

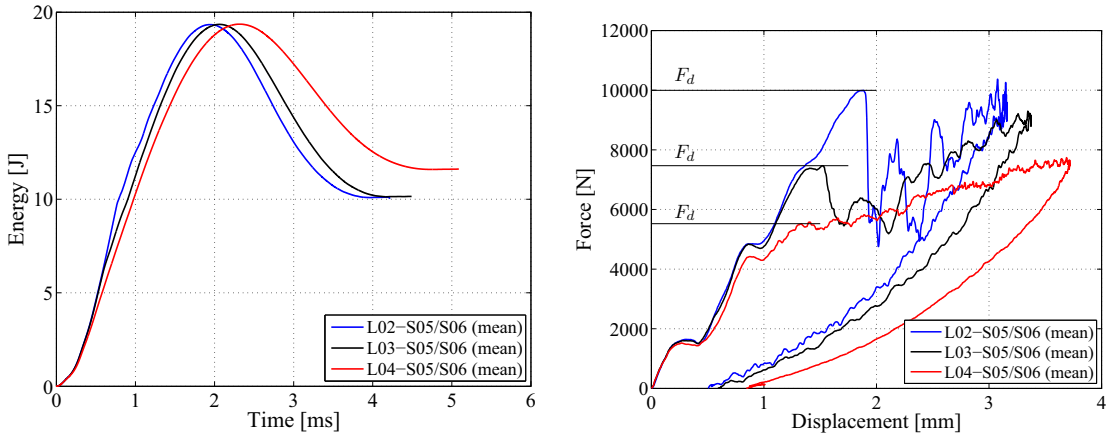

(a) (b)

Figure 3.14: Evolution of the (a) absorbed energy and (b) impact force versus impactor displacement of each laminate for 19.3J.

Laminate	$E_i = 38.6$J	$E_i = 28.6$J	$E_i = 19.3$J
L02	28.3	14.9	10.1
L03	27.2	18.9	10.2
L04	28.8	19.2	12.0

Table 3.2: Absorbed energies of all laminates for each impact energy.

the quality of the inspections performed. Figure 3.15 shows a sample of the C-scan inspections of each laminate type for each impact energy.

It is observed that by increasing the impact velocity the projected area increases for all the laminates. This result correlates with the plots of the impact force histories shown previously (see Figures 3.3, 3.4 and 3.5), where the responses are extended in time when the velocity is increased due to the reduction of the bending stiffness as a consequence of the damage developed.

In addition, by reducing the number of interfaces available for delamination, the resulting projected delamination area is increased. This result is also related to the impact force histories (see Figures 3.7, 3.8 and 3.9), where the responses for laminate type L04 are more quasi-static since the bending stiffness values are reduced due to the large delaminations created.

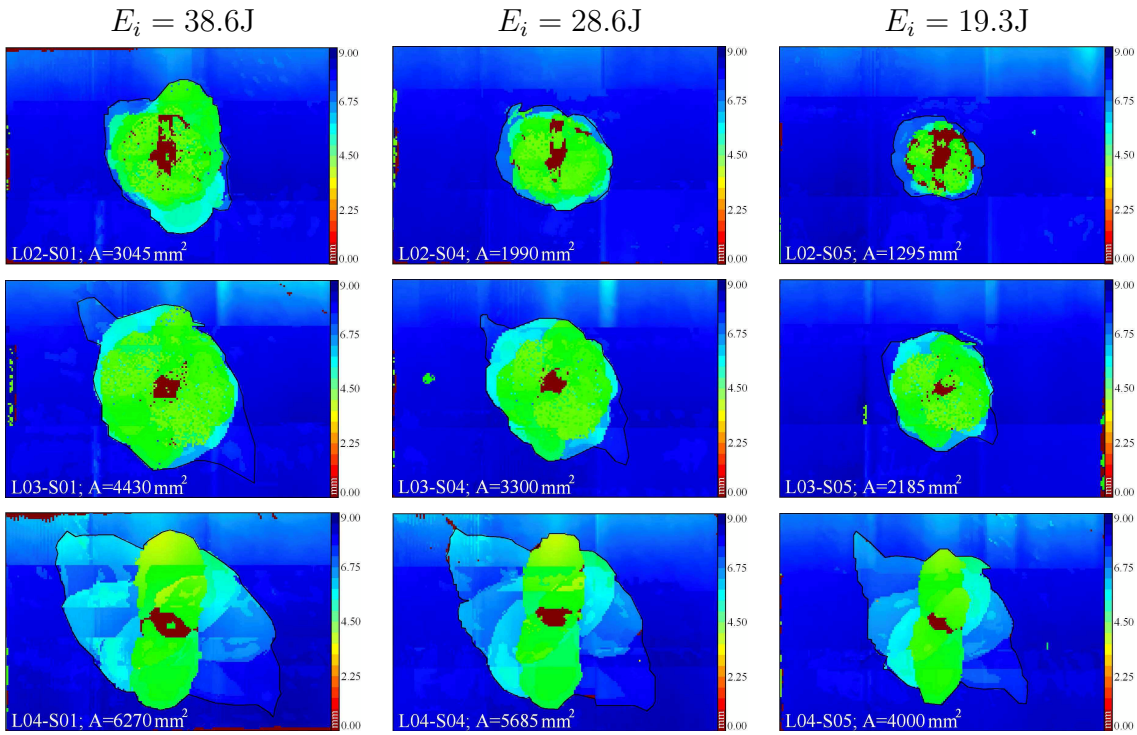

Figure 3.15: Sample of C-scan inspections of laminates L02, L03 and L04.

The shapes of the projected delamination areas are clearly different for each laminate type. The shape of laminates L02 follow a quite similar circular pattern at each impact energy. Likewise, the shapes of laminate type L03 are also fairly circular, although in contrast with laminate L02, a narrow and elongated delamination appears at the deepest interface which is more evident for the highest impact energy. Finally, the delamination shapes of laminate type L04 significantly differ from the other laminates. The areas are very large, and their shapes and locations through-the-thickness of the laminate can be easily recognized.

Although the C-scan inspections provide the resulting damaged areas after the impact tests, they can be used to check approximately if the analytical predictions for the first significant damage threshold load F_d are in agreement with the experimental results. Initially, it was predicted that the first significant damage for laminate type L02 would be a circular mid-plane delamination. However, the experimental point plotted in Figure 3.10 has evidenced that the first damage is rather a delamination at the first interface from the back face of the plate. The shape of the C-scan

inspections for laminate L02 are almost circular for all the impact energies, and then it is difficult to determine what is the associated delamination for the first drop in the impact load. For laminate type L03, the prediction was a delamination at the first interface from the back face of the plate. Observing the inspections, it is reasonable to consider that a delamination has appeared at that interface, although its existence is difficult to prove due to the fact that it is hidden by the delaminations close to the impact front face. The prediction for laminate type L04 was also a delamination at the first interface from the back face of the plate. The prediction can be considered correct since the delamination areas at the deepest interface are peanut shaped, which are typical when a large matrix crack appears on the back outer ply of the plate. However, further testing is required to verify these arguments, especially with critical impact energies which generate maximum impact forces similar to the damage threshold loads.

It is important to point out that the growth of delaminations can be affected by the finite in-plane dimensions of the plates, the stacking sequences, the impact energy and the clamping system. All the impact configurations and stacking sequences tested are in agreement with the recommendations suggested by ASTM D7136 / D7136M [45]. The standard remarks that if all the recommendations are followed, the maximum delamination diameter will be less than half of the unsupported specimen width (38mm). However, most of the delamination areas obtained have a diameter greater than this value. Therefore, the growth of these delaminations can be affected by the clamping system. Laminate type L04 has fewer interfaces for delamination than laminates L02 and L03. As such, the energy is dissipated by means of large damage areas which could be stopped by the clamping system. This is suggested by the relation between the projected delamination areas and the impact energy, as shown in Fig. 3.16. The fitting line of laminate type L04 has the lowest slope and it indicates that the growth of the delaminations could have been stopped by the clamping system. Furthermore, since the delaminations cannot grow, the energy must be dissipated by other means, such as large indentation and fiber breakage.

Impact energy: $E_i = 38.6$J		Impact energy: $E_i = 28.6$J		Impact energy: $E_i = 19.3$J	
Specimen	Area [mm^2]	Specimen	Area [mm^2]	Specimen	Area [mm^2]
L02-S01	3045	L02-S04	**1990**	L02-S05	1295
L02-S02	2710			L02-S06	1340
L02-S03	3310				Mean: **1318**
	Mean: **3022**				
L03-S01	4430	L03-S04	**3300**	L03-S05	2185
L03-S02	4115			L03-S06	1800
L03-S03	3320				Mean: **1993**
	Mean: **3955**				
L04-S01	6270	L04-S04	**5686**	L04-S05	4000
L04-S02	5930			L04-S06	6750
L04-S03	6275				Mean: **5375**
	Mean: **6158**				

Table 3.3: Projected delamination areas given by C-scan inspections.

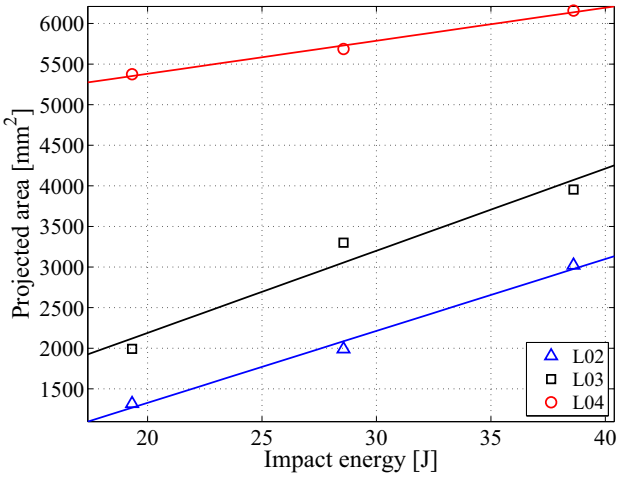

Figure 3.16: Projected delamination areas in function of the impact energy.

3.2.3 Dent-depth measurements

In Figure 3.17 are summarized the contour plots of the dent-depth measurements of the whole selected specimen sample. All these measurements were performed by

means of a 3D coordinate measuring machine.

Related with the arguments commented in previous sections, it is reasonable that by reducing the number of interfaces for delamination the indentation is increased. The impact energy can be dissipated in different ways, mainly by matrix cracking, delaminations and fiber failure. When delaminations can not growth because they have reached their maximum size (i.e. due to the fact that the clamping system stops the delamination growth or because high loads are needed in order to increase their size), the indentation could be increased, such as it is evidenced for laminates L04 in comparison with laminates L03 and L02, or laminates L03 in comparison with laminates L02.

Furthermore, it is obvious that increasing the impact velocity, the resulting indentation is increased.

3.2.4 CAI tests

It should be noted that not all the specimens impacted are tested for CAI. Moreover, no a single CAI test performed experimented unacceptable damage modes, such as those related to load introduction by the support fixture.

Residual compressive load

Table 3.4 summarizes the residual compressive loads F_{fc} obtained. It is observed that increasing the impact energy (or the impact velocity), the residual compressive loads are reduced for all the laminates tested.

In addition, the damage tolerance estimated by means of the residual compressive load does not seem to be reduced by increasing the ply thickness, because all laminate types show similar values of the residual compressive loads at each impact energy (except for specimen L04-S05). As it was noted in Section 2.2.2, this result is due to the fact that the compressive load depends on a combination of variables such the number of delamination planes, the size of the delaminations, and their locations through-the-thickness of the laminate. However, more tests are needed in order to further support these conclusions since the repeatability of the CAI tests is not as good as in the impact tests.

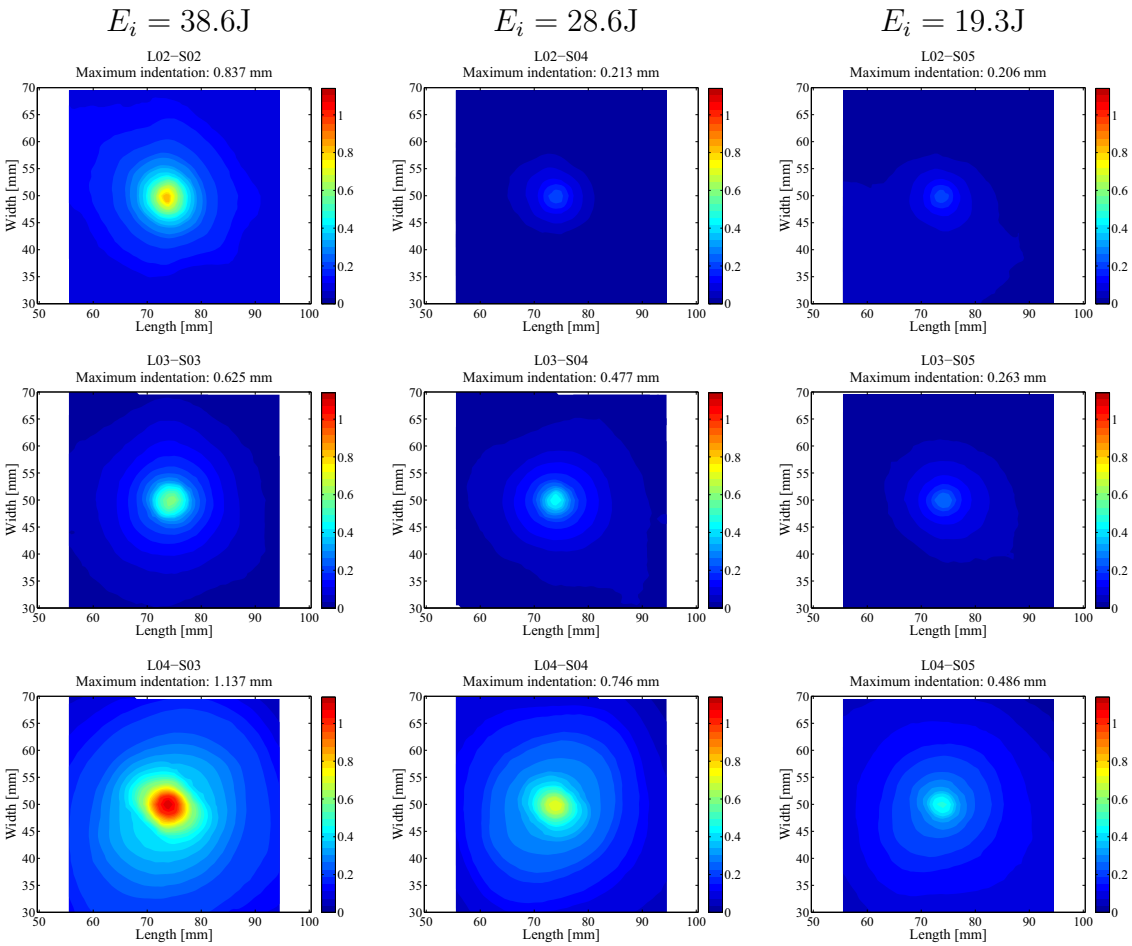

Figure 3.17: Dent-depth inspections of laminates L02, L03 and L04.

Lectures of the displacement transducers (LVDT)

Table 3.5 summarizes the maximum values of the readings of the two displacement transducers used during the CAI tests (see Figure 2.8 in Chapter 2). As it can be observed, the displacements of laminate type L04 are often higher than in the other laminate types. However, this evidence does not imply that the damage tolerance is worse than in the other laminates because the failure loads read have been quite similar.

By means of the profile of the two out-of-plane displacement histories, it is possible to describe the buckling mode which is experimented at the instrumented back face of the corresponding impacted specimens. For instance, Figure 3.18 shows the

Impact energy: $E_i = 38.6$J		Impact energy: $E_i = 28.6$J		Impact energy: $E_i = 19.3$J	
Specimen	F_{fc} [kN]	Specimen	F_{fc} [kN]	Specimen	F_{fc} [kN]
L02-S01	93	L02-S04	**103**	L02-S05	**133**
L02-S02	99				
	Mean: **96**				
L03-S01	89	L03-S04	**100**	L03-S05	**134**
L03-S02	91				
	Mean: **90**				
L04-S01	98	L04-S04	**103**	L04-S05	**105**
L04-S02	97				
	Mean: **98**				

Table 3.4: Failure compressive loads F_{fc} of laminates L02, L03 and L04.

Impact energy: $E_i = 38.6$J			Impact energy: $E_i = 28.6$J			Impact energy: $E_i = 19.3$J		
Specimen	LVDT1 [mm]	LVDT2 [mm]	Specimen	LVDT1 [mm]	LVDT2 [mm]	Specimen	LVDT1 [mm]	LVDT2 [mm]
L02-S01	1.67	0.09	L02-S04	1.73	0.16	L02-S05	1.11	0.41
L02-S02	2.06	0.33						
L03-S01	2.18	0.14	L03-S04	1.93	0.08	L03-S05	Not read	Not read
L03-S02	1.94	0.15						
L04-S01	2.85	0.18	L04-S04	2.88	0.30	L04-S05	2.91	0.19
L04-S02	Not read	Not read						

Table 3.5: Maximum lectures of the displacement transducers of laminates L02, L03 and L04.

lectures for each laminate type of the specimens impacted with 29.6J. It can be concluded that the buckling mode of each laminate type is practically the same and is presented as a local bubble focused in the middle of the specimens which propagates suddenly to a bubble that takes up the whole in-plane dimensions of the specimens when the failure load is reached.

Lectures of the strain gages (SG) and Digital Image Correlation (DIC)

During the preparatory of the CAI test set-up, four strain gages are used in order to avoid loading eccentricities and induced specimen bending (see Figure 2.8 in

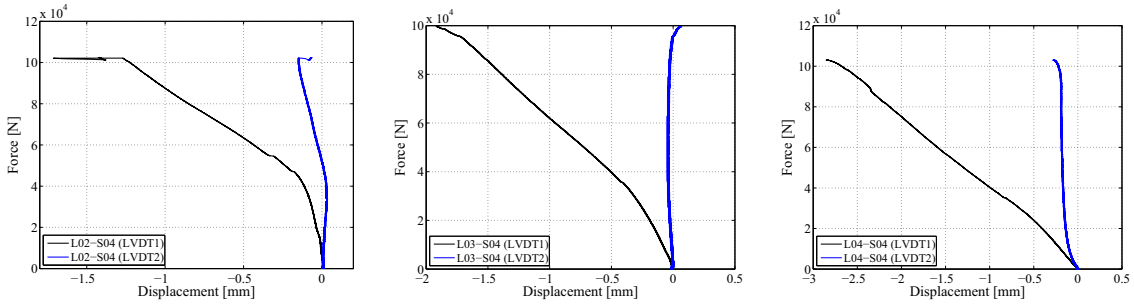

(a) (b) (c)

Figure 3.18: Displacement transducer lectures of the specimens impacted with 29.6J: (a) L02, (b) L03, and (c) L04.

Chapter 2). In addition, the lectures of these gages can be stored in a computer during the test in order to check if some bending has appeared. For instance, Figure 3.19 contains the four strain lectures of each laminate type for the impact energy of 29.6J. As it can be verified, there are differences between the lectures of the gages located at the same face (SG1 with SG2; SG3 with SG4), and also between the lectures of the back-to-back gages (SG1 with SG3; SG2 with SG4). The first offset indicates that the load applied is not completely uniform, due to the support fixture, by the frame of the test machine, or by the asymmetry induced to the laminate in the impact test. The second offset indicates that the back-to-back sub-laminates are standing different deformations due to the fact that the laminate is also subjected to a little bending. Despite the attempts previous to the CAI test to avoid possible eccentricities, bending finally appears due to the asymmetry induced by the damage created in the impact test.

These effects also can be evidenced by means of the Digital Image Correlation (DIC) lectures. For instance, Figure 3.20 shows the displacement field lectures for the specimen L04-S04 at different points of the compression test. The first column of images corresponds to the horizontal displacement field, the second corresponds to the vertical displacement field, and finally the third corresponds to the out-of-plane displacement field. Also, the horizontal, vertical and in-plane shear strain fields can be obtained. As it was detected by the strain gages (SG1 and SG2), the vertical displacement field is not uniform during the first loads of the CAI test. Also, the horizontal displacement field is not completely symmetric.

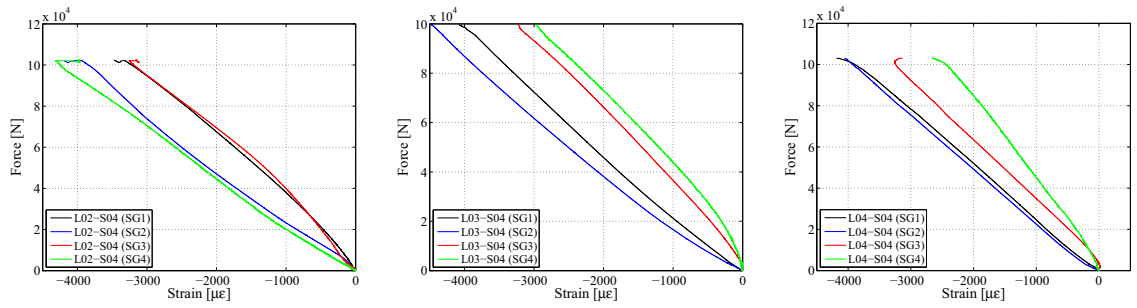

(a) (b) (c)

Figure 3.19: Strain gage lectures of the specimens impacted with 29.6J: (a) L02, (b) L03, and (c) L04.

The direct comparison between the lectures of the DIC device and the strain gages located at the same laminate face (SG1 and SG2) is not possible since the locations of the gages are far from the range of the lecture field of the DIC device.

3.3 Effect of ply mismatch angle at interfaces

3.3.1 Impact tests

Impact force versus time

Figure 3.21 shows the histories of the impactor reaction force for each impact energy of the cross-ply laminate L06. As verified in previous study, the threshold load F_d remains constant at any impact energy, and the peak loads F_{max} and the slopes of the elastic regime increase by increasing the velocity. It can be verified that for the minimum impact energy 19.3J, the damage threshold load F_d coincides with the peak load.

In addition, increasing the velocity, the response is extended in time because the plate develops more damage. Figure 3.22 shows the analytical predictions of laminate L06 for the impact configurations with 38.6J and 19.3J energies, along with the corresponding experimental profiles. The resulting elastic responses for each energy yield different slopes and peak loads, but the contact times are equal. Therefore, again it is evidenced that increasing the velocity, larger damaged areas are developed and so the impact contact duration is enlarged.

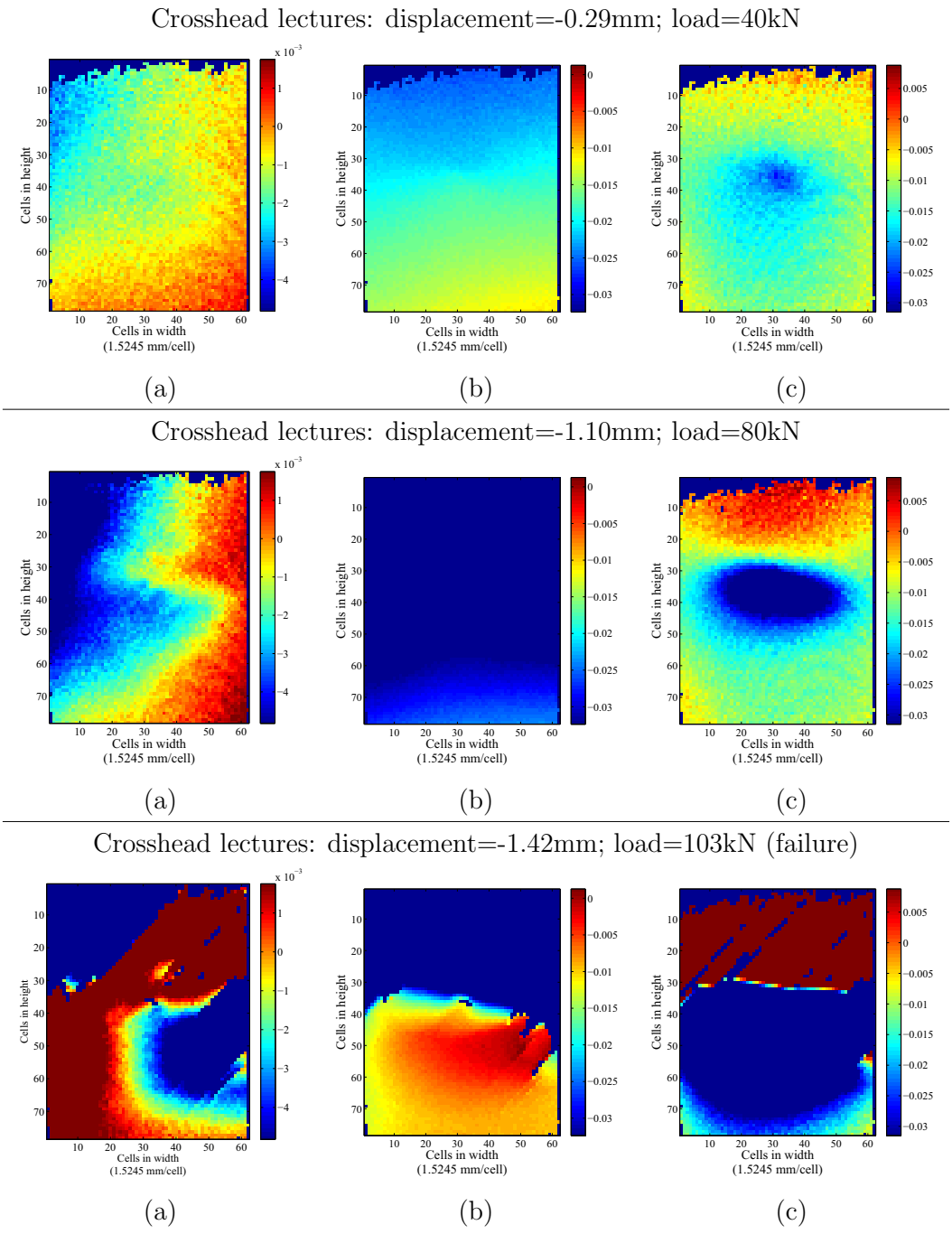

Figure 3.20: DIC lectures of the specimen L04-S04 impacted at 29.6J: (a) horizontal displacement field, (b) vertical displacement field, and (c) out-of-plane displacement field (positive values indicate displacements in the out-of-plane direction).

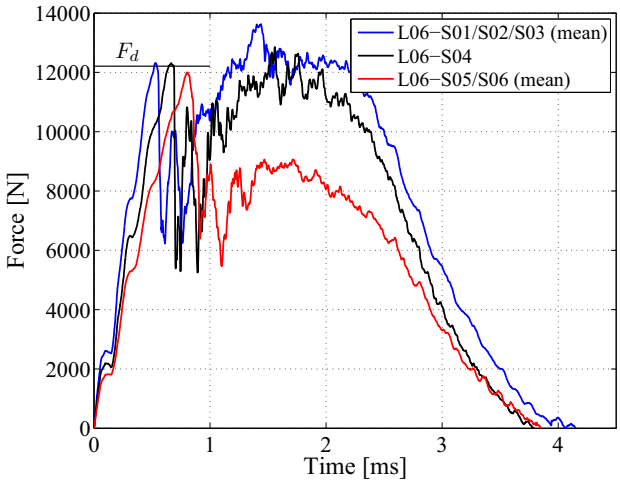

Figure 3.21: Impact force histories of laminate L06 for each impact energy (blue: 38.6J; black: 28.6J; red: 19.3J).

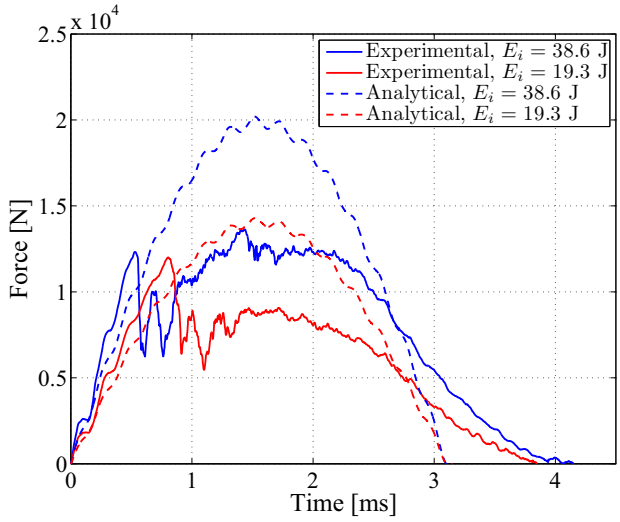

Figure 3.22: Experimental and analytical impact force histories of laminate L06 for 38.6J and 19.3J impact energies.

Figures 3.23, 3.24 and 3.25 compare the profiles of laminates L02 and L06 for each impact energy 38.6J, 28.6J and 19.3J, respectively. The elastic responses of laminate type L06 are stiffer than for L02 due to the fact that the laminate L06 is thicker. Accordingly, the contact durations for laminate L02 are larger, because L02 yields to a more quasi-static behavior in comparison with L06. Table 3.6 summarizes

the threshold loads and peak loads of each laminate for each impact energy.

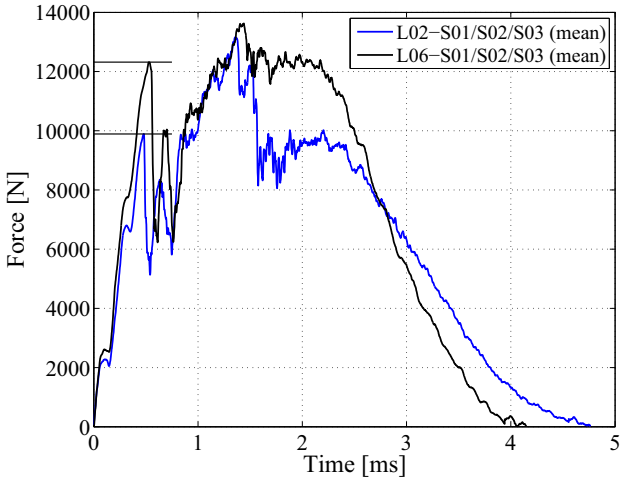

Figure 3.23: Impact force histories for 38.6J of laminates L02 (blue) and L06 (black).

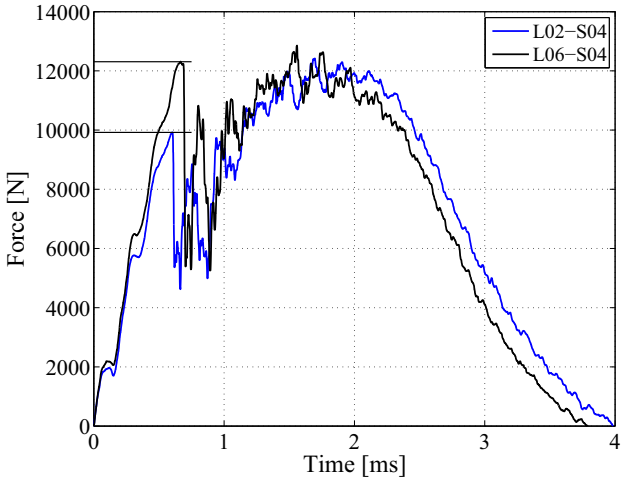

Figure 3.24: Impact force histories for 28.6J of laminates L02 (blue) and L06 (black).

Figure 3.26 shows the corresponding analytical trends (in black) and the experimental value (in cyan) for the first significant damage F_d of laminate L06. The analytical prediction of F_d for L06 was a mid-plane delamination, i.e. F_{d1}^{stat}. However, the experimental point is more close to the trend for a back face delamination, as happened for laminate L02. It can be considered that a combination of both

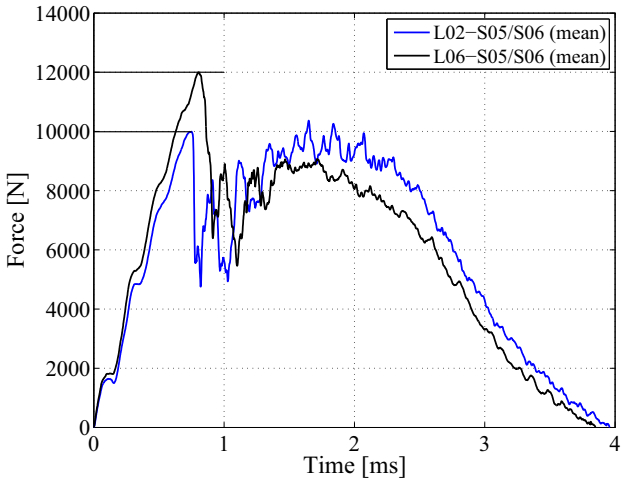

Figure 3.25: Impact force histories for 19.3J of laminates L02 (blue) and L06 (black).

Laminate	Threshold loads F_d [kN]					Peak loads F_{max} [kN]			
	Energy [J]:	38.6 (mean)	28.6	19.3 (mean)	Mean	Energy [J]:	38.6 (mean)	28.6	19.3 (mean)
L02		9.89	9.92	9.99	9.94		13.57	12.42	10.41
L06		12.32	12.31	12.00	12.21		13.92	12.86	12.00

Table 3.6: Experimental threshold loads F_d and peak loads F_{max} of laminates L02 and L06.

delamination types can occur simultaneously since that both thresholds are fairly close.

Impactor displacement, impactor velocity, and absorbed energy

As an example, Figure 3.27 shows the displacement and the velocity histories of laminates L02 and L06 for the impact energy 28.6J. The sudden changes observed in the impact force histories at F_d are also reflected in the velocity profiles.

Furthermore, the fact that laminate type L02 is thinner than laminate L06 is reflected in the displacement and velocity responses. Since the impactor mass is the same for both impact tests on L02 and L06, the impactor displacement is larger for L02 because more deflection of the plate was experimented. In other words, the quasi-static behavior is emphasized for L02 as was noted in Chapter 2, since the ζ_w parameter of L02 was greater than the one of L06. Accordingly, the velocity

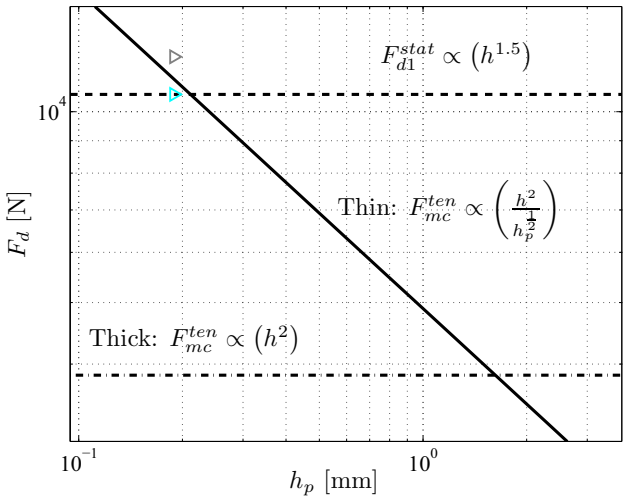

Figure 3.26: Experimental and analytical trends of the impact force as a function of the ply thickness for the creation of the first significant damage.

histories of L02 are slower than for L06.

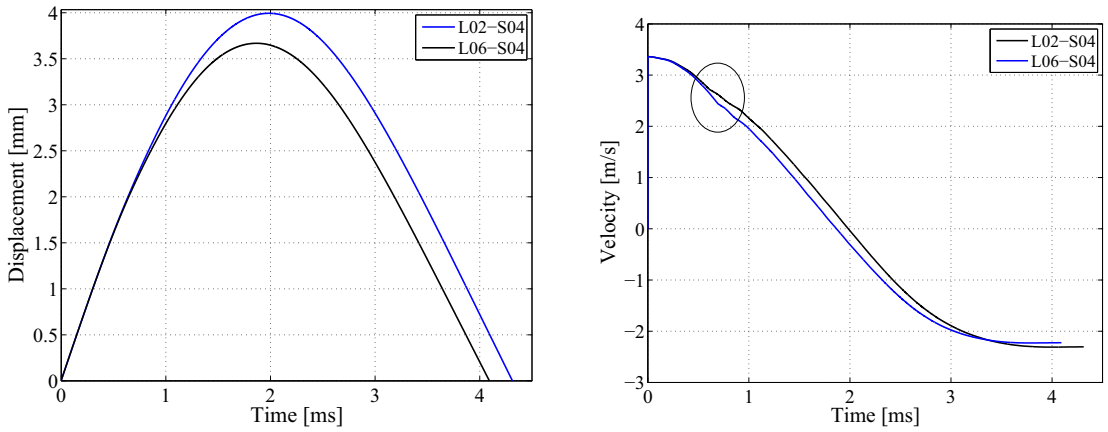

(a) (b)

Figure 3.27: Impactor (a) displacements and (b) velocities of laminates L02 and L06 for 28.6J energy.

Figures 3.28.a, 3.29.a and 3.30.a show the histories of the absorbed energy $E_a(t)$ of laminates L02 and L06 for each impact energy 38.6J, 28.6J and 19.3J, respectively. In addition, Figures 3.28.b, 3.29.b and 3.30.b show the impact force as a function of the impactor displacement. As noted in the study of the ply thickness, the

area enclosed in these charts corresponds to the dissipated energy identified in the evolutions of the absorbed energy. Table 3.7 summarizes these levels of energy and evidences that practically both laminates dissipate the same energy for each impact configuration.

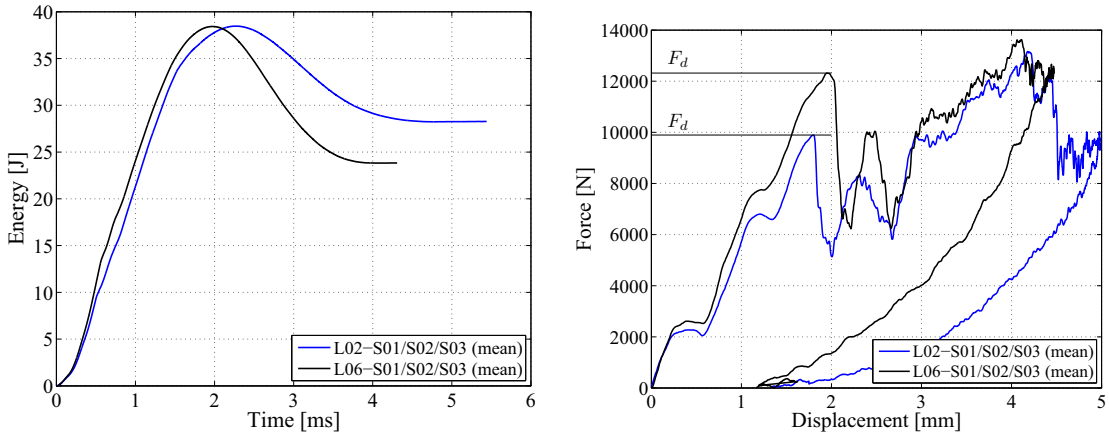

(a) (b)

Figure 3.28: Evolution of the (a) absorbed energy and (b) impact force versus impactor displacement of laminates L02 and L06 for 38.6J.

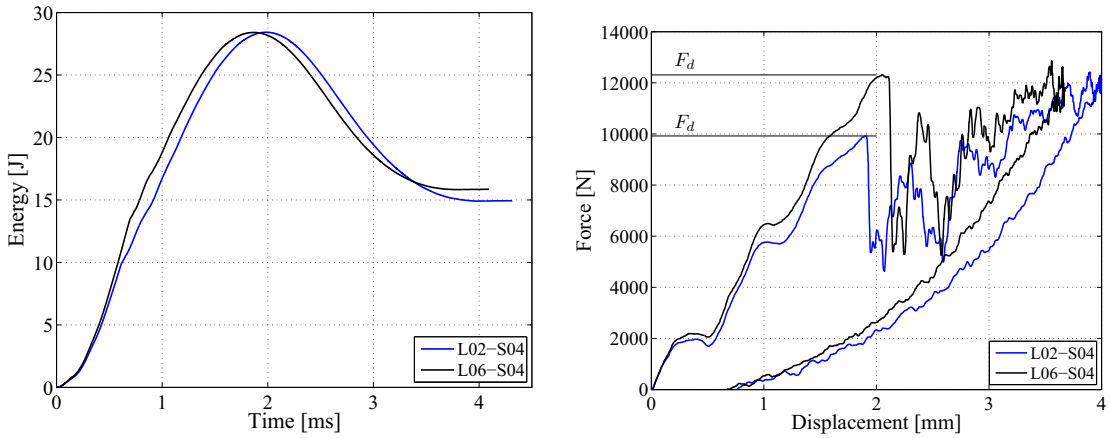

(a) (b)

Figure 3.29: Evolution of the (a) absorbed energy and (b) impact force versus impactor displacement of laminates L02 and L06 for 28.6J.

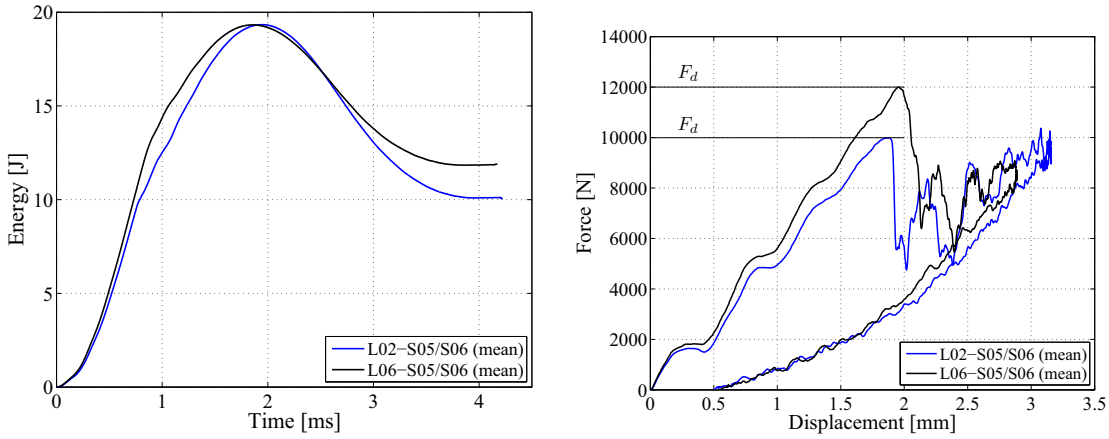

(a) (b)

Figure 3.30: Evolution of the (a) absorbed energy and (b) impact force versus impactor displacement of laminates L02 and L06 for 19.3J.

Laminate	$E_i = 38.6$J	$E_i = 28.6$J	$E_i = 19.3$J
L02	28.3	14.9	10.1
L06	26.3	15.8	11.8

Table 3.7: Absorbed energies of laminates L02 and L06 for each impact energy.

3.3.2 NDI: C-scan after impact

Figure 3.31 shows a sample of C-scan inspections of laminates L02 and L06 for each impact energy. The projected delamination areas of L06 are among square and circular shaped. Although the C-scan inspections give the resulting damaged areas after impact tests, these results can be associated with the analytical predictions for the first significant damage F_d. As was noted in the discussion of the impact force histories, F_d can be triggered by a circular mid-plane delamination. In an approximate point of view, this argument suits with the resulted inspections.

According to the results of the ply thickness study, increasing the impact velocity increases the projected delamination area for all laminates.

Looking the results presented, the mismatch angle of the interfaces has not a clear effect on the damage resistance of the plate, despite the fact that laminate L06 was selected because its stacking sequence has increased mismatch angles in

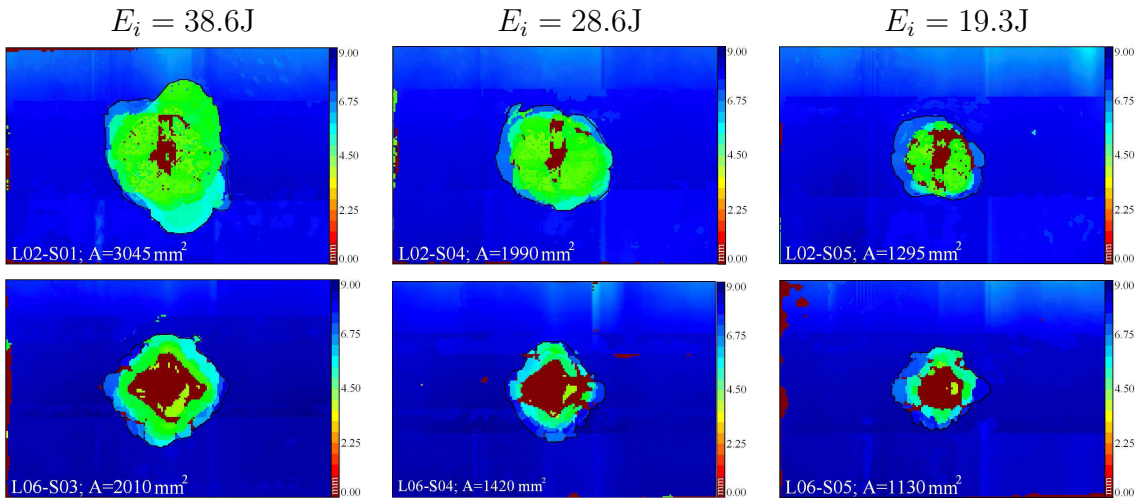

Figure 3.31: Sample of C-scan inspections of laminates L02 and L06.

comparison with laminate L02. This lack of contrast may be generated by the differences in the plate thicknesses of L02 and L06 which makes difficult to extract a possible concluding result, or simply because really the mismatch angle does not affect the damage resistance significantly.

3.3.3 Dent-depth measurements

In Figure 3.32 are collected the contour plots of the dent-depth measurements of the whole selected specimen sample of laminates L02 and L06. The shape of the contour plots for L06 are circular in the center and changes into a square shape as more far from the impact point the lecture is. As can be observed, increasing the impact velocity, the resulting indentation obviously is increased. On the other hand, an effect of the mismatch angle is not detected.

3.3.4 CAI tests

Residual compressive load

Table 3.8 summarizes the residual compressive loads F_{fc} obtained. As it can be evidenced, increasing the impact energy (or the impact velocity), the residual compressive loads are reduced for any laminate.

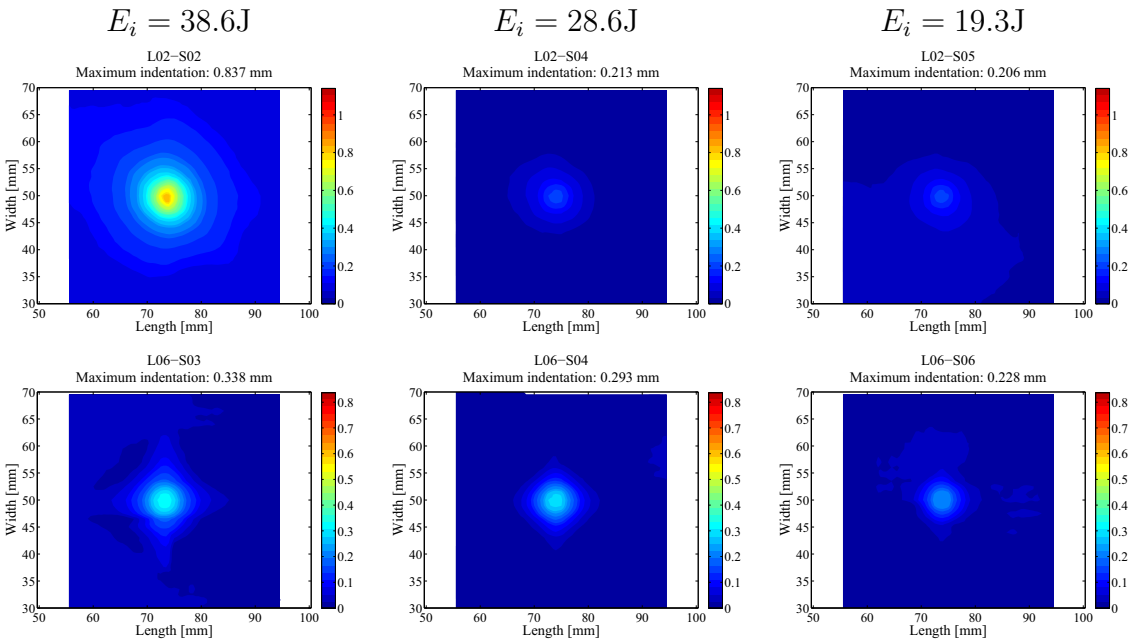

Figure 3.32: Dent-depth inspections of laminates L02 and L06.

$E_i = 38.6$J		$E_i = 28.6$J		$E_i = 19.3$J	
Specimen	F_{fc} [kN]	Specimen	F_{fc} [kN]	Specimen	F_{fc} [kN]
L02-S01	93	L02-S04	**103**	L02-S05	**133**
L02-S02	99				
	Mean: **96**				
L06-S01	113	L06-S04	**130**	L06-S06	**145**
L06-S02	114				
	Mean: **114**				

Table 3.8: Failure compressive loads F_{fc} of laminates L02 and L06.

In addition, the compressive loads of L06 are larger than for L02. This result can not be attributed to the effect of the ply mismatch angle, and even more when it is expected that the mismatch angle should give a reduced damage tolerance as noted in Chapter 2. Really, the residual loads of L06 are larger because laminate L06 has more plies than L02. Therefore, if these loads are normalized by the corresponding section subjected in compression (i.e. b x h), the compressive residual strengths

obtained for both laminates are practically equal at each impact energy (see Table 3.9).

Laminate	$E_i = 38.6$J		$E_i = 28.6$J		$E_i = 19.3$J	
	F_{fc} [kN]	σ_{fc} [MPa]	F_{fc} [kN]	σ_{fc} [MPa]	F_{fc} [kN]	σ_{fc} [MPa]
L02	96	**16.6**	103	**17.8**	133	**22.9**
L06	114	**16.8**	130	**19.1**	145	**21.3**

Table 3.9: Residual compressive strengths σ_{fc} of laminates L02 and L06.

Lectures of the displacement transducers (LVDT) and the strain gages (SG)

Table 3.10 summarizes the maximum values of the lectures of the two displacement transducers used during the CAI tests. As it can be observed, the values obtained are quite similar for both laminate types. In addition, Figure 3.33 shows the lectures for laminates L02 and L06 of the specimens impacted with 29.6J. As in the ply clustering study, the buckling mode of each laminate type is practically the same.

Impact energy: $E_i = 38.6$J			Impact energy: $E_i = 28.6$J			Impact energy: $E_i = 19.3$J		
Specimen	LVDT1 [mm]	LVDT2 [mm]	Specimen	LVDT1 [mm]	LVDT2 [mm]	Specimen	LVDT1 [mm]	LVDT2 [mm]
L02-S01	1.67	0.09	L02-S04	1.73	0.16	L02-S05	1.11	0.41
L02-S02	2.06	0.33						
L06-S01	2.08	0.30	L06-S04	1.55	0.37	L06-S06	1.50	0.22
L06-S02	2.22	0.26						

Table 3.10: Maximum lectures of the displacement transducers of laminates L02 and L06.

Finally, Figure 3.34 shows the lectures of the four strain gages of each laminate type for the impact energy of 29.6J. Again, differences between the lectures of the gages located at the same face (SG1 with SG2; SG3 with SG4), and between the lectures of the back-to-back gages (SG1 with SG3; SG2 with SG4) are evidenced. As mentioned in Section 3.2, these differences are caused by a non-uniform application of the load and also by the asymmetry of the impacted plate which produces a little bending during the test.

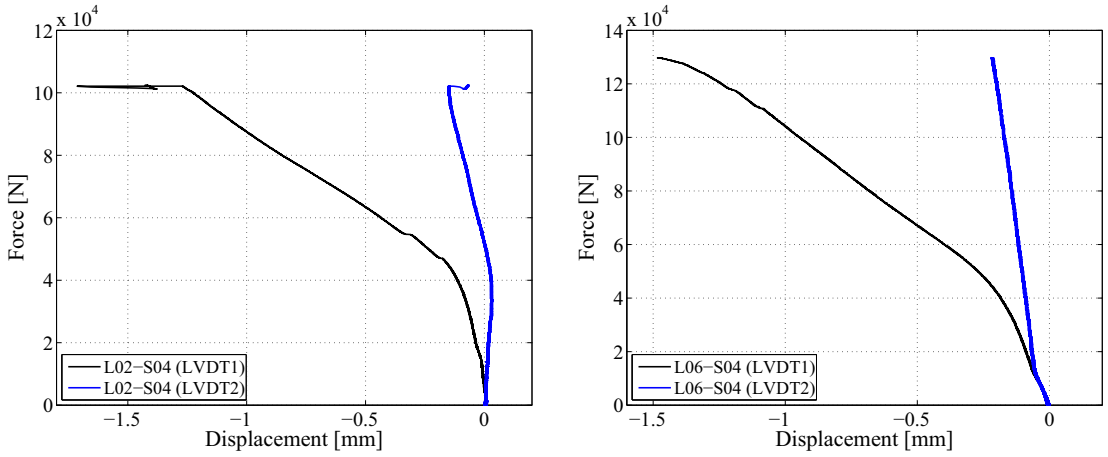

(a) (b)

Figure 3.33: Displacement transducer lectures of the specimens impacted with 29.6J: (a) L02 and (b) L06.

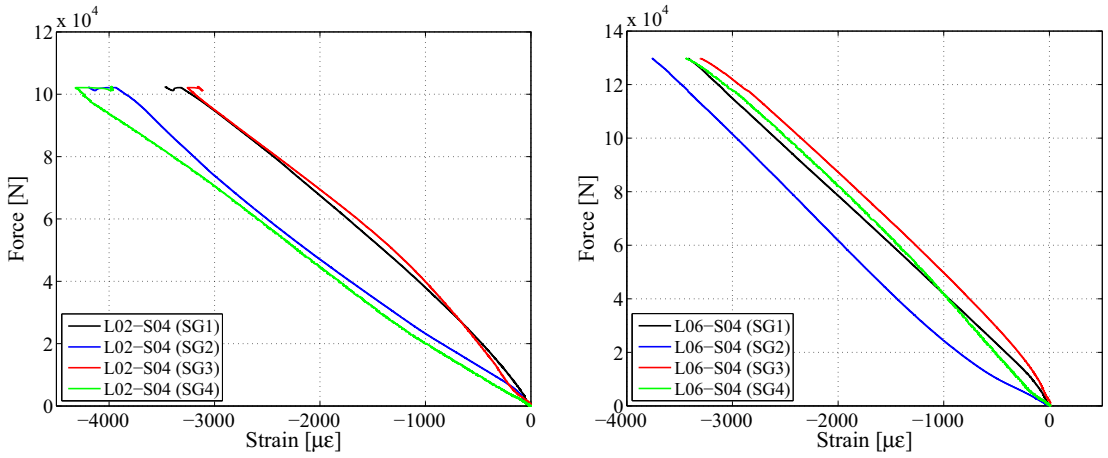

(a) (b)

Figure 3.34: Strain gage lectures of the specimens impacted with 29.6J: (a) L02 and (b) L06.

3.4 Effect of the laminate thickness

3.4.1 Impact tests

Impact force versus time

Figures 3.35 and 3.36 show the histories of the impactor reaction force for each impact configuration of laminates L01 and L05, respectively (see Chapter 2). A clear first drop in the force histories of laminate L05 is evidenced and it is constant for all impact configurations. However, the profiles of L01 are smooth and do not have a clear first drop of the impact force. This result could mean that there is not a sudden loss of stiffness after damage onset and can be related with the fact that laminate L01 stands large global deflections which generate membrane effects. These effects mean that the stiffness of the plate increases as the plate deflection is increased. As the contact time advances, more fibers are subjected to tensile stresses and they stand the majority of the impact load. The matrix and delamination damage that can occur do not change the impact response. However, the impact response is affected by progressive fiber breakage. This behavior seems to be common for any of the impact configurations of laminate L01, even with the configuration with the smaller impact energy, i.e. specimen L01-S06.

Tables 3.11 and 3.12 summarize the threshold loads F_d and the peak loads F_{max} for each impact configuration of laminates L01 and L05, respectively.

Load [kN]	Energy [J]:	38.6	19.3	19.3	12.0	Mean
	Mass [kg]:	5.0	5.0	6.0	2.0	
Threshold loads F_d		4.00	3.90	3.72	4.03	3.9
Peak loads F_{max}		4.79	4.65	4.35	4.62	-

Table 3.11: Experimental threshold loads F_d and peak loads F_{max} for laminate L01.

In detail, Figure 3.37.a shows the force responses of the impact configurations of laminate L01 with a constant impact energy, but different impactor masses and velocities. As can be observed, increasing the impactor mass the response is more quasi-static, which means that the response is slowed down. In addition, Figure 3.37.b also shows the same analysis for laminate L05, but in this case the difference

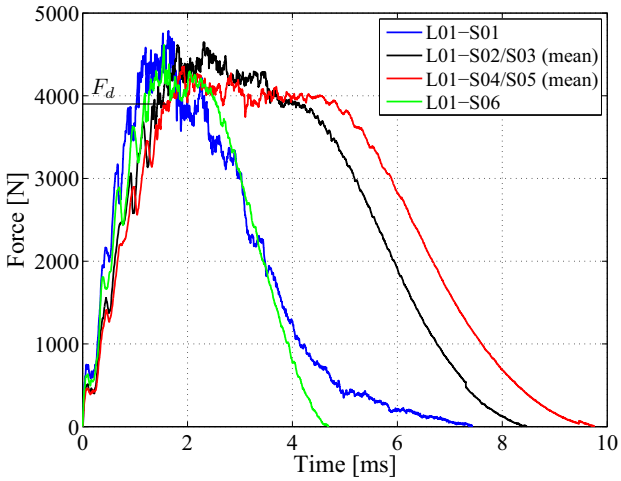

Figure 3.35: Impact force histories of laminate L01 for each impact configuration (blue: $E_i = 38.6$J, $M_i = 5$kg; black: $E_i = 19.3$J, $M_i = 5$kg; red: $E_i = 19.3$J, $M_i = 6$kg; green: $E_i = 12.0$J, $M_i = 2$kg).

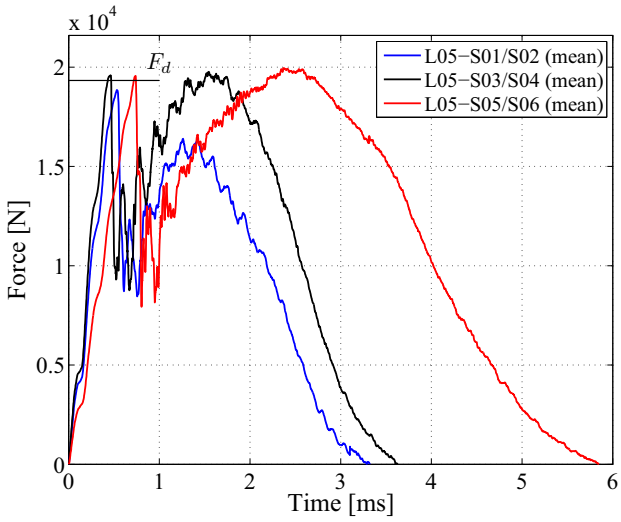

Figure 3.36: Impact force histories of laminate L05 for each impact configuration (blue: $E_i = 38.6$J, $M_i = 5$kg; black: $E_i = 57.8$J, $M_i = 6$kg; red: 57.9J, $M_i = 15$kg).

in the impactor mass is increased, yielding to more differentiable responses.

The effect of the impactor mass M_i was shown in the impact characterization diagram by means of the relative mobility parameter ζ_w (see Chapter 1). Increasing M_i, ζ_w is increased and then the behavior is changed to a more quasi-static behavior.

Load [kN]	Energy [J]:	38.6	57.8	57.9	Mean
	Mass [kg]:	5.0	6.0	15.0	
Threshold loads F_d		18.84	19.59	19.56	19.33
Peak loads F_{max}		18.84	19.77	19.95	-

Table 3.12: Experimental threshold loads F_d and peak loads F_{max} for laminate L05.

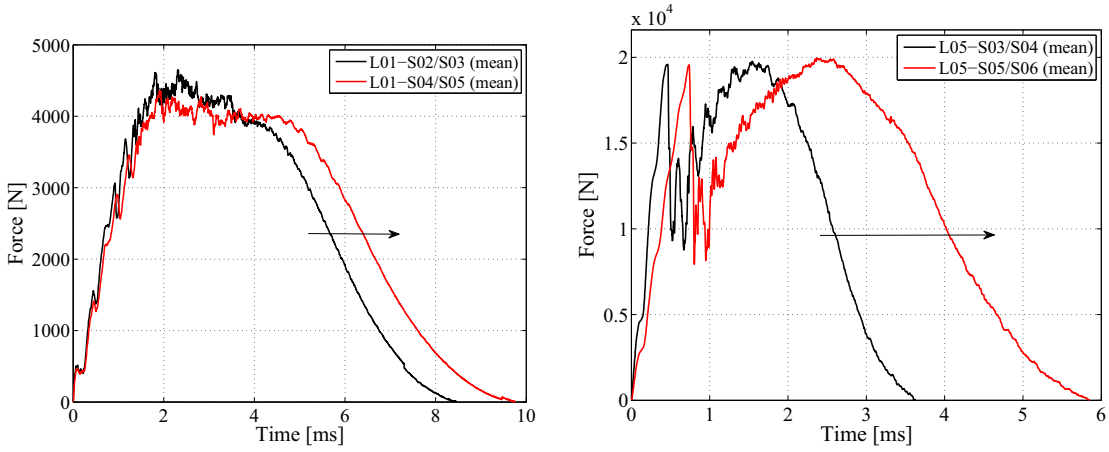

(a) (b)

Figure 3.37: (a) Impact force histories of laminate L01 for 19.3J (black: $M_i = 5$kg; red: $M_i = 6$kg), and (b) impact force histories of laminate L05 for 58J (black: $M_i = 6$kg; red: $M_i = 15$kg).

This effect can also be observed by means of the complete analytical models of the impact event. Accordingly, Figure 3.38 show the experimental and the analytical responses of laminate L01 for the impact energy 19.3J. In detail, the analytical predictions plotted in Figure 3.38.a are given by a complete model fed with the bi-lineal elastic-plastic contact law proposed by Yigit and Christoforou [31]. However, for the model used for the predictions plotted in Figure 3.38.b, the Hertz contact law is considered. For all the simulations, the number of modes applied for the Navier solution is 5 for each in-plane x and y directions. The analytical models show clearly the effect of changing the mass and the velocity under equal impact energy. As expected, the contact time of the elastic responses is enlarged when the impactor mass is increased. Finally, related to the contact laws used for the analytical models,

both cases suit the experimental profile and then no significant dependence with the contact law is detected. This result is explained with the fact that laminate L01 has small peak loads and an emphasized global behavior. Therefore, the role that plays the contact law in these impact configurations is small.

Additionally, Figure 3.39 illustrates also the effect of changing the impactor mass for laminate L05. In contrast with the predictions given for laminate L01, the role that plays the contact law is significant because a more localized behavior is experimented. As can be observed, the model which uses the Hertz contact law (in Figure 3.39.b), suits better the experimental results than the model fed with the bilineal elastic-plastic contact law (in Figure 3.39.a). Therefore, given the predictions of the complete models, it could be interesting to carry out quasi-static indentation tests or finite element simulations in order to know what is the proper contact law.

Finally, the effects of changing the impactor mass and the velocity but keeping constant the impact energy on the damage creation, can be simply analyzed, in a qualitative point of view, by observing the peak loads of the analytical profiles or by calculating the maximum elastic impact force as: $F_{max} = \bar{F}_{max}\sqrt{k_y}\sqrt{2E_i}$ (see Section 2.2). Since the impact energy E_i is kept constant, it yields to a constant maximum elastic impact force. Therefore, the resulting extension and type of damage is expected to be the same.

In Figure 3.40.a, the impact force histories corresponding to laminates L01 and L02 for an impact energy of 19.3J and an impactor mass of 5kg are compared. The effect of the plate thickness is clearly evidenced. Increasing the thickness, the response is faster, the peak load increases, and a clear first drop of the force appears. In addition, in Figure 3.40.b the impact force histories corresponding to laminates L01, L02 and L05 for an impact energy of 38.6J and an impactor mass of 5kg are compared. Again, the effects of the plate thickness under equal impact conditions can be observed. As shown, laminate L01 was perforated under an impact with a quasi-static behavior, as predicted in Chapter 2.

Recovering the experimental damage thresholds F_d of all laminates with equal ply thickness (L01, L02, L05 and L06), these can be plotted in function of the plate thickness h in a natural logarithmic scale, as shown in Figure 3.41. If a fit of the experimental points is performed (in gray), a slope of 1.47 is obtained. This value is quite close to the slope of the analytical threshold for a circular mid-plane de-

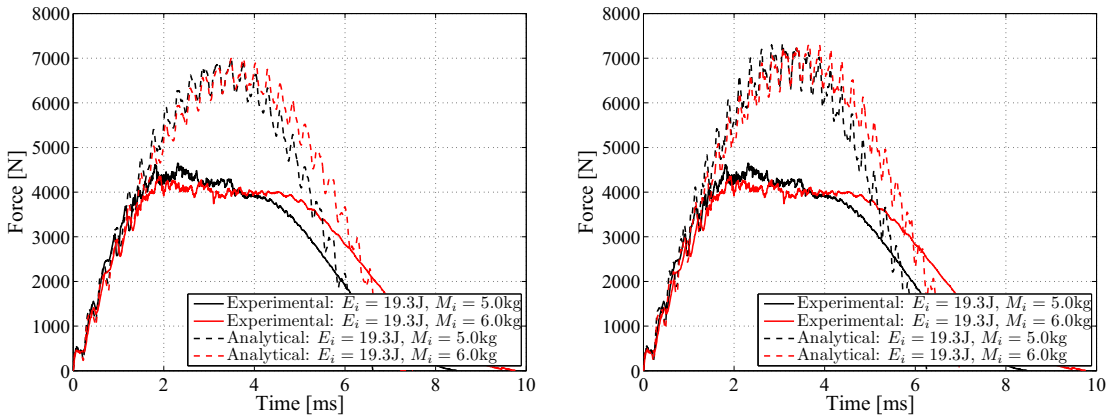

(a) (b)

Figure 3.38: Experimental and analytical impact force histories of laminate L01 for a constant impact energy 19.3J: M_i = 5kg (black), and M_i = 6kg (red). Two different contact laws are used: (a) bi-lineal elastic-plastic contact law [31], and (b) the Hertz contact law.

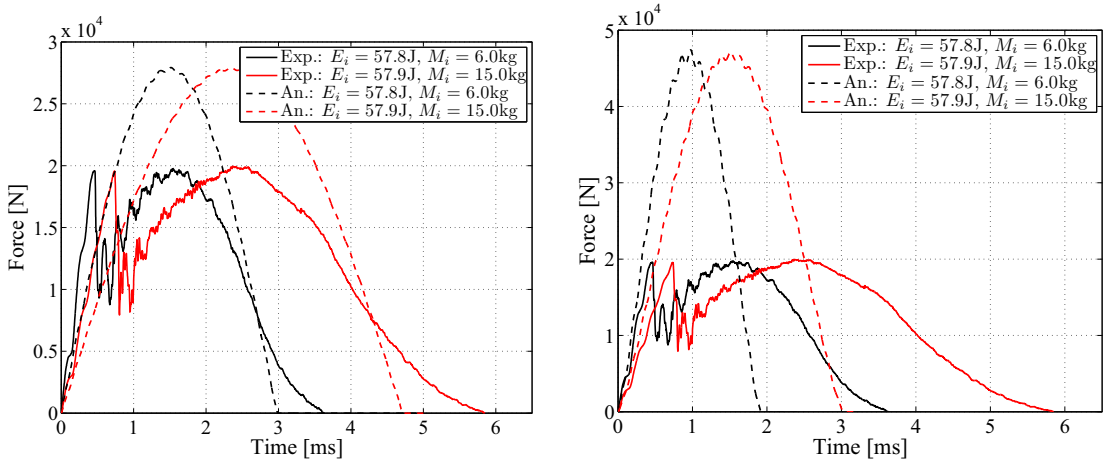

(a) (b)

Figure 3.39: Experimental and analytical impact force histories of laminate L05 for a constant impact energy 57.8J: M_i = 6kg (black), and M_i = 15kg (red). Two different contact laws are used: (a) bi-lineal elastic-plastic contact law [31], and (b) the Hertz contact law.

lamination (in black), i.e. 1.5, since $F_{d1}^{stat} \propto h^{1.5}$. Despite the constant offset that exists between the experimental and the analytical values, the significant conclusion

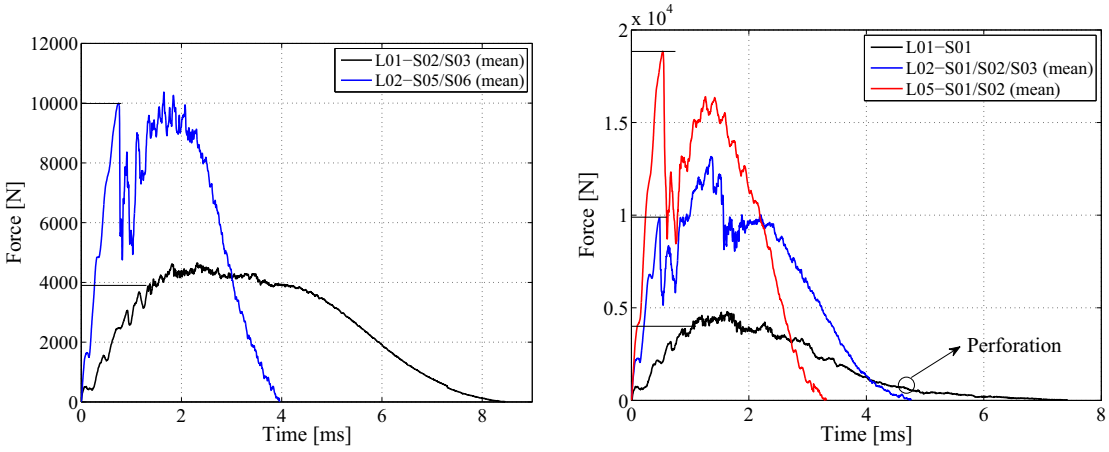

(a) (b)

Figure 3.40: (a) Impact force histories of laminates L01 (black) and L02 (blue) for 19.3J; (b) impact force histories of laminates L01 (black), L02 (blue) and L05 (red), for 38.6J.

is that the analytical trend seems to be in agreement with the experimental results. This result suggests that these laminates have a threshold load that corresponds approximately to a circular mid-plane delamination. The offset can be due to scattering of the material properties or to the assumptions considered in the formulation of the damage threshold. e.g. strain rate effects are neglected. Additionally, this result agrees with the analytical prediction for the first significant damage explained in Section 2.2.2, in exception of laminate L01. The damage threshold for L01 was related to a back-face delamination ($F_d = F_{mc}^{ten}$). This inaccurate prediction can be attributed to the fact that the identification of F_d in the impact force history is not clear, or simply a sudden delamination does not occur.

Impactor displacement, impactor velocity, and absorbed energy

Accordingly to the impact force histories, the effect of changing the impactor mass and the velocity, but keeping constant the impact energy, can also be observed in the histories of the impactor displacement and velocity plotted in Figure 3.42 for laminate L01, and in Figure 3.43 for laminate L05. Increasing the impactor mass, the displacements are enlarged and so the velocity responses are slower.

Moreover, Figure 3.44.a shows the histories of the absorbed energy of laminates

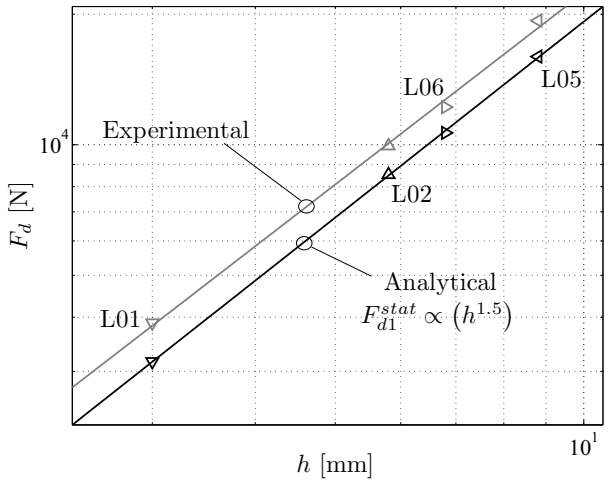

Figure 3.41: Experimental and analytical threshold loads as a function of the plate thickness.

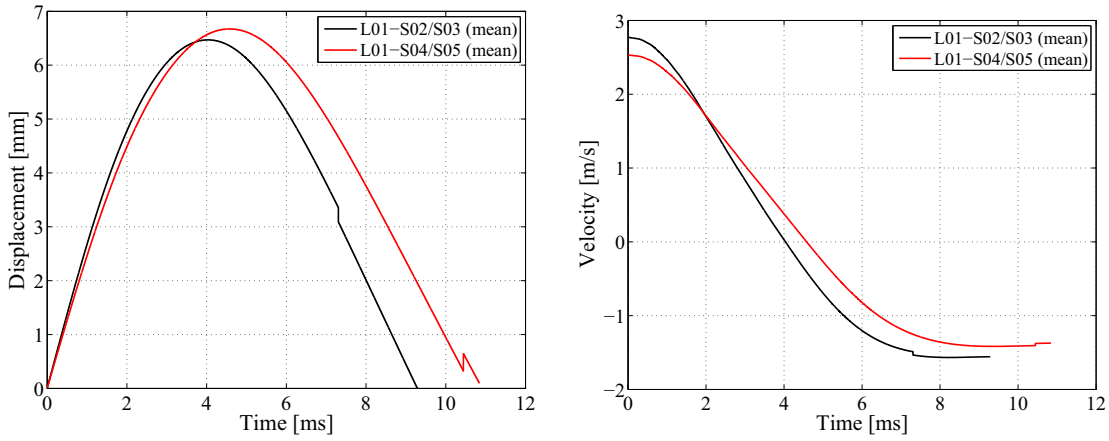

(a) (b)

Figure 3.42: Impactor (a) displacement and (b) velocity of laminate L01 for 19.3J (black: $M_i = 5$kg; red: $M_i = 6$kg).

L01, and Figure 3.44.b shows the evolutions of the impact force as a function of the impactor displacement. It can be seen that the absorbed energies are practically equal for both impact configurations, but the whole dissipation occurs at different instants. In addition, Figure 3.45 also shows these charts for laminates L05, where the effect of the impactor mass is more clear because the differences between

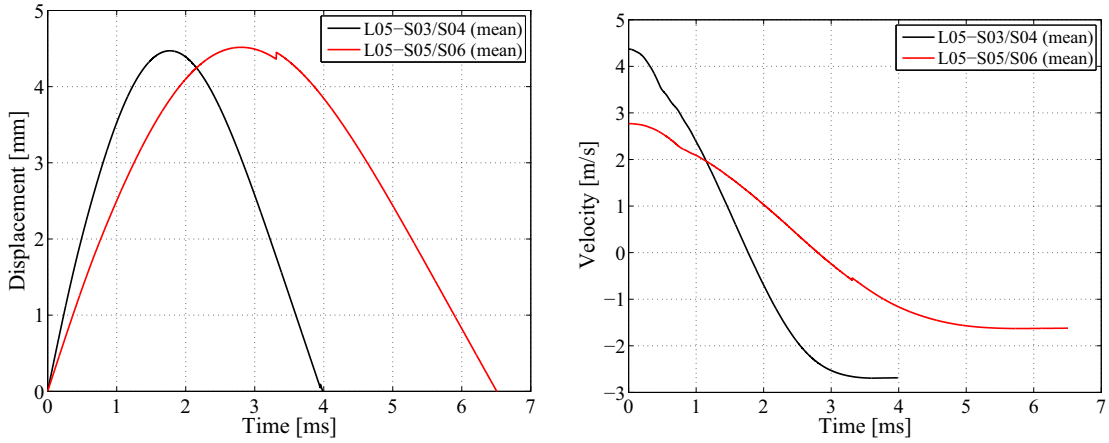

(a) (b)

Figure 3.43: Impactor (a) displacement and (b) velocity of laminate L05 for 58J (black: $M_i = 6$kg; red: $M_i = 15$kg).

configurations are greater than for L01.

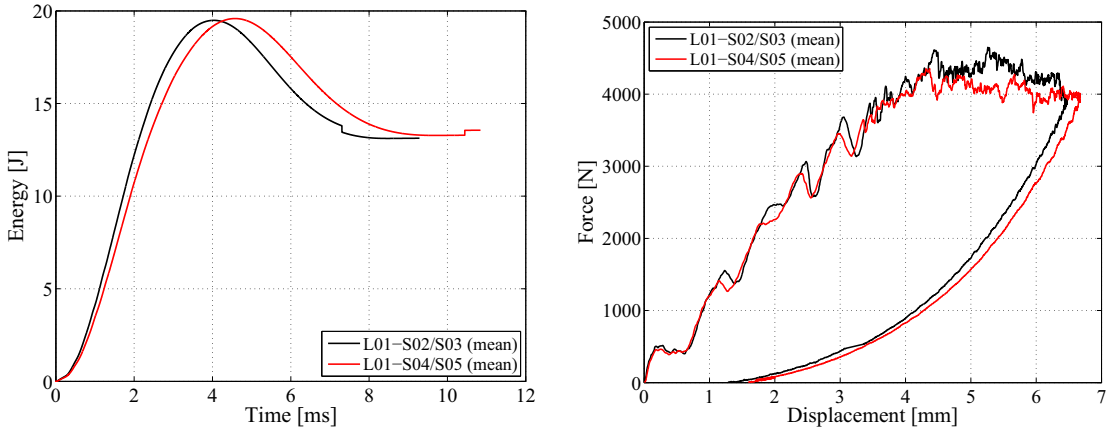

(a) (b)

Figure 3.44: Evolution of the (a) absorbed energy and (b) impact force versus impactor displacement of laminate L01 for 19.3J (black: $M_i = 5$kg; red: $M_i = 6$kg).

The result detected in Figures 3.44 and 3.45 agrees with the procedure of the guidelines for a drop-weight impact test provided by the aeronautical industry, which often do not specify the impactor mass or the velocity, rather they establish the impact energy (e.g. Airbus AITM1-0010 [81]). The reason for defining the set-up

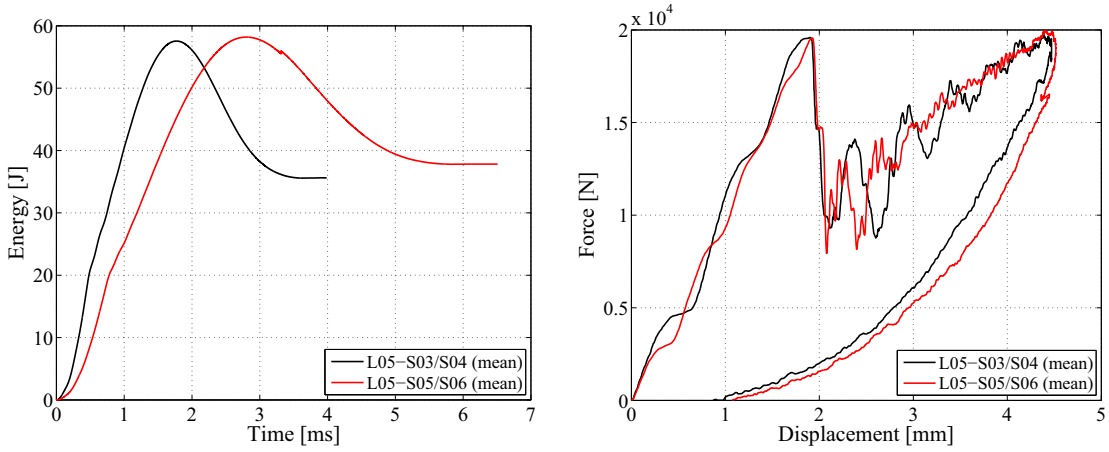

(a) (b)

Figure 3.45: Evolution of the (a) absorbed energy and (b) impact force versus impactor displacement of laminate L05 for 58J (black: $M_i = 6$kg; red: $M_i = 15$kg).

in this way is related with the fact that independently of the impactor mass and velocity selected, at the end of the test the energy dissipated will be the same. In other words, the damage developed in the specimens is the same if the impact energy is kept constant.

On the other hand, Figure 3.46 shows the displacement and the velocity histories of laminates L01 and L02 for the impact energy 19.3J. In addition, Figure 3.47 shows the corresponding histories of laminates L01, L02 and L05 for the impact energy 38.6J. Again, the effect of the laminate thickness is evidenced. Increasing the thickness, the response is more localized. This result means that the impactor displacement is smaller because less global deflection of the plate is experienced, and accordingly the response is much faster.

The absorbed energy is not the same for each laminate thickness under equal impact conditions. The trend is if the laminate thickness is increased, the absorbed energy is reduced. This effect can be observed in Figure 3.48, which shows the histories of the absorbed energy and the evolutions of the impact force as a function of the impactor displacement of laminates L01 and L02 for the impact energy 19.3J. The dissipated energies at the end of the tests are 13.1J for L01 and 10.1J for L02. Additionally, Figure 3.49 shows these evolutions corresponding to laminates L01, L02 and L05 for the impact energy 38.6J. In this case, the dissipated energies at

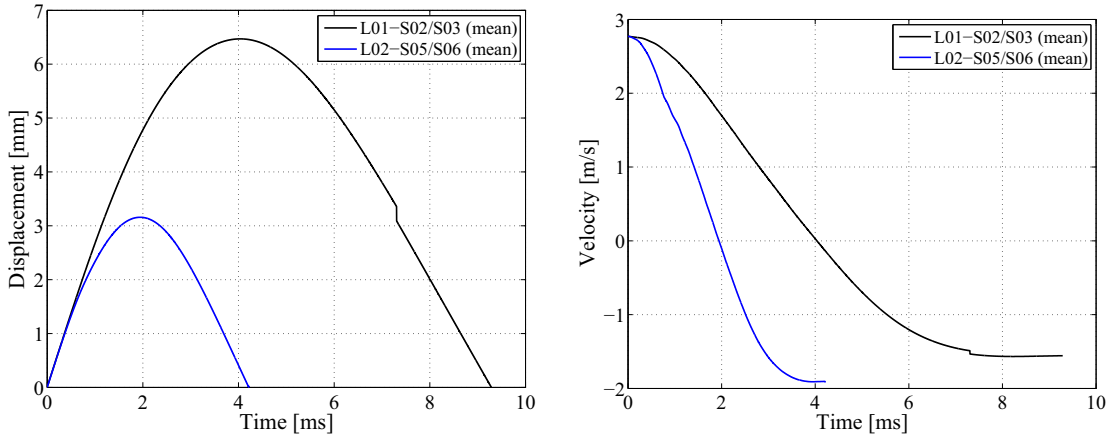

(a) (b)

Figure 3.46: Impactor (a) displacement and (b) velocity of laminates L01 and L02 for 19.3J.

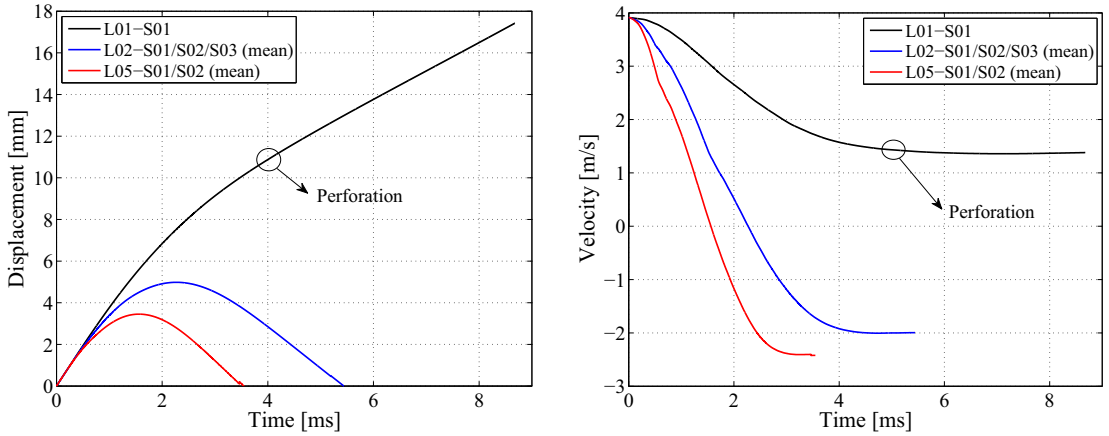

(a) (b)

Figure 3.47: Impactor (a) displacement and (b) velocity of laminates L01, L02 and L05 for 38.6J.

the end of the tests are 34.3J for L01, 28.3J for L02, and 23.6J for L05. Finally, a recovering of the elastic energy in the evolution of E_a of the perforated specimen L01-S06 is not observed.

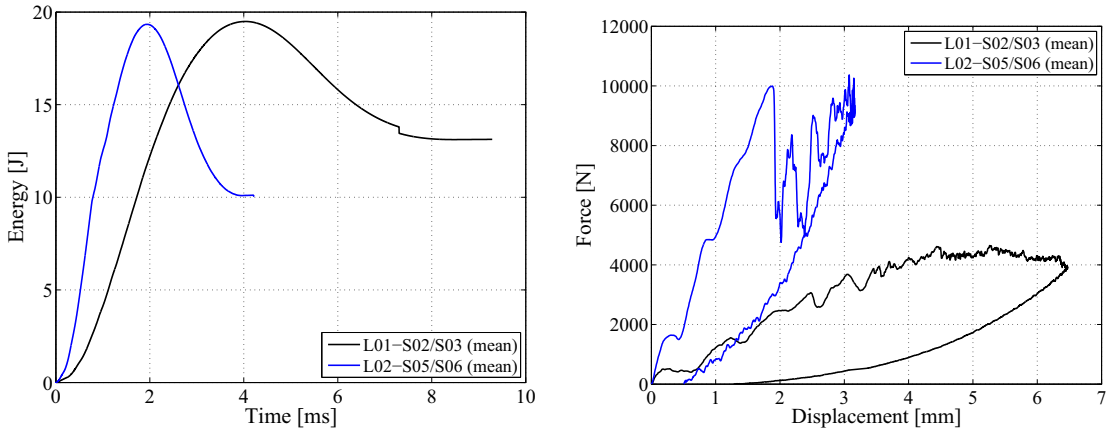

(a) (b)

Figure 3.48: Evolution of the (a) absorbed energy and (b) impact force versus impactor displacement of laminates L01 and L02 for 19.3J.

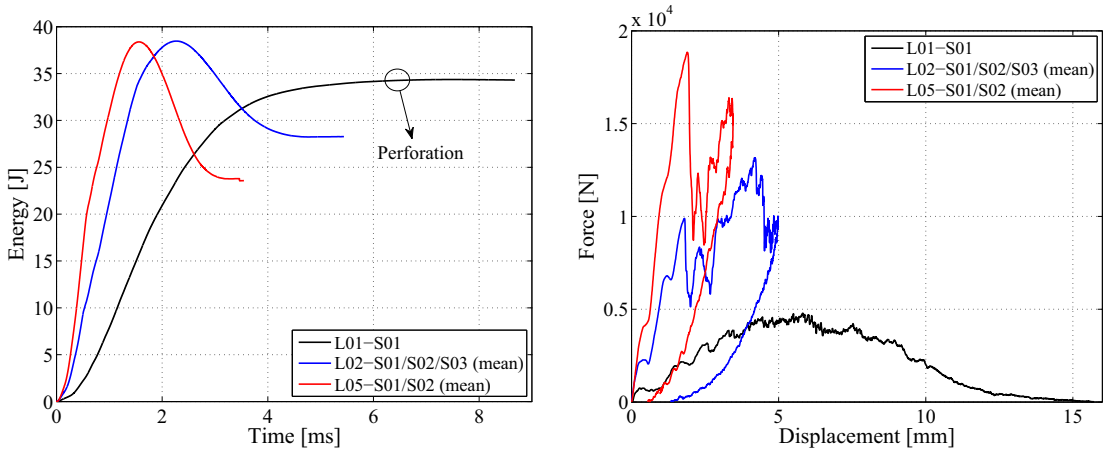

(a) (b)

Figure 3.49: Evolution of the (a) absorbed energy and (b) impact force versus impactor displacement of laminates L01, L02 and L05 for 38.6J.

3.4.2 NDI: C-scan after impact

The observations commented before about the effects of changing the impactor mass and the velocity, but keeping constant the impact energy, also can be associated with the ultrasonic C-scan inspections. Figures 3.50 and 3.51 show a sample of the projected delamination areas corresponding to laminate L01 and laminate L05,

respectively. It is observed that the projected area is practically the same when the impact energy is kept constant. This result suits with the fact that the dissipated energy is also the same for two impact cases which have the same impact energy.

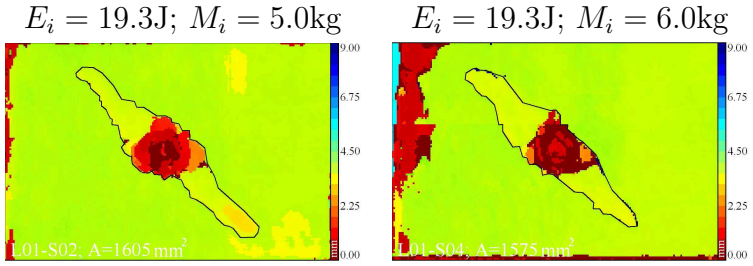

Figure 3.50: Sample of C-scan inspections of laminate L01 with equal impact energies, but different impactor masses.

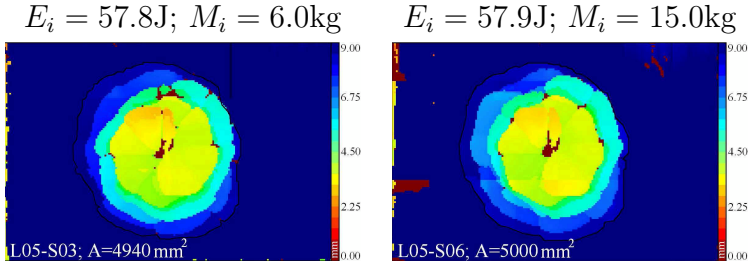

Figure 3.51: Sample of C-scan inspections of laminate L05 with equal impact energies, but different impactor masses.

On the other hand, between specimens with the same impact configuration but different laminate thicknesses, the resulting values of the projected area are quite similar, such as it is shown in Figures 3.52 and 3.53. However, it could be interesting to have at one's disposal the total values of the sum of each delaminated area of the interfaces, and then to compare these values between laminates with different thicknesses. Therefore, it could be expected that the largest area would be from laminate L01 as it was detected in the profiles of the dissipated energy. If this does not occur, then other damage mechanisms should have absorbed the energy in laminate L01, such as fiber breakage.

The shapes of the projected delamination areas can be related with the analytical predictions of F_d. For laminate type L01 was predicted a delamination at the

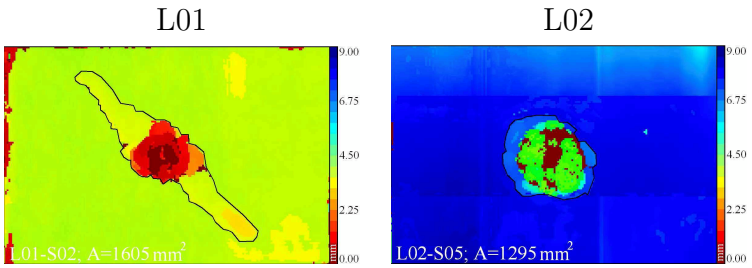

Figure 3.52: Sample of C-scan inspections of laminates L01 and L02 for 19.3J.

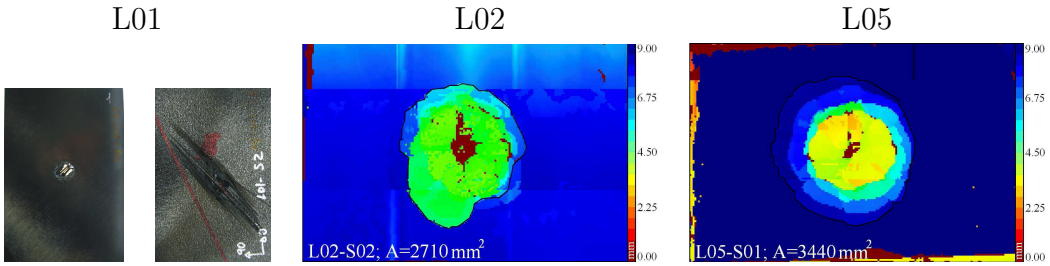

Figure 3.53: Sample of C-scan inspections of laminates L02 and L05 for 38.6J.

first interface from the back face of the plate (i.e. F_{mc}^{ten} for thin ply thickness). However, the experimental value obtained fits with the global linear trend for a circular mid-plane delamination F_{d1}^{stat}, as it was seen in Figure 3.41. Figure 3.54 shows the ultrasonic inspection for the laminate L01 with the lowest impact energy. As can be observed, the shape is equal in comparison with the shapes resulted from higher impact energies, just that with a smaller size. Therefore, for laminate L01 it is difficult to know what is the damage type associated to F_d. As was noted previously, these difficulties can be due to different factors. On the other hand, the prediction of F_d for both laminate types L02 and L05 was a mid-plane circular delamination. The shapes obtained are quite circular, but it should be noted that these circular shapes are rather a result of the superposition of peanut shaped delaminations. Furthermore, the deeper the delamination is, the larger the delamination is. These distribution of delaminations yield to the so-called pine pattern delamination distribution. In conclusion, for laminates L02 and L05 the prediction of F_d can be considered well suited although the considerations commented.

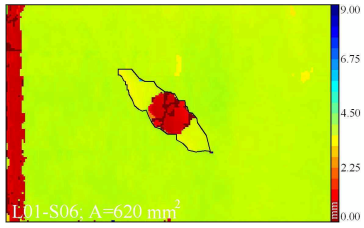

Figure 3.54: C-scan inspection of specimen L01-S06 ($E_i = 12.0$J, $M_i = 2.0$kg).

3.4.3 Dent-depth measurements

Figures 3.55 and 3.56 show the contour plots of the dent depth measurements of the impacted specimens L01 and L05, respectively. Consistent with previous observations, the resulting lectures of the dent depths are quite similar for impact cases with different impactor mass and velocity, but with equal impact energy.

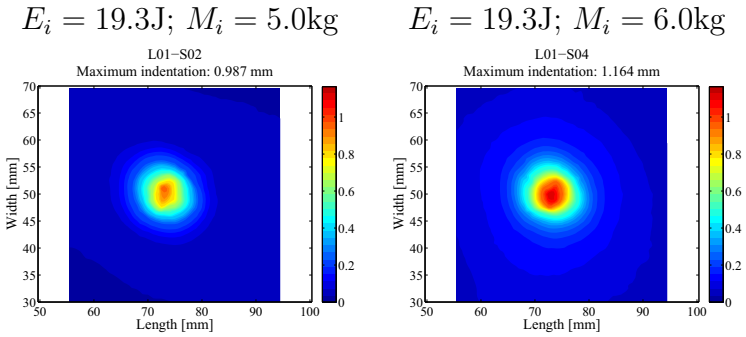

Figure 3.55: Dent-depth inspections of laminate L01 with equal impact energies, but different impactor masses.

Figures 3.57 and 3.58 show a sample of dent-depth measurements of laminates with different thicknesses. As it was observed in the histories of the impact force, increasing the laminate thickness, the response results more localized because less laminate deflection is experimented. Conversely, the dent-depth measurements demonstrate that also the indentation values are higher for thin plates. Nevertheless, it should be noted that for thin plates the indentation measurements are affected by the residual global deflection of the plate which increases the measurements obtained.

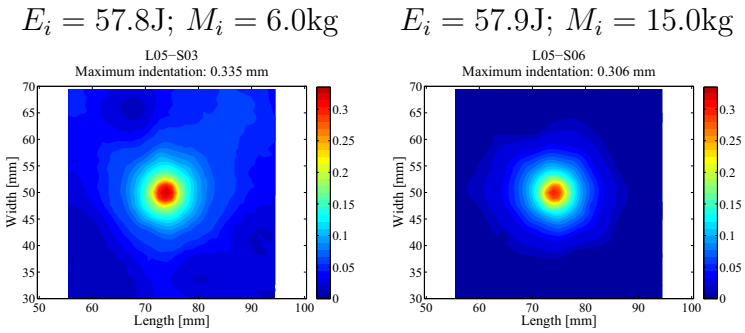

Figure 3.56: Dent-depth inspections of laminate L05 with equal impact energies, but different impactor masses.

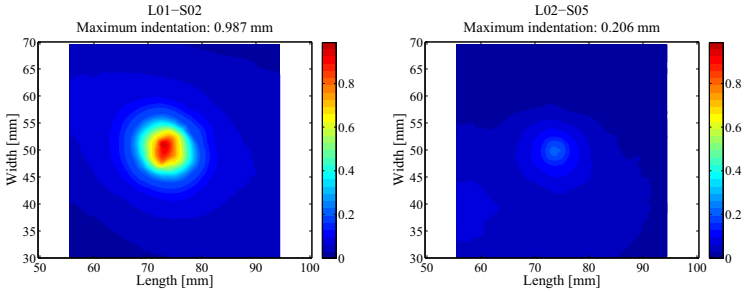

Figure 3.57: Dent-depth inspections of laminates L01 and L02 for 19.3J.

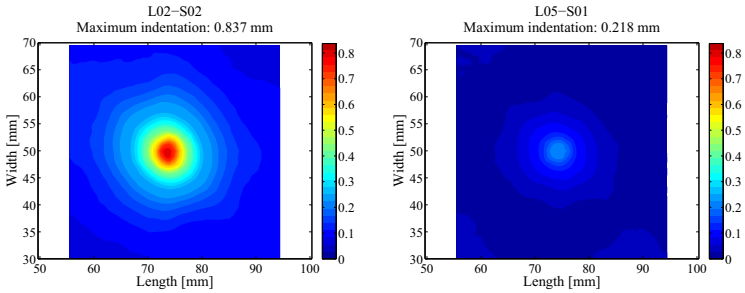

Figure 3.58: Dent-depth inspections of laminates L02 and L05 for 38.6J.

3.4.4 CAI tests

Residual compressive load

The results available from the CAI test to check the effects of changing the impactor mass but keeping constant the impact energy are those from laminate L05. The

residual compressive loads F_{fc} are: 164.5kN for $E_i = 57.8$J and $M_i = 6.0$kg, and 156.9kN for $E_i = 57.9$J and $M_i = 15.0$kg. It can be concluded that the values obtained are quite similar as can be expected after the discussion of the results presented before.

Increasing the laminate thickness under equal impact conditions, the residual compressive load increases. However, in order to compare properly these data, the normalized loads σ_{fc} must be computed. The resulting values are summarized in Table 3.13. It can be expected that the values should be similar for each impact energy, however it is not completely true because the size and the number of interface delaminations created in the impact tests are different in function of the laminate thickness. Therefore, given the available data, a valid argument can not be deduced.

	$E_i = 19.3$J		$E_i = 38.6$J	
	L01	L02	L02	L05
σ_{fc} [MPa]	19.7	22.9	16.5	20.6

Table 3.13: Residual compressive strengths σ_{fc} of laminates L01, L02 and L06.

Lectures of the displacement transducers (LVDT) and the strain gages (SG)

As an example of the displacement transducer and strain gage lectures, Figure 3.59 shows the results obtained for laminate L05. Despite the differences in the impactor mass and velocity, the responses are quite similar.

Finally, in order to illustrate the differences obtained in the responses of the transducer displacement and strain gages due to the differences in the laminate thickness, Figures 3.60 and 3.61 show the results obtained. It is observed that laminate types L01 and L02 suffer a clear global buckling on the instrumented plate face. This behavior is not observed in Figure 3.61, where both laminates L02 and L05 suffer a more localized buckling in the middle point of the specimen lengths.

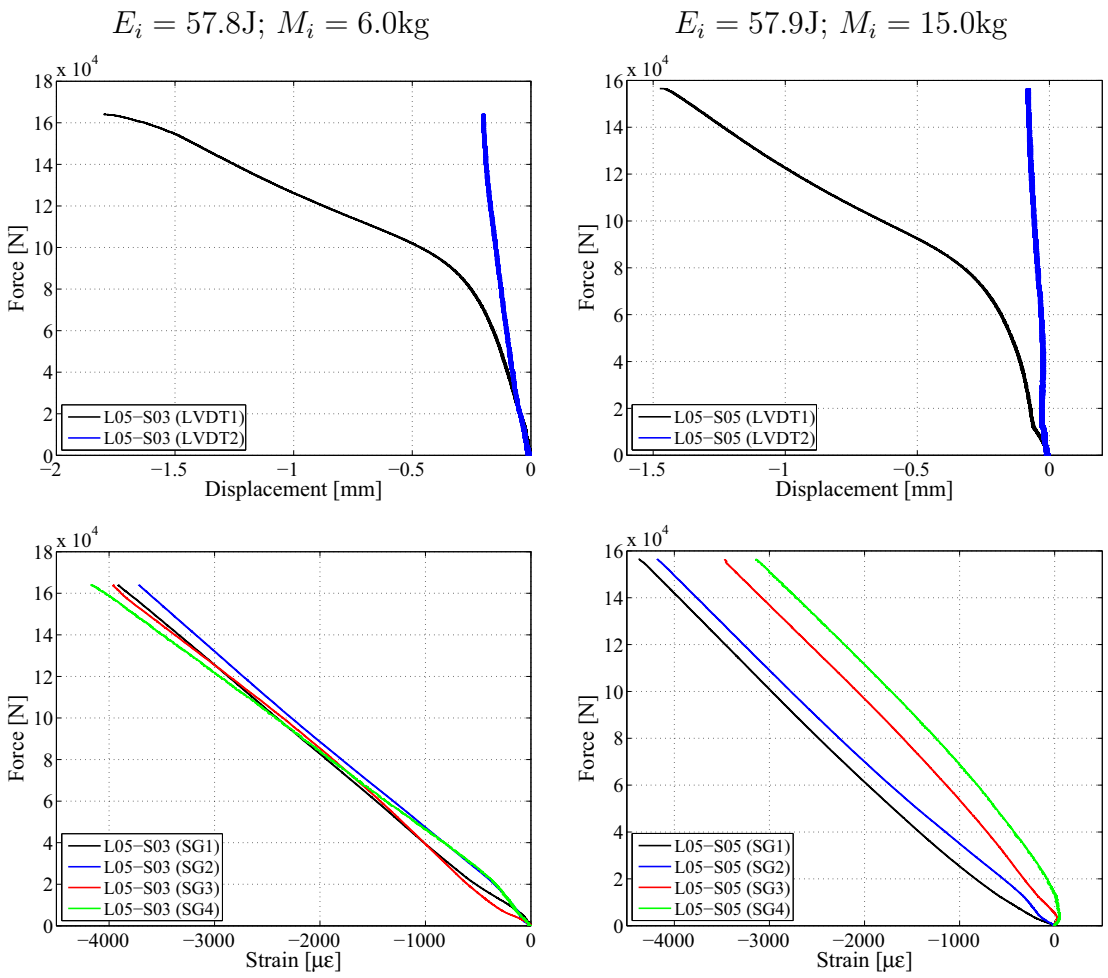

Figure 3.59: (a) Displacement transducer and (b) strain gage lectures of laminate L05.

3.5 Summary of conclusions

The main conclusions from the previous discussions of the experimental results and the analytical predictions are presented herein. These conclusions are valid for drop-weight impact events (i.e. low-velocity impacts), and most of them reaffirm some of the arguments explained in the design of the experiments of Chapter 2. The conclusions are:

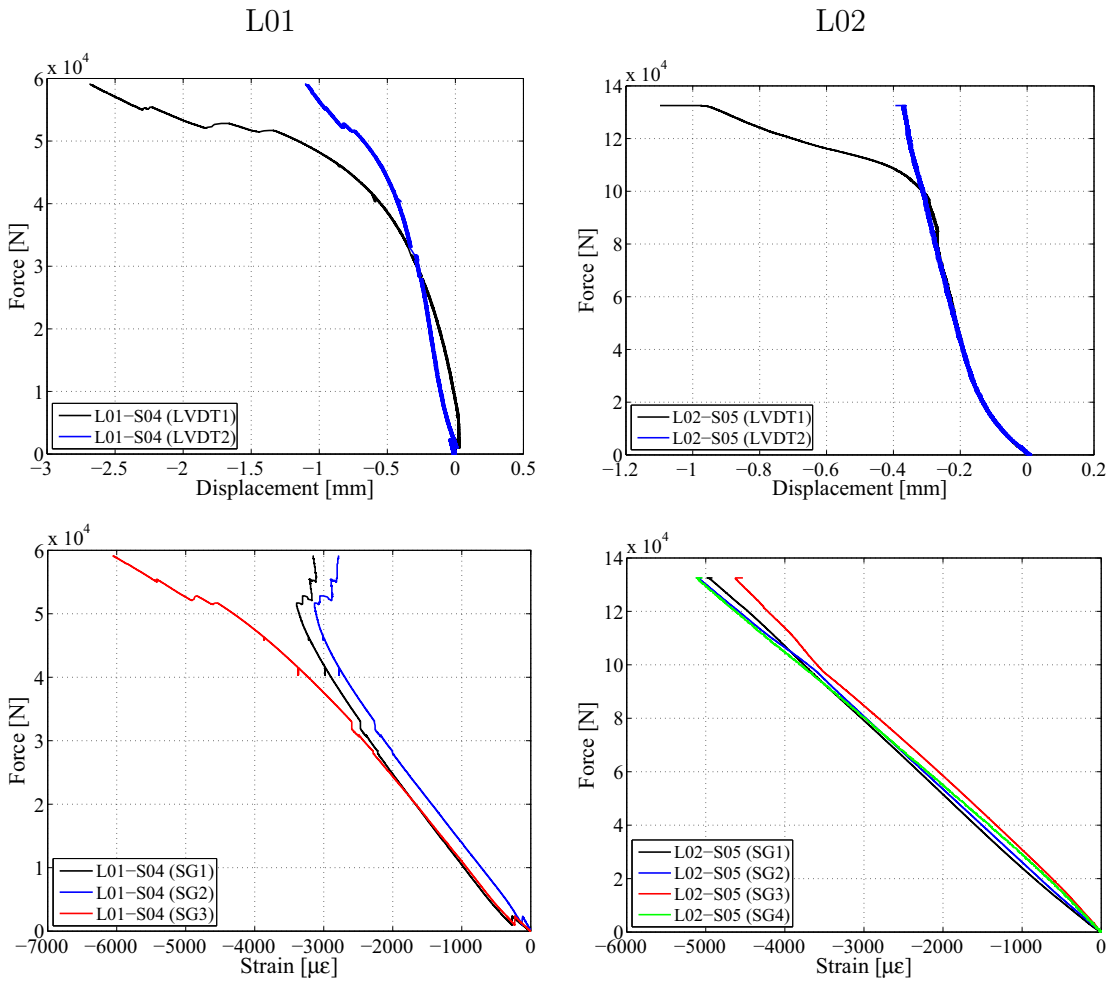

Figure 3.60: (a) Displacement transducer and (b) strain gage lectures of laminates L01 and L02 for 19.3J.

Effect of the impact velocity

- The threshold load, F_d, remains constant in front of changes of the impact velocity.

- Increasing the impact velocity, the slope of the elastic regime is increased, as predicted by means of the analytical impact models. Accordingly, the predicted maximum elastic impact force increases, indicating that more damage is created.

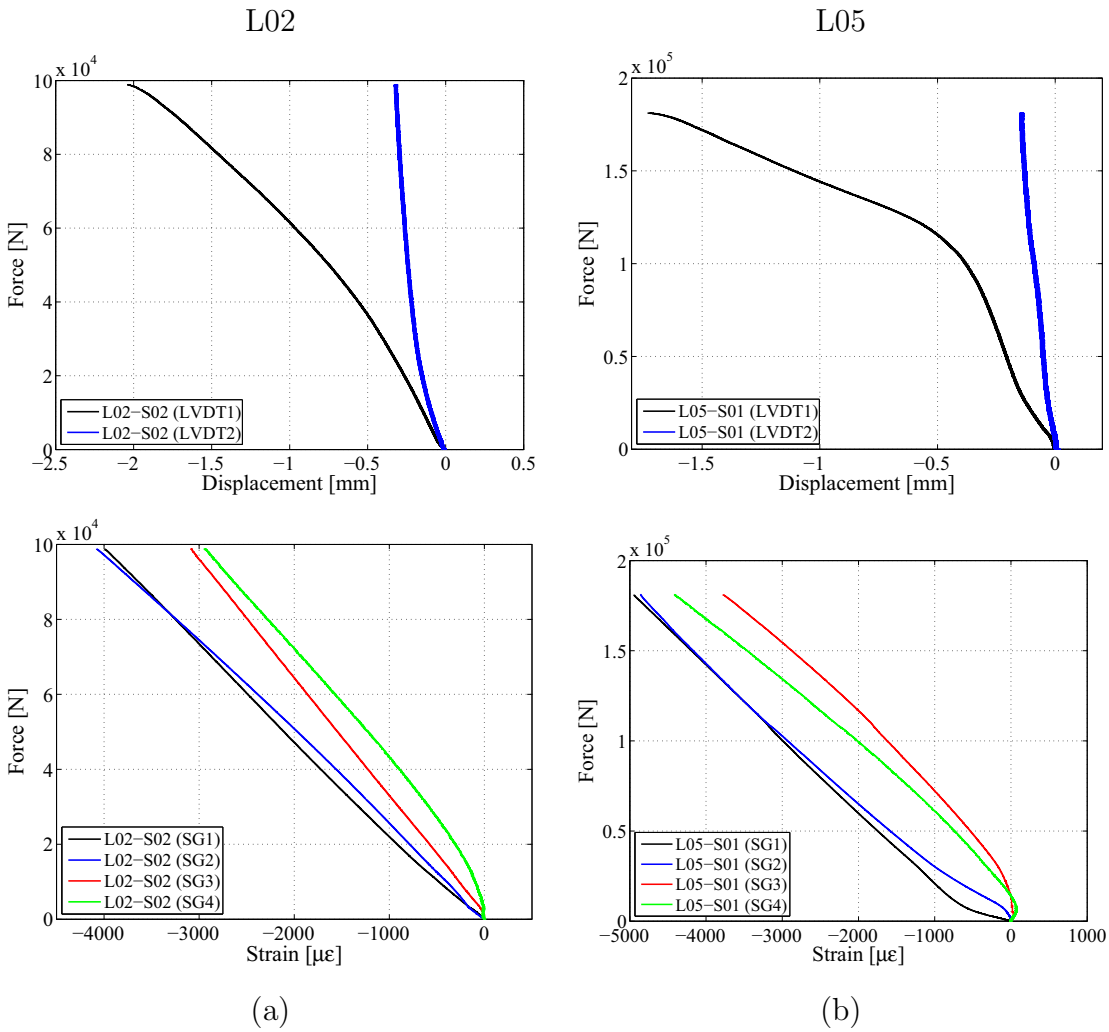

Figure 3.61: (a) Displacement transducer and (b) strain gage lectures of laminates L02 and L05 for 38.6J.

- Increasing the impact velocity, the response is extended in time because the plate develops more damage. Therefore, the damage resistance is reduced.

- Increasing the impact velocity, the damage tolerance is reduced since the residual compressive loads are reduced.

Effect of changing the impactor mass and the velocity

- The threshold load, F_d, remains constant in front of changes of the impactor mass and velocity, but keeping constant the impact energy.

- Increasing the impactor mass, the response is more quasi-static, which means that the response is slowed down. This behavior was also predicted by means of the impact characterization diagram and the complete analytical impact models.

- Given a stacking sequence, the dissipated energy or the damage developed is the same between impacts with equal impact energy. Therefore, the damage resistance and the damage tolerance remain constant under the same impact energy level. This result agrees with the guidelines provided by the aeronautical industry for a drop-weight impact test.

Effect of ply thickness (clustering)

- If the ply clustering is increased, under equal impact conditions the values of F_d and F_{max} are reduced.

- Increasing the ply clustering, the changes in the stiffness during the impact are more progressive and smooth when compared with laminates with thin plies. This result implies difficulties in the detection of F_d for laminates with thick plies.

- The response is elongated by increasing the ply clustering of the laminate. This result indicates that more damage develops for laminates with thick plies. Accordingly, by reducing the number of interfaces available for delamination, the resulting projected delamination area is increased. Therefore, ply clustering results in a lower damage resistance of a composite structure.

- Increasing the ply clustering, the indentation is increased. However, this result can be affected by the remaining global bending of the impacted laminate.

- The free growth of the delaminations can be affected by the finite in-plane dimensions of the plates. In other words, the growth of the delaminations could be braked by the clamping system. This effect occurs basically in laminates with thick plies.

- The trend of the proposed analytical thresholds for delamination are in agreement with the experimental points for all laminate types. However, the ana-

lytical values under-predict the real values. This offset can be due to scattering of the material properties or to the assumptions considered in the formulation of the damage threshold, e.g. strain rate effects are neglected. Further testing is required to verify these arguments, especially with critical impact energies which generate maximum impact forces similar to the damage threshold loads.

- The damage tolerance, quantified using the residual compressive load, is not affected by increasing the ply thickness, because all laminate types presented have shown similar values of compressive loads at each impact energy.

Effect of ply mismatch angle at interfaces

- The analytical prediction of F_d for the selected cross-ply laminate has been in agreement with the experimental result, although an offset also has appeared.

- The mismatch angle of the interfaces for delamination has not presented a clear effect on the damage resistance and on the damage tolerance. This result can be due to the fact that the plate thicknesses of the selected laminates for this study are slightly different.

Effect of the laminate thickness

- Increasing the laminate thickness, the response is faster and the drop in the impact force from point F_d increases. For the thinner laminate tested, the profiles of the impact force are smooth and do not present a clear first drop on the impact force. This result could mean that a sudden loss of stiffness from the point F_d does not occur, or the matrix and delamination damage that appear do not change the response of the impact, rather it is affected by progressive fiber breakage. This last argument can be related with the membrane effects.

- The predictions of the threshold load F_d for the different laminates considered have been in agreement except for the thinner laminate, i.e. L01. This result can be attributed to different causes: the membrane effects, the possibility that really the delaminations can not be detected in the force histories, or the

fact that simply a sudden large delamination does not occur and rather the delaminations grow progressively.

- Increasing the laminate thickness, the damage resistance is improved since the energy dissipated is lower than for thin laminates. Likewise, the damage tolerance is improved. However, the resulting structures are heavier and more expensive.

Usefulness of the analytical impact models and analytical thresholds

- With the studies presented, it has been demonstrated that the analytical impact models for the prediction of the elastic response are a powerful tool: to define a suitable test matrix of specimens, to obtain a qualitative understanding of the effects of the governing parameters on the impact response, and to interpret the experimental results obtained.

- The analytical impact models are completed with the analytical thresholds for the prediction of the damage mechanisms that can occur in a laminated composite plate under low-velocity impact loading. For low-velocity impacts, the most critical damage is the delamination. In general, it has been shown that the damage thresholds for delamination follow the trends of the experimental results. Table 3.14 summarizes the analytical and experimental thresholds obtained.

Laminate	Analytical F_d [kN] F_{d1}^{stat}	F_{mc}^{ten}	Experimental F_d [kN]	C-scan shape	Observations
L01	3.16	**2.68**	3.90		Inaccurate prediction
L02	**8.53**	10.34	9.94		Proper prediction
L03	8.49	**7.20**	7.60		Proper prediction
L04	8.34	**4.92**	5.50		Proper prediction
L05	**15.97**	23.80	19.33		Proper prediction
L06	**10.65**	11.26	12.21		Proper prediction

Table 3.14: Summary of analytical and experimental thresholds.

Chapter 4

Interlaminar damage model

4.1 Introduction

Delamination is one of the most common failure mechanisms in laminated composite materials and can appear at any life time of the structure (manufacturing, transportation, assembly, and service). Delamination reduces seriously the integrity of a structural element and can produce its collapse. Therefore, accurate analysis tools for the simulation of delamination are required.

Delamination has been largely studied and modeled in the literature. When material nonlinearities can be neglected and an initial crack is present, methods based on Linear Elastic Fracture Mechanics (LEFM) have been proven to be effective in predicting delamination growth, such as the Virtual Crack Closure Technique (Irwin [87]; Rybicki and Kanninen [88]; Raju [89]; Zou et al. [90]; Krueger [91]), the J-integral method (Rice [92]), the virtual crack extension (Hellen [93]), and the stiffness derivative (Parks [94]). These techniques are used to calculate the components of the energy release rate. Delamination growth is predicted when a combination of the components of the energy release rate is equal to, or greater than, a critical value (Griffith [95]).

When no initial macroscopic defects are present, a local approach has been frequently used to detect delamination onset, in which the key parameters are critical values of tractions (e.g. Pagano and Pipes [96], and Hashin [97]).

Another approach for delamination modeling can be developed within the framework of Damage Mechanics. Models formulated using Damage Mechanics considers

an interface as a third independent material defined by its own constitutive law. This interface links the two structural components and is based on the concept of the cohesive crack model introduced by Barenblatt [98], Dugdale [99], Hillerborg et al. [100] and others: a cohesive damage zone or softening plasticity is developed near the crack front. Cohesive damage zone models relate tractions to displacement jumps at an interface where a crack may occur. Damage initiation is related to the interfacial strength (i.e. the maximum traction on the traction-displacement jump relation). When the area under the traction-displacement jump relation is equal to the fracture toughness, the traction is reduced to zero and new crack surfaces are formed. The use of cohesive models is extremely powerful for the simulation of general fracture processes due to its simplicity and the unification of crack initiation and growth within one model.

The implementation of cohesive constitutive models normally is carried out by means of user-written subroutines in finite element codes. Generally, the examples presented in the literature implement cohesive elements (e.g. Schellekens and De Borst [101], Allix et al. [102], Mi et al. [103], Alfano and Crisfield [104], Camanho et al. [105], and De Borst [106]) or a user material definition (e.g. Pinho et al. [107], Iannucci [2], and Aymerich et al. [108]), although surface-based cohesive behaviors which eliminate the need to define cohesive elements have been also implemented (e.g. Zhang et al. [109], and Abaqus 6.8 [110]).

In cases where crack path is known in advance, either from experimental evidence, or because of the material configuration, discrete interface elements equipped with a cohesive constitutive relation are inserted a priori in the finite element mesh (e.g. Corigliano and Allix [111]). To allow for a more arbitrary direction of crack propagation, interface elements can be inserted between all continuum elements (Xu and Needleman [112]). However, this approach is limited to a number of predefined orientation crack angles since the interface elements are aligned with the element boundaries. Some authors (e.g. Martha et al. [113], and De Borst [106]) use meshing tools to redefine the position of cohesive elements in function of the stress state evolution. When the position for the appearance and progression of a crack is detected, the structure is again meshed and an interface element is located in a proper position. Alternatively, another research line in fracture modeling is to improve the kinematic description of finite elements by enriching the shape functions by means

of adding degrees of freedom. Initially, these models consider a law which relates the stresses and the strains until damage localization is detected in one plane. At this point, the law is rewritten and relates stresses and crack opening. Some of these approaches are: elements with embedded discontinuities (e.g. Oliver [114]) based on the enhanced assumed strain (Simo and Rifai [115]), and extended finite elements (e.g. Belytschko et al. [116]) based on partition of unity method (Babuska and Melenk [117]).

In the formulation of cohesive models, the energy dissipated during the crack opening has to be controlled, i.e. it is necessary to assure that the model satisfies the Clausius-Duhem inequality. Some models are well suited to simulate delamination under constant mixed-mode conditions, such as Mi et al. [103], Alfano and Crisfield [104]. However, these models do not satisfy the Clausius-Duhem inequality when the crack grows in variable mixed-mode conditions, because generally they define the damage threshold parameter as the maximum displacement and the damage variable as a function of material parameters that depend on the mixed-mode ratio. Examples of cohesive models which develop in a thermodynamically consistent way are Ortiz and Pandolfi [118], and Jansson and Larsson [119].

Turon et al. [120] proposed a thermodynamically consistent damage model for the simulation of progressive delamination in composite materials under variable mixed-mode ratio. The constitutive law follows a bilinear relationship between relative displacements and tractions at the interface, and it is defined by using a delamination onset and propagation criteria. The delamination onset criterion is based on energy terms and is proposed so the model formulation accounts for loading mode changes in a consistent thermodynamically way. The formulation also accounts for crack closure effects to avoid interfacial penetration of two adjacent layers. This model was implemented by using a user element subroutine called UEL. The zero-thickness cohesive element was focused for implicit analysis in Abaqus finite element software [110].

Some structural problems cannot be solved by using an implicit finite element code due to convergence difficulties related to material softening. To avoid these difficulties an explicit code should be used. An implicit analysis requires the assembly of the global stiffness matrix and its subsequent inversion to solve the equilibrium equations system for each iteration, whereas with an explicit analysis these opera-

tions are not necessary. Explicit integration schemes do not require the solution of a global set of equilibrium equations as the accelerations, velocities and displacements are calculated explicitly at each node recurring to a simple central differences rule applied over a time increment. Consequently, the explicit formulation is often proper in cases where severe changes in stiffness matrix occur, such as analysis with failure or degradation of the material. Other applications where explicit code is recommended and implicit analysis may lead to severe convergence difficulties are problems with complex contacts, post-buckling, and high-speed dynamic events such as impact. Explicit codes can also be used to solve problems that are essentially static by controlling some simulation variables, such as the kinetic energy that must be less than 5% of the internal energy of the system [110].

In this chapter, a modified formulation and implementation in an explicit finite element code of the cohesive model originally developed by Turon et al. [120] are presented. The model is implemented by using a user-written material subroutine, called VUMAT [110]. The user material developed is defined on sets of elements that represent the possible location for delamination. The elements can be selected to have zero-thickness (surface elements) or non-zero-thickness (continuum elements). The possibility of using continuum-based cohesive elements enables the simulation of an interface with non negligible thickness. Therefore, the macroscopic properties of the interface material, such as stiffness and strength, can be measured experimentally and used directly in the cohesive model.

In the literature, there are also available cohesive models implemented in a user-written material subroutine for explicit finite element analysis. Generally, these models are checked by simulating quasi-static standard delamination toughness tests, and a simulation of delamination in a monolithic laminated composite plate subjected to low-velocity impact is presented as the most challenging application. Under impact loading, delamination growth develops under variable mixed-mode conditions, and this phenomenon must be accounted properly in the cohesive model. However, the formulations available in the literature often do not control the crack growth in a consistent thermodynamically way.

The goal of the work detailed in this chapter is to apply the proposed model for the explicit simulation of low-velocity impact events on laminated composite plates. Loading rate effects as well as frictional effects that occur when complete separation

of the interface takes place, are not considered in the formulation.

The content of this chapter is structured as follows: first, the updated formulation of the cohesive model given by Turon et al. [120] is presented. Next, the adaptations of the formulation to be implemented in a continuum interface are described. After, the implementation of the model in a user-written material is also explained in detail. Finally, the numerical predictions of interlaminar fracture tests of polymer-based composite materials are compared with experimental data in order to validate the model.

4.2 Damage model formulation

The main aspects of the delamination model proposed by Turon et al. [120] are presented in this section with some modifications of the original formulation.

The constitutive law used is shown in Figure 4.1. This law is a bilinear relationship between relative displacements and tractions. The first line represents an elastic relationship, prior to damage onset. Damage onset is related to the interface strength τ^o. When the area under the traction-displacement relation is equal to the fracture toughness, $\mathcal{G}_c$, the interface tractions revert to zero and a new crack surface is created.

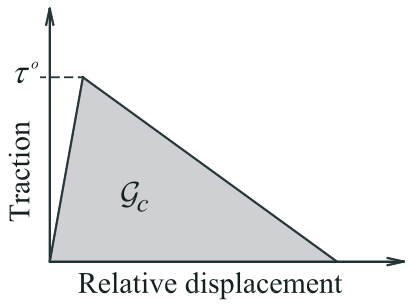

Figure 4.1: Bilinear constitutive law.

The different relative displacements between the nodes of a surface element are shown in Figure 4.2, where each displacement is directly associated with the corresponding propagation mode by assuming that the crack front is located at the indicated line. At finite element scale level, it is not possible to distinguish the

shear modes II and III because the crack front is in fact unknown. For this reason, shear modes are generally grouped together in the formulation of the cohesive models (see Section 4.2.1).

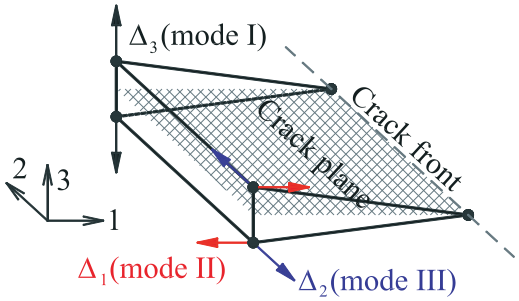

Figure 4.2: Propagation modes.

The damage model follows the general formulation of continuum damage models proposed by Mazars [121], and Simo and Ju [122]. The Helmholtz free energy by surface unit of the interface under isothermal conditions is defined as:

$$\Psi\left(\Delta_i, d\right) = \left(1 - d\right)\Psi^o\left(\Delta_i\right); \qquad i = 1,\, 2,\, 3 \tag{4.1}$$

where d is the scalar isotropic damage variable and $\Psi^o\left(\Delta_i\right)$ is a function of the relative displacement space defined as:

$$\Psi^o\left(\Delta_i\right) = \frac{1}{2}\Delta_i D^o_{ij}\Delta_j; \qquad i, j = 1,\, 2,\, 3 \tag{4.2}$$

Equation (4.1) indicates that the relative displacement components, Δ_i, are the free variables of the system (i.e. displacement driven formulation), and d is the internal variable that ensures the irreversibility of the model.

Negative values of Δ_3 (mode I) have no physical sense because the cracks are closed and no damage is produced. Therefore, the damage model has a unilateral behavior for this propagation mode, which means that the damage variable can be activated or deactivated as a function of the loading state. Therefore, Equation (4.1) is modified as:

$$\Psi\left(\Delta_i, d\right) = \left(1 - d\right)\Psi^o\left(\Delta_i\right) - d\Psi^o\left(\delta_{3i}\left\langle -\Delta_3\right\rangle\right); \qquad i = 1,\, 2,\, 3 \tag{4.3}$$

where $\langle - \rangle$ is the Macaulay brackets defined as $\langle x \rangle = \frac{1}{2}(x + |x|)$, and δ_{ij} is the Kronecker delta.

Applying Coleman method [122], the constitutive equation reads:

$$\tau_i = \frac{\partial \Psi}{\partial \Delta_i} = (1 - d)\, D^o_{ij} \Delta_j - d D^o_{ij} \delta_{3j} \langle -\Delta_3 \rangle ; \qquad i, j = 1,\, 2,\, 3 \tag{4.4}$$

D^o_{ij} is the undamaged stiffness tensor, defined as:

$$D^o_{ij} = \delta_{ij} K; \qquad i, j = 1,\, 2,\, 3 \tag{4.5}$$

where K is a scalar parameter corresponding to the slope of the first line in the constitutive law, typically called penalty stiffness. As Equation (4.5) shows, the penalty stiffness is the same for any propagation mode.

To ensure the thermodynamic consistency of the model, the dissipated energy by surface unit during the damage propagation process, Ξ, has to be equal or greater than zero:

$$\Xi = Y \dot{d} \geq 0 \tag{4.6}$$

where the thermodynamic force Y associated with the internal variable d is defined as:

$$Y = -\frac{\partial \Psi}{\partial d} \tag{4.7}$$

The value of the damage variable has to be evaluated at each time increment during the loading process. Therefore, it is necessary to define a suitable norm of the relative displacement vector, the surface for damage activation, a law for damage evolution, and criteria for damage onset and damage propagation.

4.2.1 Norm of the relative displacement vector

The selected norm of the relative displacement components is defined as:

$$\lambda = \sqrt{\langle \Delta_3 \rangle^2 + \Delta^2_{shear}} \tag{4.8}$$

where Δ_3 is the relative displacement in mode I, and Δ_{shear} is the Euclidian norm of the relative displacements in mode II and mode III:

$$\Delta_{shear} = \sqrt{\Delta_1^2 + \Delta_2^2} \tag{4.9}$$

Normally, the shear modes II and III are represented together because their individual evaluation depends on the relative displacement between homologous nodes with respect to the crack front orientation. Since at finite element scale level the crack orientation is generally unknown, it is not possible to distinguish between modes II and III.

4.2.2 Surface of damage activation and law for damage evolution

The surface of damage activation from Turon et al. [120] is modified by the expression:

$$F\left(\boldsymbol{\Delta}_t, d_t\right) = G\left(\boldsymbol{\Delta}_t\right) - d_t \leq 0 \qquad \forall t \geq 0 \tag{4.10}$$

where $G\left(\boldsymbol{\Delta}_t\right)$ is a monotonic loading function which depends on the relative displacement vector $\boldsymbol{\Delta} = \{\Delta_1, \Delta_2, \Delta_3\}^T$ at time t, and d_t is the damage variable at time t which is used as the threshold function.

The evolution of the damage variable is defined by means of the Kuhn-Tucker constraints which provide the formulation of the loading-unloading-reloading conditions as [123]:

$$\dot{d} \geq 0; \quad F\left(\boldsymbol{\Delta}_t, d_t\right) \leq 0; \quad \dot{d}F\left(\boldsymbol{\Delta}_t, d_t\right) = 0 \qquad \forall t \geq 0 \tag{4.11}$$

On the other hand, to ensure that the surface of damage activation will grow as much as the internal variable grows, the persistence (or consistency) condition is required. This is:

$$F\left(\boldsymbol{\Delta}_t, d_t\right) = 0 \Rightarrow \dot{F}\left(\boldsymbol{\Delta}_t, d_t\right) = 0 \qquad \forall t \geq 0 \tag{4.12}$$

Therefore, the damage variable d_t is explicitly defined by:

$$d_t = \max\left\{0, \max_s \left(G\left(\boldsymbol{\Delta}_t\right)\right)\right\} \qquad 0 \leq s \leq t \qquad \forall t \geq 0 \tag{4.13}$$

which fully describes the evolution of the internal variable for any loading-unloading-reloading situation. On the other hand, by using the constitutive equation (see Figure 4.3) for any mixed-mode ratio β (see Equation (4.21)), the function $G\left(\boldsymbol{\Delta}_t\right)$ is defined as:

$$G\left(\boldsymbol{\Delta}_t\right) = \min\left\{\frac{\Delta_t^f\left(\lambda_t - \Delta_t^o\right)}{\lambda_t\left(\Delta_t^f - \Delta_t^o\right)},\ 1\right\} \qquad \forall t \geq 0 \tag{4.14}$$

Equation (4.14) defines the loading function by means of the bilinear constitutive equation, where Δ_t^o and Δ_t^f are the onset and propagation damage parameters at time t, respectively. The values of Δ^o and Δ^f are obtained by means of the onset and propagation damage criteria, respectively. These values will be constant unless the mixed-mode ratio changes. The variables used in Equation (4.14) are identified in Figure 4.3.

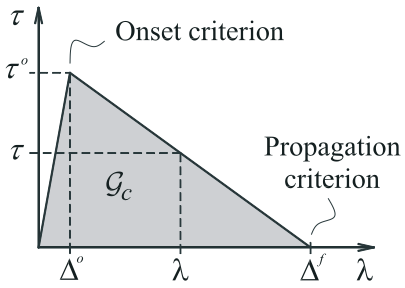

Figure 4.3: Parameters of the bilinear constitutive equation.

4.2.3 Criterion for damage propagation

The propagation criterion for delamination growth under mixed-mode loading conditions is established in terms of energy release rates and fracture toughness. The criterion is based on the work of Benzeggagh and Kenane [124], and was originally defined for mixed-mode I and II:

$$\mathcal{G}_c = \mathcal{G}_{Ic} + (\mathcal{G}_{IIc} - \mathcal{G}_{Ic}) \left(\frac{\mathcal{G}_{II}}{\mathcal{G}_I + \mathcal{G}_{II}} \right)^{\eta} \tag{4.15}$$

where $\mathcal{G}_{Ic}$ and $\mathcal{G}_{IIc}$ are the fracture toughness in mode I and II, respectively; $\mathcal{G}_I$ and $\mathcal{G}_{II}$ are the energy release rates in mode I and II, respectively. The η parameter is found by least-square fit of experimental data points of fracture toughnesses under different mixed-mode ratios.

The propagation criterion can be rewritten as follows:

$$\mathcal{G}_c = \mathcal{G}_{Ic} + (\mathcal{G}_{shear_c} - \mathcal{G}_{Ic}) \left(\frac{\mathcal{G}_{shear}}{\mathcal{G}_I + \mathcal{G}_{shear}} \right)^{\eta} \tag{4.16}$$

where $\mathcal{G}_{shear}$ and $\mathcal{G}_{shear_c}$ are the shear energy release rate and the pure mode II fracture toughness, respectively. The expressions of $\mathcal{G}_{shear}$ and $\mathcal{G}_{shear_c}$ are defined by Equations (4.17) and (4.18), respectively [105].

$$\mathcal{G}_{shear} = \mathcal{G}_{II} + \mathcal{G}_{III} \tag{4.17}$$

$$\mathcal{G}_{shear_c} = \mathcal{G}_{IIc} \, (= \mathcal{G}_{IIIc}) \tag{4.18}$$

Equation (4.17) is valid whenever the constitutive equations of modes II and III are equal. This hypothesis is very common because the fracture toughness of mode III is difficult to obtain and typically it is considered equal to $\mathcal{G}_{IIc}$.

On the other hand, Equation (4.18) ensures that the propagation criterion is consistent for pure mode loading cases II or III. As in the case of Equation (4.17), Equation (4.18) means that the constitutive equations for mode II and III are equal.

The ratio of the second term of Equation (4.16) defines the parameter B:

$$B = \frac{\mathcal{G}_{shear}}{\mathcal{G}_I + \mathcal{G}_{shear}} \tag{4.19}$$

The mixed-mode ratio β defined by Turon et al. [120] is given by:

$$\beta = \frac{\Delta_{shear}}{\langle \Delta_3 \rangle + \Delta_{shear}} \tag{4.20}$$

However, the definition of β is changed by Equation (4.21), which allows the B parameter to be equal to β by developing Equation (4.19) and considering the same penalty stiffness for all propagation modes.

$$\beta = \frac{\Delta_{shear}^2}{\langle \Delta_3 \rangle^2 + \Delta_{shear}^2} = \frac{\Delta_{shear}^2}{\lambda^2} \tag{4.21}$$

Finally, the propagation criterion defined in relative displacement terms can be obtained by means of Equation (4.16) and by knowing that the crack propagates when the fracture energy release rate is equal to the critical value. In other words, by using Equation (4.22) (deduced by means of Equation (4.16) and Equation (4.23)), the propagation criterion yields to Equation (4.24).

$$\mathcal{G}_c(\beta) = \frac{1}{2} K \Delta_3^o \Delta_3^f + \left(\frac{1}{2} K \Delta_{shear}^o \Delta_{shear}^f - \frac{1}{2} K \Delta_3^o \Delta_3^f \right) \beta^\eta \tag{4.22}$$

$$\mathcal{G}_c(\beta) = \frac{1}{2} K \Delta^o \Delta^f \tag{4.23}$$

$$\Delta^f = \frac{\Delta_3^o \Delta_3^f + \left(\Delta_{shear}^o \Delta_{shear}^f - \Delta_3^o \Delta_3^f \right) \beta^\eta}{\Delta^o} \tag{4.24}$$

Δ_3^o and Δ_{shear}^o are the relative displacements for damage onset in pure mode I and shear mode respectively, and Δ_3^f and Δ_{shear}^f are the relative displacements for damage propagation in pure mode I and shear mode respectively. The parameter Δ^o is the displacement for damage onset, and it is determined by means of the damage initiation criterion. Normally, the damage propagation criterion is formulated independently of the initiation criterion. However, Equation (4.24) shows that both criteria are linked in this model.

4.2.4 Criterion for damage onset

In this model, the criterion for damage onset is assumed the same as the applied criterion for damage propagation. This means that the onset damage criterion is also based on energy terms, which is a different characteristic of the usual cohesive damage formulations where a stress-based criterion is used. The models that account for the interaction of the stress components are usually based on Ye criterion [125].

However, experimental data of material strengths for the initiation of delamination under mixed-mode loading are not really available, and consequently, these failure criteria do not have been fully validated.

Therefore, by replacing in Equation (4.16) only the elastic energy terms of the constitutive equation, Equation (4.25) is obtained which is finally equalled to Equation (4.26) in order to find the criterion for damage onset defined in terms of relative displacements (Equation (4.27)).

$$\mathcal{G}^o(\beta) = \frac{1}{2}K\left(\Delta_3^o\right)^2 + \left(\frac{1}{2}K\left(\Delta_{shear}^o\right)^2 - \frac{1}{2}K\left(\Delta_3^o\right)^2\right)\beta^\eta \tag{4.25}$$

$$\Psi^o(\beta) = \frac{1}{2}K\left(\Delta^o\right)^2 \tag{4.26}$$

$$\Delta^o = \left(\left(\Delta_3^o\right)^2 + \left(\left(\Delta_{shear}^o\right)^2 - \left(\Delta_3^o\right)^2\right)\beta^\eta\right)^{\frac{1}{2}} \tag{4.27}$$

4.3 Formulation adaptations

Having formulated a cohesive model for zero-thickness elements, the required modifications to enable also the use of non-zero-thickness elements (i.e. continuum elements) are described in this section.

4.3.1 Relation between relative displacements and strains

If a continuum element is used, the input data are not the relative displacements, but the strain tensor. Therefore, to model a cohesive continuum model with softening, the relative displacement Δ_i and the corresponding strain component ε_{ij} can be related by means of the expression:

$$\Delta_i = h_e \varepsilon_{ij} n_j \left(2 - \delta_{3i}\right); \qquad i, j = 1,\, 2,\, 3 \tag{4.28}$$

where h_e is the element thickness, and n_j is the corresponding component of the unitary normal vector to the crack plane, $\mathbf{n} = \{0, 0, 1\}^T$ (see Figure 4.2).

As explained in the model formulation, the area under the constitutive equation g_e defined by stresses and relative displacements is directly the fracture toughness

of the material $\mathcal{G}_c$. However, if the constitutive model is defined in terms of stresses and strains, the law has to be adjusted in function of the element thickness h_e. Then, the resultant area g_e is the dissipated energy by unit of volume at the corresponding integration point of the finite element. This energy is equal to the fracture toughness of the material divided by the finite element thickness (see Equation (4.29)). This approach follows the called Crack Band Model suggested by Bažant and Oh [126], which is the procedure normally used to ensure the correct energy dissipation and mesh independency in continuum damage models.

$$\mathcal{G}_c A_{crack} = g_e \left(A_{crack} h_e\right) \quad \Rightarrow \quad g_e = \frac{\mathcal{G}_c}{h_e} \tag{4.29}$$

The dissipated energies for each case are illustrated in Figure 4.4.

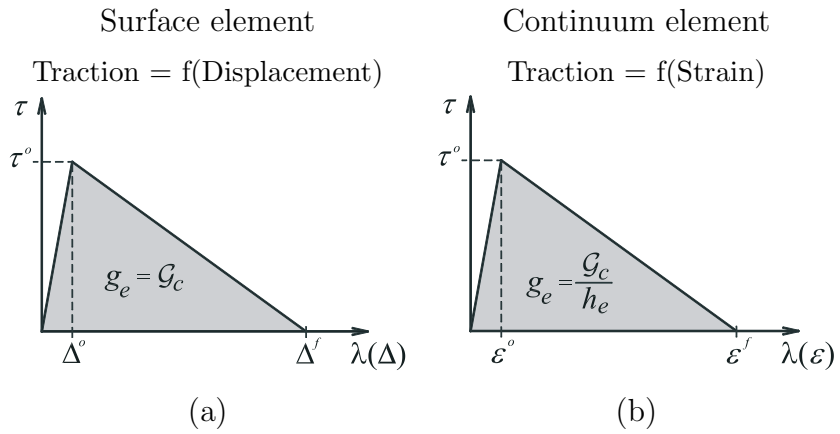

Figure 4.4: Constitutive charts defined by: (a) stresses and relative displacements, or by (b) stresses and strains.

4.3.2 Penalty stiffness

If cohesive volumetric elements are used, the penalty stiffness is here varied in function of the mixed-mode ratio. Its definition can be done in function of the element thickness and the elastic properties of the modeled interface material [102]. In particular, Equation (4.30) defines the penalty stiffness for pure mode I, and Equation (4.31) defines the penalty stiffness for pure modes II or III (shear):

$$K_1 = \frac{E_m}{h_e} \tag{4.30}$$

$$K_2 = \frac{G_m}{h_e} \tag{4.31}$$

where E_m is the Young modulus and G_m is the shear elastic modulus of the interface material. Normally, the elastic properties of the interface material are considered as the neat material, although it is generally not true [111].

For surface cohesive elements, the penalty stiffness is selected with a fixed value for all mixed-mode ratios. Ideally, the value of the penalty stiffness is infinite because these elements do not have thickness, and then they do not affect the compliance of the whole structure [127]. However, too high value of the interface stiffness can generate numerical problems such as the generation of spurious oscillations in the tractions of the element [101]. Therefore, a suitable value of the penalty stiffness should be selected in order to provide a reasonable stiffness without generating numerical problems. Based in mechanical considerations, Turon et al. [128] proposed Equation (4.32) in order to estimate the interface stiffness K for mode I crack propagation.

$$K = \frac{\alpha E_{33}}{h_a} \tag{4.32}$$

where E_{33} is the elastic modulus through-the-thickness of the composite material, α is an increasing parameter (normally it is taken about $\alpha \approx 50$), and h_a is the laminate thickness adjoining to the cohesive element. Equation (4.32) also can be developed for shear modes, by replacing E_{33} by the shear elastic modulus. However, since the model formulation for surface elements assumes the same penalty stiffness for each mixed-mode ratio, Equation (4.32) is used for all cases because it gives the biggest value.

4.3.3 Redefined onset and propagation damage criteria

Since the penalty stiffness for the volumetric elements is a function of the mixed-mode ratio, the onset and propagation damage criteria written in terms of relative displacements must be redefined. However, the procedure used in Sections 4.2.3

and 4.2.4 to find these expressions can not be exactly applied here because the function which describes the variation of the penalty stiffness under a determined mixed-mode ratio is unknown.

In order to find the onset criterion, Equation (4.33) is used. This equation is the damage criterion with the corresponding elastic energy terms replaced (i.e. Equation (4.25) with different penalty stiffness for pure mode I and pure shear mode). On the other hand, Equation (4.34) represents the elastic energy of the constitutive equation defined in terms of relative displacements of pure mode I, $\Delta_3^o(\beta)$, and pure shear mode, $\Delta_{shear}^o(\beta)$, for damage onset in a determined mixed-mode ratio.

$$\mathcal{G}^o(\beta) = \frac{1}{2}K_1\left(\Delta_3^o\right)^2 + \left(\frac{1}{2}K_2\left(\Delta_{shear}^o\right)^2 - \frac{1}{2}K_1\left(\Delta_3^o\right)^2\right)B^\eta \tag{4.33}$$

$$\Psi^o(\beta) = \frac{1}{2}K_1\left\langle\Delta_3^o(\beta)\right\rangle^2 + \frac{1}{2}K_2\left(\Delta_{shear}^o(\beta)\right)^2 \tag{4.34}$$

Using Equation (4.33) and (4.34), and the selected definition of the mixed-mode ratio (Equation (4.21)), the terms $\Delta_3^o(\beta)$ and $\Delta_{shear}^o(\beta)$ can be found:

$$\left\langle\Delta_3^o(\beta)\right\rangle = \left(\frac{2\mathcal{G}^o(\beta)}{K_1 + \left(\frac{\beta}{1-\beta}\right)K_2}\right)^{\frac{1}{2}} \tag{4.35}$$

$$\Delta_{shear}^o(\beta) = \left(\frac{\beta}{1-\beta}\right)^{\frac{1}{2}}\left\langle\Delta_3^o(\beta)\right\rangle \tag{4.36}$$

Finally, the onset damage criterion is obtained by taking the Euclidian norm of the relative displacements described by Equations (4.35) and (4.36) (see Section 4.2.1):

$$\Delta^o = \left(\left\langle\Delta_3^o(\beta)\right\rangle^2 + \left(\Delta_{shear}^o(\beta)\right)^2\right)^{\frac{1}{2}} \tag{4.37}$$

In the same sense, the propagation damage criterion can be deduced. In this case, Equation (4.38) represents the damage criterion with the corresponding pure fracture toughness terms replaced (i.e. Equation (4.22) with different penalty stiffness for pure mode I and pure shear mode). On the other hand, Equation (4.39) is the fracture toughness for a given mixed-mode ratio defined in terms of relative

displacements for damage onset in pure modes I and shear, $\Delta_3^o(\beta)$ and $\Delta_{shear}^o(\beta)$, and for damage propagation, $\Delta_3^f(\beta)$ and $\Delta_{shear}^f(\beta)$.

$$\mathcal{G}_c(\beta) = \frac{1}{2}K_1\Delta_3^o\Delta_3^f + \left(\frac{1}{2}K_2\Delta_{shear}^o\Delta_{shear}^f - \frac{1}{2}K_1\Delta_3^o\Delta_3^f\right)B^\eta \tag{4.38}$$

$$\mathcal{G}_c(\beta) = \frac{1}{2}K_1\left\langle\Delta_3^o(\beta)\right\rangle\left\langle\Delta_3^f(\beta)\right\rangle + \frac{1}{2}K_2\left(\Delta_{shear}^o(\beta)\right)\left(\Delta_{shear}^f(\beta)\right) \tag{4.39}$$

where $\Delta_3^o(\beta)$ and $\Delta_{shear}^o(\beta)$ are previously found by means of Equations (4.35) and (4.36).

Equalling Equations (4.38) and (4.39), and using again the definition of the mixed-mode ratio (Equation (4.21)), the terms $\Delta_3^f(\beta)$ and $\Delta_{shear}^f(\beta)$ can be found:

$$\left\langle\Delta_3^f(\beta)\right\rangle = \frac{K_1(1-B^\eta)\Delta_3^o\Delta_3^f + K_2B^\eta\Delta_{shear}^o\Delta_{shear}^f}{\left\langle\Delta_3^o(\beta)\right\rangle\left(K_1 + \left(\frac{\beta}{1-\beta}\right)K_2\right)} \tag{4.40}$$

$$\Delta_{shear}^f(\beta) = \left(\frac{\beta}{1-\beta}\right)^{\frac{1}{2}}\left\langle\Delta_3^f(\beta)\right\rangle \tag{4.41}$$

Finally, the propagation damage criterion is obtained by making the Euclidian norm of the relative displacements described by Equations (4.40) and (4.41) (see Section 4.2.1):

$$\Delta^f = \left(\left\langle\Delta_3^f(\beta)\right\rangle^2 + \left(\Delta_{shear}^f(\beta)\right)^2\right)^{\frac{1}{2}} \tag{4.42}$$

It should be noted that the B parameter must be redefined by Equation (4.43), since the penalty stiffnesses in pure mode I and shear modes are different and then they can not be simplified.

$$B = \frac{K_2\beta}{K_2\beta + K_1(1-\beta)} \tag{4.43}$$

If Equations (4.30) and (4.31) are replaced in Equation (4.43), the B parameter can be also defined in function of the elastic properties considered for the interface material. That is:

$$B = \frac{G_m\beta}{G_m\beta + E_m(1-\beta)} \tag{4.44}$$

4.4 Model implementation

4.4.1 Strategy of implementation

The delamination model presented by Turon et al. [120] was implemented in a user-written element subroutine called UEL [110]. This implementation was used to simulate problems in an implicit finite element code. However, the model formulated in Sections 4.2 and 4.3 is here implemented in a user-written material subroutine, called VUMAT, assigned for explicit finite element analysis.

The user material implemented has to be defined on sets of elements which represent the delamination layers. These elements can be zero-thickness (i.e. surface elements) or non-zero-thickness (i.e. continuum elements) types. In particular, when a zero-thickness interface is used, in-plane cohesive elements with four integration points of the Abaqus element library must be used [108]. This element is called COH3D8. However, when non-zero-thickness interface is desired, any tridimensional solid element can be applied.

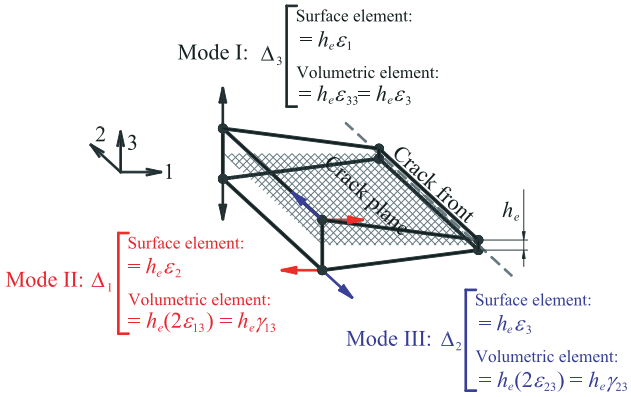

Figure 4.5: Transformations from strains to relative displacements for each propagation mode.

When surface elements are used, the input data given by the finite element software to the user material subroutine is directly the increment of the relative displacement vector, whereas the input data for continuum elements is the increment of the strain tensor. In order to use the same subroutine for both element types, Equation (4.28) is applied to transform easily the corresponding strain tensor components to relative displacements (see Figure 4.5). On the other hand, if surface

elements are used, a constitutive thickness equal to the unity has to be introduced in the user material subroutine which ensures that the strains are equal to the relative displacements.

4.4.2 Input variables to define the model

The parameters required to define completely the model in a user material subroutine are described below:

- Elastic properties (isotropic) and density of the interface material: E_m, ν_m and ρ_m.
  By means of E_m and ν_m the value of G_m can be calculated by using Equation (4.45). If surface elements are used, normally the value of E_m is taken between 10^5 and 5 x 10^6Nmm^{-3} for a sub-laminate thickness between 0.125mm and 5mm [128], and the Poisson coefficient ν_m must be equal to -0.5 in order to obtain the same penalty stiffness for all mixed-mode ratios.

$$G_m = \frac{E_m}{2\,(1+\nu_m)} \tag{4.45}$$

- Thickness of the interface cohesive element: h_e.
  If surface elements are used, the value of the constitutive thickness introduced in the subroutine must be equal to the unity (although the geometrical thickness defined in the model is equal to zero).

- Interface strengths for pure mode I and pure shear modes (II and III): τ_3^o and τ_1^o.
  By means of the interface strengths, the relative displacements which give the damage onset for pure mode loading cases are obtained. The corresponding equations are:

$$\Delta_3^o = \frac{\tau_3^o}{K_1} \tag{4.46}$$

$$\Delta_{shear}^o = \frac{\tau_1^o}{K_2} \tag{4.47}$$

- Interface fracture toughness for pure mode I and shear modes (II and III): $\mathcal{G}_{Ic}$ and $\mathcal{G}_{IIc}$.
  The relative displacements which give the damage propagation for pure mode loading cases are obtained by means of pure mode fracture toughnesses. The corresponding equations are:

$$\Delta_3^f = \frac{2\mathcal{G}_{Ic}}{K_1 \Delta_3^o} = \frac{2\mathcal{G}_{Ic}}{\tau_3^o} \tag{4.48}$$

$$\Delta_{shear}^f = \frac{2\mathcal{G}_{IIc}}{K_2 \Delta_{shear}^o} = \frac{2\mathcal{G}_{IIc}}{\tau_1^o} \tag{4.49}$$

- Parameter of the least-square fit: η.
  The experimental data used to calculate η can be obtained from MMB tests (Mixed-Mode Bending) at different mode ratios.

In a recent paper of Turon et al. [129], it was detected that changes in the local mode ratio during the evolution of damage under mixed-mode loading can cause errors in the determination of the energy dissipation and result in inaccurate predictions of the global load-displacement response. This fact occurs even under conditions where, according to Linear Elastic Fracture Mechanics, the global mode ratio is constant (e.g. Mixed-Mode Bending Test (MMB)). This is a common difficulty in current formulations of the cohesive models. To solve this problem, an engineering solution which relates the interlaminar strengths was proposed. It was demonstrated that this relation yields to accurate predictions which ensures correct energy dissipations when delamination propagates. This relation is defined as:

$$\tau_1^o = \tau_3^o \sqrt{\frac{\mathcal{G}_{IIc}}{\mathcal{G}_{Ic}}} \tag{4.50}$$

Therefore, seven input parameters are necessary in order to fed on the present cohesive model: E_m, ν_m, ρ_m, h_e, τ_3^o, $\mathcal{G}_{Ic}$ and $\mathcal{G}_{IIc}$.

4.4.3 Algorithm

After to read the input parameters and to calculate the model constants (see previous Sections 4.3.2 and 4.4.2), the steps of the algorithm which are repeated for each

stable time increment δt are numbered below:

1. Calculate the strain components at time $t + \delta t$.

$$\varepsilon_{i_{t+\delta t}} = \varepsilon_{i_t} + \delta\varepsilon_{i_{t+\delta t}} \begin{cases} i = 1, ..., 3 & \text{surface element} \\ i = 1, ..., 6 & \text{volumetric element} \end{cases} \tag{4.51}$$

2. Calculate the relative displacements at time $t + \delta t$ for each propagation mode (see Figure 4.5).

$$\text{Mode I:} \quad \Delta_{3_{t+\delta t}} = \begin{cases} h_e\varepsilon_{1_{t+\delta t}} & \text{surface element} \\ h_e\varepsilon_{3_{t+\delta t}} & \text{volumetric element} \end{cases} \tag{4.52}$$

$$\text{Mode II:} \quad \Delta_{1_{t+\delta t}} = \begin{cases} h_e\varepsilon_{2_{t+\delta t}} & \text{surface element} \\ h_e\gamma_{13_{t+\delta t}} & \text{volumetric element} \end{cases} \tag{4.53}$$

$$\text{Mode III:} \quad \Delta_{2_{t+\delta t}} = \begin{cases} h_e\varepsilon_{3_{t+\delta t}} & \text{surface element} \\ h_e\gamma_{23_{t+\delta t}} & \text{volumetric element} \end{cases} \tag{4.54}$$

3. Application of the damage model, where the following terms are calculated:

$$\Delta_{shear_{t+\delta t}} = \sqrt{\left(\Delta_{1_{t+\delta t}}\right)^2 + \left(\Delta_{2_{t+\delta t}}\right)^2} \tag{4.55}$$

$$\lambda_{t+\delta t} = \sqrt{\left\langle \Delta_{3_{t+\delta t}} \right\rangle^2 + \left(\Delta_{shear_{t+\delta t}}\right)^2} \tag{4.56}$$

$$\beta_{t+\delta t} = \frac{\Delta^2_{shear_{t+\delta t}}}{\left\langle \Delta_{3_{t+\delta t}} \right\rangle^2 + \Delta^2_{shear_{t+\delta t}}} \tag{4.57}$$

$$B_{t+\delta t} = \frac{K_2\beta_{t+\delta t}}{K_2\beta_{t+\delta t} + K_1\left(1 - \beta_{t+\delta t}\right)} \tag{4.58}$$

$$\left\langle \Delta^o_3\left(\beta\right)\right\rangle_{t+\delta t} = \left(\frac{K_1\left(1 - B^\eta_{t+\delta t}\right)\left(\Delta^o_3\right)^2 + K_2 B^\eta_{t+\delta t}\left(\Delta^o_{shear}\right)^2}{K_1 + \left(\frac{\beta_{t+\delta t}}{1-\beta_{t+\delta t}}\right)K_2} \right)^{\frac{1}{2}} \tag{4.59}$$

$$\left\langle \Delta_3^f(\beta) \right\rangle_{t+\delta t} = \frac{K_1\left(1 - B_{t+\delta t}^{\eta}\right)\Delta_3^o\Delta_3^f + K_2 B_{t+\delta t}^{\eta}\Delta_{shear}^o\Delta_{shear}^f}{\langle \Delta_3^o(\beta)\rangle_{t+\delta t}\left(K_1 + \left(\frac{\beta_{t+\delta t}}{1-\beta_{t+\delta t}}\right)K_2\right)} \tag{4.60}$$

$$\left(\Delta_{shear}^o(\beta)\right)_{t+\delta t} = \left(\frac{\beta_{t+\delta t}}{1-\beta_{t+\delta t}}\right)^{\frac{1}{2}} \langle \Delta_3^o(\beta)\rangle_{t+\delta t} \tag{4.61}$$

$$\left(\Delta_{shear}^f(\beta)\right)_{t+\delta t} = \left(\frac{\beta_{t+\delta t}}{1-\beta_{t+\delta t}}\right)^{\frac{1}{2}} \left\langle \Delta_3^f(\beta) \right\rangle_{t+\delta t} \tag{4.62}$$

$$\Delta_{t+\delta t}^o = \left(\langle \Delta_3^o(\beta)\rangle_{t+\delta t}^2 + \left(\Delta_{shear}^o(\beta)\right)_{t+\delta t}^2\right)^{\frac{1}{2}} \tag{4.63}$$

$$\Delta_{t+\delta t}^f = \left(\left\langle \Delta_3^f(\beta) \right\rangle_{t+\delta t}^2 + \left(\Delta_{shear}^f(\beta)\right)_{t+\delta t}^2\right)^{\frac{1}{2}} \tag{4.64}$$

$$G\left(\boldsymbol{\Delta}_{t+\delta t}\right) = \min\left\{\frac{\Delta_{t+\delta t}^f\left(\lambda_{t+\delta t} - \Delta_{t+\delta t}^o\right)}{\lambda_{t+\delta t}\left(\Delta_{t+\delta t}^f - \Delta_{t+\delta t}^o\right)}, 1\right\} \tag{4.65}$$

- If $G\left(\boldsymbol{\Delta}_{t+\delta t}\right) \leq d_t \quad \Rightarrow \quad d_{t+\delta t} = d_t$: elastic reloading, unloading or neutral loading.
- If $G\left(\boldsymbol{\Delta}_{t+\delta t}\right) > d_t \quad \Rightarrow \quad d_{t+\delta t} = G\left(\boldsymbol{\Delta}_{t+\delta t}\right)$: loading.

4. Calculate the stress vector at time $t + \delta t$:

$$\tau_{t+\delta t} = C_{t+\delta t}\varepsilon_{t+\delta t} \tag{4.66}$$

where:

- For surface elements:

$$C_{t+\delta t} = \begin{bmatrix} \left(1 - d_{t+\delta t}^*\right)E_m & 0 & 0 \\ 0 & \left(1 - d_{t+\delta t}\right)G_m & 0 \\ 0 & 0 & \left(1 - d_{t+\delta t}\right)G_m \end{bmatrix} \tag{4.67}$$

where:

$$d^*_{t+\delta t} = d_{t+\delta t}\frac{\left\langle \varepsilon_{1_{t+\delta t}} \right\rangle}{\left| \varepsilon_{1_{t+\delta t}} \right|} \tag{4.68}$$

- For volumetric elements:

$$C_{t+\delta t} = \begin{bmatrix} \frac{E_m\left(1-\left(1-d^*_{t+\delta t}\right)\nu_m^2\right)}{\Upsilon} & -\frac{\nu_m E_m\left(-1-\left(1-d^*_{t+\delta t}\right)\nu_m\right)}{\Upsilon} \\ -\frac{\nu_m E_m\left(-1-\left(1-d^*_{t+\delta t}\right)\nu_m\right)}{\Upsilon} & \frac{E_m\left(1-\left(1-d^*_{t+\delta t}\right)\nu_m^2\right)}{\Upsilon} \\ \frac{\nu_m E_m\left(1-d^*_{t+\delta t}\right)}{\Phi} & \frac{\nu_m E_m\left(1-d^*_{t+\delta t}\right)}{\Phi} \\ 0 & 0 \\ 0 & 0 \\ 0 & 0 \end{bmatrix}$$

$$\begin{bmatrix} \frac{\nu_m E_m\left(1-d^*_{t+\delta t}\right)}{\Phi} & 0 & 0 & 0 \\ \frac{\nu_m E_m\left(1-d^*_{t+\delta t}\right)}{\Phi} & 0 & 0 & 0 \\ -\frac{E_m\left(1-d^*_{t+\delta t}\right)(1-\nu_m)}{\Phi} & 0 & 0 & 0 \\ 0 & G_m & 0 & 0 \\ 0 & 0 & \left(1-d_{t+\delta t}\right)G_m & 0 \\ 0 & 0 & 0 & \left(1-d_{t+\delta t}\right)G_m \end{bmatrix} \tag{4.69}$$

where:

$$\Phi = 1 - 2\nu_m^2\left(1-d^*_{t+\delta t}\right) - \nu_m \tag{4.70}$$

$$\Upsilon = 1 - 2\nu_m^3\left(1-d^*_{t+\delta t}\right) - \nu_m^2\left(3-2d^*_{t+\delta t}\right) \tag{4.71}$$

$$d^*_{t+\delta t} = d_{t+\delta t}\frac{\left\langle \varepsilon_{3_{t+\delta t}} \right\rangle}{\left| \varepsilon_{3_{t+\delta t}} \right|} \tag{4.72}$$

5. Calculate the energy dissipated at time $t + \delta t$:

$$\mathcal{D}_{t+\delta t} = \mathcal{D}_t + \mathcal{D}_{\Delta t} \tag{4.73}$$

where $\mathcal{D}_t$ and $\mathcal{D}_{\delta t}$ are the accumulated and the increment of the dissipated energy, respectively. The determination of $\mathcal{D}_{\delta t}$ is given by Equation (4.74):

$$\mathcal{D}_{\delta t} = \frac{1}{2}\left(\frac{d_{t+\delta t} - d_t}{\Delta t}\right)\left(K_1\left(\Delta^2_{3_{t+\delta t}} + \Delta_{3_{t+\delta t}}\left\langle -\Delta_{3_{t+\delta t}}\right\rangle\right) + \right.$$

$$\left. + K_2\left(\Delta^2_{1_{t+\delta t}} + \Delta^2_{2_{t+\delta t}}\right)\right) \tag{4.74}$$

6. Calculate the free energy at time $t + \delta t$:

$$\Psi_{t+\delta t} = \frac{1}{2}\left((1 - d_{t+\delta t})\left(K_2\left(\Delta^2_{1_{t+\delta t}} + \Delta^2_{2_{t+\delta t}}\right) + K_1\left(\Delta^2_{3_{t+\delta t}}\right)\right) - \right.$$

$$\left. - d_{t+\delta t} K_1\left(\Delta_{3_{t+\delta t}}\left\langle -\Delta_{3_{t+\delta t}}\right\rangle\right)\right) \tag{4.75}$$

7. Calculate the internal energy at time $t + \delta t$:

$$U_{t+\delta t} = \Psi_{t+\delta t} + \mathcal{D}_{t+\delta t} \tag{4.76}$$

4.5 Sizes of cohesive elements

4.5.1 Maximum thickness of volumetric cohesive elements

For each mixed-mode ratio there is a maximum thickness of the cohesive elements in the direction perpendicular to the crack propagation plane. This is due to the fact that the propagation criterion defined in terms of relative displacements remains constant and the onset criterion changes whether the element thickness changes. The reason of the onset criterion changes is due to the introduction of penalty stiffness dependency with element thickness (see Equations (4.30) and (4.31)). Since the onset criterion should be reached before the propagation criterion, equalizing both criteria for a given mixed-mode ratio β, the maximum cohesive thickness $(h_e)_{max}$ is obtained. The resulting equation which defines the maximum thickness of the cohesive element is:

$$(h_e)_{max} = \frac{2\left(\mathcal{G}_{Ic} + \left(\mathcal{G}_{IIc} - \mathcal{G}_{Ic}\right) B^{\eta}\right)}{\frac{\left(\tau_3^o\right)^2}{E_m} + \left(\frac{\left(\tau_1^o\right)^2}{G_m} - \frac{\left(\tau_3^o\right)^2}{E_m}\right) B^{\eta}} \tag{4.77}$$

By means of Equation (4.77) it is possible to plot the variation of the maximum cohesive element thickness as a function of the mixed-mode ratio, which is included in parameter B by Equation (4.44). Taken into account the material properties shown in Tables 4.2 and 4.3, the evolution of the maximum thickness is plotted in Figure 4.6.

Equation (4.77) can also be obtained by using the onset and propagation criteria defined in terms of strains. In this case, the onset criterion remains constant versus the variations of the thickness, whereas the propagation criterion changes in order to assess the correct energy dissipation independently of the mesh size.

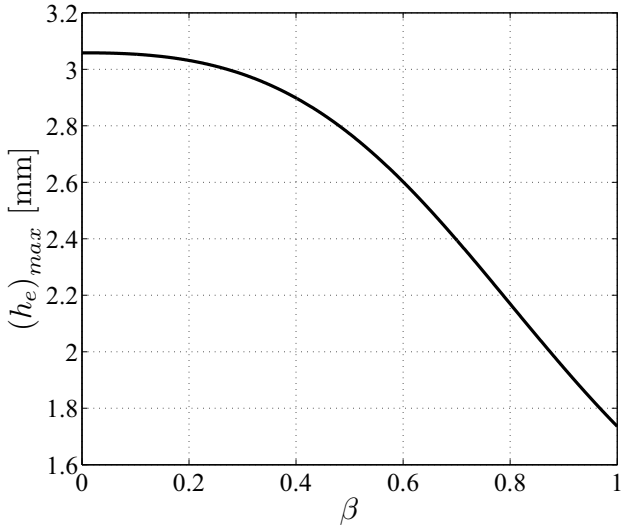

Figure 4.6: Evolution of the maximum element thickness in function of the mixed-mode ratio.

Normally, the cohesive element thickness is defined with a small value (e.g. between 0.001 and 0.1mm) and certainly the value used will be smaller than the maximum value given by Equation (4.77).

Using again the material properties shown in Tables 4.2 and 4.3, the variation of the onset criterion of the constitutive equation defined in terms of relative displacements and the variation of the propagation criterion of the constitutive equation

chart defined in terms of strains are shown in Figure 4.7. These charts correspond to the simulations in one element with constant in-plane dimensions under pure mode I loading.

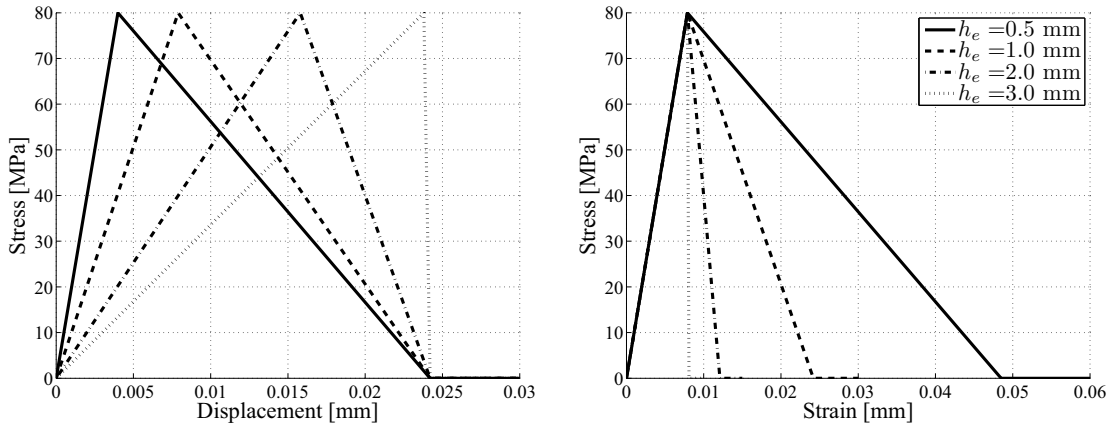

(a) (b)

Figure 4.7: Constitutive equation charts defined by (a) relative displacements and (b) strains in function of the element thickness.

4.5.2 In-plane dimensions of the cohesive elements

The in-plane dimensions of the cohesive elements are selected following the considerations and equations proposed by Turon et al. [128]. In particular, the in-plane dimensions are defined by means of the cohesive zone length l_{cz}, which is a material and structural property [130]. It is defined as the distance from the crack front until the point with the maximum interface strength τ^o. To obtain suitable results by using cohesive zone models, the tractions in the cohesive zone have to be represented correctly by a proper number of elements.

The model that will be used in this work in order to predict the length of the cohesive zone was proposed by Rice [131], and reads:

$$l_{cz} = \frac{9\pi}{32} E_m \frac{\mathcal{G}_c(\beta)}{\left(\tau^o(\beta)\right)^2} \tag{4.78}$$

where E_m is the Young modulus, and $\mathcal{G}_c(\beta)$ and $\tau^o(\beta)$ are the fracture toughness and the maximum strength of the interface for a given mixed-mode ratio, respectively.

The length of the cohesive elements l_e is easily calculated by means of:

$$l_e = \frac{l_{cz}}{N_e} \tag{4.79}$$

where N_e is the number of elements in the cohesive zone. Normally, the smallest value of the cohesive zone length resulted from the different values of mixed-mode ratio is used, and it is recommended to apply at least three or four elements in order to describe the cohesive zone accurately.

4.6 Simulations

This section presents the application of cohesive elements in the simulation of interlaminar fracture tests of composite specimens under quasi-static loading conditions. These tests allow the validation of the damage model presented without consider the interaction with other damage mechanisms which can appear inside the plies, because the damage is normally concentrated in interfaces where only delamination occurs.

Mixed-Mode Bending (MMB) and End-Notched Flexure (ENF) tests of unidirectional zero degree lay-up specimens with an initial pre-crack are considered (see Section 4.6.2). The MMB allows to test any mixed-mode case except pure mode II, which is obtained by the ENF test. The cases simulated are $B = 0.0$ (pure mode I), $B = 0.2$, $B = 0.5$, $B = 0.8$ and $B = 1.0$ (pure mode II). It should be noted that only non-zero-thickness elements have been used in all the simulations considered, which represent a resin-rich interface layer.

Different mixed-mode analysis at one finite element were simulated previously in order to check that the predicted dissipated energy at each integration point is equal to the corresponding fracture toughness adjusted by the least square fit of experimental data points of the selected material (see Table 4.3).

Simulations of quasi-static Transverse Crack Tension tests (TCT) of unidirectional zero degree lay-up specimens are also shown (see Section 4.6.3). The TCT test is an alternative to the ENF test, which determines pure mode II interlaminar fracture toughness [132].

Finally, the numerical considerations in order to carry out quasi-static simulations by using an explicit finite element code are explained in detail.

4.6.1 Considerations for quasi-static explicit simulations

The proposed simulations are solved by means of an explicit finite element code. As it has been explained in the introduction, the explicit integration schemes determine a solution to the dynamic equilibrium of the global set equations by explicitly advancing the kinematic state from the previous time increment, without solving simultaneously equations and without iterating for each time increment. For this reason, the formulation of the tangent stiffness tensor is not derived here since no iterations are carried out.

Static problems have a large time solution, which often it is unworkable to analyze the simulation in its real scale of time using an explicit code because requires an excessive number of stable small increments of time. To obtain a faster solution, the event should be accelerated in some way, but ensuring that the inertial forces remain insignificant. There are some actions to alter one or more of the factors influencing the time increment. The action here considered for increasing the efficiency of the proposed simulations is to scale the mass density of these critical elements (i.e. mass scaling). In order to control the proposed simulations, the kinetic energy and the internal energy are monitored in order to keep the kinetic energy less than 5% of the internal energy of the system.

On the other hand, the loading velocity should be such that the solution obtained is close to the real static solution and the dynamic effects remain insignificant. In an approximate way, the maximum loading velocity v_L can be estimated by means of:

$$v_L < 0.01\sqrt{\frac{E_m}{\rho_m}} \tag{4.80}$$

The loading velocity defined in all the simulations is 0.5mm/s, which is much lower than the maximum value given by Equation (4.80) (see interface properties in Tables 4.3 and 4.6).

Quasi-static analysis in explicit algorithms require the application of loading as smooth as possible. Sudden movements cause stress waves, which can introduce noisy or inaccurate results. Applying the load in the smoothest possible manner requires that the acceleration changes only a small amount from one time increment to the next. Then, if the acceleration is smooth, it follows that the changes in

velocity and displacement are also smooth. This option can be defined easily in Abaqus software by selecting a smooth amplitude table of loading in all the proposed simulations. By defining it, Abaqus software connects automatically each of the user data pairs of loading with curves, whose first and second derivatives are smooth, and whose values are zero at each of user loading data points.

It has to be noted that the selected mass scaling factor for critical elements is considerably high (i.e. approximately 1.0^3). However, since the boundary displacements are applied in a smooth manner and in a large time scale, the kinetic energy and the inertial forces of the model remain small.

Finally, the cohesive elements which reach the maximum damage value at their integration points are deleted from the mesh. These deleted elements have no ability to carry stresses and, therefore, have no contribution to the stiffness of the model. This action avoids large distortions of the damaged elements, and possible spurious stress transfer to the bodies around them. However, if damaged elements are deleted, penetration between the joined laminates can occur, mainly in tests with high percentage of mode II. To avoid it, a contact pair surfaces without friction have been defined between the two laminate surfaces that were initially linked by the cohesive elements.

4.6.2 MMB and ENF fracture toughness tests

The simulations of quasi-static MMB and ENF tests of unidirectional zero degree lay-up specimens are analyzed in this section.

Test configurations

The loading conditions in the MMB simulations are defined by means of the linear Equation (4.81) which relates the displacements in three different points of the specimen [105]:

$$\delta_{LP} = \left(\frac{c}{L}\right)\delta_I + \left(\frac{c+L}{L}\right)\delta_M \tag{4.81}$$

where L is the half specimen length and c is the length from the loading point LP to the middle point M of the specimen. The different mixed-mode cases are generated by modifying the length c, which reads:

$$c = \frac{L\left(\frac{1}{2}\sqrt{3\left(\frac{1-B}{B}\right)}+1\right)}{3-\frac{1}{2}\sqrt{3\left(\frac{1-B}{B}\right)}} \tag{4.82}$$

In Figure 4.8.a are marked the points LP, M, and I where the displacements are prescribed.

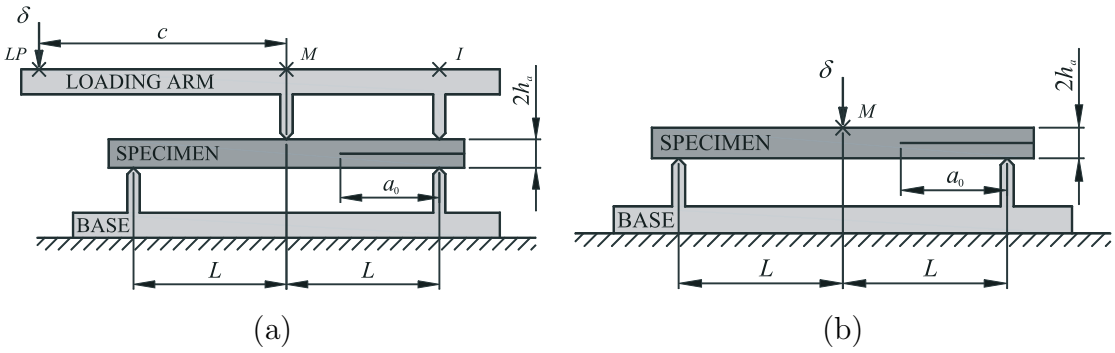

Figure 4.8: Sketches of the (a) MMB test and (b) ENF test configurations.

The loading conditions of the ENF test are also defined by displacements. Just as indicates Figure 4.8.b, it is applied a displacement in the middle point M of the specimen.

The numerical results are compared with experimental data performed by Reeder and Crews [133–135] to validate the model. These results are presented in a force-displacement chart. For the MMB test, the results are read at point LP, and in point M for the ENF test.

Sizes and types of the elements

An 8-node solid element with reduced integration (one integration point) is used to model the laminates and volumetric cohesive elements. This element is called C3D8R. For all simulations, each laminate thickness is modeled by four elements, which is enough to capture accurately the laminate rotations during the simulations. The thickness defined for the interface elements is 0.01mm, which is much smaller than the value obtained by means of Equation (4.77) (see Figure 4.6).

On the other hand, the in-plane length of the cohesive element is determined by Equations (4.78) and (4.79). If three elements are desired to be along the cohe-

sive length, the maximum in-plane length at the crack propagation direction is of 0.45mm. The length finally used is 0.3mm for all the simulations. It is not necessary to define a small length element at width specimen direction because the crack propagates on the opposite direction. Therefore, the specimen width is modeled by using only two elements.

Materials and specimen dimensions

The material used is a thermoplastic matrix-based reinforced by unidirectional carbon fibers (AS4/PEEK). The properties are set in Table 4.1:

E_{11} [MPa]	$E_{22} = E_{33}$ [MPa]	$G_{12} = G_{13}$ [MPa]	G_{23} [MPa]	$\nu_{12} = \nu_{13}$	ν_{23}	ρ [tmm^{-3}]
122700	10100	5500	3700	0.25	0.45	1600e-12

Table 4.1: AS4/PEEK properties.

The material properties defined to the interface elements are summarized in Table 4.2, and are selected by considering that these elements represent a resin-rich layer. The pure mode fracture toughnesses of the interface are written in Table 4.3. The shear strength τ_1^o is defined by means Equation (4.50), which yields to 106MPa.

E_m [MPa]	ν_m	ρ_m [tmm^{-3}]	τ_3^o [MPa]
10100	0.3	1600e-12	80

Table 4.2: Interface properties.

$\frac{\mathcal{G}_{II}}{\mathcal{G}_T}$	0%	20%	50%	80%	100% (ENF)
$\mathcal{G}_c$ [N/mm]	0.969	1.103	1.131	1.376	1.719
a_o [mm]	32.9	33.7	34.1	31.4	39.2

Table 4.3: Fracture toughnesses of the interface for different mixed-mode ratios [134, 135].

The parameter η is taken 2.284, which is obtained by means of a least-square fit of the experimental data shown in Table 4.3.

The specimen dimensions are: 102mm long, 25.4mm wide, and each laminate arm is 1.56mm thick.

Results

The force-displacement relations obtained in the experiments and in the finite element simulations of the MMB test for each proposed mixed-mode case: $B = 0.0$ (pure mode I), $B = 0.2$, $B = 0.5$, and $B = 0.8$ are respectively shown in Figures 4.9, 4.10, 4.11, and 4.12. The results of the ENF test ($B = 1.0$, pure mode II) are shown in Figure 4.13.

The corresponding analytical expressions for MMB test with $B = 0.0$ (pure mode I) and ENF test which give the relationship of the critical load and the displacement during propagation are also plotted in the corresponding figures. These equations are set in Table 4.4, and are deduced by using Linear Elastic Fracture Mechanics and Simple Beam Theory [136, 137]. In these equations, E_{11} is the longitudinal elastic modulus of the specimen, a is the crack length, and b, h_a and L are the width, the arm height and the half length of the specimen, respectively.

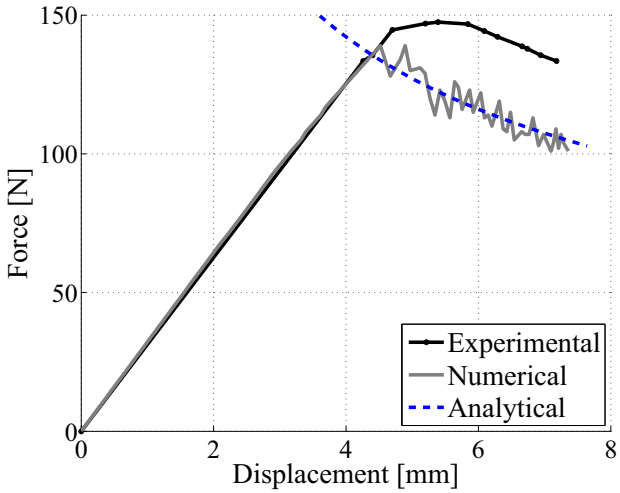

Figure 4.9: Experimental and numerical force-displacement relation of the MMB test $B = 0.0$ (pure mode I).

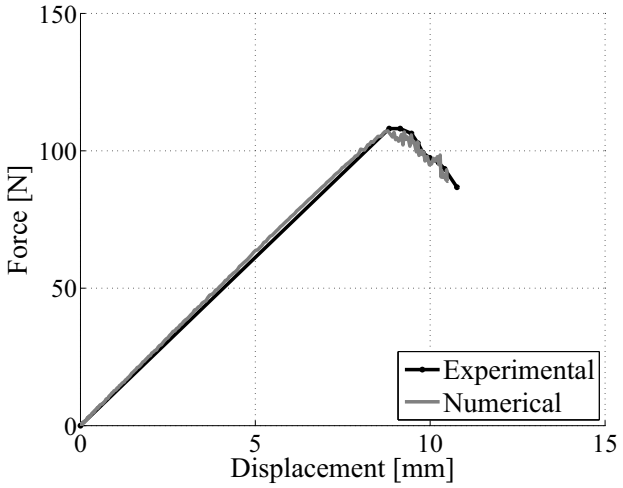

Figure 4.10: Experimental and numerical force-displacement relation of the MMB test $B = 0.2$.

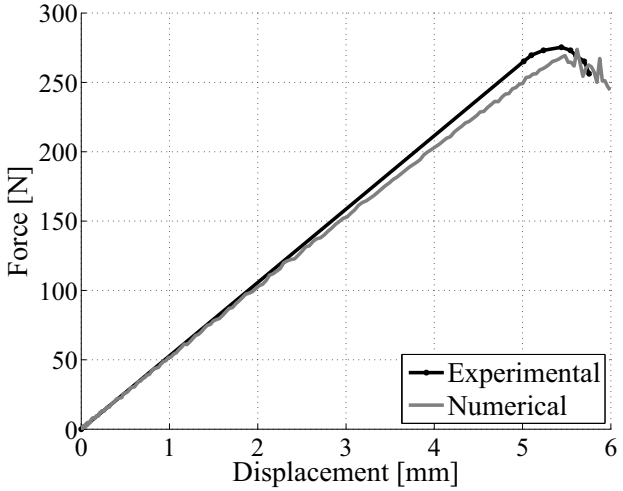

Figure 4.11: Experimental and numerical force-displacement relation of the MMB test $B = 0.5$.

Discussion

The charts obtained by numerical simulations of the proposed tests are in a good agreement with the experimental data. The predicted case of $B = 0.0$ (pure mode I) is the most far of the corresponding experimental chart. This difference is not due to limitations of the numerical simulations, but rather to the fact that the experimental

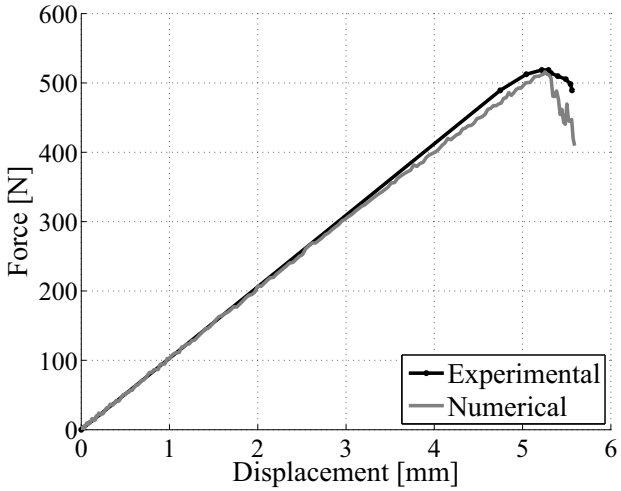

Figure 4.12: Experimental and numerical force-displacement relation of the MMB test $B = 0.8$.

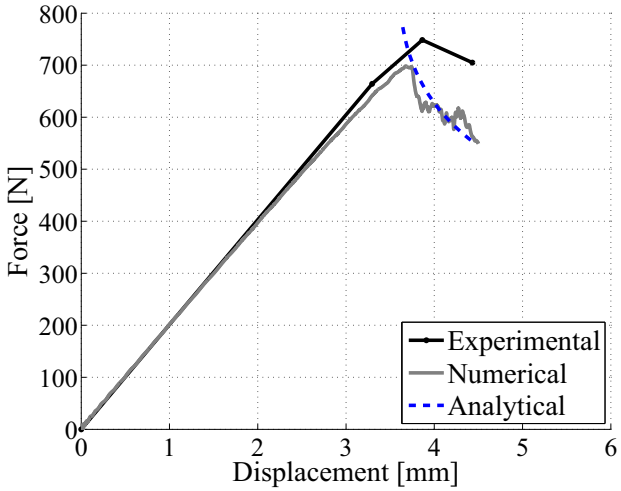

Figure 4.13: Experimental and numerical force-displacement relation of the ENF test (pure mode II).

fracture toughness used corresponds to the onset delamination and not to the propagation, which is normally larger than the onset fracture toughness. The analytical model which gives the relationship of the critical load and the displacement during propagation is plotted. The fracture toughness specified is $\mathcal{G}_c = 0.969\text{N/mm}$ (see Table 4.3), and the numerical curve shows an excellent correlation with the descend-

Test	Critical load	Compliance
MMB: ($B = 0.0$)	$P_c = \sqrt{\frac{E_{11} b^2 h_a^3 \mathcal{G}_{Ic}}{12a^2}}$	$C = \frac{8a^3}{E_{11} b h_a^3}$
ENF ($B = 1.0$)	$P_c = \sqrt{\frac{16 E_{11} b^2 h_a^3 \mathcal{G}_{IIc}}{9a^2}}$	$C = \frac{3a^3 + 2L^3}{8 E_{11} b h_a^3}$

Table 4.4: Analytical equations of MMB test with $B = 0.0$, and ENF test ($B = 1.0$).

ing part of the analytical load-displacement curve. On the other hand, the analytical model corresponding to the ENF test with a fracture toughness of $\mathcal{G}_c = 1.719$N/mm (see Table 4.3) is plotted in Figure 4.13, which also shows a good agreement between the analytical load-displacement curve and the numerical prediction.

Once the delamination is initiated, oscillations are observed in all predictions. However, the amplitude of these oscillations has been reduced by increasing the mesh refinement and by reducing the loading velocity. Other possibility allowed for propagation tests which was not shown here is to reduce the interface strength. In part, the oscillations which appear in a quasi-static explicit simulation may be a consequence of the constitutive equation shape. For implicit simulations, the shape of the constitutive equation does not affect to the results, whenever the fracture toughness is correctly accounted and the initial stiffness and maximum traction are reasonably consistent with the stiffness and strength of the material being modeled. However, in quasi-static explicit simulations, the shape has an important role for the stability simulation. The equation used has two discontinuities, one at initiation damage onset and other in the damage propagation. In some cases, stress waves appear at these points whose generate high frequency vibrations that break the cohesive element at the neighborhood. Therefore, an attractive solution is to use constitutive equation shapes without discontinuities [107].

4.6.3 TCT tests

The simulations of quasi-static Transverse Crack Tension tests (TCT) of unidirectional zero degree lay-up specimens are analyzed in this section.

Configuration of the TCT tests

The TCT specimens are manufactured by continuous fiber laminates with unidirectional stacking order whose central plies are cut prior to curing, as shown in Figure 4.14. When these specimens are loaded by tension, delaminations develop under pure mode II. Such laminates are referred by $[0_m, \emptyset_n]_S$, where the slash indicates the cut plies.

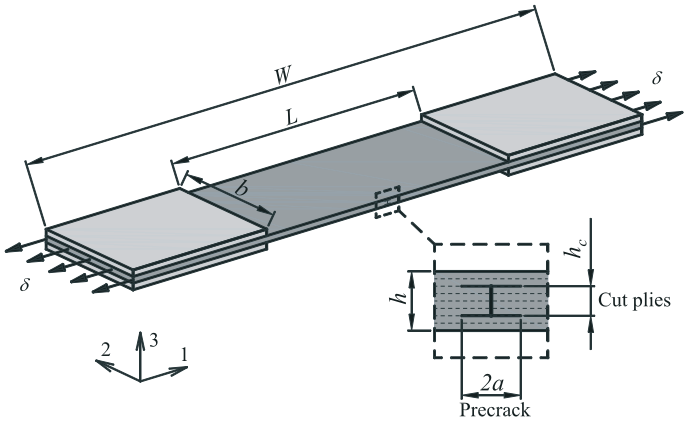

Figure 4.14: : TCT specimen.

The TCT specimens can be tested with or without pre-cracks previously induced. The specimens with pre-cracks are those undergoing a determined number of fatigue cycles at near-threshold loading for delamination growth. For no pre-cracked specimens, the gap between cut plies is a resin rich region which delaminates under pure mode I. Next, at certain load level, delamination starts at the corner point between cut and continuous plies along the fiber direction and quickly develops under pure mode II to certain length or full-scale. For pre-cracked specimens, this predelamination phase is not experimented since small initial interface cracks are previously created [138]. Consequently, the resulting critical load and fracture toughness are more representative in these specimens than for no pre-cracked specimens.

The TCT test is then an alternative to the ENF test [139]. It is assumed that in the TCT test there is less sliding friction between the delaminated plies than in the ENF test. A second advantage concerns compliance calibration for data reduction. The compliance of the TCT specimen is less sensitive to the error in crack length measurement, because the compliance is related linearly to the crack length a (see

Equation (4.83)), whereas for the ENF specimen the compliance is related to a^3 (see Table 4.4).

$$C = \frac{L\,(h - h_c) + 2ah_c}{bh\,(h - h_c)\,E_{11}} \tag{4.83}$$

E_{11} is the longitudinal elastic modulus of the specimen, a is the length of one crack, and h_c is the whole thickness of cut central plies. The geometrical variables L, b and h are the length, width, and total thickness of the specimen, respectively.

From the evaluation of the compliance C and the delamination length a, the fracture toughness $\mathcal{G}_{IIc}$ can be derived for a constant specimen width b as:

$$\mathcal{G}_{IIc} = \frac{1}{4} \cdot \frac{h_c P_c^2}{b^2 E_{11} h\,(h - h_c)} \tag{4.84}$$

The factor 1/4 is introduced because there are four crack tips. Equation (4.84) shows that $\mathcal{G}_{IIc}$ can be obtained by determining solely the critical load P_c.

Only non pre-cracked specimens are simulated. The laminates considered are: $[0_2, \emptyset_4]_S$, $[0_4, \emptyset_4]_S$ and $[0_4, \emptyset_8]_S$. The numerical results obtained are basically the critical load P_c for delamination propagation, and are compared with experimental values performed by Ye et al. [138].

Sizes and types of the elements

Two delamination planes are modeled in the TCT specimens, as shown in Figure 4.15. One corresponds to the interface of the cut central plies which delaminates under pure mode I, and is modeled by using zero-thickness type elements with four integration points of the Abaqus element library (i.e. COH3D8). The other delamination plane corresponds to the interface between cut and continuous plies along the fiber direction which delaminates under pure mode II. In this case, the interface is modeled by using non-zero-thickness type elements with reduced integration (i.e. C3D8R). The thickness defined for this interface is 0.01mm, which is much smaller than the value obtained by means of Equation (4.77). The in-plane length of these elements at the crack propagation direction is determined by means of Equations (4.78) and (4.79). If three elements are desired to be along the cohesive length, the maximum in-plane length is of 0.37mm. The length finally used is 0.33mm.

The specimen width is meshed with five elements, and each ply thickness with two elements. The composite material is modeled by using also C3D8R elements. Only half thickness of the specimen is modeled by defining symmetric boundary conditions.

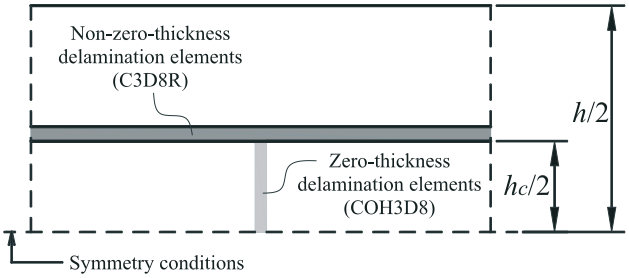

Figure 4.15: Detail of the location of the cohesive elements.

Materials and specimen dimensions

The composite material used is an epoxy matrix-based reinforced by unidirectional carbon fibers (T300/914C). The properties are extracted from Ye et al. [138] and set in Table 4.5.

The material properties defined to the interface elements located between cut and continue plies are shown in Table 4.6, and are selected by considering that these elements represent a resin-rich layer. The fracture toughness $\mathcal{G}_{IIc}$ is obtained by testing pre-cracked TCT specimens. For zero-thickness cohesive elements the properties are equal than those set in Table 4.6 except the elastic modulus (i.e. penalty stiffness) which is set 10^6, and in order to obtain the same penalty stiffness for all propagation modes the Poisson modulus is set equal to -0.5. The shear strength τ_1^o is defined by means Equation (4.50), which yields to 83MPa.

E_{11} [MPa]	$E_{22} = E_{33}$ [MPa]	$G_{12} = G_{13}$ [MPa]	G_{23} [MPa]	$\nu_{12} = \nu_{13}$	ν_{23}	ρ [tmm^{-3}]
129000	9256	5000	3306	0.28	0.4	1600e-12

Table 4.5: T300/914C properties.

The parameter η is approached to 1.47, which is obtained by means of least-square fit of mixed-mode fracture toughnesses obtained in MMB tests [139]. The

E_m [MPa]	ν_m	ρ_m [tmm^{-3}]	τ_3^o [MPa]	$\mathcal{G}_{Ic}$ [N/mm]	$\mathcal{G}_{IIc}$ [N/mm]
9256	0.3	1600e-12	50	0.17	0.467

Table 4.6: Interface properties.

dimensions of the specimens are: 140mm long (L), 20mm wide (b), and the ply thickness is approximately 0.125mm. The total length of the specimens is 380mm (W).

Results and discussion

The load-displacement relations obtained in the finite element simulations of each TCT specimen are plotted in Figure 4.16. These plots show a peak load which corresponds to the point where the interface of the cut central plies is completely damaged. Next, stationary load values appear after the drop of the peak loads (i.e. after the pre-delamination phase).

These stationary loads are the critical loads for pure mode II delamination of the interface between cut and continue plies. By means of Equation (4.84) and the numerical critical loads obtained, the fracture toughness $\mathcal{G}_{IIc}$ can be predicted. The results are set in Table 4.7 and show a good agreement with the value defined in the model: $\mathcal{G}_{IIc} = 0.467$N/mm. In addition, a comparison of the results shown in Table 4.7 indicates good correlation between the predicted peak loads and the corresponding experimental values.

Laminate	Experimental	Numerical		
	F_{peak} [N]	F_{peak} [N]	P_c [N]	$\mathcal{G}_{IIc}$ [N/mm]
$[0_2, \emptyset_4]_S$	8500	8963	8600	0.478
$[0_4, \emptyset_4]_S$	15219	14380	14200	0.488
$[0_4, \emptyset_8]_S$	14321	13080	12100	0.473

Table 4.7: Experimental and numerical results.

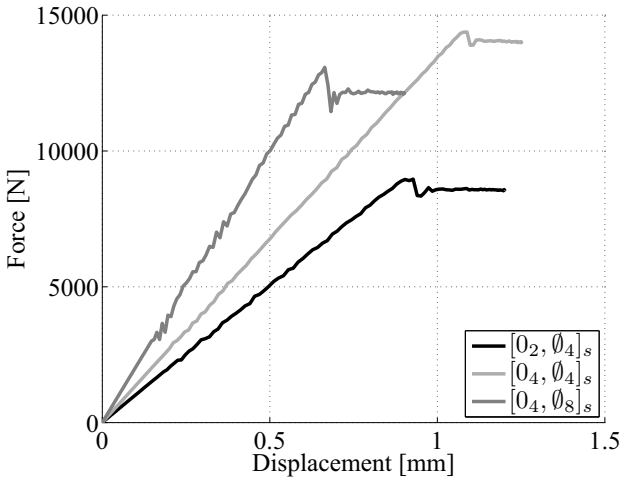

Figure 4.16: Numerical load-displacement relations for the TCT specimens.

4.7 Conclusions

The formulation and implementation of a thermodynamically consistent damage model for the simulation of progressive delamination in composite materials under variable mixed-mode ratio by using an explicit finite element code was presented. The model was formulated in the context of Damage Mechanics, and implemented by means of a user-written material subroutine. The user material can be defined on sets of elements that represent the possible location for delamination. The elements can be selected to have zero-thickness (surface elements) or non-zero-thickness (continuum elements).

The model was used to simulate the initiation and propagation of delamination in fracture toughness tests (MMB, ENF and TCT) under quasi-static loading conditions. The examples analyzed are in good agreement with the test results, and they indicate that the proposed formulation can predict the delamination process of composite structures that exhibit progressive delamination. It should be noted that some numerical predictions have shown some stability problems or oscillations which have been reduced significantly by increasing the mesh refinement and by reducing the loading velocity during the crack propagation process. However, these oscillations may be reduced even more by modifying the shape of the constitutive equation to one without discontinuity points.

To make use of the damage model implemented and of the explicit finite element code, the next step is to simulate low-velocity impacts of foreign objects on monolithic laminated composite plates, where the delamination generally propagates under variable mixed-mode conditions (see Chapter **??**). In these analysis, the study of the shape and extension of the delamination at interfaces between mismatch orientation plies is of great interest since the delamination reduces dramatically the damage tolerance of the structure. In order to carry out an accurately prediction, an intralaminar damage model must be added in these analysis (see Chapter **??**), since impact loading conditions creates intralaminar damage mechanisms which interact with the delamination failure mode.

Appendix A

Governing equations of the plate

In the present Appendix, the development of the governing equations of rectangular, flat and monolithic laminated composite plates under general loading is described. This development is widely studied in the bibliography and basically requires a knowledge of anisotropic elasticity, to select an appropriate plate theory that accounts for desired kinematics, and a method to formulate the equations. All the developments detailed in this Appendix are extracted from references Reddy [47], Ochoa and Reddy [149], Kollár and Springer [150], and Abrate [5].

As shown in Chapter 1, the governing equations of the plate for concentrated impact loading joined with the governing equation of the impactor, a suitable contact law, and a proper approximation of the unknown variables yield to typically called *complete analytical models* of the impact event [15], [7]. In these models, the most usually plate theories used in order to develop the governing equations are the *classical laminated plate theory* and the *first-order shear deformation plate theory*. These plate theories and the corresponding governing equations are explained in detail in the present Appendix.

Therefore, equations for calculating displacements, stresses, and strains are presented. Due to the configuration of the structure considered (see Figure A.1), two Cartesian coordinate systems are used in order to describe these equations: a global coordinate system (x, y, z) attached to a fixed reference point, and a local coordinate system (x_1, x_2, x_3) aligned, at a point, with the fibers of one lamina. The stress and strain notation conventions for each coordinate system are collected in Tables A.1 and A.2, respectively.

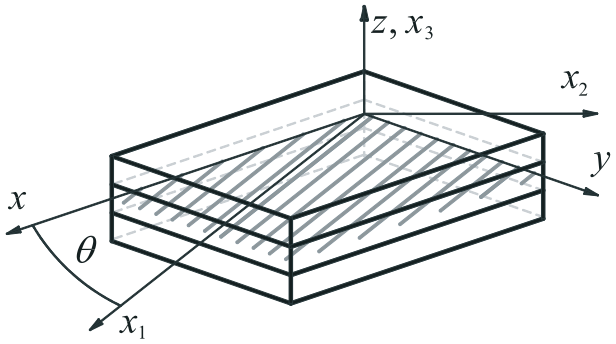

Figure A.1: Laminated composite plate and coordinate systems.

In the (x, y, z) coordinate system, the components of the displacement vector at one point are denoted by (u, v, w), and in (x_1, x_2, x_3) the displacement components are (u_1, u_2, u_3). The displacements of a point in the mid-plane of the plate are denoted by the subscript o.

	Normal stresses			Shear stresses		
(x, y, z) coordinate system						
Tensorial stress	σ_{xx}	σ_{yy}	σ_{zz}	σ_{yz}	σ_{xz}	σ_{xy}
Engineering stress	σ_x	σ_y	σ_z	τ_{yz}	τ_{xz}	τ_{xy}
Contracted notation	σ_x	σ_y	σ_z	σ_q	σ_r	σ_s
(x_1, x_2, x_3) coordinate system						
Tensorial stress	σ_{11}	σ_{22}	σ_{33}	σ_{23}	σ_{13}	σ_{12}
Engineering stress	σ_1	σ_2	σ_3	τ_{23}	τ_{13}	τ_{12}
Contracted notation	σ_1	σ_2	σ_3	σ_4	σ_5	σ_6

Table A.1: Stress notations.

A.1 Ingredients for the development of the equations

Before describing the classical laminated plate theory and the first-order shear deformation plate theory, the ingredients required for the development of these theories are presented in the following points.

	Normal strains			Shear strains		
(x, y, z) coordinate system						
Tensorial strain	ϵ_{xx}	ϵ_{yy}	ϵ_{zz}	ϵ_{yz}	ϵ_{xz}	ϵ_{xy}
Engineering strain	ϵ_x	ϵ_y	ϵ_z	γ_{yz}	γ_{xz}	γ_{xy}
Contracted notation	ϵ_x	ϵ_y	ϵ_z	ϵ_q	ϵ_r	ϵ_s
(x_1, x_2, x_3) coordinate system						
Tensorial strain	ϵ_{11}	ϵ_{22}	ϵ_{33}	ϵ_{23}	ϵ_{13}	ϵ_{12}
Engineering strain	ϵ_1	ϵ_2	ϵ_3	γ_{23}	γ_{13}	γ_{12}
Contracted notation	ϵ_1	ϵ_2	ϵ_3	ϵ_4	ϵ_5	ϵ_6

Table A.2: Strain notations. The engineering and contracted notation shear strains are twice the tensorial shear strain.

A.1.1 Strain-displacement relations

For full geometric nonlinear analysis, the components of the Green-Lagrange strain tensor referenced to a (x_1, x_2, x_3) Cartesian coordinate system are (sum on repeated subscript is implied):

$$\epsilon_{ij} = \frac{1}{2}\left(\frac{\partial u_i}{\partial x_j} + \frac{\partial u_j}{\partial x_i} + \frac{\partial u_m}{\partial x_i}\frac{\partial u_m}{\partial x_j}\right); \quad i, j, m = 1, 2, 3 \tag{A.1}$$

If the gradients of the displacements are so small that products of partial derivatives of u_i are negligible compared with linear derivative terms (i.e. first-order), the infinitesimal strain components are given by:

$$\epsilon_{ij} = \frac{1}{2}\left(\frac{\partial u_i}{\partial x_j} + \frac{\partial u_j}{\partial x_i}\right); \quad i, j = 1, 2, 3 \tag{A.2}$$

The plate problem that is considered here may involve moderate rotations, such as 10º-15º [149]. Hence, the following terms associated with rotations of transverse normals are small but not negligible:

$$\left(\frac{\partial u_3}{\partial x_1}\right)^2, \left(\frac{\partial u_3}{\partial x_2}\right)^2, \frac{\partial u_3}{\partial x_1}\frac{\partial u_3}{\partial x_2} \tag{A.3}$$

Using Equations (A.1) and the restriction (A.3), the called *von Kármán strain components* are obtained:

$$
\begin{aligned}
\epsilon_{11} &= \frac{\partial u_1}{\partial x_1} + \frac{1}{2}\left(\frac{\partial u_3}{\partial x_1}\right)^2 \\
\epsilon_{22} &= \frac{\partial u_2}{\partial x_2} + \frac{1}{2}\left(\frac{\partial u_3}{\partial x_2}\right)^2 \\
\epsilon_{33} &= \frac{\partial u_3}{\partial x_3} \\
\epsilon_{12} &= \frac{1}{2}\left(\frac{\partial u_1}{\partial x_2} + \frac{\partial u_2}{\partial x_1} + \frac{\partial u_3}{\partial x_1}\frac{\partial u_3}{\partial x_2}\right) \\
\epsilon_{13} &= \frac{1}{2}\left(\frac{\partial u_1}{\partial x_3} + \frac{\partial u_3}{\partial x_1}\right) \\
\epsilon_{23} &= \frac{1}{2}\left(\frac{\partial u_2}{\partial x_3} + \frac{\partial u_3}{\partial x_2}\right)
\end{aligned}
\tag{A.4}
$$

A.1.2 Lamina constitutive equation

The linear relation between the stress and strain components is known as the generalized Hooke law. Taking as the reference the Cartesian coordinate system (x_1, x_2, x_3), the Hooke law is expressed by:

$$\sigma_{ij} = c_{ijkl}\epsilon_{kl}; \quad i, j, k, l = 1, 2, 3 \tag{A.5}$$

where c_{ijkl} is the fourth-order stiffness tensor with 81 components. The fact that the stress and strain tensors are symmetric, it allows to write:

$$c_{ijkl} = c_{jikl} = c_{ijlk} = c_{jilk} \tag{A.6}$$

which effectively reduces the number of independent components from 81 to 36. The 36 independent components can be written as a second-order stiffness tensor which allows to rewrite Equation (A.5) in contracted notation (see Tables A.1 and A.2):

$$\sigma_i = C_{ij}\epsilon_j; \quad i, j = 1, 2, ..., 6 \tag{A.7}$$

On the other hand, by postulating the existence of a function called strain energy density it is possible to demonstrate that the stiffness tensor is symmetric $C_{ij} = C_{ji}$. Because of this symmetry, there are only 21 independent stiffness components for anisotropic materials.

As shown in Figure A.1, the structure configuration considered in the present thesis corresponds to laminated composite plates manufactured by stacking unidirectional fiber reinforced laminae with randomly distributed fibers in their cross section. The cross section of each lamina presents isotropy which allows to model each one as a transversely isotropic material (see Figure A.2). Therefore, the constitutive equation of a lamina is defined by:

$$\begin{Bmatrix} \sigma_1 \\ \sigma_2 \\ \sigma_3 \\ \sigma_4 \\ \sigma_5 \\ \sigma_6 \end{Bmatrix} = \begin{bmatrix} C_{11} & C_{12} & C_{12} & 0 & 0 & 0 \\ & C_{22} & C_{23} & 0 & 0 & 0 \\ & & C_{22} & 0 & 0 & 0 \\ & & & \hat{C} & 0 & 0 \\ & sym. & & & C_{66} & 0 \\ & & & & & C_{66} \end{bmatrix} \begin{Bmatrix} \epsilon_1 \\ \epsilon_2 \\ \epsilon_3 \\ \epsilon_4 \\ \epsilon_5 \\ \epsilon_6 \end{Bmatrix} \tag{A.8}$$

where $\hat{C} = (C_{22} - C_{23})/2$, and the stiffness coefficients are written as:

$$\begin{aligned} C_{11} &= \frac{(1-\nu_{23}^2)\,E_{11}}{(1+\nu_{23})\,(1-\nu_{23}-2\nu_{12}\nu_{21})}, \quad C_{12} = \frac{\nu_{12}\,(1+\nu_{23})\,E_{11}}{(1+\nu_{23})\,(1-\nu_{23}-2\nu_{12}\nu_{21})} \\ C_{22} &= \frac{(1-\nu_{12}\nu_{21})\,E_{22}}{(1+\nu_{23})\,(1-\nu_{23}-2\nu_{12}\nu_{21})}, \quad C_{23} = \frac{\nu_{23}+(\nu_{12}\nu_{21})\,E_{22}}{(1+\nu_{23})\,(1-\nu_{23}-2\nu_{12}\nu_{21})} \\ C_{66} &= G_{12} \end{aligned} \tag{A.9}$$

Only five elastic properties are required in order to define the constitutive relation of transversely isotropic materials. These properties are the longitudinal Young modulus (i.e. along the fiber direction) E_{11}, the transverse Young modulus E_{22}, the in-plane shear modulus G_{12}, the major in-plane Poisson coefficient ν_{12} (or minor ν_{21}) and the transverse Poisson coefficient ν_{23}.

The stiffness matrix C_{ij} depends on the coordinate system used. For the unidirectional lamina shown in Figure A.3, the fiber orientation is rotated θ degrees respect to the global coordinate system (x, y, z). The corresponding relationship between the stresses and strains at local and global coordinate system are defined by:

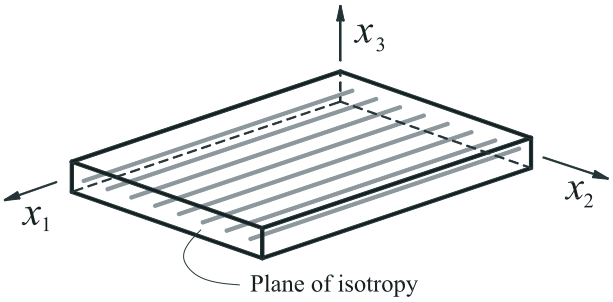

Figure A.2: Transverse isotropic lamina.

$$\begin{Bmatrix} \sigma_1 \\ \sigma_2 \\ \sigma_3 \\ \sigma_4 \\ \sigma_5 \\ \sigma_6 \end{Bmatrix} = [T] \begin{Bmatrix} \sigma_x \\ \sigma_y \\ \sigma_z \\ \sigma_q \\ \sigma_r \\ \sigma_s \end{Bmatrix}; \quad \begin{Bmatrix} \epsilon_1 \\ \epsilon_2 \\ \epsilon_3 \\ \epsilon_4 \\ \epsilon_5 \\ \epsilon_6 \end{Bmatrix} = [T]_\gamma \begin{Bmatrix} \epsilon_x \\ \epsilon_y \\ \epsilon_z \\ \epsilon_q \\ \epsilon_r \\ \epsilon_s \end{Bmatrix} \tag{A.10}$$

Letting $c = \cos(\theta)$ and $s = \sin(\theta)$, the rotation matrixes $[T]$ and $[T]_\gamma$ are defined as:

$$[T] = \begin{bmatrix} c^2 & s^2 & 0 & 0 & 0 & 2cs \\ s^2 & c^2 & 0 & 0 & 0 & -2cs \\ 0 & 0 & 1 & 0 & 0 & 0 \\ 0 & 0 & 0 & c & -s & 0 \\ 0 & 0 & 0 & s & c & 0 \\ -cs & cs & 0 & 0 & 0 & c^2 - s^2 \end{bmatrix} \tag{A.11}$$

$$[T]_\gamma = \left([T]^{-1}\right)^T \tag{A.12}$$

The constitutive equation for an off-axis lamina defined in the global coordinate system (x, y, z) is:

$$\begin{Bmatrix} \sigma_x \\ \sigma_y \\ \sigma_z \\ \sigma_q \\ \sigma_r \\ \sigma_s \end{Bmatrix} = \underbrace{[T]^{-1}[C][T]_\gamma}_{[\overline{C}]} \begin{Bmatrix} \epsilon_x \\ \epsilon_y \\ \epsilon_z \\ \epsilon_q \\ \epsilon_r \\ \epsilon_s \end{Bmatrix} \tag{A.13}$$

where $[C]$ is the second-order stiffness tensor written in matrix form referenced to the local coordinate system (x_1, x_2, x_3), and $[\overline{C}]$ is the stiffness tensor referenced to the global coordinate system (x, y, z).

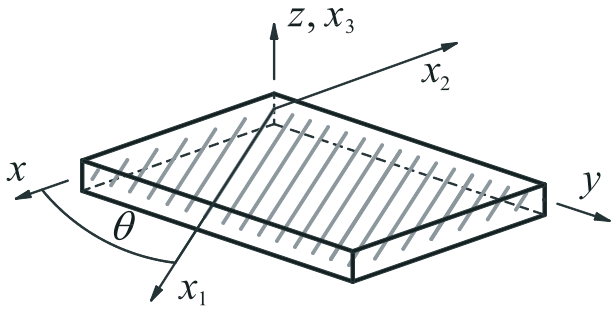

Figure A.3: Lamina coordinate systems.

A.1.3 Laminate resultants

Assuming unitary width in x and y axes, the resulting in-plane forces N_x, N_y, N_{xy} and through-the-thickness shear forces Q_x, Q_y, and in-plane moments M_x, M_y, M_{xy} of lamina p (see Figure A.4) can be calculated from equilibrium conditions as:

$$\begin{Bmatrix} N_x \\ N_y \\ N_{xy} \end{Bmatrix}_p = \int_{z_{p-1}}^{z_p} \begin{Bmatrix} \sigma_x \\ \sigma_y \\ \sigma_{xy} \end{Bmatrix}_p dz \tag{A.14}$$

$$\begin{Bmatrix} Q_x \\ Q_y \end{Bmatrix}_p = \int_{z_{p-1}}^{z_p} \begin{Bmatrix} \sigma_{xz} \\ \sigma_{yz} \end{Bmatrix}_p dz \tag{A.15}$$

$$\left\{\begin{array}{c} M_x \\ M_y \\ M_{xy} \end{array}\right\}_p = \int_{z_{p-1}}^{z_p} \left\{\begin{array}{c} \sigma_x \\ \sigma_y \\ \sigma_{xy} \end{array}\right\}_p z\,dz \tag{A.16}$$

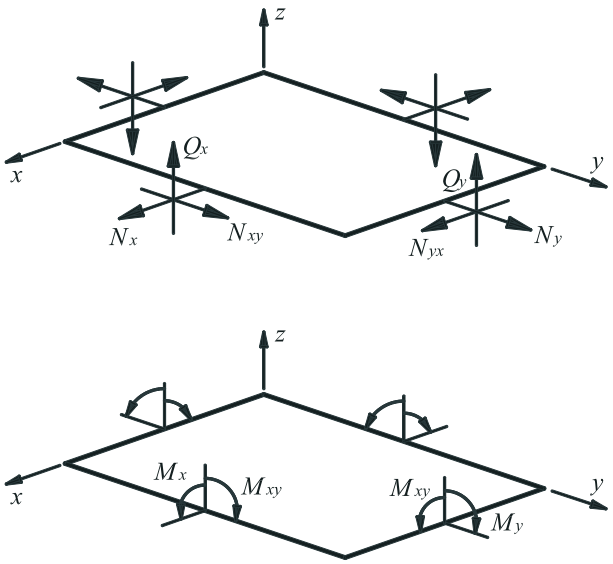

Figure A.4: Force and moment resultants on a lamina (or laminate).

where z_{p-1} and z_p are the thickness coordinates of the bottom and top of lamina p (see Figure A.5). The superposition of different laminae, with different fiber orientations or not, configures the laminate. For a laminate with N laminae, the resulting forces and moments are:

$$\left\{\begin{array}{c} N_x \\ N_y \\ N_{xy} \end{array}\right\} = \int_{-h/2}^{h/2} \left\{\begin{array}{c} \sigma_x \\ \sigma_y \\ \sigma_{xy} \end{array}\right\} dz = \sum_{p=1}^{N} \int_{z_{p-1}}^{z_p} \left\{\begin{array}{c} \sigma_x \\ \sigma_y \\ \sigma_{xy} \end{array}\right\}_p dz \tag{A.17}$$

$$\left\{\begin{array}{c} Q_x \\ Q_y \end{array}\right\} = \int_{-h/2}^{h/2} \left\{\begin{array}{c} \sigma_{xz} \\ \sigma_{yz} \end{array}\right\} dz = \sum_{p=1}^{N} \int_{z_{p-1}}^{z_p} \left\{\begin{array}{c} \sigma_{xz} \\ \sigma_{yz} \end{array}\right\}_p dz \tag{A.18}$$

$$\left\{\begin{array}{c} M_x \\ M_y \\ M_{xy} \end{array}\right\} = \int_{-h/2}^{h/2} \left\{\begin{array}{c} \sigma_x \\ \sigma_y \\ \sigma_{xy} \end{array}\right\} z\,dz = \sum_{p=1}^{N} \int_{z_{p-1}}^{z_p} \left\{\begin{array}{c} \sigma_x \\ \sigma_y \\ \sigma_{xy} \end{array}\right\}_p z\,dz \tag{A.19}$$

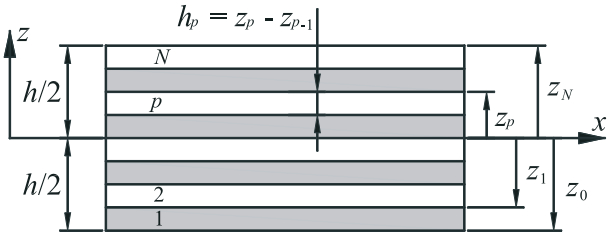

Figure A.5: Lamina location in a laminate.

A.1.4 Frameworks to develop the governing equations

The equations of motion (i.e. governing equations defined by displacement variables) of a solid body can be derived using either vector mechanics or energy principles. In vector mechanics, a representative volume element of the body is isolated with all its applied and reactive forces. Then, the vector sum of all static and dynamic forces and moments acting on the element is set to zero to obtain the equations. In methods based on energy principles, the total work done or energy stored in a body due to actual forces in moving through virtual displacements that are consistent with the essential (i.e. geometric) constrains of the body is set to zero to obtain the equations of motion. The energy approach also yield to the natural (i.e. force) boundary conditions as well as the form of the variables involved in the specification of geometric boundary conditions.

Principle of virtual displacements

The principle of virtual displacements states: *if a body is in static or dynamic equilibrium, the total virtual work done by all externally applied and internally generated forces in moving through their respective virtual displacements must be zero.* That is:

$$\delta W \equiv \delta W_I + \delta W_E = 0 \tag{A.20}$$

where δW is the total virtual work of the body, δW_I and δW_E are the internal and external virtual works, respectively. The delta symbol δ is used in conjunction with virtual displacements and forces, and it is interpreted as an operator called the *variational operator*. It is used to denote a variation (or change) in a given quantity.

The external work done due to virtual displacements $\delta\mathbf{u}$ in a solid body Ω subjected to body forces $\mathbf{f}$ per unit of mass and surface tractions $\mathbf{T}$ per unit area of the boundary Γ_σ is given by:

$$\delta W_E = -\int_\Omega \rho\mathbf{f}\cdot\delta\mathbf{u}\,dv - \int_{\Gamma_\sigma}\mathbf{T}\cdot\delta\mathbf{u}\,ds \tag{A.21}$$

where ρ is the density, ds denotes a surface element, dv denotes a volume element and Γ_σ denotes the portion of the boundary in which the stresses are specified. The negative sign of Equation (A.21) indicates that the work is performed on the body. The external virtual work can also be done due to virtual body forces and surface tractions, which yield to called *complementary virtual work*.

The forces applied on a deformable body cause it to deform and the body experiences internal stresses. The relative movement of the material particles in the body can be measured in terms of strains. Therefore, the work done on the body by external forces is responsible for the internal work. The internal virtual work is also called *virtual strain energy* and is expressed by:

$$\delta W_I = \delta U = \int_\Omega \sigma : \delta\epsilon\,dv \tag{A.22}$$

where σ is the stress tensor and $\delta\epsilon$ is the virtual strain tensor due to the virtual displacement $\delta\mathbf{u}$.

Replacing Equations (A.21) and (A.22), the principle of virtual work written in terms of Cartesian rectangular components yields to (sum on repeated subscripts is implied):

$$\int_\Omega \left(\sigma_{ij}\delta\epsilon_{ij} - \rho f_i\delta u_i\right)\,dv - \int_{\Gamma_\sigma} T_i\delta u_i\,ds = 0; \quad i,j = 1,2,3 \tag{A.23}$$

By means of the fundamental lemma of variational calculus [47], the principle of virtual works can be expressed by differential equations called *Euler-Lagrange equations*. These equations are the usually form used to write the governing equations.

Hamilton principle

The *Hamilton principle* states that *of all possible paths that a material particle could travel from its position at time t_1 to its position at time t_2, its actual path will be*

one for which the following integral is an extremum:

$$\int_{t_1}^{t_2} (K - W)\, dt \tag{A.24}$$

The difference between the kinetic and potential energies is called the *Lagrangian function*:

$$L = K - W = K - W_I - W_E \tag{A.25}$$

Thus, Hamilton principle can be expressed as:

$$\int_{t_1}^{t_2} (\delta K - \delta W_I - \delta W_E)\, dt = 0 \tag{A.26}$$

The kinetic energy of a continuous body Ω is given by:

$$K = \frac{1}{2} \int_{\Omega} \rho \frac{\partial \mathbf{u}}{\partial t} \cdot \frac{\partial \mathbf{u}}{\partial t}\, dv \tag{A.27}$$

where $\dfrac{\partial \mathbf{u}}{\partial t}$ denotes the velocity of the material particle.

Principle of minimum total potential energy

A special case of the principle of virtual displacements is the *principle of minimum total potential energy*. The difference between the principle of virtual displacements and the principle of minimum total potential energy is that, in the latter a constitutive law is invoked. Thus, the principle of virtual displacements is more general and it is applied to all material bodies independent of their constitutive behavior.

The sum $U + V = \Pi$ is called the *total potential energy* of the elastic body, where V is a potential equal to W_E and U is the strain energy which is equal to W_I. The principle of minimum total potential energy states that: *of all admissible displacements, those that satisfy the equilibrium equations make the total potential energy a minimum.* Thus, the principle of virtual work takes the form:

$$\partial U + \partial V \equiv \partial \Pi = 0 \tag{A.28}$$

The Euler-Lagrange equations resulting from the principle of virtual displacements are always in terms of the stresses or stress resultants, whereas those from

the principle of minimum total potential energy are in terms of the strains or displacements.

Variational methods

In general, exact solutions for the dynamic response of rectangular and flat plates with a certain boundary conditions are not available. Under these circumstances, methods known as *classical variational methods* can be applied (e.g. *Ritz method*; *Galerkin method*).

In variational methods it is seek an approximate solution to the problem in terms of adjustable parameters that are determined by substituting the assumed solution into the energy principle ($\partial W = 0$ or $\partial \Pi = 0$) that is equivalent to the governing equations of the problem. Such solution methods are called *direct methods* because the approximate solutions are obtained directly by applying the same energy principle that was used to derive the governing equations. The assumed solutions in the energy methods are in the form of a finite linear combination of undetermined parameters and appropriately chosen functions. Since the solution of a continuum problem, in general, cannot be represented by a infinite set of functions, error is introduced into the solution.

In the Ritz method, a dependent unknown displacement u is approximated by a finite linear combination U_N of the form:

$$u \approx U_N = \sum_{j=1}^{N} c_j \varphi_j + \varphi_0 \tag{A.29}$$

where φ_0 represents the particular solution, while $\sum c_j \varphi_j$ is the homogeneous part of the solution. c_j denote undetermined parameters and φ_j are called the *approximation functions* which are appropriately selected functions of position. In order to ensure that the algebraic equations resulting from the Ritz approximation have a solution which converges to the true solution of the problem as the number of parameters N is increased, the approximation functions have to satisfy some requirements:

1. $\varphi_j (j = 1, 2, \ldots, N)$ should satisfy the following three conditions:

(a) Each φ_j is continuous, as required in the variational statement (i.e. $\partial W = 0$ or $\partial\Pi = 0$).

(b) Each φ_j satisfies the homogeneous form of the specified essential boundary conditions.

(c) The set $\{\varphi_j\}$ is linearly independent and complete.

2. φ_0 has to satisfy only the specified essential boundary conditions associated with the variational formulation since the natural boundary conditions are included in the functional Π or the statement δW; φ_0 plays the role of the particular solution. It is necessarily equal to zero when the specified essential boundary conditions are homogeneous.

Once the approximation functions φ_0 and φ_j are selected, the parameters c_j in Equation (A.29) are determined by requiring U_N to minimize the total potential energy functional Π or satisfy the principle of virtual displacements of the problem.

For the principle of minimum total potential energy, upon substitution of the approximation $u \approx U_N$, $\Pi(U_N)$ becomes a function of $c_1, c_1, \ldots, c_N$. Hence, minimization of the functional $\Pi(c_1, c_1, \ldots, c_N)$ is reduced to the minimization of a function of several variables:

$$0 = \delta\Pi(U_N) = \sum_{j=1}^{N} \frac{\delta\Pi}{\delta c_j} c_j \quad \text{or} \quad \frac{\delta\Pi}{\delta c_j} = 0 \tag{A.30}$$

The same procedure applies to the principle of virtual displacements. That is:

$$0 = \delta W(U_N) = \sum_{j=1}^{N} \frac{\delta W}{\delta c_j} c_j \quad \text{or} \quad \frac{\delta W}{\delta c_j} = 0 \tag{A.31}$$

Equation (A.30) or (A.31) gives N algebraic equations in the N coefficients $(c_1, c_2, \ldots, c_N)$,

$$0 = \frac{\delta\Pi}{\delta c_j} = \sum_{j=1}^{N} R_{ij} c_j - F_i \quad \text{or} \quad \mathbf{Rc} = \mathbf{F} \tag{A.32}$$

where R_{ij} and F_i are known coefficients that depend on the problem parameters (e.g. geometry, material coefficients and loads) and the approximation functions.

Equation (A.32) is then solved for c_i and substituted back into Equation (A.29) to obtain the Ritz solution with N parameters.

A.2 Plate theories and governing equations

A plate is a structural element with planform dimensions that are large compared to its thickness and is subjected to loads that cause bending deformation in addition to stretching. Because of the smallness of thickness dimension, it is often not necessary to model them using 3-D elasticity equations. Simple 2D plate theories can be developed by making assumptions concerning the variation of the displacement field. Therefore, the *compatibility conditions* which provide single-valued solution of the displacements by means of the strain-displacement relations (i.e. Equations (A.1)) are not necessary since the displacements are directly assumed.

In this section only are shown the resulting governing equations for the *classical laminated plate theory* and for the *first-order shear plate theory*. These plate theories are the most easier and used in the literature in order to develop complete analytical impact models of laminated composite plates. Other more accurate plate theories can be used but are often dismissed since the development of the governing equations becomes algebraic complicated and their integration imply high computational effort without improving significantly the accuracy of the results.

A.2.1 Classical laminated plate theory

Displacement field and kinematics

The displacement field of the classical laminated plate theory is based on the *Kirchhoff-Love hypothesis*, which involve the following assumptions:

1. Straight lines perpendicular to the mid-plane (i.e. transverse normals) before deformations remain straight after deformation.

2. The transverse normals do not experience elongation (i.e. they are inextensible).

3. The transverse normals rotate such that they remain perpendicular to the mid-plane after deformation.

The first two assumptions of the hypothesis require that in-plane displacements u and v vary linearly through-the-thickness of the laminate, and the transverse displacement w is constant through-the-thickness of the laminate (see Figure A.6). That is:

$$\begin{aligned} u(x,y,z) &= u_o(x,y) + z\phi_1(x,y) \\ v(x,y,z) &= v_o(x,y) + z\phi_2(x,y) \\ w(x,y,z) &= w_o(x,y) \end{aligned} \tag{A.33}$$

where u_o, v_o, w_o are the displacement components of a point on the mid-plane of the laminate, ϕ_1 is the rotation of a transverse normal about the y axis, and ϕ_2 is the rotation of a transverse normal about the x axis. The third assumption of the Kirchhoff-Love hypothesis implies that the rotations ϕ_1 and ϕ_2 are equal to:

$$\phi_1 = -\frac{\partial w_o}{\partial x}; \quad \phi_2 = -\frac{\partial w_o}{\partial y} \tag{A.34}$$

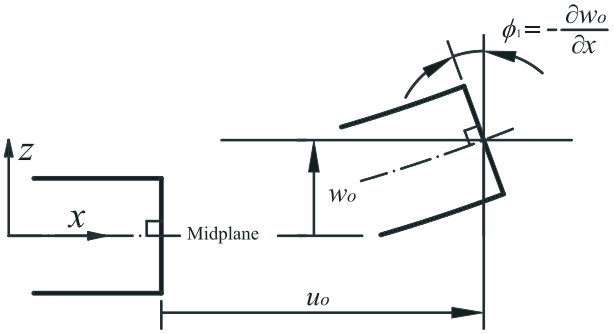

Figure A.6: Behavior of transverse section in classical plate theory.

Using the von Kármán strain-displacement relations (Equations (A.4)) referenced to the coordinate system (x, y, z) and the assumed displacement field (Equations (A.33) and (A.34)) the strain components yield to the following expressions:

$$
\begin{aligned}
\epsilon_x \equiv \epsilon_{xx} &= \frac{\partial u}{\partial x} + \frac{1}{2}\left(\frac{\partial w}{\partial x}\right)^2 = \frac{\partial u_o}{\partial x} + \frac{1}{2}\left(\frac{\partial w_o}{\partial x}\right)^2 - z\frac{\partial^2 w_o}{\partial x^2} \\
\epsilon_y \equiv \epsilon_{yy} &= \frac{\partial v}{\partial y} + \frac{1}{2}\left(\frac{\partial w}{\partial y}\right)^2 = \frac{\partial v_o}{\partial y} + \frac{1}{2}\left(\frac{\partial w_o}{\partial y}\right)^2 - z\frac{\partial^2 w_o}{\partial y^2} \\
\epsilon_z \equiv \epsilon_{zz} &= \frac{\partial w}{\partial z} = \frac{\partial w_o}{\partial z} = 0 \\
\epsilon_q \equiv 2\epsilon_{yz} &= \frac{\partial v}{\partial z} + \frac{\partial w}{\partial y} = -\frac{\partial w_o}{\partial y} + \frac{\partial w_o}{\partial y} = 0 \\
\epsilon_r \equiv 2\epsilon_{xz} &= \frac{\partial u}{\partial z} + \frac{\partial w}{\partial x} = -\frac{\partial w_o}{\partial x} + \frac{\partial w_o}{\partial x} = 0 \\
\epsilon_s \equiv 2\epsilon_{xy} &= \frac{\partial u}{\partial y} + \frac{\partial v}{\partial x} + \frac{\partial w}{\partial x}\frac{\partial w}{\partial y} = \frac{\partial u_o}{\partial y} + \frac{\partial v_o}{\partial x} + \frac{\partial w_o}{\partial x}\frac{\partial w_o}{\partial y} - 2z\frac{\partial^2 w_o}{\partial x \partial y}
\end{aligned}
\tag{A.35}
$$

The three assumptions considered lead to the neglect of the transverse strains ϵ_{xz}, ϵ_{yz} and ϵ_z. Neglecting these strains leads to the omission of σ_{xz}, σ_{yz} and σ_z. Thus the classical laminated plate theory does not account for out-of-plane deformations and stresses. This implies that plates are infinitely rigid in the transverse direction, whereas in reality laminated composite plates are weaker in this direction.

Equations (A.35) can be expressed in a general form by:

$$
\epsilon_i = \epsilon_i^o + z\kappa_i; \quad i = x, y, s \tag{A.36}
$$

The strains $\epsilon_i^o = \left(\epsilon_x^o, \epsilon_y^o, \epsilon_s^o\right)$ are associated with the in-plane stretching and shearing of the mid-plane, and are called the *membrane strains*. The quantities $\kappa_i = (\kappa_x, \kappa_y, \kappa_s)$ are the curvatures which multiplied by z gives the bending strains. Equations (A.35) shows that membrane strains and curvatures for the classic laminate plate theory have the following explicit form:

$$
\begin{aligned}
\epsilon_x^o &= \frac{\partial u_o}{\partial x} + \underline{\frac{1}{2}\left(\frac{\partial w_o}{\partial x}\right)^2}, & \kappa_x &= -\frac{\partial^2 w_o}{\partial x^2} \\
\epsilon_y^o &= \frac{\partial v_o}{\partial y} + \underline{\frac{1}{2}\left(\frac{\partial w_o}{\partial y}\right)^2}, & \kappa_y &= -\frac{\partial^2 w_o}{\partial y^2} \\
\epsilon_s^o &= \frac{\partial u_o}{\partial y} + \frac{\partial v_o}{\partial x} + \underline{\frac{\partial w_o}{\partial x}\frac{\partial w_o}{\partial y}}, & \kappa_s &= -2\frac{\partial^2 w_o}{\partial x \partial y}
\end{aligned}
\tag{A.37}
$$

where the underlined terms are the von Kármán nonlinear strains.

Laminate resultants

The in-plane laminate forces (A.17) and moment resultants (A.19) can be expressed in function of the membrane strains and curvatures resulted in the classical laminated plate theory (Equation (A.36)) by replacing the constitutive equation of each lamina (Equation (A.13)) of the laminate (see Figure A.5), referenced to the coordinate system (x, y, z). The in-plane resultants of the laminated plate yield to:

$$\begin{Bmatrix} N_x \\ N_y \\ N_{xy} \end{Bmatrix} = \begin{bmatrix} A_{11} & A_{12} & A_{16} \\ A_{12} & A_{22} & A_{26} \\ A_{16} & A_{26} & A_{66} \end{bmatrix} \begin{Bmatrix} \epsilon_x^o \\ \epsilon_y^o \\ \epsilon_s^o \end{Bmatrix} + \begin{bmatrix} B_{11} & B_{12} & B_{16} \\ B_{12} & B_{22} & B_{26} \\ B_{16} & B_{26} & B_{66} \end{bmatrix} \begin{Bmatrix} \kappa_x \\ \kappa_y \\ \kappa_s \end{Bmatrix} \tag{A.38}$$

$$\begin{Bmatrix} M_x \\ M_y \\ M_{xy} \end{Bmatrix} = \begin{bmatrix} B_{11} & B_{12} & B_{16} \\ B_{12} & B_{22} & B_{26} \\ B_{16} & B_{26} & B_{66} \end{bmatrix} \begin{Bmatrix} \epsilon_x^o \\ \epsilon_y^o \\ \epsilon_s^o \end{Bmatrix} + \begin{bmatrix} D_{11} & D_{12} & D_{16} \\ D_{12} & D_{22} & D_{26} \\ D_{16} & D_{26} & D_{66} \end{bmatrix} \begin{Bmatrix} \kappa_x \\ \kappa_y \\ \kappa_s \end{Bmatrix} \tag{A.39}$$

where A_{ij} denote the extensional stiffness, B_{ij} the bending-extensional coupling stiffness, and D_{ij} the bending stiffness of a laminate. They are defined by:

$$A_{ij} = \sum_{p=1}^{N} \overline{C}_{ij,p} \left(z_p - z_{p-1}\right); \quad i,j = 1,2,6 \tag{A.40}$$

$$B_{ij} = \frac{1}{2} \sum_{p=1}^{N} \overline{C}_{ij,p} \left(z_p^2 - z_{p-1}^2\right); \quad i,j = 1,2,6 \tag{A.41}$$

$$D_{ij} = \frac{1}{3} \sum_{p=1}^{N} \overline{C}_{ij,p} \left(z_p^3 - z_{p-1}^3\right); \quad i,j = 1,2,6 \tag{A.42}$$

Governing equations

The boundary conditions considered for the test ASTM - D7136 / D7136M [45] are approached to simply supported boundary conditions. In this case, the application of a variational method is not necessary since the assumed solutions of the displacements provided by the *Navier solutions* yield, for some laminate configurations, to the exact solution of the governing equations. Therefore, the governing equations are obtained by applying the Hamilton principle.

The virtual strain energy for classical plate theory in a solid element of the plate is done by:

$$\delta U = \int_{\Omega} \left(\sigma_x \delta\epsilon_x + \sigma_y \delta\epsilon_y + \sigma_s \delta\epsilon_s\right)\, dv \tag{A.43}$$

By replacing the assumed kinematics (Equation (A.36)) and the stress resultants of the laminate (Equations (A.17) and (A.19)), the virtual strain energy results:

$$\delta U = \int_{\Omega} \left(N_x \delta\epsilon_x^o + M_x \delta\kappa_x + N_y \delta\epsilon_y^o + M_y \delta\kappa_y + N_{xy} \delta\epsilon_s^o + M_{xy} \delta\kappa_s\right)\, dxdy \tag{A.44}$$

The virtual kinetic energy is defined by:

$$\delta K = \int_{\Omega} \int_{-h/2}^{h/2} \rho \left(\dot{u}\delta\dot{u} + \dot{v}\delta\dot{v} + \dot{w}\delta\dot{w}\right)\, dz\, dxdy \tag{A.45}$$

where the superposed dot indicates first derivative respect time. By replacing the assumed displacement field (Equations (A.33)) and integrating over the plate thickness, the virtual kinetic energy yields to:

$$\begin{aligned} \delta K = \int_{\Omega} \Bigg[& -I_1 \left(\dot{u}_o \delta\dot{u}_o + \dot{v}_o \delta\dot{v}_o + \dot{w}_o \delta\dot{w}_o\right) + I_2 \left(\frac{\partial \delta\dot{w}_o}{\partial x} \dot{u}_o \right. \\ & \left. + \frac{\partial \dot{w}_o}{\partial x} \delta\dot{u}_o + \frac{\partial \delta\dot{w}_o}{\partial y} \dot{v}_o + \frac{\partial \dot{w}_o}{\partial y} \delta\dot{v}_o \right) - I_3 \left(\frac{\partial \dot{w}_o}{\partial x} \frac{\partial \delta\dot{w}_o}{\partial x} + \frac{\partial \dot{w}_o}{\partial y} \frac{\partial \delta\dot{w}_o}{\partial y} \right) \Bigg]\, dxdy \end{aligned} \tag{A.46}$$

For laminates composed by plies with the same material and by considering that the center of masses is located in the laminate centerline, the inertia terms (I_1, I_2, I_3) are defined by:

$$\begin{Bmatrix} I_1 \\ I_2 \\ I_3 \end{Bmatrix} = \int_{-h/2}^{h/2} \begin{Bmatrix} 1 \\ z \\ z^2 \end{Bmatrix} \rho\, dz = \rho \begin{Bmatrix} h \\ 0 \\ \dfrac{h^3}{12} \end{Bmatrix} \tag{A.47}$$

The external applied forces consist of a distributed transverse load q over the surface located at $(x, y, \dfrac{h}{2})$, and forces and moments due to in-plane normal stress

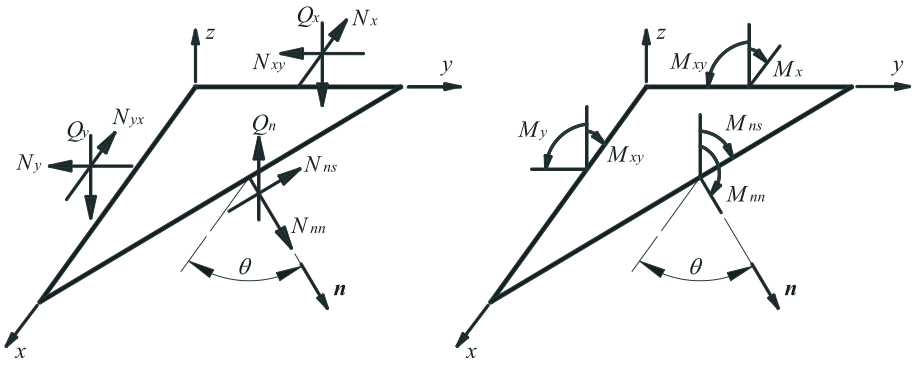

Figure A.7: Stress resultants on an arbitrary edge of a laminate.

$\hat{\sigma}_{nn}$, in-plane tangential stress $\hat{\sigma}_{ns}$, and transverse shear stress $\hat{\sigma}_{nz}$, all acting on and edge with normal $\hat{\mathbf{n}}$ (see Figure A.7).

Then, the virtual work done by the external forces is:

$$\begin{aligned}\delta V = &- \int_{\Omega} q(x,y)\delta w_o(x,y,\frac{h}{2})\,dxdy \\ &- \int_{\Gamma_\sigma}\int_{-h/2}^{h/2} [\hat{\sigma}_{nn}\delta u_n + \hat{\sigma}_{ns}\delta u_s + \hat{\sigma}_{nz}\delta w]\;dzds\end{aligned} \tag{A.48}$$

The stresses $\hat{\sigma}_{nn}$, $\hat{\sigma}_{ns}$, and stress $\hat{\sigma}_{nz}$ can be expressed in force and moment resultants by:

$$\begin{aligned}&\begin{Bmatrix}\hat{N}_{nn}\\ \hat{N}_{ns}\end{Bmatrix} = \int_{-h/2}^{h/2}\begin{Bmatrix}\hat{\sigma}_{nn}\\ \hat{\sigma}_{ns}\end{Bmatrix} dz, \quad \begin{Bmatrix}\hat{M}_{nn}\\ \hat{M}_{ns}\end{Bmatrix} = \int_{-h/2}^{h/2}\begin{Bmatrix}\hat{\sigma}_{nn}\\ \hat{\sigma}_{ns}\end{Bmatrix} z\,dz \\ &\hat{Q}_n = \int_{-h/2}^{h/2}\hat{\sigma}_{nz}\,dz\end{aligned} \tag{A.49}$$

Applying Hamilton principle, the principle yields to the following equation defined in terms of the force and moment resultants:

$$
\begin{aligned}
0 = \int_0^T \int_\Omega \Bigg[& -\left(\frac{\partial N_x}{\partial x} + \frac{\partial N_{xy}}{\partial y} - I_1 \ddot{u}_o \right) \delta u_o \\
& - \left(\frac{\partial N_{xy}}{\partial x} + \frac{\partial N_y}{\partial y} - I_1 \ddot{v}_o \right) \delta v_o \\
& - \left(\frac{\partial^2 M_x}{\partial x^2} + 2\frac{\partial^2 M_{xy}}{\partial x \partial y} + \frac{\partial^2 M_y}{\partial y^2} + \mathcal{N}(u_o, v_o, w_o) \right. \\
& \left. + q - I_1 \ddot{w}_o + I_3 \frac{\partial^2 \ddot{w}_o}{\partial x^2} + I_3 \frac{\partial^2 \ddot{w}_o}{\partial y^2} \right) \delta w_o \Bigg] \, dx dy \, dt \\
& + \int_0^T \int_{\Gamma_\sigma} \Bigg[\left(N_{nn} - \hat{N}_{nn} \right) \delta u_{on} + \left(N_{ns} - \hat{N}_{ns} \right) \delta u_{os} \\
& + \left(V_n - \hat{V}_n \right) \delta w_o - \left(M_{nn} - \hat{M}_{nn} \right) \frac{\partial \delta w_o}{\partial n} \Bigg] \, ds \, dt
\end{aligned}
\tag{A.50}
$$

where $\mathcal{N}(u_o, v_o, w_o)$, V_n and $\hat{V}_n$ are defined by:

$$
\mathcal{N}(u_o, v_o, w_o) = \frac{\partial}{\partial x} \left(N_x \frac{\partial w_o}{\partial x} + N_{xy} \frac{\partial w_o}{\partial y} \right) + \frac{\partial}{\partial y} \left(N_{xy} \frac{\partial w_o}{\partial x} + N_y \frac{\partial w_o}{\partial y} \right) \tag{A.51}
$$

$$
\begin{aligned}
V_n \equiv & \frac{\partial M_x}{\partial x} n_x + \frac{\partial M_{xy}}{\partial y} n_x + \frac{\partial M_y}{\partial y} n_y + \frac{\partial M_{xy}}{\partial x} n_y + \frac{\partial M_{ns}}{\partial s} n_x \\
& + \mathcal{P}(u_o, v_o, w_o) + I_3 \frac{\partial \ddot{w}_o}{\partial x} n_x + I_3 \frac{\partial \ddot{w}_o}{\partial y} n_y
\end{aligned}
\tag{A.52}
$$

$$
\hat{V}_n = \hat{Q}_n + \frac{\partial \hat{M}_{ns}}{\partial s} \tag{A.53}
$$

where $\mathcal{P}(u_o, v_o, w_o)$ is defined by:

$$
\mathcal{P}(u_o, v_o, w_o) = \left(N_x \frac{\partial w_o}{\partial x} + N_{xy} \frac{\partial w_o}{\partial y} \right) n_x + \left(N_{xy} \frac{\partial w_o}{\partial x} + N_y \frac{\partial w_o}{\partial y} \right) n_y \tag{A.54}
$$

From Equation (A.50) the Euler-Lagrange governing equations are obtained:

$$
\frac{\partial N_x}{\partial x} + \frac{\partial N_{xy}}{\partial y} = I_1 \ddot{u}_o - I_2 \frac{\partial \ddot{w}_o}{\partial x} \tag{A.55}
$$

$$
\frac{\partial N_{xy}}{\partial x} + \frac{\partial N_y}{\partial y} = I_1 \ddot{v}_o - I_2 \frac{\partial \ddot{w}_o}{\partial y} \tag{A.56}
$$

$$\begin{aligned}&\frac{\partial^2 M_x}{\partial x^2} + 2\frac{\partial^2 M_{xy}}{\partial x \partial y} + \frac{\partial^2 M_y}{\partial y^2} + \mathcal{N}(u_o, v_o, w_o) + q \\ &= I_1 \ddot{w}_o + I_2 \left(\frac{\partial \ddot{u}_o}{\partial x} + \frac{\partial \ddot{v}_o}{\partial y} \right) - I_3 \left(\frac{\partial^2 \ddot{w}_o}{\partial x^2} + \frac{\partial^2 \ddot{w}_o}{\partial y^2} \right)\end{aligned} \tag{A.57}$$

where the terms involving I_3 are called rotary (or rotatory) inertia terms, and are often omitted because it is small in comparison to the $I_1\ddot{u}$ and $I_1\ddot{v}$.

And the natural boundary conditions [47] are:

$$\begin{aligned}&N_{nn} - \hat{N}_{nn} = 0, \quad N_{ns} - \hat{N}_{ns} = 0 \\ &M_{nn} - \hat{M}_{nn} = 0, \quad V_n - \hat{V}_n = 0\end{aligned} \tag{A.58}$$

When transient response of a plate is of interest, it is necessary to know the initial displacement field and velocity field throughout the domain of the plate. In classical laminated plate theory, the initial conditions at time $t = 0$ for all points in Ω are:

$$\begin{aligned}&u_n = u_n^0, \quad u_s = u_s^0, \quad w_o = w_o^0 \\ &\dot{u}_n = \dot{u}_n^0, \quad \dot{u}_s = \dot{u}_s^0, \quad \dot{w}_o = \dot{w}_o^0\end{aligned} \tag{A.59}$$

The governing Equations (A.55-A.57) can be expressed in terms of displacements u_o, v_o, w_o by substituting Equations (A.38) and (A.39), and the resulting expressions of the strains (Equations (A.37)). Neglecting the third order derivative terms in the space, the resulting motion equations are:

$$\begin{aligned}&\frac{\partial}{\partial x}\left[A_{11}\frac{\partial u_o}{\partial x} + A_{12}\frac{\partial v_o}{\partial y} + A_{16}\left(\frac{\partial u_o}{\partial y} + \frac{\partial v_o}{\partial x} \right) + B_{11}\left(-\frac{\partial^2 w_o}{\partial x^2} \right) + \right. \\ &B_{12}\left(-\frac{\partial^2 w_o}{\partial y^2} \right) + B_{16}\left(-2\frac{\partial^2 w_o}{\partial x \partial y} \right)\Big] + \frac{\partial}{\partial y}\left[A_{16}\frac{\partial u_o}{\partial x} + A_{26}\frac{\partial v_o}{\partial y} + \right. \\ &A_{66}\left(\frac{\partial u_o}{\partial y} + \frac{\partial v_o}{\partial x} \right) + B_{16}\left(-\frac{\partial^2 w_o}{\partial x^2} \right) + B_{26}\left(-\frac{\partial^2 w_o}{\partial y^2} \right) \\ &\left. + B_{66}\left(-2\frac{\partial^2 w_o}{\partial x \partial y} \right)\right] = I_1 \frac{\partial^2 u_o}{\partial t^2} - I_2 \frac{\partial \ddot{w}_o}{\partial x}\end{aligned} \tag{A.60}$$

$$\begin{aligned}
&\frac{\partial}{\partial x}\left[A_{16}\frac{\partial u_o}{\partial x}+A_{26}\frac{\partial v_o}{\partial y}+A_{66}\left(\frac{\partial u_o}{\partial y}+\frac{\partial v_o}{\partial x}\right)+B_{16}\left(-\frac{\partial^2 w_o}{\partial x^2}\right)\right.\\
&\left.+B_{26}\left(-\frac{\partial^2 w_o}{\partial y^2}\right)+B_{66}\left(-2\frac{\partial^2 w_o}{\partial x\partial y}\right)\right]+\frac{\partial}{\partial y}\left[A_{12}\frac{\partial u_o}{\partial x}+A_{22}\frac{\partial v_o}{\partial y}\right.\\
&\left.+A_{26}\left(\frac{\partial u_o}{\partial y}+\frac{\partial v_o}{\partial x}\right)+B_{12}\left(-\frac{\partial^2 w_o}{\partial x^2}\right)+B_{22}\left(-\frac{\partial^2 w_o}{\partial y^2}\right)\right.\\
&\left.+B_{26}\left(-2\frac{\partial^2 w_o}{\partial x\partial y}\right)\right]=I_1\frac{\partial^2 v_o}{\partial t^2}-I_2\frac{\partial\ddot{w}_o}{\partial y}
\end{aligned}\tag{A.61}$$

$$\begin{aligned}
&\frac{\partial^2}{\partial x^2}\left[B_{11}\frac{\partial u_o}{\partial x}+B_{12}\frac{\partial v_o}{\partial y}+B_{16}\left(\frac{\partial u_o}{\partial y}+\frac{\partial v_o}{\partial x}\right)+D_{11}\left(-\frac{\partial^2 w_o}{\partial x^2}\right)\right.\\
&\left.+D_{12}\left(-\frac{\partial^2 w_o}{\partial y^2}\right)+D_{16}\left(-2\frac{\partial^2 w_o}{\partial x\partial y}\right)\right]+2\frac{\partial^2}{\partial x\partial y}\left[B_{16}\frac{\partial u_o}{\partial x}\right.\\
&\left.+B_{26}\frac{\partial v_o}{\partial y}+B_{66}\left(\frac{\partial u_o}{\partial y}+\frac{\partial v_o}{\partial x}\right)+D_{16}\left(-\frac{\partial^2 w_o}{\partial x^2}\right)\right.\\
&\left.+D_{26}\left(-\frac{\partial^2 w_o}{\partial y^2}\right)+D_{66}\left(-2\frac{\partial^2 w_o}{\partial x\partial y}\right)\right]+\frac{\partial^2}{\partial y^2}\left[B_{12}\frac{\partial u_o}{\partial x}+B_{22}\frac{\partial v_o}{\partial y}\right.\\
&\left.+B_{26}\left(\frac{\partial u_o}{\partial y}+\frac{\partial v_o}{\partial x}\right)+D_{12}\left(-\frac{\partial^2 w_o}{\partial x^2}\right)+D_{22}\left(-\frac{\partial^2 w_o}{\partial y^2}\right)\right.\\
&\left.+D_{26}\left(-2\frac{\partial^2 w_o}{\partial x\partial y}\right)\right]+\mathcal{N}(u_o,v_o,w_o)+q=I_1\frac{\partial^2 w_o}{\partial t^2}\\
&+I_2\left(\frac{\partial\ddot{u}_o}{\partial x}+\frac{\partial\ddot{v}_o}{\partial y}\right)-I_3\left(\frac{\partial^2\ddot{w}_o}{\partial x^2}+\frac{\partial^2\ddot{w}_o}{\partial y^2}\right)
\end{aligned}\tag{A.62}$$

A.2.2 First-order shear plate theory

The classical laminated plate theory is not recommended for composites that are likely to fail in transverse shear or delamination, because the transverse shears and normal stresses are not accounted for. A refinement to the classical plate theory is provided by the *first-order shear deformation plate theory* (also known as *Mindlin plate theory*). There are numerous plate theories documented in the literature (not shown here) that also include transverse shear deformations. In all these theories, the displacements are expanded as linear combinations of the thickness coordinate and undetermined functions of position in the reference surface.

Displacement field and kinematics

The assumptions of the first-order shear deformation theory are the same as in the classical laminated plate theory, with the exception of the transverse normals sections can rotate such that they can not remain perpendicular to the mid-plane after deformation. Therefore, the displacement field described for classical laminated plate theory by Equations (A.33) also can be used for first-order shear plate theory, but the rotations ϕ_1 and ϕ_2 of a transverse normals are now independent of $\partial w_o/\partial x$ and $\partial w_o/\partial y$ (see Figure A.8).

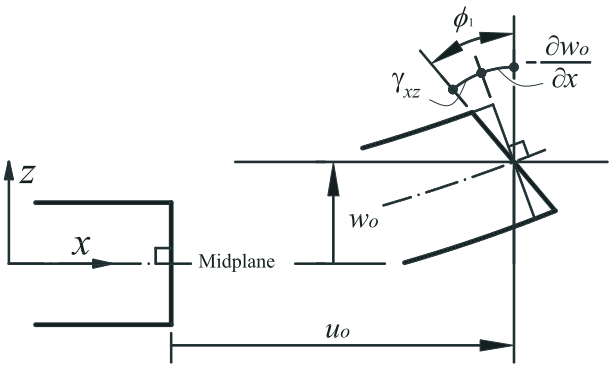

Figure A.8: Behavior of transverse section in first-order shear plate theory.

Using the von Kármán strain-displacement relations (Equations (A.4)) referenced to the coordinate system (x, y, z) and the assumed displacement field (Equations (A.33)), the strain components yield to the following expressions:

$$
\begin{aligned}
\epsilon_x \equiv \epsilon_{xx} &= \frac{\partial u}{\partial x} + \frac{1}{2}\left(\frac{\partial w}{\partial x}\right)^2 = \frac{\partial u_o}{\partial x} + \frac{1}{2}\left(\frac{\partial w_o}{\partial x}\right)^2 + z\frac{\partial \phi_1}{\partial x} \\
\epsilon_y \equiv \epsilon_{yy} &= \frac{\partial v}{\partial y} + \frac{1}{2}\left(\frac{\partial w}{\partial y}\right)^2 = \frac{\partial v_o}{\partial y} + \frac{1}{2}\left(\frac{\partial w_o}{\partial y}\right)^2 + z\frac{\partial \phi_2}{\partial y} \\
\epsilon_z \equiv \epsilon_{zz} &= \frac{\partial w}{\partial z} = \frac{\partial w_o}{\partial z} = 0 \\
\epsilon_q \equiv 2\epsilon_{yz} &= \frac{\partial v}{\partial z} + \frac{\partial w}{\partial y} = \phi_2 + \frac{\partial w_o}{\partial y} \\
\epsilon_r \equiv 2\epsilon_{xz} &= \frac{\partial u}{\partial z} + \frac{\partial w}{\partial x} = \phi_1 + \frac{\partial w_o}{\partial x} \\
\epsilon_s \equiv 2\epsilon_{xy} &= \\
&= \frac{\partial u}{\partial y} + \frac{\partial v}{\partial x} + \frac{\partial w}{\partial x}\frac{\partial w}{\partial y} = \frac{\partial u_o}{\partial y} + \frac{\partial v_o}{\partial x} + \frac{\partial w_o}{\partial x}\frac{\partial w_o}{\partial y} + z\left(\frac{\partial \phi_1}{\partial y} + \frac{\partial \phi_2}{\partial x}\right)
\end{aligned}
\tag{A.63}
$$

As in classical laminated plate theory, Equations (A.63) can be expressed in a general form by:

$$
\epsilon_i = \epsilon_i^o + z\kappa_i; \quad i = x, y, q, r, s \tag{A.64}
$$

where the strains $\epsilon_i^o = \left(\epsilon_x^o, \epsilon_y^o, \epsilon_s^o\right)$ are the membrane strains, the quantities $\kappa_i = (\kappa_x, \kappa_y, \kappa_s)$ are the curvatures, and ϵ_q^o and ϵ_r^o are the transverse shear strains. Equations (A.63) show that membrane strains, shear strains and curvatures for the first-order shear deformation plate theory have the following explicit form:

$$
\begin{aligned}
\epsilon_x^o &= \frac{\partial u_o}{\partial x} + \underline{\frac{1}{2}\left(\frac{\partial w_o}{\partial x}\right)^2}, & \kappa_x &= \frac{\partial \phi_1}{\partial x} \\
\epsilon_y^o &= \frac{\partial v_o}{\partial y} + \underline{\frac{1}{2}\left(\frac{\partial w_o}{\partial y}\right)^2}, & \kappa_y &= \frac{\partial \phi_2}{\partial y} \\
\epsilon_z^o &= 0, & \kappa_z &= 0 \\
\epsilon_q^o &= \phi_2 + \frac{\partial w_o}{\partial y}, & \kappa_q &= 0 \\
\epsilon_r^o &= \phi_1 + \frac{\partial w_o}{\partial x}, & \kappa_r &= 0 \\
\epsilon_s^o &= \frac{\partial u_o}{\partial y} + \frac{\partial v_o}{\partial x} + \underline{\frac{\partial w_o}{\partial x}\frac{\partial w_o}{\partial y}}, & \kappa_s &= \frac{\partial \phi_1}{\partial y} + \frac{\partial \phi_2}{\partial x}
\end{aligned}
\tag{A.65}
$$

where the underlined terms are the von Kármán nonlinear strains.

Laminate resultants

The in-plane laminate forces (A.17) and moment resultants (A.19) expressed in function of the membrane strains and curvatures resulted in the first-order shear deformation plate theory (Equation (A.64)) yield to the same expressions obtained for classical laminated plate theory (Equations (A.38) and (A.39)). However, the transverse shear resultants have also to be defined. Replacing the strains of Equation (A.64) in the transverse shear forces (A.18) by using the constitutive equation of each lamina of the laminate referenced to the coordinate system (x, y, z) (Equation (A.13)), the shear forces result:

$$\begin{Bmatrix} Q_y \\ Q_x \end{Bmatrix} = \begin{bmatrix} A_{44} & A_{45} \\ A_{45} & A_{55} \end{bmatrix} \begin{Bmatrix} \epsilon_q^o \\ \epsilon_r^o \end{Bmatrix} \tag{A.66}$$

The transverse shear stiffness A_{ij} are defined by:

$$A_{ij} = K_{ij} \sum_{p=1}^{N} \overline{C}_{ij,p} \left(z_p - z_{p-1} \right); \quad i, j = 4, 5 \tag{A.67}$$

where K_{ij} are the dimensionless shear correction factors. Modeling transverse shear strains and stresses to be constant through the thickness results in the transverse shear energy being too large when compared to that coming from a more realistic parabolic distribution. In addition, equilibrium is not satisfied at the surfaces. Therefore, the shear correction factors are used so that the constant distribution of transverse shear strains and stresses has the same strain energy as the parabolic distribution. Normally, K_{ij} are taken as an isotropic material (i.e. 5/6).

Governing equations

The virtual strain energy for first-order shear deformation plate theory in a solid element of the plate is done by:

$$\delta U = \int_{\Omega} \left(\sigma_x \delta\epsilon_x + \sigma_y \delta\epsilon_y + \sigma_s \delta\epsilon_s + \sigma_q \delta\epsilon_q + \sigma_r \delta\epsilon_r \right) \, dv \tag{A.68}$$

By replacing the assumed kinematics (Equation (A.64)) and the stress resultants of the laminate (Equations (A.17), (A.18) and (A.19)), the virtual strain energy results:

$$\begin{aligned}\delta U = \int_\Omega \big(& N_x \delta\epsilon_x^o + M_x \delta\kappa_x + N_y \delta\epsilon_y^o + M_y \delta\kappa_y + N_{xy} \delta\epsilon_s^o \\ & + M_{xy} \delta\kappa_s + Q_x \delta\epsilon_r^o + Q_y \delta\epsilon_q^o \big)\, dxdy\end{aligned} \tag{A.69}$$

The virtual kinetic energy was previously defined by Equation (A.45). By replacing in the assumed displacement field which coincides with that of classical laminated plate theory (Equations (A.33)) and integrating over the plate thickness, the virtual kinetic energy yields to:

$$\begin{aligned}\delta K = \int_\Omega \Big[& -I_1 \left(\dot{u}_o \delta\dot{u}_o + \dot{v}_o \delta\dot{v}_o + \dot{w}_o \delta\dot{w}_o \right) - I_2 \Big(\dot{\phi}_1 \delta\dot{u}_o \\ & + \dot{\phi}_2 \delta\dot{v}_o + \delta\dot{\phi}_1 \dot{u}_o + \delta\dot{\phi}_2 \dot{v}_o \Big) - I_3 \left(\dot{\phi}_1 \delta\dot{\phi}_1 + \dot{\phi}_2 \delta\dot{\phi}_2 \right) \Big]\, dxdy\end{aligned} \tag{A.70}$$

where the inertia terms (I_1, I_2, I_3) were defined by Equation (A.47).

The virtual work done by the external forces was previously defined by Equation (A.48).

Applying Hamilton principle, the principle yields to the following equation defined in terms of the force and moment resultants:

$$\begin{aligned}0 = \int_0^T \int_\Omega \Bigg[& -\left(\frac{\partial N_x}{\partial x} + \frac{\partial N_{xy}}{\partial y} - I_1 \ddot{u}_o - I_2 \ddot{\phi}_1 \right) \delta u_o \\ & - \left(\frac{\partial N_{xy}}{\partial x} + \frac{\partial N_y}{\partial y} - I_1 \ddot{v}_o - I_2 \ddot{\phi}_2 \right) \delta v_o \\ & - \left(\frac{\partial M_x}{\partial x} + \frac{\partial M_{xy}}{\partial y} - Q_x - I_3 \ddot{\phi}_1 - I_2 \ddot{u}_o \right) \delta\phi_1 \\ & - \left(\frac{\partial M_{xy}}{\partial x} + \frac{\partial M_y}{\partial y} - Q_y - I_3 \ddot{\phi}_2 - I_2 \ddot{v}_o \right) \delta\phi_2 \\ & - \left(\frac{\partial Q_x}{\partial x} + \frac{\partial Q_y}{\partial y} + \mathcal{N}(u_o, v_o, w_o) + q - I_1 \ddot{w}_o \right) \delta w_o \Bigg]\, dxdy \\ & + \int_0^T \int_{\Gamma_\sigma} \Big[\left(N_{nn} - \hat{N}_{nn} \right) \delta u_{on} + \left(N_{ns} - \hat{N}_{ns} \right) \delta u_{os} \\ & + \left(Q_n - \hat{Q}_n \right) \delta w_o + \left(M_{nn} - \hat{M}_{nn} \right) \delta\phi_n + \left(M_{ns} - \hat{M}_{ns} \right) \delta\phi_s \Big]\, ds\, dt\end{aligned} \tag{A.71}$$

where $\mathcal{N}(u_o, v_o, w_o)$ was previously defined by Equation (A.51). The boundary expressions were arrived by expressing ϕ_1 and ϕ_2 in terms of the normal and tangential rotations (ϕ_n, ϕ_s):

$$\phi_1 = n_x\phi_n - n_y\phi_s, \quad \phi_2 = n_y\phi_n + n_x\phi_s \tag{A.72}$$

From Equation (A.71) the Euler-Lagrange governing equations are obtained:

$$\frac{\partial N_x}{\partial x} + \frac{\partial N_{xy}}{\partial y} = I_1\frac{\partial^2 u_o}{\partial t^2} + I_2\frac{\partial^2 \phi_1}{\partial t^2} \tag{A.73}$$

$$\frac{\partial N_{xy}}{\partial x} + \frac{\partial N_y}{\partial y} = I_1\frac{\partial^2 v_o}{\partial t^2} + I_2\frac{\partial^2 \phi_2}{\partial t^2} \tag{A.74}$$

$$\frac{\partial Q_x}{\partial x} + \frac{\partial Q_y}{\partial y} + \mathcal{N}(u_o, v_o, w_o) + q = I_1\frac{\partial^2 w_o}{\partial t^2} \tag{A.75}$$

$$\frac{\partial M_x}{\partial x} + \frac{\partial M_{xy}}{\partial y} - Q_x = I_3\frac{\partial^2 \phi_1}{\partial t^2} + I_2\frac{\partial^2 u_o}{\partial t^2} \tag{A.76}$$

$$\frac{\partial M_{xy}}{\partial x} + \frac{\partial M_y}{\partial y} - Q_y = I_3\frac{\partial^2 \phi_2}{\partial t^2} + I_2\frac{\partial^2 v_o}{\partial t^2} \tag{A.77}$$

And the natural boundary conditions [47] are:

$$\begin{aligned} &N_{nn} - \hat{N}_{nn} = 0, \quad N_{ns} - \hat{N}_{ns} = 0, \quad Q_n - \hat{Q}_n = 0 \\ &M_{nn} - \hat{M}_{nn} = 0, \quad M_{ns} - \hat{M}_{ns} = 0 \end{aligned} \tag{A.78}$$

where $Q_n \equiv Q_x n_x + Q_y n_y + \mathcal{P}(u_o, v_o, w_o)$. The term $\mathcal{P}(u_o, v_o, w_o)$ was previously defined in Equation (A.54).

The initial conditions of the theory involve specifying the values of the displacements and their first derivatives with respect to time at $t = 0$ for all points in Ω:

$$\begin{aligned} &u_n = u_n^0, \quad u_s = u_s^0, \quad w_o = w_o^0, \quad \phi_n = \phi_n^0, \quad \phi_s = \phi_s^0 \\ &\dot{u}_n = \dot{u}_n^0, \quad \dot{u}_s = \dot{u}_s^0, \quad \dot{w}_o = \dot{w}_o^0, \quad \dot{\phi}_n = \dot{\phi}_n^0, \quad \dot{\phi}_s = \dot{\phi}_s^0 \end{aligned} \tag{A.79}$$

The governing Equations (A.73-A.77) can be expressed in terms of displacements (u_o, v_o, w_o) and rotations (ϕ_1, ϕ_2) by substituting Equations (A.38), (A.39)

and (A.66), and the resulting expressions of the strains (A.65). Neglecting the third order derivative terms in the space, the resulting motion equations are:

$$\begin{aligned}
&\frac{\partial}{\partial x}\left[A_{11}\frac{\partial u_o}{\partial x}+A_{12}\frac{\partial v_o}{\partial y}+A_{16}\left(\frac{\partial u_o}{\partial y}+\frac{\partial v_o}{\partial x}\right)+B_{11}\frac{\partial \phi_1}{\partial x}\right.\\
&\left.+B_{12}\frac{\partial \phi_2}{\partial y}+B_{16}\left(\frac{\partial \phi_1}{\partial y}+\frac{\partial \phi_2}{\partial x}\right)\right]+\frac{\partial}{\partial y}\left[A_{16}\frac{\partial u_o}{\partial x}+A_{26}\frac{\partial v_o}{\partial y}\right.\\
&\left.+A_{66}\left(\frac{\partial u_o}{\partial y}+\frac{\partial v_o}{\partial x}\right)+B_{16}\frac{\partial \phi_1}{\partial x}+B_{26}\frac{\partial \phi_2}{\partial y}+B_{66}\left(\frac{\partial \phi_1}{\partial y}+\frac{\partial \phi_2}{\partial x}\right)\right]\\
&=I_1\frac{\partial^2 u_o}{\partial t^2}+I_2\frac{\partial^2 \phi_1}{\partial t^2}
\end{aligned} \tag{A.80}$$

$$\begin{aligned}
&\frac{\partial}{\partial x}\left[A_{16}\frac{\partial u_o}{\partial x}+A_{26}\frac{\partial v_o}{\partial y}+A_{66}\left(\frac{\partial u_o}{\partial y}+\frac{\partial v_o}{\partial x}\right)+B_{16}\frac{\partial \phi_1}{\partial x}\right.\\
&\left.+B_{26}\left(\frac{\partial \phi_2}{\partial y}\right)+B_{66}\left(\frac{\partial \phi_1}{\partial y}+\frac{\partial \phi_2}{\partial x}\right)\right]+\frac{\partial}{\partial y}\left[A_{12}\frac{\partial u_o}{\partial x}+A_{22}\frac{\partial v_o}{\partial y}\right.\\
&\left.+A_{26}\left(\frac{\partial u_o}{\partial y}+\frac{\partial v_o}{\partial x}\right)+B_{12}\frac{\partial \phi_1}{\partial x}+B_{22}\frac{\partial \phi_2}{\partial y}+B_{26}\left(\frac{\partial \phi_1}{\partial y}+\frac{\partial \phi_2}{\partial x}\right)\right]\\
&=I_1\frac{\partial^2 v_o}{\partial t^2}+I_2\frac{\partial^2 \phi_2}{\partial t^2}
\end{aligned} \tag{A.81}$$

$$\begin{aligned}
&\frac{\partial}{\partial x}\left[A_{45}\left(\frac{\partial w_o}{\partial y}+\phi_2\right)+A_{55}\left(\frac{\partial w_o}{\partial x}+\phi_1\right)\right]\\
&+\frac{\partial}{\partial y}\left[A_{44}\left(\frac{\partial w_o}{\partial y}+\phi_2\right)+A_{45}\left(\frac{\partial w_o}{\partial x}+\phi_1\right)\right]\\
&+\mathcal{N}(u_o,v_o,w_o)+q=I_1\frac{\partial^2 w_o}{\partial t^2}
\end{aligned} \tag{A.82}$$

$$\begin{aligned}
&\frac{\partial}{\partial x}\left[B_{11}\frac{\partial u_o}{\partial x}+B_{12}\frac{\partial v_o}{\partial y}+B_{16}\left(\frac{\partial u_o}{\partial y}+\frac{\partial v_o}{\partial x}\right)+D_{11}\frac{\partial \phi_1}{\partial x}\right.\\
&\left.+D_{12}\left(\frac{\partial \phi_2}{\partial y}\right)+D_{16}\left(\frac{\partial \phi_1}{\partial y}+\frac{\partial \phi_2}{\partial x}\right)\right]+\frac{\partial}{\partial y}\left[B_{16}\frac{\partial u_o}{\partial x}+B_{26}\frac{\partial v_o}{\partial y}\right.\\
&\left.+B_{66}\left(\frac{\partial u_o}{\partial y}+\frac{\partial v_o}{\partial x}\right)+D_{16}\frac{\partial \phi_1}{\partial x}+D_{26}\frac{\partial \phi_2}{\partial y}+D_{66}\left(\frac{\partial \phi_1}{\partial y}+\frac{\partial \phi_2}{\partial x}\right)\right]\\
&-\left[A_{45}\left(\frac{\partial w_o}{\partial y}+\phi_2\right)+A_{55}\left(\frac{\partial w_o}{\partial x}+\phi_1\right)\right]=I_3\frac{\partial^2 \phi_1}{\partial t^2}+I_2\frac{\partial^2 u_o}{\partial t^2}
\end{aligned} \tag{A.83}$$

$$\begin{aligned}
&\frac{\partial}{\partial x}\left[B_{16}\frac{\partial u_o}{\partial x}+B_{26}\frac{\partial v_o}{\partial y}+B_{66}\left(\frac{\partial u_o}{\partial y}+\frac{\partial v_o}{\partial x}\right)+D_{16}\frac{\partial \phi_1}{\partial x}\right.\\
&\left.+D_{26}\left(\frac{\partial \phi_2}{\partial y}\right)+D_{66}\left(\frac{\partial \phi_1}{\partial y}+\frac{\partial \phi_2}{\partial x}\right)\right]+\frac{\partial}{\partial y}\left[B_{12}\frac{\partial u_o}{\partial x}+B_{22}\frac{\partial v_o}{\partial y}\right.\\
&\left.+B_{26}\left(\frac{\partial u_o}{\partial y}+\frac{\partial v_o}{\partial x}\right)+D_{12}\frac{\partial \phi_1}{\partial x}+D_{22}\frac{\partial \phi_2}{\partial y}+D_{26}\left(\frac{\partial \phi_1}{\partial y}+\frac{\partial \phi_2}{\partial x}\right)\right]\\
&-\left[A_{44}\left(\frac{\partial w_o}{\partial y}+\phi_2\right)+A_{45}\left(\frac{\partial w_o}{\partial x}+\phi_1\right)\right]=I_3\frac{\partial^2 \phi_2}{\partial t^2}+I_2\frac{\partial^2 v_o}{\partial t^2}
\end{aligned} \tag{A.84}$$

Bibliography

[1] Richardson, M.O.W., Wisheart, M.J.. Review of low-velocity impact properties of composite materials. Composites Part A-Applied Science and Manufacturing 1996;27(12):1123–1131.

[2] Iannucci, L.. Dynamic delamination modelling using interface elements. Computers and Structures 2006;84(15-16):1029–1048.

[3] Olsson, R.. Mass criterion for wave controlled impact response of composite plates. Composites Part A-Applied Science and Manufacturing 2000;31(8):879–887.

[4] Astm d 7137/d7137m - 05. standard test method for compressive residual strength properties of damaged polymer matrix composite plates. 2005;.

[5] Abrate, S.. Impact on composite structures. UK: Cambridge University Press; 1998.

[6] Christoforou, A.P.. Impact dynamics and damage in composite structures. Composite Structures, 2001;52(2):181–188.

[7] Christoforou, A.P., Yigit, A.S.. Characterization of impact in composite plates. Composite Structures 1998;43(1):15–24.

[8] Davies, G.A.O., Olsson, R.. Impact on composite structures. The Aeronautical Journal 2004;:541.

[9] Olsson, R.. Impact response of composite laminates - a guide to closed form solutions, ffa tn 1992-33. Bromma: The Aeronautical Research Institute of Sweden 1993;.

[10] Olsson, R., Donadon, M.V., Falzon, B.G.. Delamination threshold load for dynamic impact on plates. International Journal of Solids and Structures 2006;43(10):3124–3141.

[11] Olsson, R.. Analytical prediction of large mass impact damage in composite laminates. Composites Part A-Applied Science and Manufacturing 2001;32(9):1207–1215.

[12] Olsson, R.. Closed form prediction of peak load and delamination onset under small mass impact. Composite Structures 2003;59(3):341–349.

[13] Yigit, A.S., Christoforou, A.P.. Limits of asymptotic solutions in low-velocity impact of composite plates. Composite Structures 2007;81(4):568–574.

[14] Christoforou, A.P., Yigit, A.S.. Effect of flexibility on low velocity impact response. Journal of Sound and Vibration, 1998;217(3):563–578.

[15] Abrate, S.. Modeling of impacts on composite structures. Composite Structures 2001;51(2):129–138.

[16] Lin, C., Fatt, M.S.H.. Perforation of composite plates and sandwich panels under quasi-static and projectile loading. Journal of Composite Materials 2006;40(20):1801–1840.

[17] Schoeppner, G.A., Abrate, S.. Delamination threshold loads for low velocity impact on composite laminates. Composites Part A: Applied Science and Manufacturing 2000;31(9):903–915.

[18] Godwin, W., Davies, G.A.O.. Impact behaviour of thermoplastic composites. Composite Material Technology 1988;.

[19] Robinson, P., Davies, G.A.O.. Impactor mass and specimen geometry-effects in low velocity impact of laminated composites. International Journal of Impact Engineering 1992;12(2):189–207.

[20] Johnson, K.L.. Contact mechanics. Cambridge Univ. Press; 1985. ISBN 0521255767 (ISBN); 9780521255769 (ISBN).

[21] Olsson, R.. Impact response of orthotropic composite plates predicted from a one-parameter differential equation. AIAA journal 1992;30(6):1587–1596.

[22] Dahan, M., Zarka, J.. Elastic contact between a sphere and a semi infinite transversely isotropic body. International Journal of Solids and Structures, 1977;13(3):229–238.

[23] Turner, J.R.. Contact on a transversely isotropic half-space, or between two transversely isotropic bodies. International Journal of Solids and Structures 1980;16(5):409–419.

[24] Wu, E., Yen, C.S.. The contact behavior between laminated composite plates and rigid spheres. J Appl Mech 1994;61(1):60–66.

[25] Chao, C.C., Tu, C.Y.. Three-dimensional contact dynamics of laminated plates: Part 1. normal impact. Composites Part B: Engineering 1999;30(1):9–22.

[26] Swanson, S.R.. Hertzian contact of orthotropic materials. International Journal of Solids and Structures 2004;41(7):1945–1959.

[27] Yang, S.H., Sun, C.T.. Indentation law for composite laminates. 1982, p. 425–449.

[28] Wu, E., Shyu, K.. Response of composite laminates to contact loads and relationship to low-velocity impact. Journal of Composite Materials 1993;27(15):1443–1464.

[29] Cairns, D.S.. A simple, elasto-plastic contact law for composites. Journal of Reinforced Plastics and Composites 1991;10(4):423–433.

[30] Christoforou, A.P.. On the contact of a spherical indenter and a thin composite laminate. Composite Structures, 1993;26(1-2):77–82.

[31] Yigit, A.S., Christoforou, A.P.. On the impact of a spherical indenter and an elastic-plastic transversely isotropic half-space. Composites Engineering, 1994;4(11):1143–1152.

[32] Tan, T.M., Sun, C.T.. Use of statical indentation laws in the impact analysis of laminated composite plates. Journal of Applied Mechanics, Transactions ASME 1985;52(1):6–12.

[33] Suemasu, H., Kerth, S., Maier, M.. Indentation of spherical head indentors on transversely isotropic composite plates. Journal of Composite Materials 1994;28(17):1723–1739.

[34] Chen, P., Xiong, J., Shen, Z.. Thickness effect on the contact behavior of a composite laminate indented by a rigid sphere. Mechanics of Materials 2008;40(4-5):183–194.

[35] Swanson, S.R.. Contact deformation and stress in orthotropic plates. Composites Part A: Applied Science and Manufacturing 2005;36(10):1421–1429.

[36] Greszczuk, L.B.. Damage in composite materials due to low velocity impact. New York: John Wiley and Sons; 1982.

[37] Crook, A.W.. A study of some impacts between metal bodies by a piezoelectric method. Proceedings of the Royal Society of London Series A, Mathematical and Physical 1952;.

[38] Christoforou, A.P., Swanson, S.R.. Analysis of impact response in composite plates. International Journal of Solids and Structures, 1991;27(2):161–170.

[39] Yigit, A.S., Christoforou, A.P.. On the impact between a rigid sphere and a thin composite laminate supported by a rigid substrate. Composite Structures, 1995;30(2):169–177.

[40] Christoforou, A.P., Yigit, A.S.. Scaling of low-velocity impact response in composite structures. Composite Structures 2009;91(3):358–365.

[41] Choi, I.H., Lim, C.H.. Low-velocity impact analysis of composite laminates using linearized contact law. Composite Structures 2004;66(1-4):125–132.

[42] Davies, G.A.O.. Structural Impact and Crashworthiness 1984;.

[43] Morton, J.. Scaling of impact-loaded carbon-fiber composites. AIAA Journal 1988;26(8):989–994.

[44] Vlot, A.. 1991.

[45] Astm d 7136/d7136m - 05. standard test method for measuring the damage resistance of a fiber-reinforced polymer matrix composite to a drop-weight impact event. 2005.

[46] Fuoss, E., Straznicky, P.V., Poon, C.. Effects of stacking sequence on the impact resistance in composite laminates - part 1: Parametric study. Composite Structures 1998;41(1):67–77.

[47] Reddy, J.N.. Theory and analysis of elastic plates and shells. Philadelphia: Taylor and Francis; 2007. ISBN 9780849384158.

[48] Clough, R.W., Penzien, J.. Dynamics of structures. New Yok etc.: McGraw-Hill; 1993. ISBN 0071132414.

[49] Mittal, R.K.. A simplified analysis of the effect of transverse shear on the response of elastic plates to impact loading. International Journal of Solids and Structures 1987;23(8):1191–1203.

[50] Olsson, R.. Engineering method for prediction of impact response and damage in sandwich panels. Journal of Sandwich Structures and Materials 2002;4(1):3–29.

[51] Zener, C.. The intrinsic inelasticity of large plates. Physical Review 1941;59(8):669–673.

[52] Swanson, S.R.. Limits of quasi-static solutions in impact of composite structures. Composites Engineering 1992;2(4):261–267.

[53] Shivakumar, K.N., Elber, W., Illg, W.. Prediction of impact force and duration due to low-velocity impact on circular composite laminates. Journal of Applied Mechanics, Transactions ASME 1985;52(3):674–680.

[54] Sierakowski, R.L., Newaz, G.M.. Damage tolerance in advanced composites. 1995.

[55] Davies, G.A.O., Zhang, X., Zhou, G., Watson, S.. Numerical modelling of impact damage. Composites 1994;25(5):342–350.

[56] Elder, D.J., Thomson, R.S., Nguyen, M.Q., Scott, M.L.. Review of delamination predictive methods for low speed impact of composite laminates. Composite Structures 2004;66(1-4):677–683.

[57] Sjoblom, P.O., Hartness, J.T., Cordell, T.M.. On low-velocity impact testing of composite materials. Journal of Composite Materials 1988;22(1):30–52.

[58] Nettles, A.T.. Basic mechanics of laminated composite plates 1994;:1351.

[59] Dávila, C.G., Camanho, P.P.. Physically based failure criteria for transverse matrix cracking. ????,.

[60] Camanho, P.P., Davila, C.G., Pinho, S.T., Iannucci, L., Robinson, P.. Prediction of in situ strengths and matrix cracking in composites under transverse tension and in-plane shear. Composites Part A-Applied Science and Manufacturing 2006;37(2):165–176.

[61] Hahn, H.T.. Mixed-mode fracture criterion for composite materials. Composites technology review 1983;5(1):26–29.

[62] Da´vila, C.G., Jaunky, N., Goswami, S.. Failure criteria for frp laminates in plane stress. vol. 7. 2003, p. 5380–5390.

[63] Pinho, S.T., Dávila, C.G., Camanho, P.P., Iannucci, L., Robinson, P.. Failure models and criteria for frp under in-plane or three-dimensional stress states including shear non-linearity. NASA/TM-2005-213530 2006;.

[64] Davila, C.G., Camanho, P.P., Rose, C.A.. Failure criteria for frp laminates. Journal of Composite Materials 2005;39(4):323–345.

[65] Conway, H.D., Farnham, K.A., Ku, T.C.. The indentation of a transversely isotropic half-space by a rigid sphere. JApplMech 1967;34:491–492.

[66] Olsson, R., Nilsson, S.. Simplified prediction of stresses in transversely isotropic composite plates under hertzian contact load. Composite Structures 2006;73(1):70–77.

[67] Liu, D.. Impact-induced delamination - a view of bending stiffness mismatching. Journal of Composite Materials 1988;22(7):674–692.

[68] Morita, H., Adachi, T., Tateishi, Y., Matsumoto, H.. Characterization of impact damage resistance of cf/peek and cf/toughened epoxy laminates under low and high velocity impact tests. Journal of Reinforced Plastics and Composites 1997;16(2):131–143.

[69] Davies, G.A.O., Zhang, X.. Impact damage prediction in carbon composite structures. International Journal of Impact Engineering 1995;16(1):149–170.

[70] Zhang, X.. Impact damage in composite aircraft structuresexperimental testing and numerical simulation. Proceedings of the Institution of Mechanical Engineers, Part G: Journal of Aerospace Engineering 1998;212(4):245–259.

[71] Jackson, W.C., Poe, C.C.. Use of impact force as a scale parameter for the impact response of composites laminates. Journal of Composites Technology and Research 1993;15(4):282–289.

[72] Davies, G.A.O., Robinson, P.. Predicting failure by debonding delaminations. In: debonding/delamination of composites, AGARD-CP-530, advisory group for aerospace research and development, Neuilly Sur Seine, France 1992;.

[73] Davies, G.A.O., Hitchings, D., Wang, J.. Prediction of threshold impact energy for onset of delamination in quasi-isotropic carbon/epoxy composite laminates under low-velocity impact. Composites Science and Technology, 2000;60(1):1–7.

[74] Suemasu, H., Majima, O.. Multiple delaminations and their severity in circular axisymmetric plates subjected to transverse loading. Journal of Composite Materials 1996;30(4):441–453.

[75] Suemasu, H., Majima, O.. Multiple delaminations and their severity in nonlinear circular plates subjected to concentrated loading. Journal of Composite Materials 1998;32(2):123–140.

[76] Caprino, G., Lopresto, V.. On the penetration energy for fibre-reinforced plastics under low-velocity impact conditions. Composites Science and Technology 2001;61(1):65–73.

[77] Sjoblom, P.. Simple design approach against low-velocity impact damage. vol. 32. 1987, p. 529–539.

[78] Wen, H.M.. Predicting the penetration and perforation of frp laminates struck normally by projectiles with different nose shapes. Composite Structures 2000;49(3):321–329.

[79] Wen, H.M.. Penetration and perforation of thick frp laminates. Composites Science and Technology 2001;61(8):1163–1172.

[80] Hsiao, H.M., Daniel, I.M., Cordes, R.D.. Strain rate effects on the transverse compressive and shear behavior of unidirectional composites. Journal of Composite Materials 1999;33(17):1620–1642.

[81] Aitm airbus test method. fibre reinforced plastics. determination of compression strength after impact. 2005;(3):1–15.

[82] Advanced composite compression tests. Boeing Specification Support Standard BSS 7260 1988;.

[83] Standard test for toughened resin composites. NASA Reference Publication 1982;1092.

[84] Lopes, C.S., Camanho, P.P., Gürdal, Z., Maimí, P., González, E.V.. Low-velocity impact damage on dispersed stacking sequence laminates. part ii: Numerical simulations. Composites Science and Technology 2009;69(7-8):937–947.

[85] Lopes, C.S., Seresta, O., Coquet, Y., Gürdal, Z., Camanho, P.P., Thuis, B.. Low-velocity impact damage on dispersed stacking sequence laminates. part i: Experiments. Composites Science and Technology 2009;69(7-8):926–936.

[86] AG, G.I.. ????

[87] Irwin, G.R.. Analysis of stresses and strains near the end of a crack traversing a plate. JApplMech 1957;24(3):361–364.

[88] Rybicki, E.F., Kanninen, M.F.. A finite element calculation of stress intensity factors by a modified crack closure integral. Engineering Fracture Mechanics 1977;9(4):931–938.

[89] Raju, I.S.. Calculation of strain-energy release rates with higher order and singular finite elements. Engineering Fracture Mechanics 1987;28(3):251–274.

[90] Zou, Z., Reid, S.R., Soden, P.D., Li, S.. Mode separation of energy release rate for delamination in composite laminates using sublaminates. International Journal of Solids and Structures 2001;38(15):2597–2613.

[91] Krueger, R.. Virtual crack closure technique: History, approach, and applications. Applied Mechanics Reviews 2004;57(1-6):109–143.

[92] Rice, J.R.. A path independent integral and the approximate analysis of strain concentration by notches and cracks. Journal of Applied Mechanics 1968;35:379–386.

[93] Hellen, T.K.. On the method of virtual crack extensions. International Journal for Numerical Methods in Engineering 1975;9(1):187–207.

[94] Parks, D.M.. A stiffness derivative finite element technique for determination of crack tip stress intensity factors. International Journal of Fracture 1974;10(4):487–502.

[95] Griffith, A.A.. The phenomena of rupture and flow in solids. PhilosTransR-SocLondon 1920;221:163–198.

[96] Pagano, N.J., Pipes, R.B.. Some observations on the interlaminar strength of composite laminates. International Journal of Mechanical Sciences 1973;15(8):679–686,IN1–IN2,687–688.

[97] Hashin, Z.. Failure criteria for unidirectional fiber composites. Journal of Applied Mechanics 1980;47(4):329–334.

[98] Barenblatt, G.I.. The mathematical theory of equilibrium cracks in brittle fracture. Advances in Applied Mechanics 1962;7:55–129.

[99] Dugdale, D.S.. Yielding of steel sheets containing slits. Journal of the Mechanics and Physics of Solids 1960;8(2):100–104.

[100] Hillerborg, A., Modéer, M., Petersson, P.E.. Analysis of crack formation and crack growth in concrete by means of fracture mechanics and finite elements. Cement and Concrete Research 1976;6(6):773–781.

[101] Schellekens, J.C.J., Borst, R.D.. A non-linear finite element approach for the analysis of mode-i free edge delamination in composites. International Journal of Solids and Structures 1993;30(9):1239–1253.

[102] Allix, O., Ladevéze, P., Corigliano, A.. Damage analysis of interlaminar fracture specimens. Composite Structures 1995;31(1):61–74.

[103] Mi, Y., Crisfield, M.A., Davies, G.A.O., Hellweg, H.B.. Progressive delamination using interface elements. Journal of Composite Materials 1998;32(14):1246–1272.

[104] Alfano, G., Crisfield, M.A.. Finite element interface models for the delamination analysis of laminated composites: Mechanical and computational issues. International Journal for Numerical Methods in Engineering 2001;50(7):1701–1736.

[105] Camanho, P.P., Davila, C.G., de Moura, M.F.. Numerical simulation of mixed-mode progressive delamination in composite materials. Journal of Composite Materials 2003;37(16):1415–1438.

[106] de Borst, R.. Numerical aspects of cohesive-zone models. Engineering Fracture Mechanics 2003;70(14):1743–1757.

[107] Pinho, S.T., Iannucci, L., Robinson, P.. Formulation and implementation of decohesion elements in an explicit finite element code. Composites Part a-Applied Science and Manufacturing 2006;37(5):778–789.

[108] Aymerich, F., Dore, F., Priolo, P.. Prediction of impact-induced delamination in cross-ply composite laminates using cohesive interface elements. Composites Science and Technology 2008;68(12):2383–2390.

[109] Zhang, Y., Zhu, P., Lai, X.. Finite element analysis of low-velocity impact damage in composite laminated plates. Materials and Design 2006;27(6):513–519.

[110] Abaqus 6.7 user's manual. 2006;.

[111] Corigliano, A., Allix, O.. Some aspects of interlaminar degradation in composites. Computer Methods in Applied Mechanics and Engineering 2000;185(2-4):203–224.

[112] Xu, X.P., Needleman, A.. Numerical simulations of fast crack growth in brittle solids. Journal of the Mechanics and Physics of Solids 1994;42(9):1397–1434.

[113] Martha, L.F., Wawrzynek, P.A., Ingraffea, A.R.. Arbitrary crack representation using solid modeling. Engineering with Computers 1993;9(2):63–82.

[114] Oliver, J.. On the discrete constitutive models induced by strong discontinuity kinematics and continuum constitutive equations. International Journal of Solids and Structures 2000;37(48):7207–7229.

[115] Simo, J.C., Rifai, M.S.. Class of mixed assumed strain methods and the method of incompatible modes. International Journal for Numerical Methods in Engineering 1990;29(8):1595–1638.

[116] Belytschko, T., Moës, N., Usui, S., Parimi, C.. Arbitrary discontinuities in finite elements. International Journal for Numerical Methods in Engineering 2001;50(4):993–1013.

[117] Babuška, I., Melenk, J.M.. The partition of unity method. International Journal for Numerical Methods in Engineering 1997;40(4):727–758.

[118] Ortiz, M., Pandolfi, A.. Finite-deformation irreversible cohesive elements for three-dimensional crack-propagation analysis. International Journal for Numerical Methods in Engineering 1999;44(9):1267–1282.

[119] Jansson, N.E., Larsson, R.. Rotational interface formulation for delamination analysis of composite laminates. Computers and Structures 2003;81(30-31):2705–2716.

[120] Turon, A., Camanho, P.P., Costa, J., Dávila, C.G.. A damage model for the simulation of delamination in advanced composites under variable-mode loading. Mechanics of Materials, 2006;38(11):1072–1089.

[121] Mazars, J.. Mechanical Damage and Fracture of Concrete Structures. Oxford: Pergamon Press; 1982.

[122] Simo, J.C., Ju, J.W.. Strain- and stress-based continuum damage models-i. formulation. International Journal of Solids and Structures 1987;23(7):821–840.

[123] Oliver, J., Cervera, M., Oller, S., Lubliner, J.. Isotropic damage models and smeared crack analysis of concrete. Computer Aided Analysis and Design of Concrete Structures 1990;2:945–958.

[124] Benzeggagh, M.L., Kenane, M.. Measurement of mixed-mode delamination fracture toughness of unidirectional glass. Composites Science and Technology 1996;56(4):439–449.

[125] Ye, L.. Role of matrix resin in delamination onset and growth in composite laminates. Composites Science and Technology 1988;33(4):257–277.

[126] Bažant, Z.P., Oh, B.H.. Crack band theory for fracture of concrete. Matériaux et Constructions 1983;16(3):155–177.

[127] Remmers, J.J.C., Borst, R.D., Needleman, A.. A cohesive segments method for the simulation of crack growth. Computational Mechanics 2003;31(1-2 SPEC.):69–77.

[128] Turon, A., Davila, C.G., Camanho, P.P., Costa, J.. An engineering solution for mesh size effects in the simulation of delamination with cohesive zone models. 2005.

[129] Turon, A., Camanho, P.P., Costa, J., Renart, J.. Accurate simulation of delamination growth under mixed-mode loading using cohesive elements: Definition of interlaminar strengths and elastic stiffness. Composite Structures 2010;.

[130] Yang, Q., Cox, B.. Cohesive models for damage evolution in laminated composites. International Journal of Fracture 2005;133(2):107–137.

[131] Rice, J.R.. The mechanics of earthquake rupture. Physics of the Earth's Interior 1980;:555–649.

[132] Prinz, R., Cao, L.. Analysis of strain-energy-release rates for unidirectional graphite/epoxy laminates with separated central plies under fatigue loading. Proceedings of Seventh International Conference on Composite Materials: ICCM-VII (Beijing 1989;.

[133] Reeder, J.R., Jr., J.H.C.. Mixed-mode bending method for delamination testing. AIAA Journal 1990;28(7):1270–1276.

[134] Reeder, J.R., Jr., J.H.C.. Redesign of the mixed-mode bending delamination test to reduce nonlinear effects. Journal of Composites Technology and Research 1992;14(1):12–19.

[135] Crews, J.H., Reeders, J.R.. Mixed-mode bending method apparatus for delamination testing. NASA TM 1998;:100662.

[136] Kinloch, A.J., Wang, Y., Williams, J.G., Yayla, P.. The mixed-mode delamination of fibre composite materials. Composites Science and Technology 1993;47(3):225–237.

[137] Carlsson, L.A., Jr., J.W.G., Pipes, R.B.. On the analysis and design of the end notched flexure (enf) specimen for mode ii testing. Journal of Composite Materials 1986;20(6):594–604.

[138] Ye, L., Prinz, R., Klose, R.. Characterization of interlaminar shear fracture toughness and delamination fatigue growth of composite materials using tct specimen. Report IB 1990;.

[139] König, M., Krüger, R., Kussmaul, K., Alberti, M.V., Gädke, M.. Characterizing static and fatigue interlaminar fracture behavior of a first generation graphite/epoxy composite. ASTM Special Technical Publication 1997;1242:60–81.

[140] Bergan, P.G., Mollestad, E.. An automatic time-stepping algorithm for dynamic problems. Computer Methods in Applied Mechanics and Engineering 1985;49(3):299–318.

[141] 3039M-00, A.S.D.D.. Standard test method for tensile properties of polymer matrix composite materials 2000;.

[142] 3410-87, A.S.D.. Standard test method for compressive properties of unidirectional or cross-ply fibre-resin composites of unidirectional or cross-ply fibre-resin composites 1987;.

[143] D3518/3518M-94, A.. Standard test method for in-plane shear response of polymer matrix composite materials by test of a +-45 laminate 1994;.

[144] 5528-01, A.D.. Standard test methods for mode i interlaminar fracture toughness of unidirectional fibre-reinforced polymer matrix composites 2001;.

[145] Martin, R.H., Elms, T., Bowron, S.. Characterization of mode ii delamination using the 4enf. Proceedings of the 4th European Conference on Composites: Testing and Standardization 1998;:161–170.

[146] Pinho, S.T., Robinson, P., Iannucci, L.. Fracture toughness of the tensile and compressive fibre failure modes in laminated composites. Composites Science and Technology 2006;66(13):2069–2079.

[147] Maimí, P., Camanho, P.P., Mayugo, J.A., Dávila, C.G.. A continuum damage model for composite laminates: Part i constitutive model. Mechanics of Materials 2007/10;39(10):897–908.

[148] Maimí, P., Camanho, P.P., Mayugo, J.A., Dávila, C.G.. A continuum damage model for composite laminates: Part ii computational implementation and validation. Mechanics of Materials 2007/10;39(10):909–919.

[149] Ochoa, O.O.. Finite Element Analysis of Composite Laminates. 1992.

[150] Kollár, L., Springer, G.S.. Mechanics of composite structures. Cambridge etc.: Cambridge University Press; 2003. ISBN 0521801656.